

# Modelling of Tape Casting for Ceramic Applications

**Jabbari, Masoud**

*Publication date:*
2014

*Document Version*
Peer reviewed version

# Modelling of Tape Casting for Ceramic Applications


Masoud Jabbari

Department of Mechanical Engineering

Technical University of Denmark

A thesis submitted for the degree of

*Doctor of Philosophy*

February 2014

**To my father ...**

# Acknowledgements

This work has been carried out at the Department of Mechanical Engineering (MEK), Technical University of Denmark (DTU), during the period 2011-2014. The work was supervised by Professor Jesper H. Hattel (MEK), and co-supervised by Professor Nini Pryds from DTU Energy Conversion (EC). The work was funded by the Danish Agency for Science Technology and Innovation (FTP) (Contract No. 09-072888), which is part of the Danish Council for Independent Research (DFF). This Ph.D. project was a part of a larger project called "optimized processing of multi-material architectures for functional ceramics" (OPTIMAC). The project consists of three work packages and DTU-MEK was the leader of WP1 whose focus was on process modelling. The present project was carried out in close collaboration between DTU-MEK and DTU-EC.

I would like to express my sincere gratitude to Professor Hattel for his unfailing guidance and support throughout my studies, critical review of my work, and most importantly for his great patience and enthusiasm. He has set an example I hope to match some day. I would like to thank Professor Pryds for the fruitful discussions and being more than a co-supervisor.

I would like to express my thanks to Dr. Christian Bahl and Ms. Regina Bulatova as well as Dr. Anderas Kaiser and Mrs. Cristine Grings Schmidt from DTU Energy Conversion (EC) for the fruitful meetings and discussions that we have had and for the continuous collaboration that we have made.

Many thanks to Dr. Jon Spangenberg for being highly inspirational and helpful from first encounter. I would also like to thank Dr. Jesper Thoborg for always being ready for any kind of support.

I extend my deepest gratitude to all my colleagues at the Process Modelling Group for creating such a nice and warm workplace filled with humor. Furthermore, my fellow Ph.D. students; Raphal Cominal, Peter Christiansen, Mads Rostgaard Sonne, Ismet Baran, Patrick Guerrier, Sankhya Mohanty, Shizhao Li, as well as my former colleagues Dr. Micheal W. Nielsen, Dr. Elham Moumeni, Dr. Ali Sarhadi, Dr. Cem C. Tutum and Dr. Petr Kotas are wished the best of luck with their research projects and careers.

It was a privilege to meet Professor James M. McDonough at the University of Kentucky, Computational Fluid Dynamic Group and have an opportunity to discuss on the numerical solution of the Navier-Stokes equations and modelling of non-Newtonian fluids. My keen appreciation goes to him for the inspiration he provided. Additionally, I deeply thank my new friends; Mohammad Souri, Hojjat Sarvari, Mohammad Saghaian, and all the others for making my stay in Kentucky an incredible experience.

I am deeply and forever indebted to my parents for their love, support and encouragement throughout my entire life. It was under their watchful eye that I gained so much drive and an ability to tackle challenges head on.

Finally, and most importantly, I would like to express my deepest appreciations to my beloved wife, my better half, Elham. She already has my heart so I will just give her a heartfelt "thanks.". Elham, if I wrote down everything I ever wanted in a wife and best friend I would not have believed I could meet anyone better!

Masoud Jabbari

Kgs. Lyngby, January 2014

## Abstract

Functional ceramics find use in many different applications of great interest, e.g. thermal barrier coatings, piezoactuators, capacitors, solid oxide fuel cells and electrolysis cells, membranes, and filters. It is often the case that the performance of a ceramic component can be increased markedly if it is possible to vary the relevant properties (e.g. electrical, electrochemical, or magnetic) in a controlled manner along the extent of the component. Such composites in which ceramic layers of different composition and/or microstructure are combined provide a new and intriguing dimension to the field of functional ceramics research. Advances in ceramic forming have enabled low cost shaping techniques such as tape casting and extrusion to be used in some of the most challenging technologies. These advances allow the design of complex components adapted to desired specific properties and applications. However, there is still only very limited insight into the processes determining the final properties of such components. Hence, the aim of the present PhD project is to obtain the required knowledge basis for the optimized processing of multi-material functional ceramics components.

Recent efforts in the domain of ceramic processing are generally focused on the control of the microstructure while the importance of shaping is often underestimated. Improved performance requires the design and shaping of both controlled architectures and microstructures. Novel functionally graded ceramic materials may be formed by multilayers or adjacent grading of different ceramic materials. Such grading is often desired for optimal performance. An example is when there is a gradient in temperature or chemical environment along the component during operation; in this case the properties of each section of the component should be optimized for the local environment by grading. The grading may be between entirely different ceramic materials or merely a minor compositional alteration within one type of material. However, there are several challenges to be met for the successful fabrication of such complex structures. Rheological properties play an extremely important role for the co-processing of more than one material. Only by matching the rheological properties of the different pastes, a reproducible and well defined gradient composite will be formed.

*Tape casting* involves the casting of a slurry onto a flat moving carrier surface. The slurry passes beneath a knife edge (doctor blade) as the carrier surface advances along a supporting table. The solvents evaporate to leave a relatively dense flexible sheet that may be stored on rolls or stripped from the carrier in a continuous process. Today, multilayers are achieved by laminating layers of different materials on top of each other. The challenge is to be able to tape cast layers of different materials simultaneously both stratified in the horizontal and in the lateral direction. Understanding how to achieve that and perfection of such a technique will open up a large variety of applications.

General challenges with this process is, as mentioned, controlling the rheological

properties of the slurries/pastes as they strongly affect the process and the quality of the final product, maintaining uniform composition during the process and controlling/understanding the shrinkage in drying and sintering. Furthermore, understanding the tape delamination and film cracking of multilayers as well as of interface fracture modes in multilayers is also an important topic that needs to be considered and understood.

In the present PhD thesis the focus is on the numerical modelling of the tape casting process of functionally graded ceramic materials for fuel cell applications as well as magnetic refrigeration. Models to simulate the shaping of monolayer/multilayer and graded materials by tape casting are developed. The emphasis is on analyzing the entry flow of multiple slurries from the reservoir into the doctor-blade region as well as the exit region where a free surface (meniscus) forms. This encompasses a detailed fluid model capable of tracking the material flow/deformation taking the formation of the free surface into account. In the work it was chosen to focus on developing analytical/numerical flow solvers in both Ansys Fluent and Matlab.

Analytical approaches for fluid flow analysis in the tape casting process showed that a relative good agreement could be achieved between the results of the modelling and the experimental data. The study, furthermore, demonstrated that the aforementioned agreement was increased by improving the steady state model with a quasi-steady state analytical model. In order to control the most important process parameter, tape thickness, the two-doctor blade configuration was also modeled analytically. The model was developed to control the tape thickness based on the machine configuration and the material constants. Many of the affecting parameters in the process were embedded and they can easily be varied to evaluate their influence.

This study showed that using computational fluid dynamics (CFD) the process can be modeled with more details in order to better control the produced tapes. Very importantly, the free surface of the ceramic as leaving the doctor blade region was modeled. The rheological behavior of the ceramic slurry was also taken into account. The influence of the main process parameters, i.e. the substrate velocity, the initial slurry load, and the doctor blade height, were investigated. Based on the developed model, one phenomenon inherit to the process called side flow was also modeled. The results showed that to reach a desired uniform tape the side flow factor should be kept as close as to the value of one. The impact of the process parameters were also discussed in details in order to control the side flow, and consequently the tape thickness. Moreover, a CFD model was developed to simulate multiple flow of the ceramic slurry in tape casting. The simulation was aimed to analyze the production of functionally graded ceramics (FGCs) which are used for magnetic refrigeration applications.

Numerical models were developed to track the migration of the particles inside the ceramic slurry. The results showed the presence of some areas inside the ceramic in

which the concentration of the particles is higher compared to other parts, creating the resulting packing structure. And finally a numerical code was developed to simulate the drying process. The results showed that the mass loss due to the evaporation is increasing close to linearly with the drying time corresponding to an almost constant drying rate. However, the rate starts to decrease after some time in the simulation. This is in good agreement with the real life process where the drying categorized into two stages: (1) constant rate period (CRP), in which the rate of evaporation per unit area of the drying surface is independent of time, (2) falling rate period (FRP), in which the evaporation rate is reduced, as a consequence of low migration of the water from the bottom layers to the top ones due to diffusion (which is highly dependent to the temperature).

# Resumé

Funktionelle keramiske materialer finder anvendelse i mange forskellige applikationer af industriel interesse, fx termiske barrierebelægninger, piezoactuatorer, kondensatorer, solid oxide brændselsceller og elektrolyseceller, membraner og filtre. Ydelsen af den keramiske komponent kan ofte øges markant, hvis det er muligt at variere de relevante egenskaber (fx elektriske, elektrokemiske eller magnetiske) på en kontrolleret måde "langs med" eller "igennem" komponenten. Sådanne keramiske kompositmaterialer med keramiske lag af forskellig sammensætning og/eller mikrostruktur åbner helt nye muligheder inden de tekniske anvendelser af funktionel keramik.

Udviklingen indenfor fremstillingsteknologier med relativt lave omkostninger såsom tape casting og ekstrudering har gjort det muligt at fremstille komplekse keramiske komponenter, der er tilpasset til de ønskede egenskaber og anvendelser. Forståelsen for de fænomener og processer, der bestemmer de endelige egenskaber af de fremstillede komponenter er dog i dag stadig relativt sparsom. Det er derfor formålet med nærværende ph.d.-projekt at adressere denne problemstilling for derved at opnå øget videnskabelig indsigt, der kan danne grundlag for optimerede multi-materiale funktionelle keramikkomponenter.

Det meste videnskabelige arbejde indenfor keramisk processering har været fokuseret på at kunne forstå og kontrollere den resulterende mikrostruktur, hvorimod vigtigheden af endelig geometri, form og tolerancer ofte er blevet undervurderet. Der er derfor ingen tvivl om, at både mikrostrukturer såvel som den overordnede komponentarkitektur skal adresseres mere ligeligt, hvis ønsket om optimerede keramiske komponenter skal realiseres.

Funktionaliteten i funktionelle keramiske materialer opnås for eksempel ved at have flere lag af keramiske materialer, der giver den tilsigtede "graduering" igennem komponenten. Et eksempel på dette kan være, når der f.eks. optræder en temperaturgradient igennem komponenten under drift, og det derfor er ønskeligt at komponentens egenskaber gennem tykkelsen er tilpasset denne driftssituation. Gradueringen gennem materialet kan opnås ved at lade lag af helt forskellige keramiske materialer grænse op til hinanden eller ved at indbygge relativt små ændringer i kompositionen af et keramisk materiale igennem komponenten. Dette stiller dog store krav til de reologiske egenskaber af de forskellige keramiske "slurries", idet disse i høj grad kontrollerer materialeflowet under processen.

Tape casting er en proces, hvor den keramiske "slurry" bæres frem af et fladt bånd, der bevæger sig og derved "trækker" den keramiske pasta ud, efter den har forladt "doctor blade" området. Efter tørring og sintring opnås et relativt fleksibelt, tyndt plademateriale, som kan rulles op og opbevares på store ruller. Ønskes en flerlaksstruktur opnås den i dag ved at tape caste individuelle plader og derefter fremstille et laminat

af dem. Udfordringen ligger i at tape caste lagdelte materialer (både vertikalt og horisontalt) i en enkelt proces i stedet for flere. Hvis det kan kontrolleres og styres på den rette måde, vil det åbne for en række nye applikationer for tape casting.

De generelle udfordringer indenfor tape casting er som nævnt at styre de reologiske egenskaber af de keramiske "slurries" og forstå deres opførsel under processen og derved sikre en ensartet sammensætning under processen for derved at have det bedst mulige udgangspunkt for den efterfølgende tørring og sintring. Dertil kommer forståelsen af revnedannelse under delaminering i plader med flere lag fremstillet ved tape casting.

I nærværende ph.d. afhandling er der blevet arbejdet med modellering af tape casting af funktionelle keramiske materialer til brændselscelle applikationer samt magnetisk køling. Der er udviklet modeller for både enkeltlag og flere lag. Fokus har været på at beskrive materialeflowet fra slurrybeholderen til området, hvor slurrien forlader doctor blade regionen, og der dannes en fri væskeoverflade. Dette er blevet adresseret v.h.a. både analytiske og numeriske modeller implementeret Ansys-Fluent og Matlab.

Flere analytiske metoder til beskrivelse af materialeflowet i tape casting processen viste sig at give resultater, der var i god overensstemmelse med de eksperimentelle data. Studiet demonstrerede yderligere, at overensstemmelsen blev forbedret, da den analytiske stationære løsning blev modificeret til at være quasi-stationær. For at kunne kontrollere tykkelsen af tape-laget, der er den vigtigste enkeltstående procesparameter, blev tilfældet med two-doctor blade også inkluderet i den analytiske løsning. Modellen kan således bruges på simpel vil til at kontrollere tykkelsen af tape-laget baseret på maskinkonfigurationen og materialeparametrene.

Dette studie understregede ydermere det forhold, at hvis processen skal modelleres i mere detalje er det nødvendigt at bruge computational fluid dynamics (CFD). Vigtigt i denne sammenhæng er det at kunne modellereden frie overflade, når den forlader "doctor blade" området. Den reologiske opførsel af den keramiske "slurry" blev også taget i betragtning. De vigtige procesparametre, så som underlagets hastighed, den initiale "slurry" højde og "doctor blade" højden, blev derefter undersøgt. Modellen var også i stand til at modellere to forskellige materialer, der flød ved siden af hinanden (side flow). Resultaterne for denne undersøgelse viste at "side flow" faktoren skulle være tæt på en for at få et uniformt materiale. Det blev også diskuteret hvilken indflydelse de forskellige procesparametre havde på "side flow" og tykkelsen af materialet. Derudover blev der udviklet en CFD model, der kunne simulere tape casting med flere forskellige materialer. Målet for disse simuleringer var at analysere funktionelle keramiske materialer, der anvendes i magnetisk køling.

Endelig blev flere numeriske modeller udviklet til at følge partiklerne inde i den keramiske "slurry". Resultaterne viste, at der opstod områder med høje partikelkoncentrationer i det keramiske materiale, hvilket resulterede i en mere tæt struktur. Afslutningsvis blev tørringsprocessen simuleret med en numerisk kode, der var udviklet

til formålet. Disse resultater viste, at fordampningsvægttabet forøges nærmest lineært med tørringstiden og dette svarer til en næsten konstant tørringshastighed. Denne hastighed formindskes dog efter noget tid i simuleringen. Dette er i god overensstemmelse med den virkelige proces, hvor tørringen typisk kategoriseres i to stadier: (1) Den konstante hastigheds periode, hvori hastigheden af fordampningen per enhed af tørret overflade er uafhængig af tiden og (2) Den faldende hastighedsperiode, hvor vandet pga. diffusion (som er yderst afhængig af temperaturen) bevæger sig fra de nederste lag til de øverste lag og derved formindsker fordampningshastigheden.

# List of publications

## Appended Publications

1. M. Jabbari, R. Bulatova, J. Hattel, C. R. H. Bahl, "Quasi-steady State Power Law Model for the Flow of $(La_{0.85}Sr_{0.15})_{0.9}MnO_3$ Ceramic Slurry in Tape Casting", *Materials Science & Technology* 29 (2013) 1080-1087 [PAPER I].

2. M. Jabbari, J. Hattel, "Numerical Modelling of the Side Flow in Tape Casting of a Non-Newtonian Fluid", *Journal of the American Ceramic Society* 96 (2013) 1414-1420 [PAPER II].

3. M. Jabbari, J. Hattel, "Bingham-Plastic Fluid Flow Model in Tape Casting of Ceramics Using Two Doctor Blades–An Analytical Approach", *Materials Science & Technology* 30 (2014) 283-288 [PAPER III].

4. M. Jabbari, J. Spangenberg, J. Hattel, "Modeling of the Interface Behavior in Tape Casting of Functionally Graded Ceramics for Magnetic Refrigeration Parts", *International Journal of Refrigeration* 36 (2013) 2403-2409 [PAPER IV].

5. M. Jabbari, R. Bulatova, J. Hattel, C. R. H. Bahl, "An Evaluation of Interface Capturing Methods in a VOF Based Model for Multiphase Flow of a Non-Newtonian Ceramic in Tape Casting", *Applied Mathematical Modelling* 38 (2014) 3222-3232 [PAPER V].

6. M. Jabbari, J. Spangenberg, J. Hattel, "Particle Migration Using Local Variation of the Viscosity (LVOV) Model in Tape Casting of Ceramics", *Applied Mathematical Modelling*, 2013 (under review) [PAPER VI].

7. M. Jabbari, J. Hattel, "Modelling the drying process in tape casting with a simple ceramics-water system", *Continuum Mechanics and Thermodynamics*, 2014 (to be submitted) [PAPER VII].

## Non-Appended Publications

1. M. Jabbari, J. Hattel, "Numerical Modelling of Fluid Flow in the Tape Casting Process", A I P Conference Proceedings Series 1389 (2011) 143-146. (Numerical Analysis and Applied Mathematics, ICNAAM 2011, 2011, Halkidiki, Greece).

2. M. Jabbari, J. Hattel, "Numerical modelling of the Flow of a Power Law Ceramic Slurry in the Tape Casting Process", AES-ATEMA' 2012 Tenth International Conference on Advances and Trends in Engineering Materials and their Applications, June 18-22, 2012, Montreal, Canada.

3. M. Jabbari, R. Bulatova, J. H. Hattel, C. R. H. Bahl, "Interface Oscillation in the Side-by-Side (SBS) Tape Casting of Functionally Graded Ceramics (FGCs)", American Physical Society, 65th Annual DFD Meeting, November 18-20, 2012, San Diego, USA.

4. R. Bulatova, M. Jabbari, K. B. Andersen, C. R. H. Bahl, "The Variation of Interface Formation with Slurry Viscosity Change in Side-By-Side Tape Casting", 5th International Conference on Shaping of Advanced Ceramics, January 29-31, 2013, Mons, Belgium.

5. M. Jabbari, J. Spangenberg, J. Hattel, "Interface Behavior in Functionally Graded Ceramics for the Magnetic Refrigeration: Numerical Modeling", *Journal of Applied Mechanics and Materials* 325-326 (2013) 1362-1367.

6. M. Jabbari, J. M. McDonough, J. Hattel, "Application of a projection method for simulating flow of a non-Newtonian fluid", *Computers & Fluids*, 2014 (under review)

7. M. Jabbari, J. Hattel, R. Bulatova, C. R. H. Bahl, "On the Modelling of Tape Casting: A Review of Current Methods and New Trends", *Journal of the American Ceramic Society*, 2014 (to be submitted).

# Contents

**Contents** xiii

**List of Figures** xvii

**List of Tables** xxi

**1 Introduction** 1

1.1 Tape casting process . . . 1

1.1.1 Applications of tape casting . . . 2

1.1.1.1 Substrates . . . 2

1.1.1.2 Multilayered ceramics . . . 3

1.1.1.3 Solid oxide fuel cell (SOFC) . . . 3

1.1.1.4 Functionally graded materials (FGMs) . . . 3

1.2 Existent models . . . 4

1.2.1 Rheological investigations . . . 4

1.2.2 Numerical/analytical models . . . 5

1.3 Objectives of the Thesis . . . 6

1.4 Methodology . . . 6

1.5 Structure of the thesis . . . 7

**2 Theory** 9

2.1 Governing Equations . . . 9

2.2 Rheological Models . . . 10

2.2.1 Shear-thinning . . . 11

2.2.2 Visco-plastic fluids . . . 13

2.3 Multiphase Flow Models . . . 14

2.3.1 Volume of Fluid (VOF) . . . 15

2.3.2 Mixture Model . . . 16

2.4 Particle Migration . . . 17

**3 Modelling Approaches** **21**
3.1 Analytical Models . . . 21
3.1.1 Steady State Model . . . 21
3.1.2 Quasi-steady state model . . . 24
3.1.3 Steady state two doctor blade model . . . 27
3.2 Numerical models . . . 29
3.2.1 General fluid flow . . . 30
3.2.2 Free surface tracking . . . 31
3.2.3 Side flow . . . 32
3.2.4 Side-by-Side Tape Casting . . . 33
3.2.5 Tracking of Particles . . . 35

**4 Drying Kinetics** **41**
4.1 Introduction . . . 41
4.2 Mathematical model . . . 45
4.2.1 Simulation domain . . . 45
4.2.2 Thermal calculations . . . 46
4.2.3 Diffusion . . . 49
4.3 Preliminary Results . . . 49

**5 Summary of Appended Papers** **57**
5.1 PAPER I . . . 57
5.2 PAPER II . . . 57
5.3 PAPER III . . . 58
5.4 PAPER IV . . . 58
5.5 PAPER V . . . 59
5.6 PAPER VI . . . 59
5.7 PAPER VII . . . 60

**6 Conclusions and Future Work** **61**
6.1 Summary of Results . . . 61
6.1.1 Analytical Models . . . 61
6.1.2 Numerical Models . . . 61
6.2 Future Work . . . 63

**References** **65**

**Appdx A** **75**

**Appdx B** **85**

**Appdx C** 93

**Appdx D** 101

**Appdx E** 109

**Appdx F** 121

**Appdx G** 149

# List of Figures


1.1 The tape casting process [th1]. . . . . 2

1.2 (a) Schematic illustration of a SOFC, (b) cross-sectional fracture surface of anode support, anode and electrolyte produced by tape casting after application of cathode and current collector and second firing step [Shanti et al., 2012]. . . . . 3

1.3 Schematic illustration of the newly developed method of tape casting to produce FGMs for magnetic refrigeration applications [Dinesen et al., 2012]. . . . . 4

2.1 Rheological classification of different flows [Jabbari and Hattel, 2011]. . 11

2.2 Rheology behavior of LSM ceramic [Jabbari et al., 2013b]. . . . . 13

2.3 The influence of the particle volume fraction on (a) the viscosity based on equation (2.15) and (b) the settling rate of the particles based on equation (2.16) [PAPER VI]. . . . . 19

3.1 Schematic geometry of the tape casting machine in 2D. . . . . 22

3.2 Results of analytical modelling for (a) velocity profile below the doctor blade region with different pressure head [Huang et al., 1997; Joshi et al., 2002], and (b) influence of the casting velocity on the tape thickness [Joshi et al., 2002; Pitchumani and Karbhari, 1995]. . . . . 23

3.3 Schematic illustration of the effect of the increased pressure head on the tape thickness ($P_1 > P_2 > P_3$) [Kim et al., 2006]. . . . . 25

3.4 Effect of substrate velocity on tape thickness with a doctor blade height of 1 $mm$ [Jabbari et al., 2013b]. ([PAPER I]) . . . . . 26

3.5 Comparison of the quasi-steady state model proposed by the author with steady state model and experiments for $v_0 = 3.67mm/s$ [Jabbari et al., 2013b]. ([PAPER I]) . . . . . 26

3.6 The non-dimensional velocity profile in the doctor blade region on the basis of different $\varpi$ [Jabbari and Hattel, 2011]. . . . . 27

3.7 Results of modelling and their comparison with experimental data for tape casting of LSM slurry with a substrate velocity of $v_0 = 3.67mm/s$ and an initial slurry height of (a) $H_0 = 6.67mm$ and (b) $H_0 = 20.8mm$ [Jabbari et al., 2013b]. ([PAPER I]) . . . . . 28

3.8 2D illustration of the tape casting process with two doctor blades [Jabbari and Hattel, 2014]. ([PAPER III]) . . . . . 28

3.9 Variation of the tape thickness by the substrate velocity for (a) $h_2 = 4mm$, and (b) $h_2 = 5mm$ [Jabbari and Hattel, 2014]. ([PAPER III]) . . 29

3.10 Shear rates below the doctor blade region for (a) $v_0 > v_{cr}$ and different $k$, and (b) $v_0 \leq v_{cr}$ and different $k$. The value of the critical velocity in these cases is equal to $10.5mm/s$ [Jabbari and Hattel, 2014]. ([PAPER III]) . . . . . 30

3.11 Impact of increasing the value of the tape thickness on the required height of the slurry behind both doctor blades with (a) sufficient and (b) insufficient belt velocity [Jabbari and Hattel, 2014]. ([PAPER III]) . 30

3.12 Flow pattern inside the reservoir solved by (a) finite element formulation [Gaskell et al., 1997], and (b) corresponding finite volume modelling that we conducted. . . . . 31

3.13 Flow of LSM ceramic slurry in tape casting in different simulation time (a) 2.5 sec, (b) 5 sec, and (c) 7.5 sec. The dark blue surface is the symmetry plane. . . . . 32

3.14 Numerical modelling and corresponding experiments values of side flow factor ($\alpha$) influenced by (a) substrate velocity, (b) doctor blade height, and (c) slurry height [Jabbari and Hattel, 2013]. The dash lines are guides to the eye. ([PAPER II]) . . . . . 33

3.15 (a) Schematic example of FGCs used in magnetic refrigeration, and (b) schematic representation of the interface between the two adjacent layers [Jabbari et al., 2012]. ([PAPER IV]) . . . . . 35

3.16 The change in the predicted interface between the adjacent layers for different cases, (a) $v_0 = 3.67mm/s$, $\rho_{F2} = 2\rho_{F1} = 4kg/m^3$ and $\mu_{F2} = 2\mu_{F1} = 6Pa.s$, (b) $v_0 = 3.67mm/s$, $\rho_{F2} = 2\rho_{F1} = 4kg/m^3$ and $\mu_{F2} = \mu_{F1} = 3Pa.s$, (c) $v_0 = 7.34mm/s$, $\rho_{F2} = 2\rho_{F1} = 4kg/m^3$ and $\mu_{F2} = 2\mu_{F1} = 6Pa.s$, (d) $v_0 = 7.34mm/s$, $\rho_{F2} = 2\rho_{F1} = 4kg/m^3$ and $\mu_{F2} = \mu_{F1} = 3Pa.s$. The gray lines indicate the geometry at the exit from the tape caster [PAPER IV]. . . . . 36

3.17 Distribution of the volume fraction for the particles inside the ceramic slurry, (a) without applying, and (b) with applying the LVOV model [PAPER VI]. . . . . 37

3.18 (a) The velocity profile, and (b) the shear rate distribution in the doctor blade region [PAPER VI]. . . . . 38
3.19 Distribution of the volume fraction for the particles inside the ceramic slurry with the increase (doubled) substrate velocity [PAPER VI]. . . . 38
3.20 (a) The velocity profile, and (b) the shear rate distribution in the doctor blade region [PAPER VI]. . . . . 39
3.21 Distribution of the volume fraction in the thickness of the produced tapes at two different distances of doctor blade exit, (a) $d = 10$, and (b) $d = 20cm$ [PAPER VI]. . . . . 40

4.1 Schematic of the tape casting process with three sub-processes [PAPER VII]. . . . . 42
4.2 Schematic illustration for distribution of solvent content for (a) ideal, (b) best obtainable, and (c) worst cases[Mistler and Twiname, 2000]. . . 44
4.3 Schematic illustration of the simulation domain [PAPER VII]. . . . . 46
4.4 Simulation domain for a 1D inter-diffusion phenomenon. . . . . 50
4.5 Concentration variation along the $x$ axis for $L_x = 400\mu m$, and for different diffusion coefficient of (a) $D = 1e - 8$, and (b) $D = 1e - 7$. . . . . 50
4.6 Fitted data used for the temperature-dependent diffusion coefficient of water [Holz et al., 2000] [PAPER VII]. . . . . 52
4.7 (a) Variation of water content due to evaporation, and (b) the temperature profiles for the top control volume in the tape [PAPER VII]. . . . 53
4.8 Amount of mass loss for three different tape thickness [PAPER VII]. . . 54
4.9 The results of numerical modelling for the different drying modes for the tape thickness of $\delta = 400\mu m$ [PAPER VII]. . . . . 55

# List of Tables

1.1 List of existent models based on the rheological behavior. . . . . 5
1.2 List of existent models based on the solution approaches. . . . . 5

4.1 Thermo-physical material properties used in this study . . . . . 52

6.1 Updated version of Table 1.1 based on the findings of this thesis . . . . 62
6.2 Updated version of Table 1.2 based on the findings of this thesis . . . . 63

# Chapter 1

# Introduction

This chapter includes an introduction to the present thesis. A brief introduction of the tape casting process together with its different applications will be given in section 1.1. A short review of the existent models in the tape casting process will be given in section 1.2, and based on this the objectives of this thesis will be presented in section 1.3. The methodologies applied to achieve the objectives will be discussed in section 1.4. Finally, the structure of the thesis is presented in section 1.5.

## 1.1 Tape casting process

Tape Casting was first introduced in the 1940s during the second world war when there was a serious lack of the quartermaster materials to produce mica capacitors. In tape casting, sometimes referred to as the doctor-blade process, the slurry is spread over a surface using a carefully controlled blade referred to as a doctor blade. For the production of long tapes, the blade is stationary and the surface moves, whereas for the production of short tapes in the laboratory, the blade is pulled over a stationary surface. The schematic of the tape casting process from beginning (powder preparation) to the end, is illustrated in Figure 1.1. The tape casting process was firstly reported publicly by Howatt et al. [Howatt et al., 1947] to produce thin ceramic sheets for usage of capacitor dielectrics, and was shortly after applied to industrial production of ceramic capacitors [Howatt, 1952].

Years after, Stetson and Gyurk [Stetson and Gyurk, 1967] prepared alumina ($Al_2O_3$) substrates by tape casting, which were used as substrates for thin film circuits, devices, and integrated circuits. Meanwhile, Schwartz and Kirkpatrick [Schwartz and Kirk-

patrick, 1967] together with the IBM corporation developed a layer packaging material for use in computers by means of the tape casting process. In the 1970s many new products were successfully developed and a number of tape casting applications emerged [Bellosi and Vincenzini, 1979; Fiori et al., 1979; Newnham et al., 1978]. Many works on materials development and process improvement were published in the 1980s-1990s [Bowen, 1980; Chartier and Bruneau, 1993; Claaen and Claussen, 1992; Hotza and Greil, 1995; Lindqvist and Lidn, 1997; Mikeska and Cannon, 1988; Schwartz, 1984; Vasconcelos et al., 1998; Yamamoto, 1989]. Basically this era was a period in which the technology matured and new applications were being explored, such as the production of thin membranes for fuel cells [Appleby, 1996; Riley, 1990]. Most of the work later on is dedicated to the different material investigations and development of different products by means of tape casting.

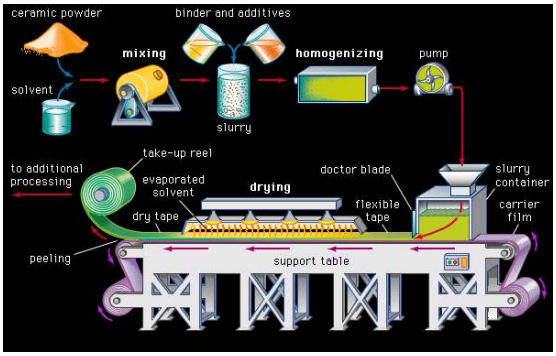


Figure 1.1: The tape casting process [th1].

### 1.1.1 Applications of tape casting

As mentioned earlier, the initial motivation for the tape casting process was to produce thin ceramic sheets for usage in capacitors. However, after almost 60 years, the usage of the tape casting process has become more broad in the ceramic industry. A summary of the different applications of tape casting will be given shortly henceforth.

#### 1.1.1.1 Substrates

For many years almost all of the (single-layered) substrate materials produced for the electronics industry were manufactured by tape casting. Substrates can be defined as the carrier or "backbone" of the electronic circuit. They are the ceramic insulator upon which the circuitry is deposited and patterned. These substrates range in size from as small as $6 \times 6mm$ $(0.25 \times 0.25in)$ to as large as $30 \times 30cm$ $(12 \times 12in)$, and in some cases larger sizes have been produced. What all of these substrates have in common is their very small thickness, usually $1.5mm$ $(0.060in)$ or less.

#### 1.1.1.2 Multilayered ceramics

Multilayered ceramic packages (MLC) would not exist if tape casting had not been invented. The basis for the multilayer industry is the ability to individualize layers with respect to metallization and via interconnections and then to laminate a set of these individual layers together into a package that can be sintered into a monolithic structure. Multilayered ceramic packages with as few as two layers up to structures with as many as a hundred or more layers are common in the electronic ceramics industry today [Yuping et al., 2000]. Moreover, multilayered ceramics produced by tape casting, has also been developed and used for flue gas purification [He et al., 2013], thus underlying the growing diversity of today's applications of the tape casting process.

#### 1.1.1.3 Solid oxide fuel cell (SOFC)

Solid oxide fuel cells (SOFCs) are generally based on the same principle as the oxygen sensor, where the electrical energy is produced from a reaction of gases such as hydrogen and oxygen or natural gas and oxygen with water as a by-product [Stver et al., 2004]. The electrolyte in these fuel cells is the stabilized zirconia, which becomes a conductor of oxygen ions at elevated temperatures. In many cases the zirconia membrane, which is relatively large in the $x$ and $y$ directions and has a very thin cross section (see Figure 1.2) is manufactured by tape casting.

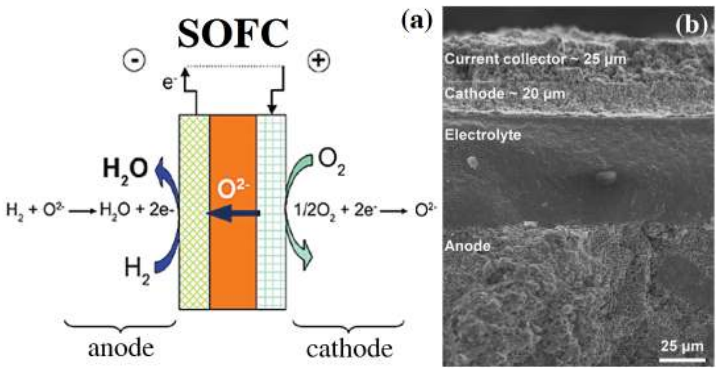


Figure 1.2: (a) Schematic illustration of a SOFC, (b) cross-sectional fracture surface of anode support, anode and electrolyte produced by tape casting after application of cathode and current collector and second firing step [Shanti et al., 2012].

#### 1.1.1.4 Functionally graded materials (FGMs)

A considerable amount of research has been conducted recently to produce functionally gradient materials (FGMs) for a wide variety of applications, e.g. [Bever and Duwez, 1972; Shen and Bever, 1972]. The ability to tape-cast and laminate several layers of

materials with differing chemical compositions makes these FGMs possible [Acikbas et al., 2006; Yeo et al., 1998]. Although FGMs produced by tape casting are used for different applications, i.e. metal/ceramic composites and electronically graded composites, the newly developed FGMs for magnetic refrigeration applications [Dinesen et al., 2012] (see Figure 1.3) are of particular interest.

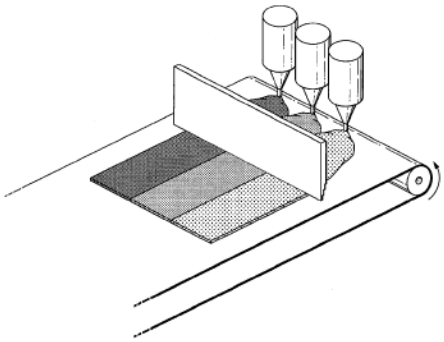

Figure 1.3: Schematic illustration of the newly developed method of tape casting to produce FGMs for magnetic refrigeration applications [Dinesen et al., 2012].

## 1.2 Existent models

In general, the flow behavior of a fluid system can be analyzed using the principles of fluid dynamics. There have been extensive studies on fluid dynamics and transport phenomena in processing organic engineering materials, e.g., petroleum and polymers [Cheneviere et al., 1991; Molaei et al., 2013; Nghiem et al., 2006; Sjoblom et al., 1997; Zhao et al., 2013]. The same principles are applicable to the flow of ceramic slurries during the tape casting process. However, taking a closer look at the tape casting process, one will find that it is a multidisciplinary field combining different aspects to investigate. The most important aspects that have been investigated deal with the fluid behavior (rheology of the fluid) and numerical/analytical models to simulate the process with the aforementioned rheology behavior taken to account. A presentation of this will be given shortly henceforth.

### 1.2.1 Rheological investigations

The rheological behavior of the ceramic slurry used in the tape casting process is one the defining parameters for the analysis of flow in the parallel doctor blade region. The simplest option is to assume that there is a linear correlation between the shear rate ($\dot{\gamma}$) and the shear stress ($\tau$), and the correlation parameter is called the Newtonian viscosity, which in this case is constant. In case the viscosity itself is dependent on shear rates, the rheological behavior will change to show non-Newtonian behavior. The

existent models based on this definition between Newtonian and non-Newtonian models are summarized in Table 1.1.

Table 1.1: List of existent models based on the rheological behavior.

| Newtonian behavior | Non-Newtonian behavior |
|---|---|
| [Chou et al., 1987] | [Ring, 1989] |
| [Gaskell et al., 1997] | [Loest et al., 1994] |
| [Kim et al., 2006] | [Pitchumani and Karbhari, 1995] |
| | [Huang et al., 1997] |
| | [Terrones et al., 1997] |
| | [Tok et al., 2000] |
| | [Joshi et al., 2002] |
| | [Joshi et al., 2002] |
| | [Zhang et al., 2002] |

Based on the reported studies it is evident that a non-Newtonian behavior of the fluid gives a better assumption for the ceramic flow in tape casting, however the Newtonian assumption has also shown to be reliable under some conditions. One of the challenging points in this area is to develop a material model for a specific ceramic slurry. However, this is not in the scope of the current research as it requires detailed experimental investigations in order to extract material parameters for the rheology of a ceramic slurry. The interesting point in this respect is to investigate the influence of material parameters on the produced tapes.

### 1.2.2 Numerical/analytical models

Dealing with the flow in tape casting, the coupled momentum and continuity equations should in general be solved. These equations can be solved either analytically or numerically. The existent models, based on the classification whether numerical or analytical approaches are used, are summarized in Table 1.2.

Table 1.2: List of existent models based on the solution approaches.

| Analytical modelling | Numerical modelling |
|---|---|
| [Chou et al., 1987] | [Loest et al., 1994] |
| [Ring, 1989] | [Gaskell et al., 1997] |
| [Pitchumani and Karbhari, 1995] | [Joshi et al., 2002] |
| [Pitchumani and Karbhari, 1995] | |
| [Huang et al., 1997] | |
| [Tok et al., 2000] | |
| [Joshi et al., 2002] | |
| [Tok et al., 2000] | |
| [Kim et al., 2006] | |

All of the published results based on numerical/analytical approaches are solved

under steady state conditions assuming constant slurry height in the reservoir. In most of the work conducted by other authors so far, moreover, the only parameter which has been investigated is the tape thickness (being a very important one for the result of the process), and its variation by changing the substrate velocity. In addition, when it comes to the numerical approaches, the free surface of the ceramic slurry in the doctor blade exit has not been investigated. These observations are taken as the current state of the art in the field of analytical/numerical tape casting of ceramics and are hence used in order to motivate the project. This will be discussed in details in the following section.

## 1.3 Objectives of the Thesis

In the present thesis, analytical/numerical models are developed in order to optimize the architecture of the thin ceramic layers produced by tape casting. The investigation is categorized into four main groups as follows:

In the first series of investigations analytical models are developed to capture/simulate the variation of the tape thickness in the doctor blade exit, while the slurry height is decreasing in the reservoir. The developed generalized models contain the materials constitutive behavior as well as the process parameters.

For the second series of investigations 2D numerical models are developed in order to simulate the tape casting process in which the free surface of the ceramic slurry in the doctor blade exit is taken into account. Moreover, the transient behavior of the slurry height in the reservoir is implemented. The 2D numerical model is further developed in order to capture the migration of particles inside the ceramic slurry.

As for the third part of the investigations, 3D numerical models are developed to simulate the side flow phenomenon in the tape casting of ceramics. The developed 3D model is modified thus being capable of simulating flow of two adjacent fluids used in tape casting of functionally graded ceramics (FGCs).

Finally, the evaporation of water from thin layers are modeled with the purpose of simulating the drying process in tape casting.

## 1.4 Methodology

The applied methodology can be split into two main parts in order to meet the aforementioned objective.

- All analytical models are developed and written in Matlab scripts.
- For all numerical models the finite volume based commercial code, ANSYS Fluent, is used. However, in order to make the model more efficient, some subroutines

are written in C language and linked to the CFD code. Moreover, for the last part of the thesis which is dealing with the drying process, the numerical model is developed in Matlab.

## 1.5 Structure of the thesis

The thesis consists of six chapters and seven papers. The content of the chapters is as follows

**Chapter 1: Introduction**

- This chapter gives an introduction to the thesis by first describing the tape casting process and its applications. Then, the existent fluid flow based models in analyzing the tape casting are shortly reviewed. Finally, the objectives of the thesis are described.

**Chapter 2: Theory**

- This chapter presents all the governing equations for the flow simulation, expressions for rheological behavior of fluids, different schemes of multiphase flow modelling and free surface capturing as well as particle migration in a non-Newtonian fluid.

**Chapter 3: Modelling Approaches**

- In this chapter the results of different numerical/analytical models of fluid flow simulating of tape casting of single material are presented. Numerical results of the side-by-side tape casting of a two-fluid system as well as particle migration inside a ceramic slurry are also presented.

**Chapter 4: Drying Kinetics**

- This chapter includes a brief introduction to the drying process of thin ceramic sheets as well as the results of a single analysis of water evaporation from a ceramic-water mixture.

**Chapter 5: Summary of Appended Papers**

- In this chapter a short summary of the seven appended papers is given.

**Chapter 6: Conclusion and Future Work**

- The conclusions of the different investigations from this thesis are given in this chapter and the future perspectives of numerical modelling in the tape casting process are described.

# Chapter 2

# Theory

This chapter presents all the hypotheses, theory and governing equations which are used in this thesis. Thus, the governing equations for the flow simulation, expressions for rheological behavior of fluids, different schemes of multiphase flow modelling and free surface capturing as well as particle migration in a non-Newtonian fluid are presented.

## 2.1 Governing Equations

The general equations of flow for the ceramic slurry in tape casting described as a non-Newtonian fluid are the mass conservation equation, which is in the form of the continuity equation and the momentum conservation equations. Hence, when dealing with the flow in tape casting, the coupled momentum and continuity equations [Wonisch et al., 2011] should in general be solved:

$$\rho\left(\frac{\partial u}{\partial t} + u \cdot \nabla u\right) = -\nabla p + \nabla \cdot T + F \tag{2.1}$$

$$\frac{\partial \rho}{\partial t} + \nabla \cdot (\rho u) = 0 \tag{2.2}$$

where $\rho$ is density, $u$ is velocity, $p$ is pressure, $T$ is stress tensor and $F$ is the contribution from external forces. Here, the momentum equation (2.1) expresses Newton's second law of motion, and the continuity equation (2.2) ensures conservation of mass. The aforementioned equations can be solved either analytically or numerically, where the first approach however puts a natural limitation to the complexity of the application.

## 2.2 Rheological Models

Rheology is the study of the flow of matter, primarily in the liquid state, but also as soft solids or solids under conditions in which they respond with plastic flow rather than deforming elastically in response to an applied force. It almost applies to everything, but it is interesting to study for the materials which have a complex molecular structure, such as muds, sludges, suspensions, polymers and other glass formers (e.g., silicates), as well as many foods and additives, bodily fluids (e.g., blood) and other biological materials.

Some liquids exhibit Newtonian flow characteristics, i.e., at constant temperature and pressure, in simple shear, the shear stress ($\tau$) is proportional to the rate of shear ($\dot{\gamma}$) and the constant of proportionality is the well-known dynamic viscosity ($\mu$). Such fluids are classically known as Newtonian fluids. The first models that were developed for the flow analysis in tape casting were based on a simple Newtonian assumption, i.e.:

$$\tau = \mu \left( \frac{\partial u}{\partial y} \right) = \mu \dot{\gamma} \tag{2.3}$$

In particular, the first model for predicting the tape thickness was developed by Chou et al. [Chou et al., 1987]. In their work Newtonian behavior was used and they assumed that the flow in the parallel doctor blade region was a linear combination of pressure and drag flow. The Newtonian fluid assumption was also used by Gaskell et al. [Gaskell et al., 1997] to investigate the impact of the reservoir geometry on the flow behavior inside the tape caster. Kim et al. [Kim et al., 2006] developed an analytical model to investigate the impact of the relative magnitudes of the driving forces (wall shear and pressure gradient) on the resulting tape thickness. They also compared the beveled and parallel blades in terms of productivity, minimum thickness, and potential influence on particle alignment. The author also used the Newtonian fluid assumption in the numerical modelling of fluid flow in the doctor blade region by further developing existing models from literature and introducing a non-dimensional tape thickness [Jabbari and Hattel, 2011]. However, in the tape casting process of ceramics the slurry seldom behaves like a Newtonian fluid, and consequently more general non-Newtonian fluid description should be applied if higher accuracy models are the goal. This will be addressed in more detail in the following.

The simplest possible deviation from the Newtonian fluid behavior occurs when the simple shear data $\tau - \dot{\gamma}$ does not pass through the origin (equation (2.3)) and/or does not result in a linear relationship between $\tau$ and $\dot{\gamma}$. Conversely, the apparent viscosity, defined as $\tau/\dot{\gamma}$, is not constant and is hence a function of $\tau$ or $\dot{\gamma}$. Indeed, under appropriate circumstances, the apparent viscosity of certain materials is not only a function of flow conditions (geometry, rate of shear, etc.), but it also depends on the

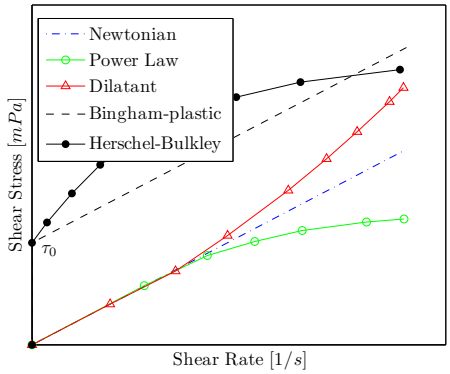


Figure 2.1: Rheological classification of different flows [Jabbari and Hattel, 2011].

kinematic history of the fluid element under consideration. Thus, the steady shear behavior may be described by a relation of the form,

$$\dot{\gamma}_{yx} = f(\tau_{yx}) \tag{2.4}$$

Depending upon the form of equation (2.4), three possibilities exist:

1. Shear-thinning or pseudoplastic behavior (power law)
2. Visco-plastic behavior with or without shear-thinning behavior (Bingham-plastic and Herschel-Bulkley plastic)
3. Shear-thickening or dilatant behavior

Figure 2.1 shows qualitatively the flow curves (also called rheograms) for the above-noted three categories of fluid behavior [Jabbari and Hattel, 2011]. The third type of the non-Newtonian fluids (dilatant) will not be discussed in the present review, since it is not relevant for tape casting.

### 2.2.1 Shear-thinning

The shear-thinning (power law) materials are probably the most widely encountered type of time-independent non-Newtonian fluid behavior in engineering practice. Often the relationship between shear stress ($\tau$)-shear rate ($\dot{\gamma}$) plotted on log-log co-ordinates for a shear-thinning fluid can be approximated by a straight line over an interval of shear rate, i.e.,

$$\tau = k \cdot \dot{\gamma}^n \tag{2.5}$$

or, in terms of the apparent viscosity,

$$\mu = k \cdot \dot{\gamma}^{n-1} \tag{2.6}$$

Obviously, $0 < n < 1$ will yield $d\mu/d\dot{\gamma} < 0$, i.e., shear-thinning behavior fluids are characterized by a value of $n$ (power-law index) smaller than unity. Many polymer melts and solutions exhibit a value of $n$ in the range $0.3 - 0.7$ depending upon the concentration and molecular weight of the polymer, etc. Even smaller values of power-law index ($n \sim 0.1 - 0.15$) are encountered with fine particle suspensions like kaolin-in-water, bentonite-in-water, etc [Barnes et al., 1989]. Naturally, the smaller the value of $n$, the more shear-thinning the material is. The other constant, $k$, (consistency index) is a measure of the consistency of the substance.

The power law model is the most common used constitutive behavior for the rheology of the ceramic slurry in tape casting. Pitchumani and Karbhari [Pitchumani and Karbhari, 1995] evaluated the effects of an imposed pressure gradient due to the height of the slurry in the casting head, as well as those of the drag due to the moving substrate on the slurry flow by modelling the slurry discharge as a generalized power law flow. Tok et al. [Tok et al., 2000] also used the power law constitutive model in analytical modelling of flow below the doctor blade region and the resultant tape thickness. The power law constitutive behavior was also implemented when we developed the quasi-steady state analytical model capable of modelling a non-constant height of the ceramic slurry in the reservoir and its resultant variation in the tape thickness [Jabbari et al., 2013b]. We also conducted a 2D simulation of a power law ceramic in combination with a multiphase model (VOF) to track the free surface of the $La_{0.85}Sr_{0.15}MnO_3$ (LSM) ceramic slurry [Jabbari and Hattel, 2012]. More specifically, the power law behavior of LSM is given in equation (2.7) and shown in Figure 2.2.

$$\tau = 3.31 \left( \frac{\partial u}{\partial y} \right)^{0.90} \tag{2.7}$$

In order to rectify some of the weaknesses of the power-law, Cross [Cross, 1965] presented the following empirical form which has gained wide acceptance in the literature. In simple shear, it is written as

$$\frac{\mu - \mu_\infty}{\mu_0 - \mu_\infty} = \frac{1}{1 + k \cdot \dot{\gamma}^n} \tag{2.8}$$

It is readily seen that for $n < 1$, this model also predicts shear-thinning behavior. Furthermore, the Newtonian limit is recovered here when $k \to 0$. Though initially Cross [Cross, 1965] proposed that $n = 2/3$ was satisfactory for numerous substances, it is now thought that treating it as an adjustable parameter offers significant improvement in terms of the degree of fit [Barnes et al., 1989]. Evidently, equation (2.8) correctly predicts $\mu = \mu_0$ and $\mu = \mu_\infty$ in the limits of $\dot{\gamma} \to 0$ and $\dot{\gamma} \to \infty$ respectively. The

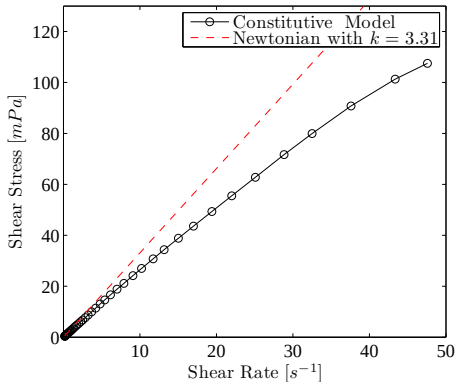


Figure 2.2: Rheology behavior of LSM ceramic [Jabbari et al., 2013b].

Cross model was used by Wonisch et al. [Wonisch et al., 2011] in the tape casting for numerical modelling both the macroscopic flow behavior and the orientation of individual particles inside the ceramic slurry.

The inherent deficiencies in the power-law model are remedied by the Carreau model [Bird, 1976]:

$$\frac{\mu - \mu_\infty}{\mu_0 - \mu_\infty} = \frac{1}{\left[1 + (\lambda \cdot \dot{\gamma})^2\right]^{(1-n)/2}} \tag{2.9}$$

where $\lambda$ is the time constant in seconds. The Carreau model was used by Terrones et al. [Terrones et al., 1997] to predict the tape thickness of the aqueous suspensions numerically.

### 2.2.2 Visco-plastic fluids

This type of non-Newtonian fluid behavior is characterized by the existence of a threshold stress (called yield stress or apparent yield stress, $\tau_0$) which must be exceeded for the fluid to deform (shear) or flow. Conversely, such a substance will behave like an elastic solid when the externally applied stress is less than the yield stress, $\tau_0$. Of course, once the magnitude of the external yield stress exceeds the value of $\tau_0$, the fluid may exhibit Newtonian behavior (constant value of $\mu$) or shear-thinning characteristics, i.e., $\mu(\dot{\gamma})$. It therefore stands to reason that, in the absence of surface tension effects, such a material will not level out under gravity to form an absolutely flat free surface. Quantitatively this type of behavior can be hypothesized as follows: such a substance at rest consists of three-dimensional structures of sufficient rigidity to resist any external stress less than $|\tau_0|$ and therefore offers an enormous resistance to flow, albeit it still might deform elastically. For stress levels above $|\tau_0|$, however, the structure breaks down and the substance behaves like a viscous material. In some cases, the build-up

and breakdown of structure has been found to be reversible, i.e., the substance may regain its (initial or somewhat lower) value of the yield stress.

A fluid with a linear flow curve for $|\tau| > |\tau_0|$ is called a Bingham plastic fluid, and is characterized by a constant value of viscosity $\mu_B$. Thus, in one-dimensional shear, the Bingham model is written as:

$$\begin{aligned} \tau_{yx} &= \tau_0^B + \mu_B \dot{\gamma}_{yx} \qquad & |\tau_{yx}| > \left|\tau_0^B\right| \\ \dot{\gamma}_{yx} &= 0 & |\tau_{yx}| < \left|\tau_0^B\right| \end{aligned} \tag{2.10}$$

Application of the Bingham constitutive model for the tape casting process was attempted by Ring [Ring, 1989]. However, he used shear rate, rather than shear stress as a yield criterion. The Bingham model was used by Zhang et al. [Zhang et al., 2002] to model the flow behavior below the doctor blade region and the resultant tape thickness. They proposed a critical velocity ($v_c$) and derived an analytical equation based on sufficient ($v_c \leq v_0$) or insufficient ($v_c > v_0$) belt velocity ($v_0$) to overcome the yielding point. Joshi et al. [Joshi et al., 2002] also used the Bingham model in their analytical models to predict the tape thickness and compared with the corresponding data from Huang et al. [Huang et al., 1997]. The Bingham constitutive model was also used for analytical modelling of the fluid flow in a two doctor blade configuration by the author of this thesis [Jabbari and Hattel, 2014], however this will be discussed later in section (3.1.3).

## 2.3 Multiphase Flow Models

Flow processes often involve the presence of free surfaces, the tracking of which has significant impact on the manufacturing and the final quality of the product. Examples abound, e.g., casting processes, mold filling, thin film processes, extrusion, coatings, spray deposition, fluid jetting devices in which material interfaces are inherently present. This phenomenon is also considered in multi-material flows with sharp immiscible interfaces [Tang et al., 2004]. Several CFD methods have been developed in the last decades with the aim of simulating such complex flows with free surfaces. Two very well-known examples of this is the volume of fluid (VOF) and level set methods. In general, there are a lot of different research papers which are dedicated to free surface modeling, different interpolation schemes, liquid/gas phase flow, multi fluid flow, multiphase flow and different numerical methods to simulate the flow field with the presence of an interface [Aulisa et al., 2004; Gueyffier et al., 1999; Huerta and Liu, 1988; Hyman, 1984; Jr and Puckett, 2004; Shin et al., 2011; Tang et al., 2004; Tavakoli et al., 2006; Wang et al., 2004].

A proper discretization of the convective term in the equation for transport of the VOF is crucial for simulation of a multiphase flow. It is well-known that numerical

schemes, commonly used for discretization of the convection term, introduce numerical diffusion or numerical dispersion phenomena [Ubbink and Issa, 1999]. For this reason, some additional techniques are needed, i.e., high-resolution schemes. Examples of these can be found in [Dendy et al., 2002; Muzaferija and Peric, 1997; Panahi et al., 2006; Queutey and Visonneau, 2007] with special focus on capturing sharp interfaces.

### 2.3.1 Volume of Fluid (VOF)

The volume of fluid (VOF)[1] model is a surface-tracking technique applied to a fixed Eulerian mesh. It is designed for two or more immiscible fluids where the position of the interface between the fluids is of interest. In the VOF model, a single set of momentum equations is shared by the fluids, and the volume fraction of each of the fluids in each computational cell is tracked throughout the domain [Hirt and Nichols, 1981].

The properties appearing in the transport equation are determined by the presence of the component phases in each control volume. In a two-phase system, for example, if the phases are represented by the subscripts 1 and 2, and if the volume fraction of the second of these is being tracked, the density in each cell is given by

$$\rho = f_2\rho_2 + (1 - f_2)\,\rho_1 \tag{2.11}$$

The evolution of the scalar $f$ (volume fraction) is governed by the simple advection equation:

$$\frac{\partial f}{\partial t} + \frac{\partial u_i f}{\partial x_i} = 0 \tag{2.12}$$

When coupled with the Navier-Stokes equations, the volume fraction is treated as an active scalar (it has influence on the velocity field). The main numerical difficulties connected with discretization of the transport equation for the volume fraction are: keeping constant width of the interface, i.e. avoiding artificial diffusion of the step interface profile and assuring a monotonic change of the variables. This last condition is also known as the boundedness criterion [Hirt and Nichols, 1981]. In order to overcome the aforementioned problems different methods were proposed. For instance, in Hirt and Nichols [Hirt and Nichols, 1981] a Donor-Acceptor Scheme (DAS), based on the availability criterion, was introduced. Problems that arose when using this scheme provoked other proposals that follow the idea of geometric interface reconstruction; examples are the SLIC (Simple Line Interface Calculation) method, the PLIC (Piecewise Linear Interface Construction) method or more recent methods that use the least-square procedure or splines [Jr and Puckett, 2004]. Methods that employ these ideas give good approximation of the shape of the interface and they allow for proper calculation of

[1] More information on the VOF method can be found in the original work by Hirts and Nichols [Hirt and Nichols, 1981].

the fluxes through faces of the control volumes. However, their application is often restricted to structured grids with simple shapes of the control volumes. Moreover, since estimation of a spatial orientation of the interface from the distribution of the volume fraction needs a substantial number of numerical operations, interface reconstruction methods increase the computational effort [Waclawczyk and Koronowicz, 2008].

Unlike geometric interface reconstruction methods, the high-resolution schemes, i.e. Compressive Interface Capturing Scheme for Arbitrary Meshes (CICSAM) [Ubbink and Issa, 1999] and High Resolution Interface Capturing (HRIC) [Muzaferija and Peric, 1997], do not introduce geometrical representation of the interface but try to satisfy the aforementioned conditions by properly chosen discretization scheme [Waclawczyk and Koronowicz, 2008]. The different VOF differencing schemes of the volume fraction equation, i.e. geometrical reconstruction, donor-acceptor, CICSAM and HRIC, and their definitions are well summarized by Lopez and Quinta-Ferreira [Lopez and Quinta-Ferreira, 2009].

The aforementioned methods were tested both for Newtonian and non-Newtonian fluids regarding interface position as well as computational time [Jabbari et al., 2013a] ([PAPER V]). The results show that the CICSAM method has the best combination of accuracy of predicting the free surface and low cost of computation, especially for the non-Newtonian fluid.

### 2.3.2 Mixture Model

Advances in computational fluid mechanics have provided the basis for further insight into the dynamics of multiphase flows. Currently there are two approaches for the numerical calculation of multiphase flows which are available in ANSYS Fluent [th7, 2009]: the Euler-Lagrange approach and Euler-Euler approach. The mixture model, which is of the latter type, is a simplified multiphase model that can be used in different ways. It can be used to model multiphase flows where the phases move at different velocities, but assuming local equilibrium over short spatial length scales. It can be used to model homogeneous multiphase flow with very strong coupling and phases moving at the same velocity, and it is recommended to use for flows with high viscosity or non-Newtonian viscosity. Moreover, a second-order time integration scheme is available together with the Mixture (and Eulerian) multiphase models, which is not the case for the conventional VOF Explicit Scheme [th7, 2009].

The mixture model solves the continuity equation, the momentum equation and the energy equation for the mixture, and the volume fraction equation for the secondary phases, as well as algebraic expressions for the relative velocities (if the phases are moving at different velocities). The only difference between the VOF method and the mixture model is that in the latter one an extra term is added to the momentum equation as follows

$$\nabla \cdot \left( \sum_{k=1}^{n} f_k \rho_k \vec{v}_{dr,k} \vec{v}_{dr,k} \right) \tag{2.13}$$

where $n$ is the number of phases, and $\vec{v}_{dr,k}$ is the drift velocity for the secondary phase $k$:

$$\vec{v}_{dr,k} = \vec{v}_k - \vec{v}_m \tag{2.14}$$

which in the case of two immiscible fluids will be zero. The drift velocity only becomes active when one of the phases is in particle form.

## 2.4 Particle Migration

Particle migration in fluids is found in many industrial applications such as transport and refining petroleum, paper manufacturing, environmental waste treatment and ceramic processing. The motion of small particles, drops, and bubbles in a viscous fluid at low Reynolds number is one of the oldest classes of problems in theoretical fluid mechanics [Leal, 1980]. A series of investigations conducted in literature have described the behavior of rigid and deformable particles suspended in very low Reynolds Newtonian liquids undergoing Couette and Poiseuille flow [Gauthier et al., 1971a,b]. Although some of the work made in this area is based on the flow equations for a non-Newtonian fluid [Frank et al., 2003; Ho and Leal, 1976; Leal, 1980], most of the investigations are based on experimental findings [Abbott et al., 1991; Gauthier et al., 1971a,b].

The ceramic slurry used in the tape casting process contains different ingredients, i.e. solvent, dispersant, binder, plasticizer and deflocculant, each of them having a specific influence on the final properties of the part [Chartier and Bruneau, 1993; Pagnoux et al., 1998]. The presence of these secondary phases inside the ceramic slurry results in the packing structure, which can be tracked in the final tapes after the sintering process [Chantaramee et al., 2008, 2007]. The art of making dense ceramics has been practiced and developed for decades. The ability to produce porous ceramics with specific pore size and porosity is less well documented. Recently, efforts have been directed towards the development of ceramic filter systems in which the microstructure is tailored to the application [Krasnyi et al., 2005; Vasconcelos et al., 1998]. Moreover, the field of porous ceramics is growing in different areas with different applications like membranes, flue gas purification, piezoelectric materials and solid oxide fuel cell (SOFC) anode substrates [Galassi, 2006; He et al., 2009; Krasnyi et al., 2005; Simwonis et al., 1999]. The main concern in the aforementioned products is to have a relatively homogenous distribution of position of the pores together with a uniform size distribution. This issue emphasizes the importance of the particle (i.e. binders or pore-formers) migration

inside the ceramic slurry during the tape casting process.

In general, the particles in a non-homogeneous shear flow will migrate from regions of higher shear rate to regions of lower shear rate [Phillips et al., 1992]. The migration takes place at particle Reynolds numbers small enough ($\sim 10^{-4}$) to preclude the importance of inertia effects. Phillips et al. [Phillips et al., 1992] developed the modified version of the model proposed by Leighton and Acrivos [Leighton and Acrivos, 1987] of the complex diffusion process associated with shear induced particle migration. They showed that the viscosity $\mu = \mu(\phi)$ of concentrated suspensions at Peclet number of $Pe \gg 1$ can be approximated by

$$\frac{\mu}{\mu_c} = \left(1 - \frac{\phi}{\phi_m}\right)^{-1.82} \tag{2.15}$$

where $\mu/\mu_c$ is the relative viscosity, and $\mu_c$ is the solvent viscosity, $\phi$ is the volume fraction of particles, and $\phi_m$ is the volume fraction at which $\mu/\mu_c$ tends to infinity, which was reported [Phillips et al., 1992] to be equal to 0.68 with volume fractions in the range $0.01 < \phi < 0.5$. The changes in the viscosity versus the volume fraction based on equation (2.15) is illustrated in Figure 2.3(a).

Moreover, the migration of the particles inside a fluid is influenced by the gravitational force. Gravity induced particle migration results from the competition between the difference in density of the mixture components that forces them to separate and the viscous drag of the flowing suspending fluid that slows down the phenomenon, leading to an advection process. A comprehensive review on the shear induced as well as the gravity induced migration of the particles inside a non-Newtonian fluid has been reported by Spangenberg et al. [Spangenberg et al., 2012a,b]. They showed that for a spherical, solid particle inside a fluid the settling velocity, $V_s$, is equal to $V_s = g\triangle\rho a^2/18\mu_s$, where $a$ is the diameter of the particle, $\triangle\rho$ is the density difference between the particle and the surrounding material, and $\mu_s$ is the viscosity of the suspending material. However, the nature of the fluid used in their research (concrete) and the process dimensions are totally different from the one in this thesis. Moreover, the rheological behavior used by Spangenberg et al. [Spangenberg et al., 2012a,b] is different from the one in this thesis, i.e. they used Bingham material behavior.

Although, in the works done by Spangenberg et al. [Spangenberg et al., 2012a,b] the settling velocity ($V_s$) has been taken into account for the migration of the particles, the impact of the particles and the volume fraction was not mentioned in their simulations. Buscall et al. [Buscall et al., 1982] showed that the rate of settling, $V$, for a dilute suspension of particles, which is not grossly aggregated can be expressed by an equation of the form

$$\frac{V}{V_s} = \left(1 - \frac{\phi}{\varrho}\right)^{k\varrho} \tag{2.16}$$

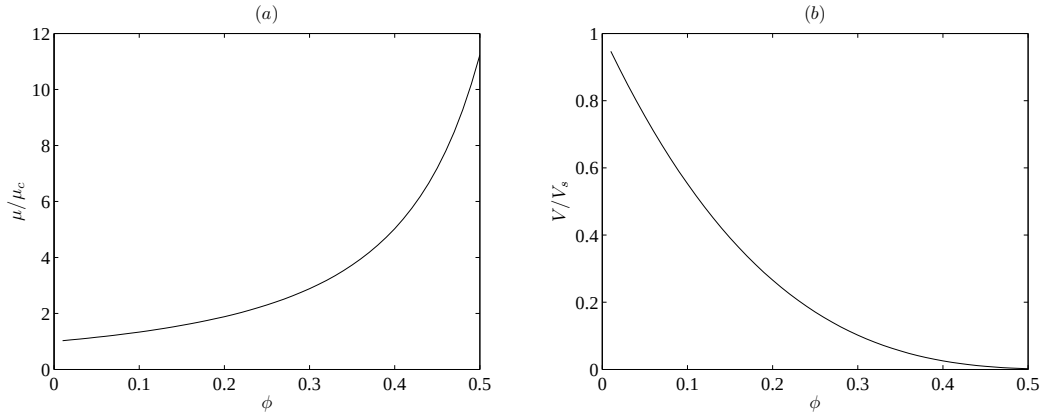


Figure 2.3: The influence of the particle volume fraction on (a) the viscosity based on equation (2.15) and (b) the settling rate of the particles based on equation (2.16) [PAPER VI].

in which $\phi$ is the volume fraction of the particles, $\varrho$ is the volume fraction when the particles approach the close packing region, and $k$ is a constant. Buscall et al. [Buscall et al., 1982] also showed that for polymeric and ceramic fluids the values for $\varrho$ and $k$ would be 0.58 and 5.4, respectively. The variation of the settling rates versus the volume fraction is illustrated in Figure 2.3(b). In this thesis both equations (2.15) and (2.16) are used in the developed local variation of the viscosity (LVOV) model as a function of the particle volume fraction.

The particle migration, which is calculated through an advection and settling procedure, is given by

$$\frac{\partial \phi}{\partial t} + \nabla \left( \phi V \right) = 0 \tag{2.17}$$

where $V$ is the settling velocity vector which is updated in the LVOV model with equation (2.16). It should be noted that having particles of very small size, results in reducing the variation in the settling velocity.

# Chapter 3

# Modelling Approaches

This chapter presents the results of different numerical/analytical models of fluid flow simulating of tape casting of single material. Numerical results of the side-by-side tape casting of two-fluid system as well as particle migration inside a ceramic slurry are also presented.

## 3.1 Analytical Models

It is well-known that analytical solutions to the coupled flow equations (2.1) and (2.2) are limited to relatively simple cases in terms of geometry, boundary conditions and material properties. This is certainly also the case for the relatively few analytical solutions for the flow in tape casting. More specifically only 1D flow is considered, constant material data is assumed as well as incompressible behavior of the slurry. Moreover, only steady state or quasi-steady state conditions are considered. Under these assumptions it is possible to develop some relatively simple, yet highly applicable analytical solutions for the flow in the doctor blade region in tape casting. The most important of these solutions will be presented next.

### 3.1.1 Steady State Model

In order to express the volume flow and thus the tape thickness, the velocity field equation in the doctor blade region must be developed. Based on the number of doctor blades there are two kinds of tape casters, a simple tape caster which has only one doctor blade (illustrated schematically in Figure 3.1), and a double-blade tape caster

(see Figure 3.8) in which a rear doctor blade is used to ensure a hydrostatic pressure in front of the rear one [Zhang et al., 2002].

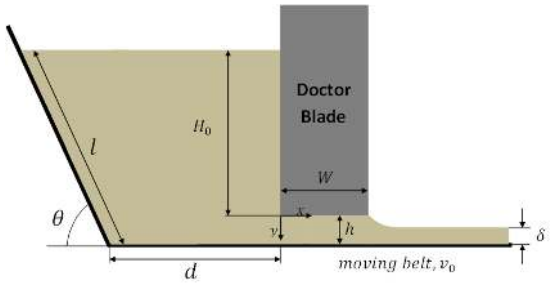


Figure 3.1: Schematic geometry of the tape casting machine in 2D.

The pressure gradient inside the channel below the doctor blade is constant, since there is a hydrostatic pressure in front of the doctor blade and it can be determined by the height of the slurry as shown below [Zhang et al., 2002],

$$\frac{dp}{dx} = -A_0 = -\frac{\rho g H_0}{W} \tag{3.1}$$

where $\rho$ is the density of the slurry, $g$ is the acceleration due to gravity, $H_0$ is the height of the slurry in front of the doctor blade, and $W$ is the width of doctor blade.

By assuming an infinitely long and wide plate as compared to the thickness and combining with momentum conservation in the $x$-direction under steady state conditions, we obtain the following [Tok et al., 2000; Zhang et al., 2002], highly simplified 1D version of the momentum equation (equation (2.1))

$$\frac{d\tau}{dy} = \frac{dp}{dx} \tag{3.2}$$

where $\tau$ is the shear stress. From equations (3.1) and (3.2), $\tau$ is found to be

$$\tau = -A_0 y + A_1 \tag{3.3}$$

where $A_1$ is an integration constant.

For the power law or the Bingham fluid the shear stress, $\tau$, is given by the constitutive equation [Tok et al., 2000; Zhang et al., 2002]:

$$\begin{aligned} \tau &= k\left(\frac{\partial u}{\partial y}\right)^n \\ \tau &= \tau_0^B + \mu_B\left(\frac{\partial u}{\partial y}\right) \end{aligned} \tag{3.4}$$

where it has been assumed that the only velocity component contributing to the shear rate is the velocity in the $x$-direction, $u$.

Rewriting equations (3.3) and (3.4) and integrating along the channel height ($h$) we get

$$\begin{aligned} \int_0^h (-A_0 y + A_1)\, dy &= \int_0^h k \left(\frac{\partial u}{\partial y}\right)^n dy \\ \int_0^h (-A_0 y + A_1)\, dy &= \int_0^h \left[\tau_0^B + \mu_B \left(\frac{\partial u}{\partial y}\right)\right] dy \end{aligned} \tag{3.5}$$

These equations compose the main structure of almost all research carried out to analytically model the fluid flow below the doctor blade region [Chou et al., 1987; Jabbari et al., 2013b; Joshi et al., 2002; Kim et al., 2006; Pitchumani and Karbhari, 1995; Tok et al., 2000; Zhang et al., 2002]. By solving the above equations the velocity profile below the doctor blade region ($u(y)$) will be found, and subsequently used to find the tape thickness as follows

$$\delta = \frac{1}{v_0} \int_0^h u(y) \cdot dy \tag{3.6}$$

which follows from mass conservation and incompressibility of the slurry. An example of such analytical model is illustrated in Figure 3.2. As seen, by decreasing the hydrostatic pressure ($P$) due to a reduction in the level of the slurry height, the velocity profile is changed and the area under the velocity profile is decreased. Moreover, an increased substrate velocity results in decreasing the tape thickness since the drag force is increased by increasing the substrate velocity, and it becomes more dominant compared to the pressure force which results in more stretching of the slurry over the peeling belt.

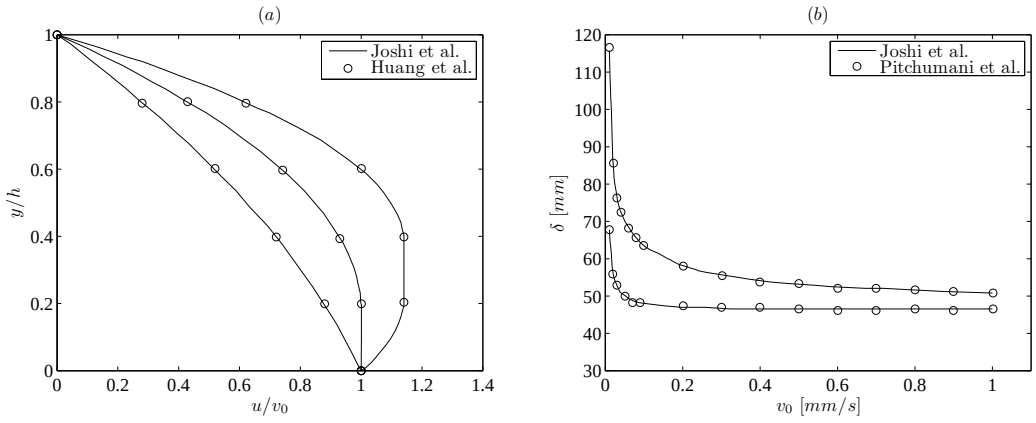


Figure 3.2: Results of analytical modelling for (a) velocity profile below the doctor blade region with different pressure head [Huang et al., 1997; Joshi et al., 2002], and (b) influence of the casting velocity on the tape thickness [Joshi et al., 2002; Pitchumani and Karbhari, 1995].

### 3.1.2 Quasi-steady state model

By assuming that $k$ and $n$ are constants, equation (3.5) for the power law material can be solved for $u$ [Jabbari et al., 2013b]

$$u = \left(-\frac{1}{A_0 \cdot k^{\frac{1}{n}}}\right) \cdot \left(\frac{1}{\frac{1}{n}+1}\right) \cdot (-A_0 y + A_1)^{\frac{1}{n}+1} + A_2, (0 < y < h) \tag{3.7}$$

where $A_2$ is another integration constant.

The boundary conditions for equation (3.7) in the doctor blade region of tape casting are

$$\left\{ \begin{array}{c} u(0) = 0 \\ u(h) = v_0 \end{array} \right\} \tag{3.8}$$

where $v_0$ is the velocity of the moving belt.

Applying these boundary conditions in equation (3.7), and introducing the expressions that $\frac{1}{n} + 1 = \chi$ and $\frac{-1}{A_0 \cdot k^{\frac{1}{n}}} = \psi$, the thickness of the green tape, $\delta$, can be determined by integrating $u$ over the channel height and dividing by the tape velocity as indicated in equation (3.6) [Jabbari et al., 2013b], i.e.:

$$\delta = \frac{1}{v_0}\int_0^h u \cdot dy = \frac{-\left[(-A_0 h + A_1)^{\chi+1} - (A_1)^{\chi+1}\right]}{v_0 \cdot A_0 \cdot \psi \cdot \chi \cdot (\chi+1)} + A_2 h \tag{3.9}$$

Reaching a constant tape thickness is not an impossible goal, since most of the manufacturing processes for tape casting are of the continuous form in which the reservoir at all times is fed by slurry. Moreover, using two doctor blades in the design of the machine will result in having almost constant hydrostatic pressure during the casting process (see section (3.1.3)). However, it is of great importance to control the tape thickness in small tape casters especially in small scale production and laboratories, in which the slurry height is not constant in the reservoir but gradually decreasing with time. This phenomenon leads to a modification of the standard steady state model [Chou et al., 1987; Joshi et al., 2002; Kim et al., 2006; Pitchumani and Karbhari, 1995; Tok et al., 2000; Zhang et al., 2002] making it dependent on the slurry height variation.

The steady state formulation shown previously is developed based on the continuity equation [Jabbari et al., 2013b]. For the quasi-steady state solution a similar approach was adopted. Thus, assuming that the slurry is incompressible the volume of the slurry which drops down in the reservoir is equal to the volume of the slurry which is conveyed out of the doctor blade region by the peeling belt. Further assuming that during the time period equal to $\Delta t$, the height of the slurry will decrease from the initial value of $H_0$ to $H_1$, the aforementioned decrease in volume (which equals the area in the present 2D model) in the reservoir will be given as:

$$\Delta S_1 = \left[ d + \frac{1}{2} \cdot l \cdot \cos\theta \left( 1 + \frac{H_1 + h}{H_0 + h} \right) \right] \cdot (H_0 - H_1) \tag{3.10}$$

This area is moved out of the doctor blade region with the constant velocity of $v_0$ and the distance of $v_0 \times \triangle t$, hence it is equal to $v_0 \times \Delta t \times \delta_1$. The new initial height in the next time step is now $H_1$ and the new $\Delta S_2$ is found from using $H_1$ as initial height in equation (3.10) and so forth.

As seen in Figure 3.2a, since the hydrostatic pressure ($P$) decreases by time due to the reduction in level of the slurry height, the velocity profile is changed and the area under the velocity profile is decreased, and consequently the "area" out of the blade is decreased. On the contrary, decreasing the pressure head for a constant velocity, the thickness of the tape is decreased in the exit and vice versa. This behavior very much emphasizes the importance and relevance of the proposed quasi-steady state model, in which the transient effect of the slurry height in the reservoir (which resembles the pressure head) is implemented. This phenomenon can easily be seen in Figure 3.3, where the tape thickness decreases in the casting direction due to the transient decrease of the slurry height (the pressure head) in the reservoir.

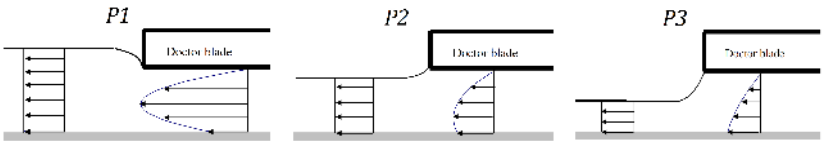


Figure 3.3: Schematic illustration of the effect of the increased pressure head on the tape thickness ($P_1 > P_2 > P_3$) [Kim et al., 2006].

Figure 3.4 shows the effect of the substrate velocity on the dried tape thickness based on experimental findings as well as steady state and quasi-steady state analytical models for the same set-up [Jabbari et al., 2013b]. As seen from the figure for all types of data, an increased substrate velocity results in decreasing the tape thickness. More specifically, it is found that the tape thickness decreases hyperbolically with substrate velocity [Chou et al., 1987; Pitchumani and Karbhari, 1995], which is also seen from equation (3.9). From previous work [Chou et al., 1987; Jabbari and Hattel, 2011; Pitchumani and Karbhari, 1995], it was found that when the drag force is increased by increasing the substrate velocity it becomes more dominant as compared to the pressure force which results in more stretching of the slurry over the peeling belt. Figure 3.4 shows that the quasi-steady state model proposed by the author [Jabbari et al., 2013b] is in better agreement with corresponding experiments as compared to the steady state model, since in the quasi-steady state model the effect of decreasing the level of the slurry height is taken into account.

Another comparison between the quasi-steady state model, steady state model and

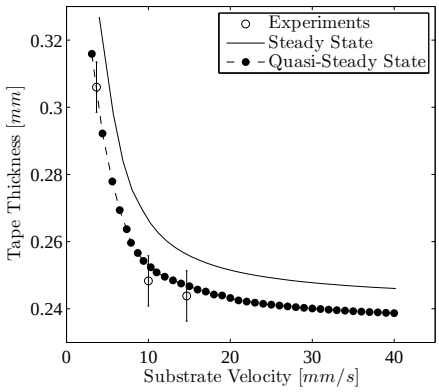


Figure 3.4: Effect of substrate velocity on tape thickness with a doctor blade height of 1 $mm$ [Jabbari et al., 2013b]. ([PAPER I])

experimental results is shown in Figure 3.5 [Jabbari et al., 2013b]. It can be seen that the proposed model by the author [Jabbari et al., 2013b] is in better agreement with experiments in comparison to the steady state model. The highest deviation between data was observed for the higher values of the doctor blade height.

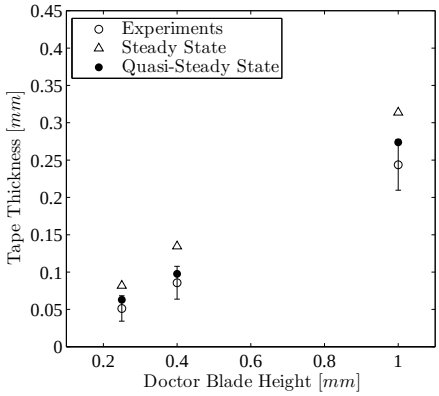


Figure 3.5: Comparison of the quasi-steady state model proposed by the author with steady state model and experiments for $v_0 = 3.67mm/s$ [Jabbari et al., 2013b]. ([PAPER I])

The slurry load, known as the hydrostatic pressure, is the other main parameter which influences the final tape thickness. This parameter is a direct consequence of the height of the fluid behind the doctor blade region ($\triangle P = \rho g H$). Using this, it is possible to define one single parameter which determines the shape of the velocity profiles as well as the wet tape thickness and this is the ratio of pressure force to viscous force ($\varpi$) [Jabbari and Hattel, 2011; Kim et al., 2006]

$$\varpi = \frac{\triangle P \cdot h}{2\mu W v_0} \tag{3.11}$$

As illustrated in Figure 3.6 increasing the value of the aforementioned ratio ($\varpi$) results in increasing of the velocity shape (area) below the doctor blade region, and as shown before in Figure 3.3, this leads to an increase of the tape thickness.

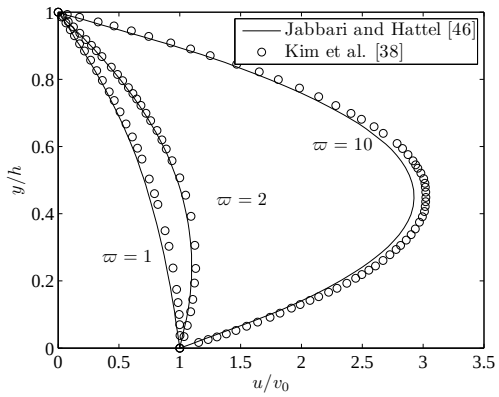


Figure 3.6: The non-dimensional velocity profile in the doctor blade region on the basis of different $\varpi$ [Jabbari and Hattel, 2011].

In most existing models [Chou et al., 1987; Jabbari and Hattel, 2011; Joshi et al., 2002; Kim et al., 2006; Pitchumani and Karbhari, 1995; Tok et al., 2000; Zhang et al., 2002] this ratio is assumed to be constant. However, as discussed earlier the height of the slurry inside the reservoir is not constant, but decreasing with time [Jabbari et al., 2013b]. As seen from Figure 3.7 the thickness of the tape in the beginning of a strip (which is the part leaving the doctor blade region first) is higher than the end of a strip. This is due to the higher level of material in the reservoir in the beginning of process. As time passes the height of the slurry in the reservoir decreases and consequently the resultant height of the tape will decrease. This means that the hydrostatic pressure decreases with time and the drag forces start to show their dominance by making the tape thinner. However, this phenomenon can of course not be detected by the steady state model.

### 3.1.3 Steady state two doctor blade model

As already mentioned, using the two doctor blade configuration is one of the ways to reach an almost constant tape thickness in the tape casting process. The interesting thing in this case is to control the height of the slurry in both doctor blade regions based on the desired tape thickness, substrate velocity, constitutive behavior of the ceramic slurry and the machine design parameters [Jabbari and Hattel, 2014]. A general schematic of the two doctor blade configuration is illustrated in Figure 3.8. The author [Jabbari and Hattel, 2014] has modeled analytically the velocity and the pressure field in both doctor blade regions assuming the Bingham-plastic model for the fluid flow.

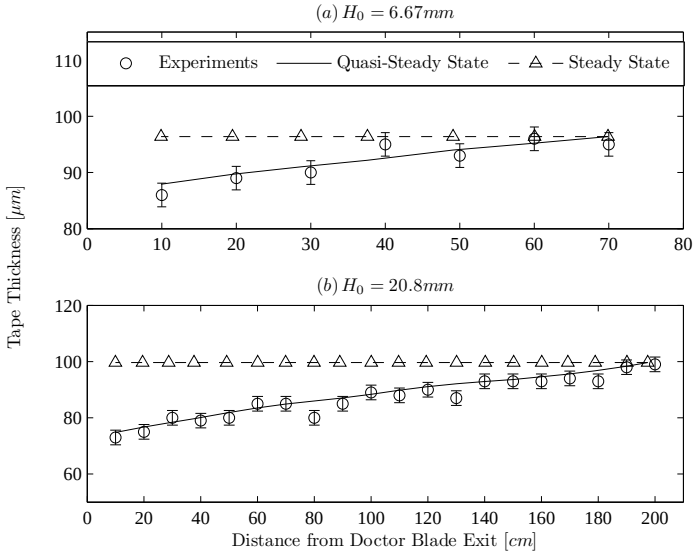


Figure 3.7: Results of modelling and their comparison with experimental data for tape casting of LSM slurry with a substrate velocity of $v_0 = 3.67mm/s$ and an initial slurry height of (a) $H_0 = 6.67mm$ and (b) $H_0 = 20.8mm$ [Jabbari et al., 2013b]. ([PAPER I])

The developed model then was used to predict the height of the slurry in both doctor blade regions based on the desired tape thickness and the belt velocity.

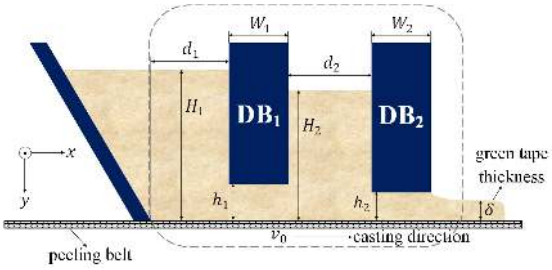


Figure 3.8: 2D illustration of the tape casting process with two doctor blades [Jabbari and Hattel, 2014]. ([PAPER III])

We showed that based on the ability of the flow to overcome the yield stress (for the Bingham-plastic fluid), there are two different zones, i.e. a sufficient one and an insufficient one, in which the predicted values for the slurry height and velocity profiles are totally different. The region with the insufficient belt velocity shifts toward the higher velocities by increasing the value of the critical velocity, $v_{cr} = \frac{A_{0i}h_i^2}{2k}$, (see Figure 3.9), when increasing the doctor blade ($h_i$), increasing the slurry height behind the doctor blade ($H_i$), decreasing the doctor blade width ($W_i$), and the plastic viscosity ($k$), which all gives an increase in the critical velocity $v_{cr} = \frac{A_{0i}h_i^2}{2k}$. Moreover, the tape thickness is always larger than half of the doctor blade height ($\delta > h_i/2$) no matter what belt velocity is used [Jabbari and Hattel, 2014].

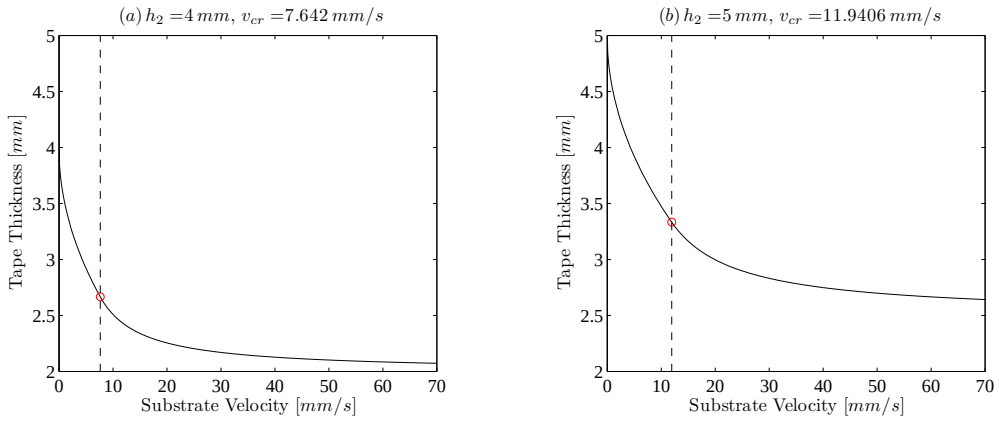


Figure 3.9: Variation of the tape thickness by the substrate velocity for (a) $h_2 = 4mm$, and (b) $h_2 = 5mm$ [Jabbari and Hattel, 2014]. ([PAPER III])

We also showed that when the belt velocity is not high enough to overcome the Bingham yield point (insufficient belt velocity), there is always a region with zero shear rate below the doctor blade (see Figure 3.10), and this region decreases its width by increasing the plastic viscosity ($k$). The results of the required slurry height based on the desired tape thickness as well as the belt velocity showed that in the insufficient condition the slurry height behind both doctor blades will increase in comparison to the sufficient condition (see Figure 3.11). Moreover, the variation of the aforementioned heights are different in the sufficient and insufficient conditions, showing a linear increase for the sufficient condition. On the other hand, increasing the doctor blade width, $W_i$, (or decreasing the reservoir size, $d_i$) with constant velocity and tape thickness, the required slurry height behind the both doctor blades will be increased. The proposed model by the author [Jabbari and Hattel, 2014] contains all main parameters which influence the process, and it has the flexibility to be used for different slurries with different constitutive behaviors as well as different machine design.

## 3.2 Numerical models

Numerical modeling is a powerful method of visualizing the dynamic behavior of physical systems. Numerical solutions have several advantages over analytical solutions such as being much more intuitive and easy to handle. Thus more realistic models of greater complexity can be investigated using numerical techniques. This is certainly the case for computational fluid dynamics (CFD) methods, which numerically solve the differential equations governing the flow, and makes them a prime tool for analyzing manufacturing processes involving material flow. Nonetheless, only few CFD studies have considered tape casting so far and those which did have been restricted to two dimensions. One reason why CFD-based simulations are not widely used to simulate

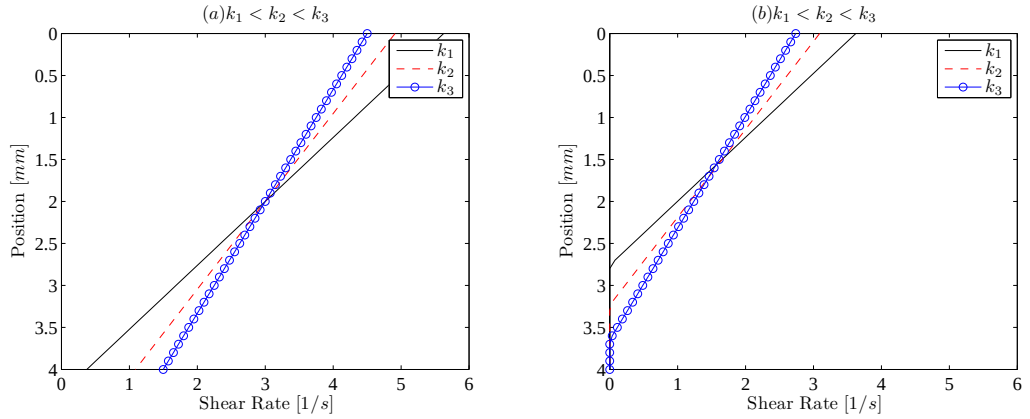


Figure 3.10: Shear rates below the doctor blade region for (a) $v_0 > v_{cr}$ and different $k$, and (b) $v_0 \leq v_{cr}$ and different $k$. The value of the critical velocity in these cases is equal to $10.5mm/s$ [Jabbari and Hattel, 2014]. ([PAPER III])

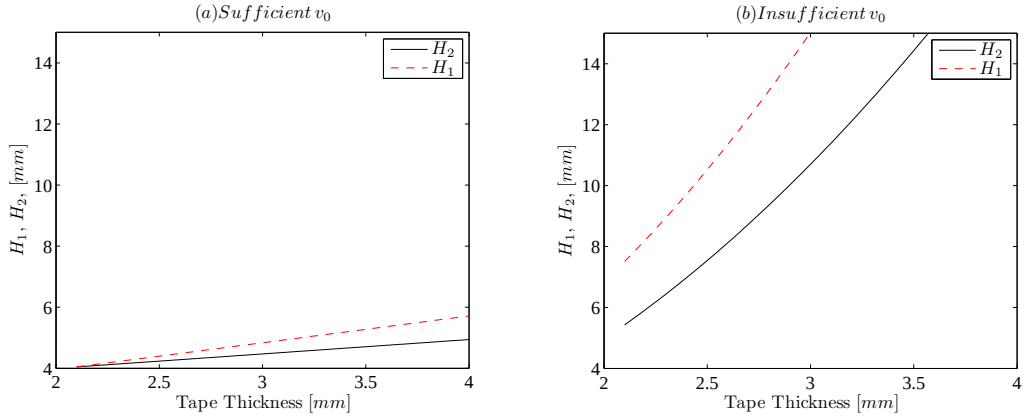


Figure 3.11: Impact of increasing the value of the tape thickness on the required height of the slurry behind both doctor blades with (a) sufficient and (b) insufficient belt velocity [Jabbari and Hattel, 2014]. ([PAPER III])

tape casting - despite their obvious benefits - might be due to their complex nature, requiring extensive know-how and special software. In the following the numerical models used for modelling the tape casting process will be reviewed.

### 3.2.1 General fluid flow

The first numerical model to solve the fluid in tape casting was introduced by Loest et al. [Loest et al., 1994], where the finite element method (FEM) was used for the forming flow of ceramic tapes having viscoplastic Bingham behavior with a yield stress. In their work the flow domain encompassed both the slurry reservoir and the doctor-blade region with free surface (the free surface modelling will be discussed in detail in part 3.2.2) and was two-dimensional. They changed the design of the doctor blade

from being a straight wall to a tapered one to avoid recirculation.

Gaskell et al. [Gaskell et al., 1997] modeled the fluid flow in the reservoir region of the tape casting process numerically using a linear finite element formulation. Their analysis showed that the flow is characterized by an ever-present primary recirculation, adjacent to the moving substrate, and that the size and number of secondary recirculations above the primary one depend upon both the aspect ratio of the reservoir (height over width) and the angle of inclination of the side walls (see Figure 3.12).

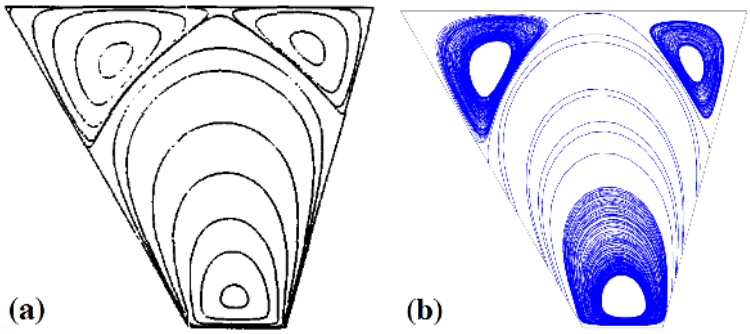


Figure 3.12: Flow pattern inside the reservoir solved by (a) finite element formulation [Gaskell et al., 1997], and (b) corresponding finite volume modelling that we conducted.

The first numerical model based on the finite volume method was conducted by the author through this thesis [Jabbari and Hattel, 2011]. The flow field was computed inside the reservoir and below the doctor blade region. Based on the velocity profiles obtained below the doctor blade region the tape thickness was predicted for a Newtonian fluid.

Wonisch et al. [Wonisch et al., 2011] also conducted a CFD calculation in the tape casting process. They used smoothed particle hydrodynamics (SPH) to simulate the flow of the non-Newtonian fluid, and consequently the orientation of the particles (and resultant anisotropic particle alignment) was predicted by Jeffery's equations of motion.

### 3.2.2 Free surface tracking

As previously introduced, Loest et al. [Loest et al., 1994] conducted FEM simulations on tape casting combined with a free surface model implemented in the close region to the doctor blade region. We modeled the flow of a slightly non-Newtonian ceramics slurry with the power law constitutive behavior as well as tracking the free surface [Jabbari and Hattel, 2012]. We also investigated the different interface capturing methods in modelling of free surface tracking of tape casting, and reported that the Compressive Interface Capturing Scheme for Arbitrary Meshes (CICSAM) method is the most reliable scheme for capturing of the free surface in the modelling of the tape casting process [Jabbari et al., 2013a]. Apart from this, the authors presented a coupled fluid flow-multiphase model to predict the influence of the process parameters on the side

flow, as the flow leaves the doctor blade region [Jabbari and Hattel, 2013]. Some 3D results for the flow of the $(La_{0.85}Sr_{0.15})_{0.9}MnO_3$ (LSM) slurry in the tape casting process are illustrated in Figure 3.13. The LSM slurry showed to follow the power law constitutive behavior for the viscosity as $\tau = 3.31 \cdot \dot{\gamma}^{0.90}$.

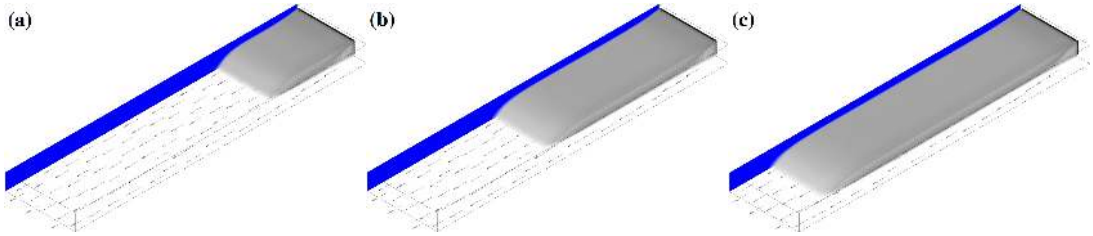


Figure 3.13: Flow of LSM ceramic slurry in tape casting in different simulation time (a) 2.5 sec, (b) 5 sec, and (c) 7.5 sec. The dark blue surface is the symmetry plane.

### 3.2.3 Side flow

One of the parameters that influences the final tape thickness is the side flow factor ($\alpha$) which is mostly measured at the end of the process by a volumetric comparison of the tape which flowed outside the casting width to the tape within the casting width. Although this side flow in tape casting is of relatively limited magnitude it is interestingly enough always mentioned as an influencing parameter in the calculations of the tape thickness and always measured experimentally [Chou et al., 1987; Jabbari et al., 2013b; Jabbari and Hattel, 2011; Joshi et al., 2002; Kim et al., 2006; Pitchumani and Karbhari, 1995; Tok et al., 2000; Zhang et al., 2002]. We have presented the first example in literature where the side flow factor ($\alpha$) is predicted numerically [Jabbari and Hattel, 2013] ([PAPER II]). Moreover, we investigated the influence of the process parameters, i.e. substrate velocity, doctor blade height and slurry height, on the side flow factor (see Figure 3.14).

The effect of substrate velocity on the side flow factor is illustrated in Figure 3.14a. The results showed that by increasing the velocity of the peeling belt, the value of the side flow factor will be increased, which means that the slurry flows less towards the sides. This is due to the increase of the drag forces in the casting direction compared to the side direction, which gives the slurry less possibility to flow towards the sides. Note that the side flow factor is defined in such a way, that when the side flow increases, the side flow factor decreases. As shown in Figure 3.14b, by increasing the doctor blade height, the size of the side flow factor ($\alpha$) increases. For the lower value of the doctor blade height, since the slurry height in the reservoir and the velocity of the peeling belt are constant, the hydrostatic pressure behind the flow is higher compared to the one with the bigger doctor blade height. Increasing the hydrostatic pressure will increase the flow to the sides and hence lead to a decrease in the resultant side flow factor. On

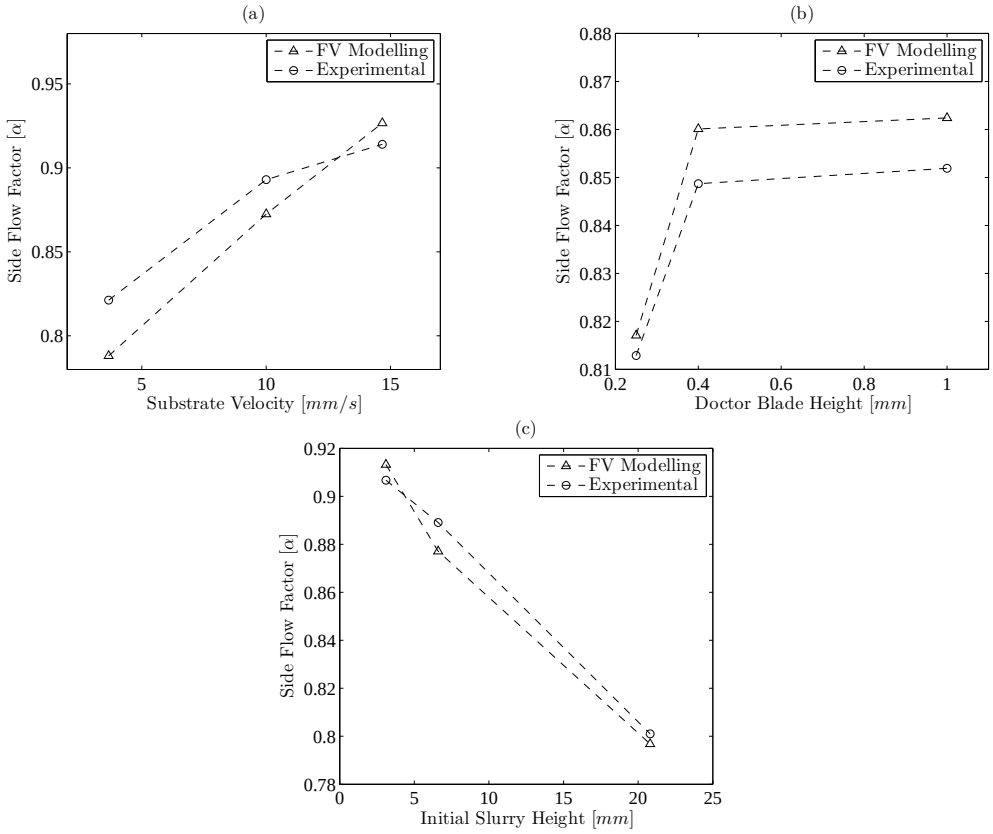


Figure 3.14: Numerical modelling and corresponding experiments values of side flow factor ($\alpha$) influenced by (a) substrate velocity, (b) doctor blade height, and (c) slurry height [Jabbari and Hattel, 2013]. The dash lines are guides to the eye. ([PAPER II])

the other hand, due to the low velocity used in these series of experiments, the ceramic slurry has much time to flow towards the sides after leaving the doctor blade region. These two phenomena obviously interact, but with the bigger doctor blade height, the effect of hydrostatic pressure decreases and leads to a decrease in the flow to the sides and hence an increase of the side flow factor. And finally, increasing the initial slurry height in the reservoir will increase the tape thickness, thereby promoting the flow towards the sides and hence decrease the resultant side flow factor (see Figure 3.14c).

### 3.2.4 Side-by-Side Tape Casting

Among the more common applications of tape casting mentioned in the introduction, the process is well suited for manufacturing of functionally graded materials (FGMs). The concept of graded materials was first established by Bever and Duwez[Bever and Duwez, 1972] for composite materials, and then further developed for polymeric materials [Shen and Bever, 1972]. FGMs are materials that have a gradual variation of material properties from one end to another. The FGMs were originally developed as

special materials which could sustain long-term exposure to high temperature and large differences of temperature. There are different techniques to produce FGMs which are well summarized by Kieback and et al. [Kieback et al., 2003], and among them tape casting is reported extensively in literature [Acikbas et al., 2006; Yeo et al., 1998] due to producing large-area, thin, flat ceramics, which can be patterned, stacked, and laminated to form three-dimensional structures [Grader and Zuri, 1993].

In an era of critical demand for the development of alternative energy sources, magnetic refrigeration attracts significant interest as an environmentally friendly and energy efficient alternative to conventional refrigeration [Jr. and Pecharsky, 2008]. The technology relies on the so-called magnetocaloric effect (MCE), for reversible heating and cooling of magnetocaloric material (MCM) in magnetization/demagnetization cycles [Smith et al., 2012]. It is known for ferromagnetic materials that the largest temperature changes, as a response to a variation in magnetic field, occur near the phase transition, also known as the Curie temperature. The Curie temperature is very sensitive to changes in electronic or crystal structure and can thus often be chemically tuned. In order for a magnetic refrigeration device to produce a temperature span, a graded magnetocaloric material is desired, where the range of Curie temperatures is close to that of the device temperature span. In perovskite ceramic materials the Curie temperature can be tuned by a small amount of chemical doping. These materials can then be shaped into parts using the recently proposed method of side-by-side (SBS) tape casting [Dinesen et al., 2012]. Plates containing materials with two different ceramic materials have been prepared by this method and successfully tested in a magnetic refrigeration test device [Bahl et al., 2012]. A large batch of plates containing five different Curie temperatures have recently been prepared and will soon be tested in a large-scale magnetic refrigeration device at DTU Energy Conversion (EC).

As explained by Dinesen et al. [Dinesen et al., 2012], in the recently developed technique of side-by-side (SBS) tape casting, multiple slurries are tape casted adjacently forming a single tape to produce functionally graded ceramics (FGCs). Then, these FGCs are used in the magnetic refrigeration process in which there is a temperature gradient along the part (see Figure 3.15(a)).

One of the most important parameters which has a significant effect on the final properties of the SBS ceramics, is the behavior of the interface ($\Phi$) between the adjacent layers (see Figure 3.15(b)) [Jabbari et al., 2012] ([PAPER IV]). The aforementioned interface in the FGCs used for magnetic refrigeration are supposed to be close in shape to its ideal form of a 2D in-plane surface (in the $y-z$ plane), which is perpendicular to the substrate plane ($x-y$ plane). However, based on the slurry properties (i.e. the density and the viscosity) and the process conditions (i.e. the initial slurry height in the reservoir and the velocity of the peeling belt), the interface between the two adjacent layers can vary from its ideal shape to have different shapes as follows:

1. $\alpha_1 = \alpha_2 \neq 90$: $\Phi$ is a planar interface.

2. $\alpha_1 \neq \alpha_2 \neq 90$: $\Phi$ is a twisted-planar interface.

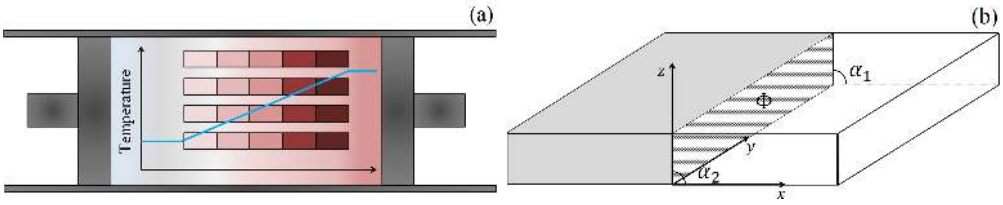


Figure 3.15: (a) Schematic example of FGCs used in magnetic refrigeration, and (b) schematic representation of the interface between the two adjacent layers [Jabbari et al., 2012]. ([PAPER IV])

We conducted numerical modeling of the SBS tape casting process with two fluid entries [Jabbari et al., 2012, 2013c,d]. The predicted interface was investigated to understand the influence of the material parameters of the two adjacent fluids, i.e. the density ($\rho$) and the viscosity ($\mu$), on the position of the interface. It was observed that the densities of the fluids do not influence the interface between the adjacent fluids, whereas the viscosity of the fluids plays a key role in the interface behavior. Specifically, it is seen that the viscosity difference ($\triangle\mu$) causes the fluid with lower viscosity to move toward the one with the higher viscosity. Moreover, increasing the aforementioned difference leads to further movement of the interface toward the fluid with the higher viscosity.

The impact of the substrate velocity was also investigated. As expected, it was found that by increasing the substrate velocity the height of both fluids decreased. Moreover, in the presence of the viscosity difference for the adjacent fluids, by increasing the substrate velocity the interface moved more toward the fluid with the higher viscosity.

Finally, it was concluded that for the magnetic refrigeration applications with the objective of an ideal (totally perpendicular) interface between the adjacent fluids, the viscosities of the fluids should be kept as close as possible. Moreover, in the presence of a viscosity difference ($\triangle\mu$), to decrease the diffusive region, as low velocities as possible for the substrate should be used. This is illustrated in Figure 3.16. This is due to an increase of the drag force by increasing the substrate velocity ($v_0$), which makes it more dominant compared to the pressure force, and results in more stretching of the slurry over the peeling belt [Jabbari et al., 2013b; Joshi et al., 2002; Kim et al., 2006; Pitchumani and Karbhari, 1995].

### 3.2.5 Tracking of Particles

As already discussed in section 2.4, the LVOV model is used in this thesis to track the migration of the ceramic particles in tape casting. The dimensions for the machine

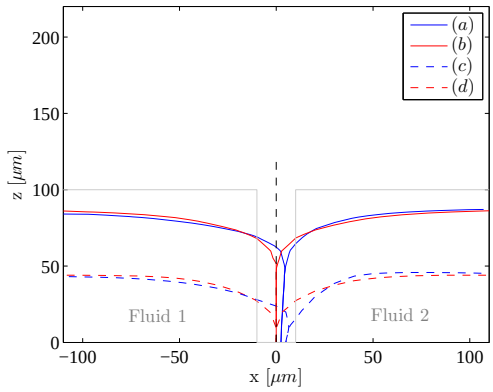


Figure 3.16: The change in the predicted interface between the adjacent layers for different cases, (a) $v_0 = 3.67mm/s$, $\rho_{F2} = 2\rho_{F1} = 4kg/m^3$ and $\mu_{F2} = 2\mu_{F1} = 6Pa.s$, (b) $v_0 = 3.67mm/s$, $\rho_{F2} = 2\rho_{F1} = 4kg/m^3$ and $\mu_{F2} = \mu_{F1} = 3Pa.s$, (c) $v_0 = 7.34mm/s$, $\rho_{F2} = 2\rho_{F1} = 4kg/m^3$ and $\mu_{F2} = 2\mu_{F1} = 6Pa.s$, (d) $v_0 = 7.34mm/s$, $\rho_{F2} = 2\rho_{F1} = 4kg/m^3$ and $\mu_{F2} = \mu_{F1} = 3Pa.s$. The gray lines indicate the geometry at the exit from the tape caster [PAPER IV].

configuration are also taken from previous works [Jabbari et al., 2013b; Jabbari and Hattel, 2012, 2013], in which the doctor blade height is equal to $h = 0.4mm$. The density of the ceramic slurry is $\rho_c = 2kg/m^3$ [Jabbari et al., 2013b; Jabbari and Hattel, 2012, 2013], and for the particles inside the slurry it is equal to $\rho_p = 10kg/m^3$ ($\kappa = \rho_p/\rho_c = 5$). The particle size ($a$) is assumed to be 0.1 $\mu m$, and moreover the initial particle load (the volume fraction of the particles in the inlet boundary) inside the slurry is assumed to be 0.35.

The particle distribution inside the ceramic slurry is shown in Figure 3.17 for two sets of simulations, with and without applying the LVOV model. As seen, the results are totally different from the constant distribution to the spatially varying one. Using the LVOV model, showed that there are some parts inside the ceramic in which the concentration of the particles are higher compared to other parts, creating the resulting packing structure [Chantaramee et al., 2008, 2007]. This can be discussed from the actual velocity distribution and corresponding shear rates for both cases in the doctor blade region. As illustrated in Figure 3.18(a) and (b), there are two high shear rate zones when using the LVOV model. These zones cause a ceramic slurry flow with higher concentrations of the particles. The high shear rate zones below the doctor blade (just before the exit) will drive the particles inside the flow in the horizontal direction ($x$). Moreover, due to relatively high shear rates in the bottom boundary, particles tend to swirl and create some regions with high concentrations (see the right hand side of Figure 3.17(b)). The high concentration region which was the first to be carried out by the peeling belt will be pushed forward by the flow coming from behind. This means that in the real life process, one should cut the aforementioned

region due to its highly nonuniform distribution of the particles. However, even the flow behind shows a somewhat layered structure (left hand side of Figure 3.17(b)) resulting in a heterogeneous particle distribution. This certifies the existence of a nonuniform distribution (or packing) of the particle in tape casting of ceramics, which was also found experimentally by Chantaramee et al. [Chantaramee et al., 2008, 2007].

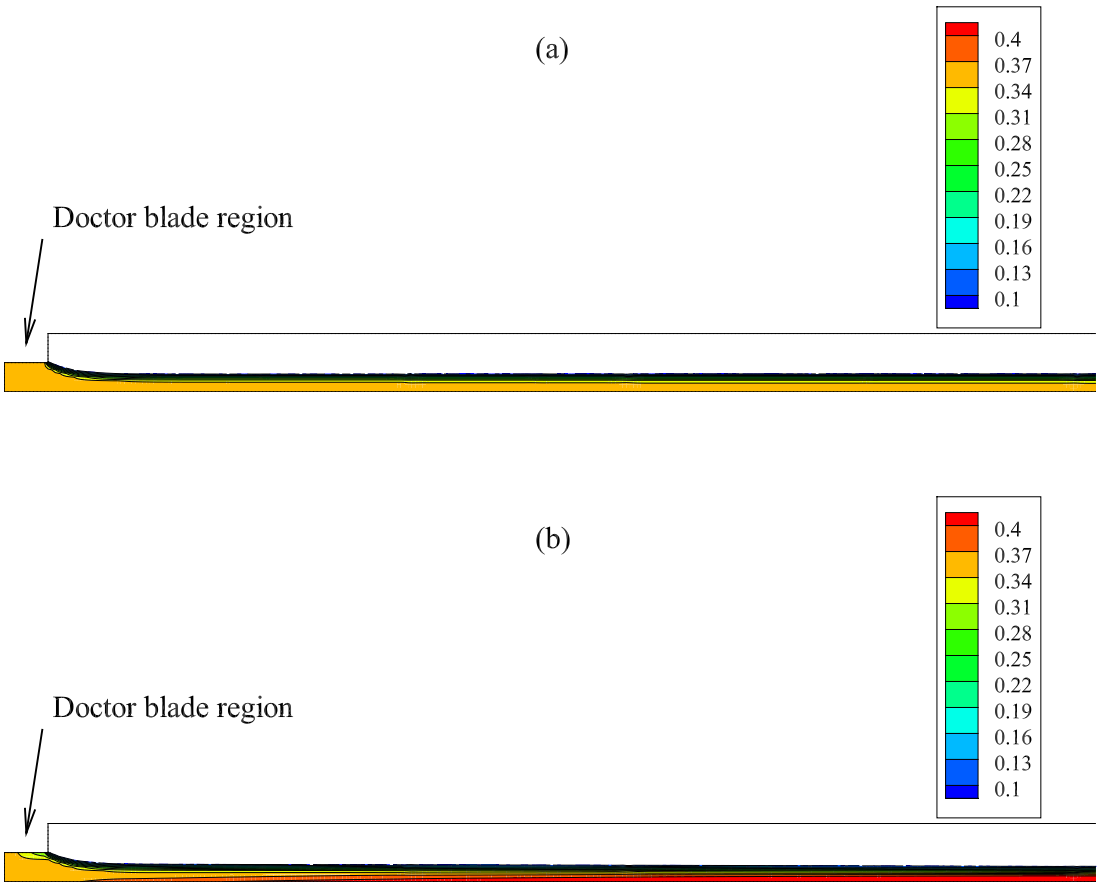


Figure 3.17: Distribution of the volume fraction for the particles inside the ceramic slurry, (a) without applying, and (b) with applying the LVOV model [PAPER VI].

The velocity of the substrate (the casting speed, $v_0$) has been increased in order to evaluate the influence of increasing the shear rates in the LVOV model. Comparing the results from Figure 3.19 with Figure 3.17(b), it is seen that the region with the concentration of particles still exists (right hand side of Figure 3.19). As mentioned earlier this region will be moved by the flow behind, and that part of the tape can be cut off at the end of process. However, the pattern of the produced layered structure in the case with the higher velocity (Figure 3.19) is different from the one with lower velocities tending to have more horizontal layers. Looking at the velocity and the shear

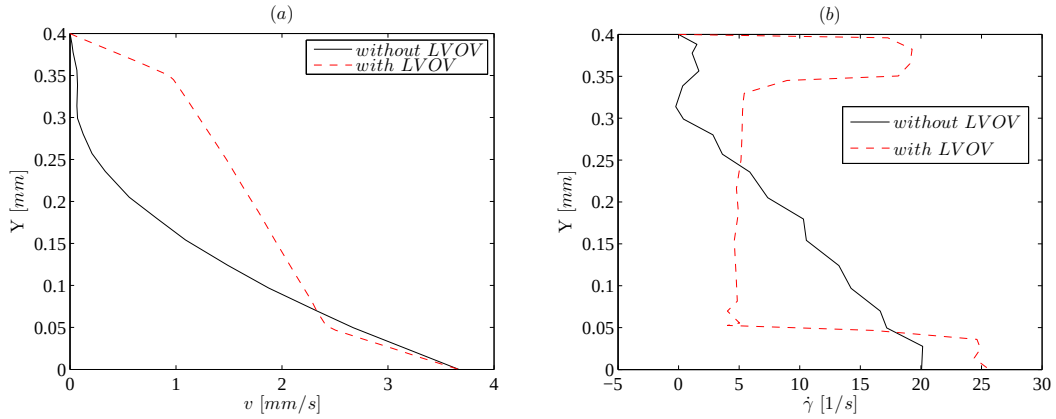


Figure 3.18: (a) The velocity profile, and (b) the shear rate distribution in the doctor blade region [PAPER VI].

rate distribution below the doctor blade, Figures 3.20(a) and (b), shows that increasing the substrate velocity will increase the shear rates and also the regions with the high shear rate zones. The presence of these zones will promote migration of the particles inside the ceramic slurry. Moreover, the higher the shear rates in the slurry, the less the gravity induced particle migration. This leads to less settlement of the particles inside the fluid.


Figure 3.19: Distribution of the volume fraction for the particles inside the ceramic slurry with the increase (doubled) substrate velocity [PAPER VI].

As mentioned earlier, the region with the highest concentration of the particles (right hand side of the Figure 3.17 and 3.19) is being carried by the flow behind. It is of course interesting to see the particle distribution in the point of time in which steady state conditions are reached. To do so, two sensors are implemented in the flow domain with a reasonable distance (here 10 and 20 *cm* from the doctor blade exit) to

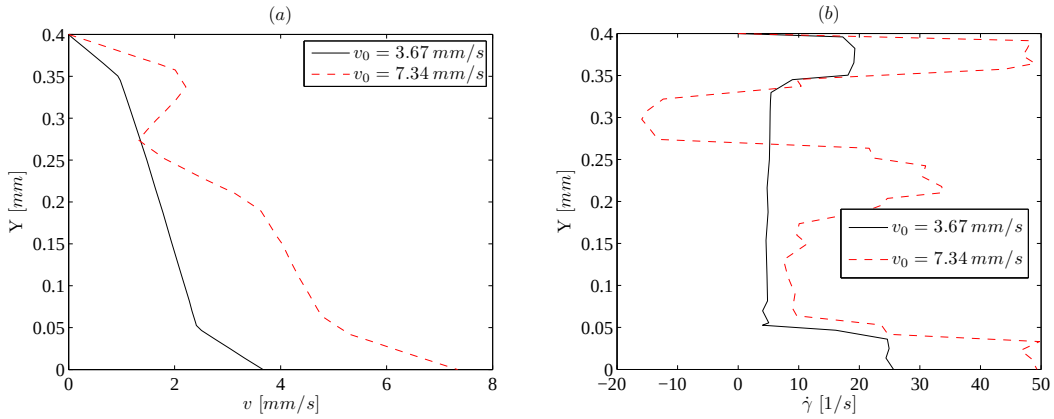


Figure 3.20: (a) The velocity profile, and (b) the shear rate distribution in the doctor blade region [PAPER VI].

check the variation of the volume fraction with time. Two different substrate velocities of $v_1 = 3.67mm/s$ and $v_2 = 2v_1 = 7.34mm/s$ as well as two different density ratios of $\kappa = 0.1$ and $\kappa = 10$ are investigated.

It was found that, after some reasonable time in the simulation, the particle distribution inside the ceramic slurry is not changing anymore. The particle volume fraction inside the ceramic slurry in the steady state condition are illustrated in Figure 3.21(a) and (b). It should be noted that the tape thickness decreases with an increase in the substrate velocity [Jabbari et al., 2013b; Jabbari and Hattel, 2012, 2013], and therefore the comparison is made by dividing the "Y" position along the tape thickness with the tape thickness itself (corresponding to normalizing with the correct tape thickness). Again, it is seen that for the case with the lower shear rates (slower speed), particles tend to settle more in the bottom resulting in a higher concentration. This confirms that, using higher velocities for casting increases the dominance of the shear induced particle migration, creating a relatively uniform distribution of the particles. However, with lower casting speed the particles have enough time to settle in the bottom of the tape forming two different layers containing different particle distributions. Based on this, one can also conclude that changing any of the process parameters, i.e. the doctor blade height and the slurry height in the reservoir, in a way that leads to higher shear rates in the flow domain, can lead to a similar behavior. As reported in the previous works [Jabbari et al., 2013b; Jabbari and Hattel, 2012, 2013], decreasing the doctor blade height as well as the slurry height in the reservoir will increase the shear driven flow in the tape casting process.

Seen from Figure 3.21(a) and (b), it can moreover be concluded that for higher density ratio ($\kappa = 10$) the gravity shows its dominance by making the particles settled in the bottom of the tape. However, for the lower values of $\kappa$ the shear induced particle migration becomes dominant producing a more uniform distribution of the particles but

in the small region of upper area of the tape. Comparing Figure 3.21(a) and Figure 3.21(b), one can see that in the closer region of the doctor blade exit ($d = 10cm$) all of the investigated cases are showing more or less the same behavior. This trend stays somewhat the same for the cases further from the doctor blade region ($d = 20cm$) but the cases with higher value of the density ratio ($\kappa = 10$). This means that the particles with higher density are moved by the shear forces in the beginning of the process more than the gravity forces. However, gravity forces show their impact mostly in the regions further from the doctor blade region.

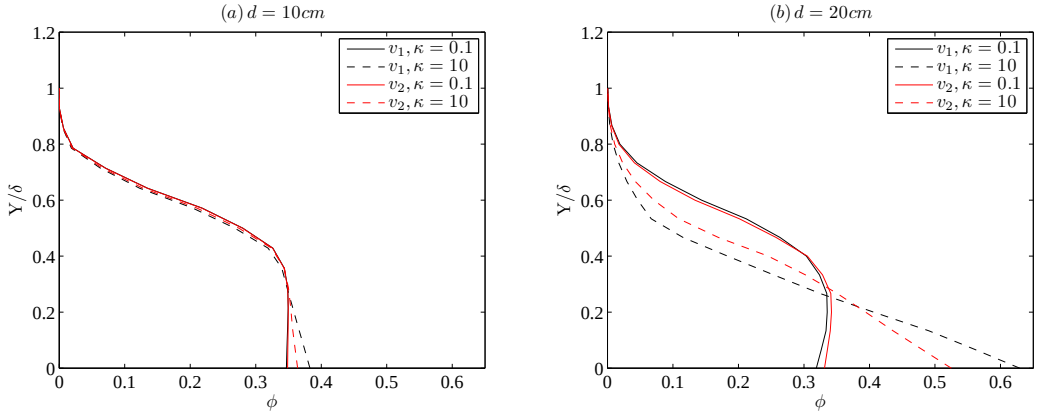


Figure 3.21: Distribution of the volume fraction in the thickness of the produced tapes at two different distances of doctor blade exit, (a) $d = 10$, and (b) $d = 20cm$ [PAPER VI].

# Chapter 4

# Drying Kinetics

This chapter presents a brief introduction to the drying process of thin ceramic sheets as well as the results of a single analysis of water evaporation from a ceramic-water mixture.

## 4.1 Introduction

As earlier mentioned in this thesis, tape casting consists of three major sub-processes which are (see Figure 4.1):

1. Tape casting of an aqueous (fluid) ceramic slurry in a doctor blade configuration
2. Drying of the green tape
3. Additional processing (which is often a sintering process).

Mostly the first and third stages have been investigated numerically [Jabbari et al., 2013b; Jabbari and Hattel, 2011, 2012, 2013, 2014; Olevsky, 1998] whereas the second has remained almost unexplored numerically. The sintering of the tape casted parts has been investigated in literature using continuum modelling [Olevsky, 1998]. The drying stage and the characterization of it in the form of final shrinkage is often measured experimentally, simply by the weight difference of the green and dried tapes, without really noticing that the drying is one of the most important steps in the tape casting process. As the solvent is removed from the green sheet (or layer) via evaporation, the tape undergoes a transformation from its initial fluid-like state to a solid-like, composite layer. This leads to changes in the rheological behavior (mostly viscosity) of the ceramic

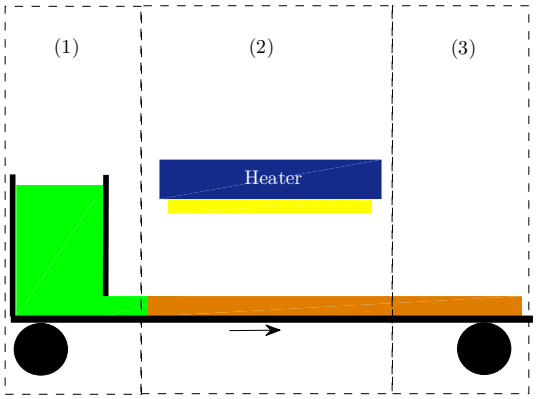


Figure 4.1: Schematic of the tape casting process with three sub-processes [PAPER VII].

slurry, and this is related to the amount of solvent (water in this study) evaporated during drying [Martinez and Lewis, 2002].

With many additives, and typically multiple solvents, drying of the tape as well as the behavior of the tape during the drying process can vary greatly from slip to slip. The tape casting process is somewhat unique among ceramic processes in the sense that a one-side drying process exists. After the slip is spread into a thin layer, all of the solvent is removed from a single side of the cast. Two things work together to cause the one-sided drying; a thin, essentially two-dimensional shape with no real height, and an impermeable carrier on the bottom. This single-sided drying is the cause of some very interesting phenomena within the tape matrix. Ideally, the chemical composition of the tape (primarily the solvent concentration) should stay uniform throughout the tape during the entire drying process. This, however, simply cannot occur, since all of the solvent must migrate to the top surface of the tape to evaporate. Hence, the two major mechanisms controlling the drying in the tape-cast layer are: (1) the rate of solvent evaporation from the surface of the cast and (2) the rate of solvent diffusion through the tape to the drying (top) surface. Of these two mechanisms, diffusion through the tape tends to be the rate-limiting factor [Scherer, 1990].

The two aforementioned mechanisms can be adjusted by various means. The volatility of the solvent at the tape surface can be adjusted by adapting the types of solvent used, the concentration of solvent vapor in the local atmosphere, the local air temperature, and the solvent temperature. The diffusion rate through the tape layers can be adjusted by changing the binder concentration, altering particle size, adjusting the wet film temperature, and keeping an open pathway to the surface. Some of these control techniques, such as particle size and binder content, need to be addressed during the preparation of the slip and factored into the initial slip recipe. Other parameters like

air temperature, slip temperature, and local vapor concentration are controlled by the drying equipment separate from the casting slip.

As the solvent on the top surface of the cast layer takes energy from the air and from the rest of the slip, it starts to evaporate into the surrounding atmosphere. The rate of evaporation is governed by the energy available to the solvent, the volatility of the solvent species, the vapor concentration of the local atmosphere, and the saturation concentration of the local atmosphere, which depends upon the gases in the atmosphere, the solvent species, and the temperature. Since evaporation requires an input of energy, raising the temperature of the solvent will speed the surface evaporation process by providing an excess of energy. Raising the air temperature will not only provide the energy for evaporation (heat of vaporization), but will also increase the saturation concentration of the atmosphere. Air heating greatly increases the surface evaporation rate, and that is why many tape casting machines are equipped with an air heating option to speed up the surface evaporation of the tape. In this study, only the raise of energy (by the temperature field) is considered for the drying process and the influences of saturation are neglected.

Diffusion of the solvent to the top surface of the tape is normally the rate limiting factor in drying. The rate of evaporation of surface solvent is normally so much faster than the solvent motion to the surface that a drying crust forms across the surface of the tape. Efforts to limit surface evaporation stem from the desire to avoid this skin on the surface. Ideally, the solvent concentration should stay nearly uniform throughout the tape during drying so that all parts of the tape dry at the same rate. This would be accomplished by making the rate of diffusion equal to the rate of evaporation. The ideal case, however, is unattainable. In practice, the drying conditions, tape structure, tape components, and solvent mixtures are balanced to get as close to ideal conditions as the downstream manufacturing needs allow.

The hypothetical progression of solvent concentration during the drying process is illustrated in Figure 4.2 graphically. On the figure, $y = 0$ represents the carrier surface whereas $y = 1$ represents tape thickness (the drying surface). It is assumed that at time equal to zero the concentration of the solvent is equal to one, and the final concentration of the solvent at $t = 1s$ is equal to $C = 0.1$. As mentioned, the ideal case shows a uniform solvent concentration through the thickness of the tape throughout the drying process (Figure 4.2(a)). In reality, the evaporation rate from the surface will always be faster than the motion of solvent to the surface. Thus the best-case scenario displays a dry film on the top of the tape, yet a diminishing amount of solvent at the slip/carrier interface (Figure 4.2(b)). This best-case scenario exists when the rates of diffusion and evaporation are as close to equal as possible. The worst-case scenario is realized when the rate of evaporation is much greater than the diffusion rate through the tape matrix. The top surface of the tape, giving off solvent much

more quickly than the diffusion mechanism can replace it at the surface, forms an ever-thickening dry layer, while the solvent concentration at the slip/carrier interface does not significantly decrease (Figure 4.2(c)).

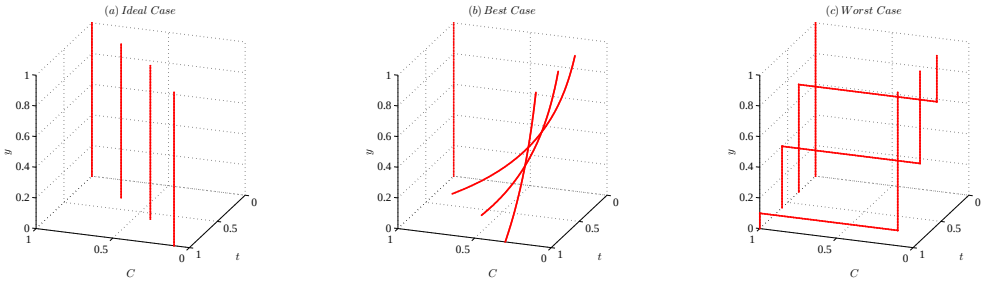


Figure 4.2: Schematic illustration for distribution of solvent content for (a) ideal, (b) best obtainable, and (c) worst cases[Mistler and Twiname, 2000].

The speed at which the solvent can move to the surface is always the slowest mechanism of drying. The rate of motion through the body of the tape is limited mainly by the body itself. The pathway for the solvent through the tape matrix is crowded with particles, binder, plasticizer, and dispersant. As the drying process progresses, the tape shrinks, creating the dense, packed bed of particles which is the goal of tape casting. This dense, packed bed, however, limits the escape paths for the solvent at the slip/carrier interface. As a rule, liquids diffuse much more quickly through a liquid medium than through any other medium [Callister, 2000]. At some point in the drying process, the binder at the top surface of the cast will lose enough solvent to form a solid sheet or skin across the top of the tape. This is unavoidable since the dry tape is simply a solid piece of this skin. The diffusion rate of the underlying solvent is much slower through this skin than through the liquid matrix of the slip. This, once again, is why effort is made to slow the surface evaporation rate to delay the formation of this low-diffusion-rate skin. The dried polymer effectively plugs up the inter-particulate spaces, creating a low-permeability layer across the top of the tape and limiting the bulk drying rate. This is where a balance must somehow be established between drying rate and tape porosity. Allowing some porosity in the tape will increase solvent diffusion to the top surface by keeping an open pathway to the top surface. The addition of a slow-drying solvent can also aid solvent migration speed by delaying skin formation and providing a liquid pathway from bottom to top. This type of additive would properly be called a skin retarder and may actually be used as one of the primary solvents in the slip.

Heating the tape body is the last general phenomenon which affects both drying mechanisms. This not only increases solvent evaporation rate by heating the solvent, but also increases the diffusion speed of solvent through the matrix, as the diffusion is a thermally controlled phenomenon. Heating the tape matrix promotes liquid-like

behavior and increases the diffusion rate of the solvent. Many practitioners in the field find that the fastest way to dry a tape is to heat the bottom of the tape without heating the air. Heating the bottom of the tape increases solvent mobility in the tape body, driving the solvent up to the surface, while air heating tends to have a greater impact on the tape surface evaporation. In most cases, the surface evaporation does not need help.

In general, modelling of the drying process deals with complex physics, e.g. heat transfer, mass transfer (Darcy's law and diffusion), and capillary forces (pressure), which are coupled together. The theory of the drying is well discussed by Schere [Scherer, 1990] for the sol-gel processing, where there is a polymer chain. On the other hand, only experimental and analytical investigations [Kiennemann et al., 2005; Martinez and Lewis, 2002] have been conducted in literature so far for the drying process of ceramic slurries. The current study is the first example of numerical investigation for coupled heat and mass transfer for drying in tape casting of ceramics. The capillary forces are neglected in this study and it is assumed that the mass transfer is governed only by diffusion of the solvent. It should, moreover, be mentioned that as the solvent used in every slurry formulation varies for every desired application, and the thermo-physical properties of each solvent are not available in literature, the solvent in this study is assumed to be water, and hence the system simulated is the mixture of ceramic and water. The first stage of drying where the solvent is evaporating from the tape matrix is simulated numerically. The 1D heat conduction equation is solved numerically to obtain the temperature field in a ceramic sheet. The change in the concentration of the water content is then used as driving force for the diffusive mass transport of water (described by Fick's second law also in 1D).

## 4.2 Mathematical model

### 4.2.1 Simulation domain

The 1D simulation domain used in this study is illustrated schematically in Figure 4.3. As seen, a heater with the length of $L_{heat}$ and the temperature of $T_{heat}$ is located above the tape layer, and the tape (which is a ceramic-water mixture) is passing beneath the heater with the velocity of $v_{cast}$. This means that the tape experiences the major part of the temperature load for a period of time equal to $L_{heat}/v_{cast}$. The domain is discretized into a number of control volumes (here $N$), in a way such that the air region is assumed to be one single control volume. This leads to the space increments as follows

$$\begin{cases} dx(1) = d_{gap} & air\ region \\ dx(2:N) = \frac{\delta}{N-1} & tape\ region \end{cases} \tag{4.1}$$

where $\delta$ is the tape thickness, and $d_{gap}$ is the distance between the heater and the top surface of the tape.

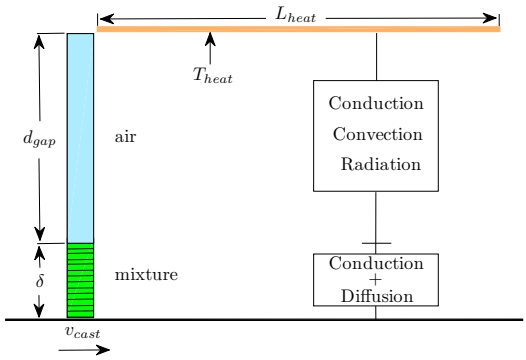


Figure 4.3: Schematic illustration of the simulation domain [PAPER VII].

The physics to be considered in this numerical study, is also shown in Figure 4.3 for each region, and will be discussed in the following.

### 4.2.2 Thermal calculations

It is well-known that in the presence of a temperature gradient, energy conducts from the high temperature region to the low one. Based on Fourier's law the heat flow per unit area is proportional to the normal temperature gradient, i.e.:

$$q = -kA\frac{\partial T}{\partial x} \tag{4.2}$$

where $q$ is the diffusive heat flux $(W)$, $A$ is the area $(m^2)$, $k$ is the thermal conductivity $(W/mK)$, $T$ is temperature $(K$ or $°C)$, and $x$ is length $(m)$. Assuming a constant thermal conductivity, the integration of Fourier's law becomes

$$q = -\frac{kA}{x_2 - x_1}(T_2 - T_1) = -\frac{\triangle T}{R_{th}^{cond}} \qquad where \qquad R_{th}^{cond} = \frac{\triangle x}{kA} \tag{4.3}$$

in which $R_{th}^{cond}$ is the thermal conductive resistance.

Based on Newton's law of cooling the overall effect of convection can be expressed by:

$$q = -hA\,(T_\infty - T_s) \tag{4.4}$$

where $h$ is the convective heat transfer coefficient $(W/m^2K)$, $T_s$ and $T_\infty$ are the body surface temperature and the cooling temperature, respectively. Comparing equations

$$R_{th}^{conv} = \frac{1}{h^{conv} A} \tag{4.5}$$

The third mode of heat transmission taking place is radiation, which is expressed with a special version of Stefan-Boltzmann's law

$$q = -A\varepsilon\sigma \left(T_2^4 - T_1^4\right) = -A\varepsilon\sigma \left(T_1^3 + T_1^2 T_2 + T_1 T_2^2 + T_2^3\right)(T_2 - T_1) \tag{4.6}$$

where $\sigma$ is the Stefan-Boltzmann constant, and equals to $5.67 \times 10^{-8}$ $(W/m^2K^4)$. This equation assumes a radiative heat exchange between two surfaces (with the same area, $A$), and accounts for the gray nature of the surface (accounting for the emissivity, $\varepsilon$). Comparing equation (4.3) and (4.6), the thermal radiative resistance can be found as

$$R_{th}^{rad} = \frac{1}{h^{rad} A} \qquad where \qquad h^{rad} = \varepsilon\sigma \left(T_1^3 + T_1^2 T_2 + T_1 T_2^2 + T_2^3\right) \tag{4.7}$$

The general heat conduction equation can be derived based on Fourier's law together with the first law of thermodynamics:

$$\rho c_p \frac{\partial T}{\partial t} = \nabla \left(k \cdot \nabla T\right) + \dot{Q} \tag{4.8}$$

where $\rho$ is the density $(kg/m^3)$, $c_p$ is the specific heat $(J/kgK)$, and $\dot{Q}$ is the generated heat per unit time per unit volume $(W/m^3)$. Assuming constant thermal conductivity, the 1D heat conduction equation finally takes the form

$$\frac{\partial T}{\partial t} = \alpha \frac{\partial^2 T}{\partial x^2} + \dot{Q} \tag{4.9}$$

where $\alpha$ is the thermal diffusivity equal to $k/\rho c_p$. In the present study the above equation is discretized in the simulation domain via the finite volume method (FVM) in order to solve it numerically [Hattel, 2005]. Mass-averaged thermal properties are assumed for the ceramic-water mixture in the initial stage. However, as the water evaporates the thermal properties of the solid ceramic become more dominant since the fraction of water approaches zero. The mass-averaged thermal properties assumed for the ceramic-water mixture then are as follows

$$\alpha_{mix} = f_{water}\alpha_{water} + \left(1 - f_{water}\right)\alpha_{ceramic} \tag{4.10}$$

where $f_{water}$ is the fraction of water in each control volume.

An implicit scheme is used to find the new temperatures in each time step [Hattel, 2005]

$$-H_i^{Con}T_{i-1}^{t+\triangle t} + \left(H_i^{Cap} + H_i^{Con} + H_{i+1}^{Con}\right)T_i^{t+\triangle t} - H_{i+1}^{Con}T_{i+1}^{t+\triangle t} = H_i^{Cap}T_i^t + \frac{\dot{Q}_{gen,i}^{t+\triangle t}}{A} \tag{4.11}$$

where $T_i^{t+\triangle t}$ is the new temperature, $T_{i,}^t$ is the old temperature, and

$$\begin{aligned} H_i^{Cap} &\equiv \tfrac{\triangle x_i(\rho c_p)_i}{\triangle t} \qquad capacity\ function \\ H_i^{Con} &\equiv \tfrac{1}{\frac{\triangle x_{i-1}}{2k_{i-1}} + \frac{\triangle x_i}{2k_i}} \qquad conductivity\ function \end{aligned} \tag{4.12}$$

It should be noted that for the nodes 2 ($i = 2$), the conductivity function is as follows

$$H_2^{Con} \equiv \frac{1}{\frac{1}{h^{tot}} + \frac{\triangle x_2}{2k_2}} \tag{4.13}$$

where $h^{tot}$ is the equivalent heat transfer coefficient for the total transfer in the air gap

$$h^{tot} = \frac{1}{R_{th}^{cond}} + h^{conv} + h^{rad} \tag{4.14}$$

where $h^{conv}$ is assumed to be 10 $(W/mK)$, and $h^{rad}$ is given by equation (4.7). The coefficients in front of the unknown temperatures on the left hand side of equation (4.11) are now called $a$, $b$, and $c$, and the right hand side is called $d$. Thus for $i = 2, ..., N-1$, we have

$$a_i \cdot T_{i-1}^{t+\triangle t} + b_i \cdot T_i^{t+\triangle t} + c_i \cdot T_{i+1}^{t+\triangle t} = d_i \tag{4.15}$$

where

$$\begin{aligned} a_i &= -H_i^{Con} \\ b_i &= H_i^{Cap} + H_i^{Con} + H_{i+1}^{Con} \\ c_i &= -H_{i+1}^{Con} \\ d_i &= H_i^{Cap}T_i^t + \dot{Q}_{gen,i}^{t+\triangle t}/A \end{aligned} \tag{4.16}$$

The system of equations for the inner nodes, $i = 2, ..., N-1$, as well as for node 1 and $N$ as boundary condition becomes

$$
\begin{array}{c}
node \\
1 \\
2 \\
\dots \\
N-1 \\
N
\end{array}
\begin{Bmatrix}
b_1 & c_1 & & & \\
a_2 & b_2 & c_2 & & \\
 & \dots & \dots & \dots & \\
 & & a_{N-1} & b_{N-1} & c_{N-1} \\
 & & & a_N & b_N
\end{Bmatrix}
\cdot
\begin{Bmatrix}
T_1 \\ T_2 \\ \dots \\ T_{N-1} \\ T_N
\end{Bmatrix}
=
\begin{Bmatrix}
d_1 \\ d_2 \\ \dots \\ d_{N-1} \\ d_N
\end{Bmatrix}
\tag{4.17}
$$

The boundary conditions express that at node $i = 1$ the temperature of the heater is $T_{heat}$, and at $i = N$ the heat flux is zero

$$
\begin{aligned}
i = 1 \quad &\Rightarrow \quad b_1 = 1 \qquad c_1 = 0 \quad d_1 = T_{heat} \\
i = N \quad &\Rightarrow \quad a_N = -1 \quad b_N = 1 \quad d_N = 0
\end{aligned}
\tag{4.18}
$$

The equation system is solved easily by Gaussian elimination.

### 4.2.3 Diffusion

Fick's second law, also known as the Diffusion Equation, states that the change of concentration in time equals to the net influx by diffusion. This leads to an equation which is totally similar to the heat conduction equation

$$
\frac{\partial \phi}{\partial t} = \frac{\partial}{\partial x}\left(D \frac{\partial \phi}{\partial x}\right) \tag{4.19}
$$

where $\phi$ is the concentration of water ($mol/m^3$), and $D$ is the diffusion coefficient ($m^2/s$), which in general is dependent on temperature in the present work. In order to solve equation (4.19), the same implicit scheme is used as described in section 4.2.2.

## 4.3 Preliminary Results

As mentioned earlier, the drying process in thin layers is derived by both the temperature load on top of the domain and the diffusion of the solvent through the tape body. In order to test the diffusion module, a simple test was conducted in which the inter-diffusion happens between two regions with different concentration values (see Figure 4.4). Inter-diffusion is popular between two semi-infinite specimens of different compositions $c_1$, $c_2$, when they are joined together and annealed, or mixed in case of two solutions (liquids). Many examples in practice fall into the case of inter-diffusion, including two semiconductor interface, metal-semiconductor interface, etc.

The magnitude of the diffusion coefficient $D$ is indicative of the rate at which atoms diffuse. The diffusing species as well as the host material influence the diffusion

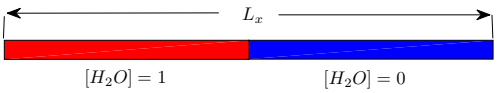


Figure 4.4: Simulation domain for a 1D inter-diffusion phenomenon.

coefficient. For example, there is a significant difference in magnitude between self- and carbon inter-diffusion in iron at 500°C, the $D$ value being greater for the carbon inter-diffusion ($3.0 \times 10^{-21}$ vs. $2.4 \times 10^{-12}$ $m^2/s$). This comparison also provides a contrast between rates of diffusion via vacancy and interstitial modes [Callister, 2000]. Self-diffusion occurs by a vacancy mechanism, whereas carbon diffusion in iron is interstitial. A very well-known analytical solution for the inter-diffusion for different initial compositions $c_1$, $c_2$, is as follows

$$c\left(x,t\right) = \left(\frac{c_1 + c_2}{2}\right) - \left(\frac{c_1 + c_2}{2}\right) erf\left(\frac{x}{2\sqrt{Dt}}\right) \tag{4.20}$$

where the error function $(erf)$ is equal to

$$erf\left(z\right) = \frac{2}{\sqrt{\pi}} \int_0^z e^{-y^2} dy \tag{4.21}$$

The results of numerical modelling for two different diffusion coefficients, $D$, and their comparison with the corresponding results from the analytical solution with $c_1 = 1$, $c_2 = 0$, are illustrated in Figure 4.5(a) and (b). As seen, not surprisingly the diffusion region becomes wider by by increasing the diffusion coefficient, $D$. Moreover, the results of numerical modelling are in a very good agreement with the analytical ones.

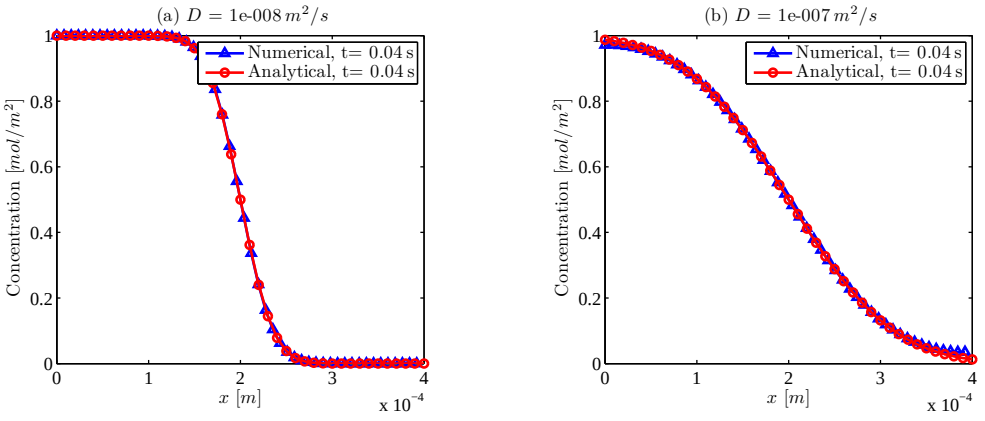


Figure 4.5: Concentration variation along the $x$ axis for $L_x = 400\mu m$, and for different diffusion coefficient of (a) $D = 1e-8$, and (b) $D = 1e-7$.

The diffusivity is found to vary in most systems as an exponential function of temperature, hence it is modeled by the Arrhenius relationship:

$$D_w = D_0 exp\left(-\frac{Q_a}{RT}\right) \tag{4.22}$$

where $Q_a$ is the activation energy for diffusion, $R$ is the gas constant, $T$ is the absolute temperature, and $D_0$ is the pre-exponential "frequency factor" which is empirically determined. The activation energy may be thought of as that energy required to produce the diffusive motion of one mole of atoms. A large activation energy results in a relatively small diffusion coefficient. Taking the natural logarithm of equation (4.22) yields

$$\ln D = \ln D_0 - \frac{Q_a}{R}\left(\frac{1}{T}\right) \tag{4.23}$$

or in terms of logarithms to the base 10

$$\log D = \log D_0 - \frac{Q_a}{2.3R}\left(\frac{1}{T}\right) \tag{4.24}$$

Since $D_0$ , $Q_a$ , and $R$ are all constants, equation (4.24) takes on the form of an equation of a straight line:

$$y = ax + b \tag{4.25}$$

where $y$ and $x$ are analogous, respectively, to the variables $\log D$ and $1/T$. Thus, if $\log D$ is plotted versus the reciprocal of the absolute temperature, a straight line should be the result, having slope and intercept of $Q_a/2.3R$ and $\log D_0$, respectively. This is, in fact, the manner in which the values of $Q_a$ and $D_0$ are determined experimentally. For this study such data are used through the fitted line from the experimental results published by Holz et al. [Holz et al., 2000] (shown in Figure 4.6), as follows:

$$\log D_w = 3 \times 10^{-7} - 8 \times 10^{-8}\left(\frac{1}{T}\right) \tag{4.26}$$

The mass-averaged diffusion coefficient is used for the ceramic-water mixture as follows

$$D_{mix} = f_{water} D_w + (1 - f_{water}) D_d \tag{4.27}$$

where $D_d$ is the diffusion coefficient in the dried control volumes which is assumed to be $\log D_d = -11$, and $D_w$ is given by equation (4.26).

All thermo-physical properties used in this study are summarized in Table 4.1. It should be noted that the thermal [Hattel, 2005] model has been validated against proper analytical solutions. The simulation domain considered for the present study is illustrated in Figure 4.3. The temperature of the heater on the top region of the

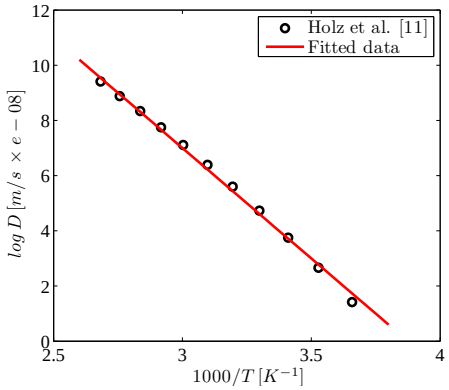


Figure 4.6: Fitted data used for the temperature-dependent diffusion coefficient of water [Holz et al., 2000] [PAPER VII].

tape matrix is assumed to be 140°C. The initial temperature of the tape matrix and the air above it is assumed to be in the room temperature (20°C). It should also be mentioned that since the saturation of air is neglected in this study, choosing a different temperature for air from the one for tape matrix does not make any sense.

Table 4.1: Thermo-physical material properties used in this study [PAPER VII].

| | Water | Ceramic | Ceramic-water mixture |
|---|---|---|---|
| $k\ (W/mK)$ | 0.6 | 2.4 | mass-averaged |
| $\rho\ (kg/m^3)$ | 997.1 | 1900 | mass-averaged |
| $c_p(J/kgK)$ | 4187 | 2000 | mass-averaged |
| $L_H^{evap}(kJ/kg)$ | 2260 | - | - |
| $\log D$ | equation (4.26) | $-11$ | mass-averaged |

Results of simulations for three different tape thicknesses, $\delta = 400, 300, 200\ \mu m$ with an initial water content of 12%, are shown in Figure 4.7(a). The results show that for each tape there is a specific time period in which the water content is not changing hence being equal to the initial value of water content (12%). This region corresponds to the period in which the tapes are heating up, and it has the highest value for the thickest tapes which of course is expected, see Figure 4.7(a).

As seen from the sub-plot of Figure 4.7(a) (which is also representative for thicknesses of 200 and 300 $\mu m$), there are two specific regions, (1) and (2), where the evaporation shows two principally different behaviors. A similar example of such plots showing these two regions can be found in the work by Kiennemann et al. [Kiennemann et al., 2005], in which mass loss, shrinkage, Young's modulus evolution and stress development of aqueous (alumina+latex) tape cast suspensions were observed experimentally during drying. They also reported that the mass loss shows a constant drying rate period, followed by a falling rate period. In region (1) the total evaporation (mass loss) is increasing almost linearly by time. This region is called the constant rate period

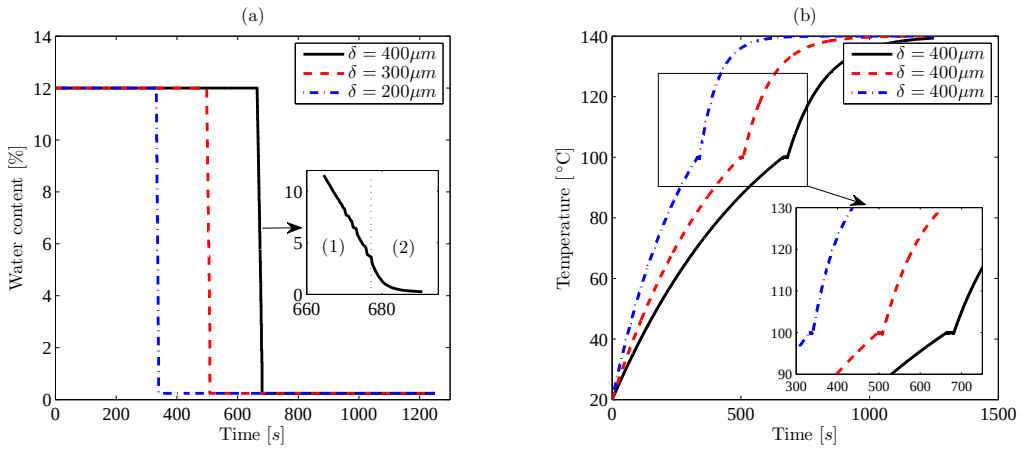


Figure 4.7: (a) Variation of water content due to evaporation, and (b) the temperature profiles for the top control volume in the tape [PAPER VII].

(CRP), in which the rate of evaporation per unit area of the drying surface is independent of time [Scherer, 1990]. During the CRP, the liquid-vapor meniscus remains at the surface of the tape layer, and evaporation occurs at a rate close to that of a free liquid surface (e.g., an open dish of liquid).

When evaporation starts, in the early stages, the temperature at the surface of the top layer drops because of a loss of heat due to the latent heat of vaporization of the water. On the other hand, heat flows to the surface from the atmosphere thus quickly establishing thermal equilibrium where transfer of heat to the surface balances the heat loss due to the latent heat of vaporization. However, when the amount of mass loss increases, the heat loss due to the latent heat of vaporization of the water will also increase. This reduces the evaporation rate, as a consequence of low migration of the water from the bottom layers to the top ones due to diffusion (which is highly dependent on the temperature). This is the late stage in the CRP, where the drying rate starts to decrease.

The top layers of the tape, which are already dried, will now act as a barrier for diffusion of the water from bottom to top. This is reflected by region (2), which is known as the falling rate period (FRP). Transport of liquid during drying can occur by flow if a pressure gradient exists in the liquid, and diffusion if a concentration gradient exists. The first type is categorized as flow in porous media where the liquid flow obeys Darcy's law. This type of liquid transport, however, is neglected in this study due to the low level of pressure gradient in the tapes. The latter type is the one considered in this study, which is highly sensitive to temperature. As mentioned, the temperature drop reduces the diffusion coefficient of the water, and consequently the drying rate is decreased drastically. It can, moreover, be seen from Figure 4.7(a) and (b) that by deceasing the tape thickness ($\delta$) the mass loss occurs in a shorter period of time. This

means that the drying rate is high in the tapes with smaller tape thickness, which can be seen in Figure 4.8. As shown, the maximum mass loss happens in the tape with smaller thickness. This is expected, as the smaller tape thickness gives the liquid ability to diffuse to the top surface more. Such information can be used in thermo-mechanical simulation in order to predict the stress evolution during drying.

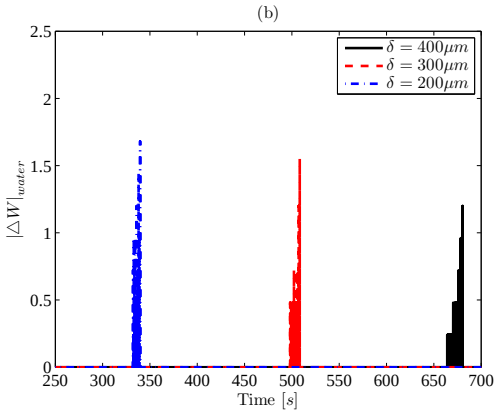


Figure 4.8: Amount of mass loss for three different tape thickness [PAPER VII].

Another interesting phenomenon in the drying process is to investigate the different drying modes, i.e. fast, intermediate, and slow. Results of such investigations are shown in Figure 4.9 based on the variation of the non-dimensional water concentration ($C^* = C^{new}/C_0$) for the thickness of $\delta = 400\mu m$. As seen, when the drying is fast, the water in the upper region evaporates fast and makes a solid-like region in almost the entire upper half of the tape. This creates a barrier for the diffusion of the bottom water and makes the rest of the drying slow. In other words, when the drying mode is fast, the diffusion of the water from bottom to the top surface is slow. This is similar to the worst case shown in Figure 4.2(c), which may happen if extensive heating is used in the drying process. Moreover, it is seen that for the slow drying mode the evaporation of water from the top region is somewhat slow, though the drying (diffusion) from the bottom region is faster. This case is also similar to the ideal case shown in Figure 4.2(a). The mode of drying can hence be argued based on the competition between the evaporation rate from the top surface and the diffusion of the water from bottom to the top. As mentioned before, in reality, the evaporation rate from the top surface will always be much faster than the motion of solvent (water in this study) to the surface.

By this simulation, we have shown that the developed model for the evaporation of water from a ceramic-water mixture can be used with the purpose of understanding the drying rate in the drying process of thin sheets produced by the tape casting process. The results showed that initially, the mass loss due to the evaporation is increasing close to linearly with the drying time corresponding to an almost constant drying rate. However, the rate starts to decrease after some time in the simulation. This is in

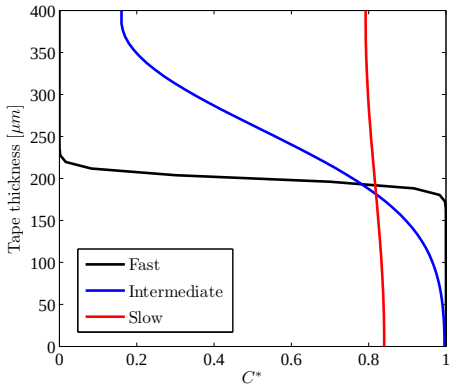


Figure 4.9: The results of numerical modelling for the different drying modes for the tape thickness of $\delta = 400\mu m$ [PAPER VII].

good agreement with experimental findings of the real life process where the drying is categorized into two stages: (1) a constant rate period (CRP), in which the rate of evaporation per unit area of the drying surface is independent of time, and (2) a falling rate period (FRP), in which the evaporation rate is reduced, as a consequence of low migration of the water from the bottom layers to the top ones due to diffusion (which is highly dependent to the temperature).

# Chapter 5

# Summary of Appended Papers

In this chapter a short summary of the seven appended papers are given.

## 5.1 PAPER I

M. Jabbari, R. Bulatova, J. Hattel, C. R. H. Bahl, "Quasi-steady State Power Law Model for the Flow of $(La_{0.85}Sr_{0.15})_{0.9}MnO_3$ Ceramic Slurry in Tape Casting", *Journal of Materials Science & Technology* 29 (2013) 1080-1087.

In the present work, the flow in the doctor blade region of a slurry containing $(La_{0.85}Sr_{0.15})_{0.9}MnO_3$ (LSM) material is described with a simple quasi-steady momentum equation in combination with an Ostwald-de Waele power law constitutive equation. Based on rheometer experiments, the constants in the Ostwald-de Waele power law are identified for the considered LSM material and applied in the analytical solution for the tape thickness. This solution is then used for different values of substrate velocity and doctor blade height and compared with experimental findings of the wet tape thickness, and good agreement is found.

## 5.2 PAPER II

M. Jabbari and J. Hattel, "Numerical Modelling of the Side Flow in Tape Casting of a Non-Newtonian Fluid", *Journal of the American Ceramic Society* 96 (2013) 1414-1420.

In this study, the flow of $(La_{0.85}Sr_{0.15})_{0.9}MnO_3$ (LSM) slurry in the tape casting process is modeled numerically with ANSYS Fluent in combination with an Ostwald-de Waele power law constitutive equation. Based on rheometer experiments, the constants in the Ostwald-de Waele power law are identified for the considered LSM material and applied in the numerical modeling. This model is then used for different values of substrate velocity, initial doctor blade height and material load in the reservoir, to investigate their effect on the side flow factor, $\alpha$. It is found that this factor mostly ranges between 0.8 and 0.9. Results of the modeling are compared with experimental findings and good agreement is found.

## 5.3 PAPER III

M. Jabbari and J. Hattel, "Numerical Modelling of the Side Flow in Tape Casting of a Non-Newtonian Fluid", *Journal of the American Ceramic Society* 96 (2013) 1414-1420.

One of the most common processes used in manufacturing of multilayer ceramic packages, multilayer capacitors and large scale integration circuits is tape casting. In this process, the wet tape thickness is one of the single most determining parameters affecting the final properties of the product, and it is therefore of great interest to be able to control it. One way to control the tape thickness is to use a two doctor blade configuration in the tape casting machine. In this case, it becomes important to fix the height of the slurry in front of both doctor blades according to the desired tape thickness and casting speed (belt velocity). In the present work, the flow in both doctor blade regions of a slurry is described with a steady state momentum equation in combination with a Bingham plastic constitutive equation, and this is integrated to a closed form analytical solution for both reservoirs based on the desired wet tape thickness and casting speed. The developed model is used to investigate the impact of different material parameters and machine designs on the required slurry height. The solution is compared with experimental findings from the literature, and good agreement is found.

## 5.4 PAPER IV

M. Jabbari, J. Spangenberg, J. Hattel, "Modeling of the Interface Behavior in Tape Casting of Functionally Graded Ceramics for Magnetic Refrigeration Parts", *International Journal of Refrigeration* 36 (2013) 2403-2409.

The main goal of this work is to study the multiple material flows in side-by-side

(SBS) tape casting and analyze the influence of the different material properties, i.e. the density and the viscosity, on the interface between the fluids, since this is highly important for the efficiency of a graded configuration of the magnetocaloric materials. The Newtonian flow behavior with relatively high viscosity is assumed for each fluid and used in the simulation with a commercial CFD code (ANSYS Fluent). The results show that the density difference does not affect the interface between the adjacent fluids, whereas the viscosity of the fluids plays the most important role in the behavior of the interface. Moreover, increasing the viscosity difference of the adjacent fluids, $\triangle\mu$, leads to increasing the diffusive region between them. However, this can be counteracted by decreasing the velocity of the substrate.

## 5.5 PAPER V

M. Jabbari, R. Bulatova, J. Hattel, C. R. H. Bahl, "An Evaluation of Interface Capturing Methods in a VOF Based Model for Multiphase Flow of a Non-Newtonian Ceramic in Tape Casting", *Applied Mathematical Modelling* 38 (2014) 3222-3232.

The aim of the present study is to evaluate the different interface capturing methods as well as to find the best approach for flow modelling of the ceramic slurry in the tape casting process. The conventional Volume Of Fluid (VOF) method with three different interpolation methods for interface capturing, i.e. the Geometric Reconstruction Scheme (GRS), High Resolution Interface Capturing (HRIC) and Compressive Interface Capturing Scheme for Arbitrary Meshes (CICSAM), are investigated for the advection of the VOF, both for Newtonian and non-Newtonian cases. The main purpose is to find the best method for the free surface capturing during the flow of a ceramic slurry described by a constitutive power law equation in the tape casting process. First the developed model is tested against well-documented and relevant solutions from literature involving free surface tracking and subsequently it is used to investigate the flow of a $La_{0.85}Sr_{0.15}MnO_3$ (LSM) ceramic slurry modeled with the Ostwald-de Waele power law. Results of the modeling are compared with corresponding experimental data and good agreement is found.

## 5.6 PAPER VI

M. Jabbari, J. Spangenberg, J. Hattel, "Particle Migration Using Local Variation of the Viscosity (LVOV) Model in Tape Casting of Ceramics", *Applied Mathematical Modelling*, 2013 (under review).

In this paper, the migration of secondary particles in a non-Newtonian ceramic slurry in the tape casting process is investigated with the purpose of understanding the particle distribution patterns along the casting direction. The Ostwald-de Waele power law model for the non-Newtonian flow behavior is assumed in the simulation of the ceramic slurry flow. A local variation of the viscosity (LVOV) model as a function of the particle volume fraction is introduced and taken into account in the advection and the settling of the particles in the flow field. The results show that using the LVOV model changes the particle distribution pattern from being a constant distribution to a semi-layered one. The presence of such layered structure is highly affecting the subsequent sintering process, which in turn causes an anisotropic shrinkage behavior of the dried tapes. It is also found that increasing the substrate velocity (casting speed) leads to a more uniform distribution of the particles inside the ceramic slurry, in which case the shear induced particle migration is dominating over the gravity induced one.

## 5.7 PAPER VII

M. Jabbari, J. Hattel, "Modelling the drying process in tape casting with a simple ceramics-water system", *Continuum Mechanics and Thermodynamics*, 2014 (under review).

In this study, the evaporation of water from a ceramic-water mixture is investigated with the purpose of understanding the drying rate in the drying process of thin sheets produced by the tape casting process. The rate of mass loss in the drying process is a key factor which often is of interest, as it affects the final properties of the tapes. The 1D heat conduction equation is solved numerically to obtain the temperature field in a ceramic sheet. The change in the concentration of the water content is then used as the driving force for diffusive mass transport of the water. Mass-averaged thermal properties are assumed for the ceramic-water mixture in the initial stage, and as the water evaporates, the thermal properties of the solid ceramic become more dominant since the fraction of water approaches zero. The developed model is used to simulate a simple test for the drying process. The drying rate is simply calculated by examining the water content in each time step. It is found that the mass loss due to the evaporation is increasing close to linearly with the drying time corresponding to an almost constant drying rate. However, the rate starts to decrease after some time in the simulation.

# Chapter 6

# Conclusions and Future Work

In the present chapter the conclusions of the analytical/numerical investigations are summarized and a description of the future perspectives within the field of modelling of the tape casting process are given.

## 6.1 Summary of Results

### 6.1.1 Analytical Models

Analytical approaches for fluid flow analysis in the tape casting process showed that a relative good agreement could be achieved between the results of the modelling and the experimental data. The study, furthermore, demonstrated that the aforementioned agreement was increased by improving the steady state model with a quasi-steady state analytical model. In order to control the most important process parameter, tape thickness, the two-doctor blade configuration was also modeled analytically. The model was developed to control the tape thickness based on the machine configuration and the material constants. Many of the affecting parameters in the process were embedded and they can easily be varied to evaluate their influence. Overall, the proposed analytical models describe the general flow characteristics of tape casting well. Based on the findings of this thesis, Table 1.1 can be updated as follows

### 6.1.2 Numerical Models

This study showed that using computational fluid dynamics (CFD) the process can be modeled with more details in order to better control the produced tapes. Very importantly, the free surface of the ceramic as leaving the doctor blade region was

Table 6.1: Updated version of Table 1.1 based on the findings of this thesis.

| Newtonian behavior | Non-Newtonian behavior |
|---|---|
| [Chou et al., 1987] | [Ring, 1989] |
| [Gaskell et al., 1997] | [Loest et al., 1994] |
| [Kim et al., 2006] | [Pitchumani and Karbhari, 1995] |
| ©[Jabbari and Hattel, 2011] | [Huang et al., 1997] |
| ©[Jabbari et al., 2013c,d] | [Terrones et al., 1997] |
| | [Tok et al., 2000] |
| | [Joshi et al., 2002] |
| | [Joshi et al., 2002] |
| | [Zhang et al., 2002] |
| | ©[Jabbari and Hattel, 2012, 2013, 2014] |
| | ©[Jabbari et al., 2012, 2013a,b] |

modeled. The rheological behavior of the ceramic slurry was also taken into account. The influence of the main process parameters, i.e. the substrate velocity, the initial slurry load, and the doctor blade height, were investigated.

Based on the developed model, one phenomenon inherit to the process called side flow was also modeled. The results showed that to reach a desired uniform tape the side flow factor should be kept as close as to the value of one. The impact of the process parameters were also discussed in details in order to control the side flow, and consequently the tape thickness.

Moreover, a CFD model was developed to simulate multiple flow of the ceramic slurry in tape casting. The simulation was aimed to analyze the production of functionally graded ceramics (FGCs) which are used for magnetic refrigeration applications. The results identified that the densities of the fluids do not influence the interface between the adjacent fluids, whereas the viscosities of the fluids play a key role in the interface behavior. Specifically, it is seen that the viscosity difference ($\triangle\mu$) causes the fluid with lower viscosity to move toward the one with higher viscosity. Moreover, increasing the aforementioned difference leads to further movement of the interface toward the fluid with the higher viscosity. The impact of the substrate velocity was also investigated. As expected, it was found that by increasing the substrate velocity the height of both fluids decreased. Moreover, in the presence of a viscosity difference for the adjacent fluids, by increasing the substrate velocity the interface moved more toward the fluid with the higher viscosity.

Numerical models were developed to track the migration of the particles inside the ceramic slurry. The results showed the presence of some areas inside the ceramic in which the concentration of the particles is higher compared to other parts, creating the resulting packing structure. It was shown that the movement of the particles is influenced by two forces, shear rates and gravity. As expected, the numerical simulation demonstrated that particles with higher values of the relative density tend to settle

in the lower parts of the tape. Moreover, numerical simulation suggested that by increasing the substrate velocity the settlement of the particles can be avoided due to increase of shear force inside the flow.

And finally a numerical code was developed to simulate the drying process. The results showed that the mass loss due to the evaporation is increasing close to linearly with the drying time corresponding to an almost constant drying rate. However, the rate starts to decrease after some time in the simulation. This is in good agreement with the real life process where the drying categorized into two stages: (1) constant rate period (CRP), in which the rate of evaporation per unit area of the drying surface is independent of time, (2) falling rate period (FRP), in which the evaporation rate is reduced, as a consequence of low migration of the water from the bottom layers to the top ones due to diffusion (which is highly dependent to the temperature).

Based on the findings of this thesis, Table 1.2 can be updated as follows

Table 6.2: Updated version of Table 1.2 based on the findings of this thesis.

| Analytical modelling | Numerical modelling |
|---|---|
| [Chou et al., 1987] | [Loest et al., 1994] |
| [Ring, 1989] | [Gaskell et al., 1997] |
| [Pitchumani and Karbhari, 1995] | [Joshi et al., 2002] |
| [Pitchumani and Karbhari, 1995] | ©[Jabbari and Hattel, 2011, 2012, 2013] |
| [Huang et al., 1997] | ©[Jabbari et al., 2012, 2013a,c,d] |
| [Tok et al., 2000] | |
| [Joshi et al., 2002] | |
| [Tok et al., 2000] | |
| [Kim et al., 2006] | |
| ©[Jabbari et al., 2013b] | |
| ©[Jabbari and Hattel, 2014] | |

## 6.2 Future Work

The developed models in this thesis have the flexibility of adding additional physics. Most of the models used in this study were based on fluid flow analysis, which possibly can be coupled with energy equations.

One of the interesting phenomena that was investigated in this thesis was simulating the side flow. However, the rheological behavior of the flow was assumed to be constant during the process. It could be interesting to investigate the side flow factor for some fluids with different rheological behavior. The correlation between the rheological parameters and the side flow factor would create a valuable bench mark.

The flow of two adjacent ceramic slurries in the side-by-side tape casting produced valuable information from a practical view point. One of the potential investigations in this respect could be aimed to evaluate the behavior of the interface between the

adjacent fluids by changing the shape of the notch between the two fluids in the doctor blade region. This will need to extend the present model to evaluate the shape effect of the notch, and of course comparing with corresponding experiments.

Another beneficial investigation in this study was to model the migration of the particles inside the ceramic slurry. The particles in this study were assumed to have a spherical shape. The extension of the present model to track particles of more general shape, such as elliptical would be of great interest. By modelling the migration of elliptical particles, the anisotropic behavior of the particles and their impact on the subsequent processes (i.e. drying and sintering) can be argued.

And finally, as described in the last part of the numerical investigations, the drying process needs further improvement. In order to simulate the real life drying process, the current model needs to be extended by adding more physics to the equations of the state. This is the core potential to continue the current project for the next couple of years.

# References

*http://www.britannica.com/EBchecked/media/262/Steps-in-doctor-blading-a-tape-casting-process-employed-in.* xvii, 2

(2009). *ANSYS Inc., FLUENT 12.0 Theory Guide.* 16

Abbott, J. R., Tetlow, N., Graham, A. L., Altobelli, S. A., Fukushima, E., Mondy, L. A., and Stephens, T. S. (1991). Experimental observations of particle migration in concentrated suspensions: Couette flow. *Journal of Rheology*, 35:773–795. 17

Acikbas, N. C., Suvaci, E., and Mandal, H. (2006). Fabrication of Functionally Graded SiAlON Ceramics by Tape Casting. *Journal of American Ceramic Society*, 89:3255–3257. 4, 34

Appleby, A. J. (1996). Fuel cell technology: Status and future prospects. *Energy*, 21:521–653. 2

Aulisa, E., Manservisi, S., and Scardovelli, R. (2004). A surface marker alghorithm coupled to an area-preserving marker redistribution method for three-dimentional interface tracking. *Journal of Computational Physics*, 197:555–584. 14

Bahl, C. R. H., Velzquez, D., Nielsen, K. K., Engelbrecht, K., Andersen, K. B., Bulatova, R., , and Pryds, N. (2012). High performance magnetocaloric perovskites for magnetic refrigeration. *Applied Physics Letters*, 100:121905. 34

Barnes, H., Hutton, J., and Walters, K. (1989). *An introduction to rheology.* Elsevier. 12

Bellosi, A. and Vincenzini, P. (1979). Microstructural observations on sintered alpha alumina. *Materials Chemistry*, 4:721–729. 2

Bever, M. B. and Duwez, P. E. (1972). Gradients in Composite Materials. *Materials Science and Engineering*, 10:1–8. 3, 33

Bird, R. B. (1976). Useful Non-Newtonian Models. *Annual Reviews of Fluid Mechanic*, 8:13–34. 13

Bowen, H. (1980). Basic research needs on high temperature ceramics for energy applications. *Materials Science and Engineering*, 44:1–56. 2

Buscall, R., Goodwin, J. W., and Ottewill, R. H. (1982). The Settling of Particles through Newtonian and Non-Newtonian Media. *Journal of Colloid and Interface Science*, 85:78–86. 18, 19

Callister, W. D. (2000). *Fundamentals of Materials Science and Engineering*. John Wiley & Sons, Inc. 44, 50

Chantaramee, N., Tanaka, S., Takahashi, T., and Uematsu, K. (2008). Evolution of Discontinuity in Particle Orientation in Ceramic Tape Casting. *Journal of American Ceramic Society*, 91:3181–3184. 17, 36, 37

Chantaramee, N., Tanaka, S., and Uematsu, K. (2007). Development of Packing Structure of Powder Particles in Tape Casting. *Journal of the Ceramic Society of Japan*, 15:136–140. 17, 36, 37

Chartier, T. and Bruneau, A. (1993). Aqueous tape casting of alumina substrates. *Journal of the European Ceramic Society*, 12:243–247. 2, 17

Cheneviere, P., Sardin, M., Farcy, P. D., and Putz, A. (1991). Ch. R-20 Transient Transport of Bacterial Suspensions in Natural Porous Media: Modeling of the Adsorption Phenomenon. *Developments in Petroleum Science*, 31:311–329. 4

Chou, Y. T., Ko, Y. T., and Yan, M. F. (1987). Fluid Flow Model for Ceramic Tape Casting. *Journal of American Ceramic Society*, 70:280–282. 5, 10, 23, 24, 25, 27, 32, 62, 63

Claaen, T. and Claussen, N. (1992). Processing of ceramic-matrix/platelet composites by tape casting and lamination. *Journal of the European Ceramic Society*, 10:263–271. 2

Cross, M. M. (1965). Rheology of non-Newtonian fluids: A new flow equation for pseudoplastic systems. *Journal of Colloid Science*, 20:417–437. 12

Dendy, E. D., Padial-Collins, N. T., and VanderHeyden, W. B. (2002). A General-Purpose Finite-Volume Advection Scheme for Continuous and Discontinuous Fields on Unstructured Grids. *Journal of Computational Physics*, 180:559–583. 15

Dinesen, A. R., Linderoth, S., Pryds, N., and Smith, A. (2012). Magnetic regenerator, a method of making a magnetic regenerator, a method of making an active magnetic refrigerator and an active magnetic refrigerator. xvii, 4, 34

Fiori, C., Fusaroli, G., Krajewski, A., and Vincenzini, P. (1979). On the fracture strength of tape-casted alumina substrates. *Ceramurgia International*, 5:124–126. 2

Frank, M., Anderson, D., Weeks, E. R., and Morris, J. F. (2003). Particle migration in pressure-driven flow of a Brownian suspension. *Journal of Fluid Mechanics*, 493:363–378. 17

Galassi, C. (2006). Processing of porous ceramics: Piezoelectric materials. *Journal of European Ceramic Society*, 26:2951–2958. 17

Gaskell, P. H., Rand, B., Summers, J. L., and Thompson, H. M. (1997). The Effect of Reservoir Geometry on the Flow Within Ceramic Tape Casters. *Journal of European Ceramic Society*, 17:1185–1192. xviii, 5, 10, 31, 62, 63

Gauthier, F., Goldsmith, H. L., and Mason, S. G. (1971a). Particle motions in non-Newtonian media I: Couette flow. *Rheologica Acta*, 10:344–364. 17

Gauthier, F., Goldsmith, H. L., and Mason, S. G. (1971b). Particle Motions in Non-Newtonian Media. II. Poiseuille Flow. *Journal of Rheology*, 15:297–330. 17

Grader, G. S. and Zuri, L. (1993). Tape Casting Slip Preparation by in Situ Polymerization. *Journal of American Ceramic Society*, 76:1809–14. 34

Gueyffier, D., Li, J., Nadim, A., Scardovelli, R., and Zaleski, S. (1999). Volume-of-Fluid Interface Tracking with Smoothed Surface Stress Methods for Three-Dimensional Flows. *Journal of Computational Physics*, 152:423–456. 14

Hattel, J., editor (2005). *Fundamentals of Numerical Modelling of Casting Processes*. Polyteknisk Forlag. 47, 51

He, Z., Andersen, K. B., Keel, L., Nygaard, F. B., Menon, M., and Hansen, K. K. (2009). Processing and characterization of porous electrochemical cells for flue gas purification. *Ionics*, 15:427–431. 17

He, Z., Andersen, K. B., Nygaard, F. B., and Hansen, K. K. (2013). A combined SEM, CV and EIS study of multi-layered porous ceramic reactors for flue gas purification. *Ceramics International*, 39:847–851. 3

Hirt, C. W. and Nichols, B. D. (1981). Volume of Fluid (VOF) Method for the Dynamics of Free Boundaries. *Journal of Computational Physics*, 39:201–225. 15

Ho, B. P. and Leal, L. G. (1976). Migration of rigid spheres in a two-dimensional unidirectional shear flow of a second-order fluid. *Journal of Fluid Mechanics*, 76:783–799. 17

Holz, M., Heil, S. R., and Sacco, A. (2000). Temperature-dependent self-diffusion coefficients of water and six selected molecular liquids for calibration in accurate $^1$H NMR PFG measurements Manfred. *Physical Chemistry Chemical Physics*, 2:4740–4742. xix, 51, 52

Hotza, D. and Greil, P. (1995). Review: aqueous tape casting of ceramic powders. *Materials Science and Engineering A*, 202:206–217. 2

Howatt, G. N. (1952). Method of Producing High Dielectric High Insulation Ceramic Plates. US Patents No. 2582993. 1

Howatt, G. N., Breckenridge, R. G., and Brownlow, J. M. (1947). Fabrication of Thin Ceramic Sheets for Capacitors. *Journal of American Ceramic Society*, 30:237–242. 1

Huang, X. Y., Liu, C. Y., and Gong, H. Q. (1997). A Viscoplastic Flow Modeling of Ceramic Tape Casting. *Materials and Manufacturing Processes*, 12:935–943. xvii, 5, 14, 23, 62, 63

Huerta, A. and Liu, W. K. (1988). Viscous Flow With Large Free Surface Motion. *Computer Methods in Applied Mechanics and Engineering*, 69:277–324. 14

Hyman, J. M. (1984). Numerical Methods for Tracking Interfaces. *Physica D: Nonlinear Phenomena*, 12D:396–407. 14

Jabbari, M., Bulatova, R., Hattel, J., and Bahl, C. (2012). Interface Oscillation in the Side-by-Side (SBS) Tape Casting of Functionally Graded Ceramics (FGCs). *American Physical Society Bulletin*, 57:H7.00002. xviii, 34, 35, 62, 63

Jabbari, M., Bulatova, R., Hattel, J. H., and Bahl, C. R. H. (2013a). An Evaluation of Interface Capturing Methods in a VOF Based Model for Multiphase Flow of a Non-Newtonian Ceramic in Tape Casting. *Applied Mathematical Modelling*. In Press. 16, 31, 62, 63

Jabbari, M., Bulatova, R., Hattel, J. H., and Bahl, C. R. H. (2013b). Quasi-Steady State Power Law Model for the Flow of $(La_{0.85}Sr_{0.15})_{0.9}MnO_3$ Ceramic Slurry in Tape Casting. *Materials Science and Technology*, 29:1080–1087. xvii, xviii, 12, 13, 23, 24, 25, 26, 27, 28, 32, 35, 36, 39, 41, 62, 63

Jabbari, M. and Hattel, J. (2011). Numerical Modeling of Fluid Flow in the Tape Casting Process. volume 1389 of *AIP Conference Proceedings Series*, pages 143–146. Numerical Analysis and Applied Mathematics : ICNAAM. xvii, 10, 11, 25, 26, 27, 31, 32, 41, 62, 63

Jabbari, M. and Hattel, J. (2012). Numerical Modeling of the Flow of a Power Law Ceramic Slurry in the Tape Casting Process. Tenth International Conference on

Advances and Trends in Engineering Materials and their Applications, pages 151–157. AES-ATEMA INTERNATIONAL CONFERENCE. 12, 31, 36, 39, 41, 62, 63

Jabbari, M. and Hattel, J. (2013). Numerical Modeling of the Side Flow in Tape Casting of a Non-Newtonian Fluid. *Journal of American Ceramic Society*, 96:1414–1420. xviii, 32, 33, 36, 39, 41, 62, 63

Jabbari, M. and Hattel, J. (2014). Bingham-Plastic Fluid Flow Model in Tape Casting of Ceramics Using Two Doctor Blades - An Analytical Approach. *Materials Science and Technology*, 30:283–288. xviii, 14, 27, 28, 29, 30, 41, 62, 63

Jabbari, M., Spangenberg, J., and Hattel, J. (2013c). Interface Behavior in Functionally Graded Ceramics for the Magnetic Refrigeration: Numerical Modeling. *Applied Mechanics and Materials*, 325-326:1362–1367. 35, 62, 63

Jabbari, M., Spangenberg, J., and Hattel, J. (2013d). Modeling of the Interface Behavior in Functionally Graded Ceramics for Magnetic Refrigeration Parts. *International Journal of Refrigeration*, 36:2403–2409. 35, 62, 63

Joshi, S. C., Lam, Y. C., Boey, F. Y. C., and Tok, A. I. Y. (2002). Power law fluids and Bingham plastics flow models for ceramic tape casting. *Journal of Materials Processing Technology*, 120:215–225. xvii, 5, 14, 23, 24, 27, 32, 35, 62, 63

Jr, J. E. P. and Puckett, E. G. (2004). Second-order accurate volume-of-fluid algorithms for tracking materials interfaces. *Journal of Computational Physics*, 199:465–502. 14, 15

Jr., K. A. G. and Pecharsky, V. K. (2008). Thirty years of near room temperature magnetic cooling: Where we are today and future prospects. *International Journal of Refrigeration*, 31:945–961. 34

Kieback, B., Neubrand, A., and Riedel, H. (2003). Processing techniques for functionally graded materials. *Materials Science and Engineering A*, 362:81–105. 34

Kiennemann, J., Chartier, T., Pagnoux, C., Baumard, J. F., Huger, M., and Lamérant, J. M. (2005). Drying mechanisms and stress development in aqueous alumina tape casting. *J. Eur. Ceram. Soc.*, 25:1551–1564. 45, 52

Kim, H. J., Krane, M. J. M., Trumble, K. P., and Bowman, K. J. (2006). Analytical Fluid Flow Models for Tape Casting. *Journal of American Ceramic Society*, 89:2769–2775. xvii, 5, 10, 23, 24, 25, 26, 27, 32, 35, 62, 63

Krasnyi, B. L., Tarasovskii, V. P., Valdberg, A. Y., and Kaznacheeva, T. O. (2005). Porous Permeable Ceramics for Filter Elements Cleaning Hot Gases from Dust. *Glass & Ceramics*, 62:134–138. 17

Leal, L. G. (1980). Particle Motions in A Viscous Fluid. *Annual Review of Fluid Mechanics*, 12:435–476. 17

Leighton, D. and Acrivos, A. (1987). The shear-induced migration of particles in concentrated suspensions. *Journal of Fluid Mechanics*, 181:415–439. 18

Lindqvist, K. and Lidn, E. (1997). Preparation of alumina membranes by tape casting and dip coating. *Journal of the European Ceramic Society*, 17:359–366. 2

Loest, H., Lipp, R., and Mitsoulis, E. (1994). Numerical Flow Simulation of Viscoplastic Slurries and Design Criteria for a Tape Casting Unit. *Journal of American Ceramic Society*, 77:254–262. 5, 30, 31, 62, 63

Lopez, R. J. G. and Quinta-Ferreira, R. M. (2009). Voulme-of-Fluid-Based Model for Multiphase Flow in High-Pressure Trickle-Bed Reactor: Optimization of Numerical Parameters. *AIChE Journal*, 55:2920–2933. 16

Martinez, C. J. and Lewis, J. A. (2002). Rheological, Structural, and Stress Evolution of Aqueous $Al_2O_3$: Latex Tape-Cast Layers. *Journal of American Ceramic Society*, 85:2409–2416. 42, 45

Mikeska, K. and Cannon, W. (1988). Non-aqueous dispersion properties of pure barium titanate for tape casting. *Colloids and Surfaces*, 29:305–321. 2

Mistler, R. E. and Twiname, E. R. (2000). *Tape Casting, Theory and Practice*. The American Ceramic Society. xix, 44

Molaei, E. A., Amrei, S. H., Dehkordi, A. M., and Haghi, M. (2013). Transient and steady-state analysis of heat, mass, and momentum transfer in developing and fully-developed regions of homogeneous tubular reactors with non-Newtonian fluid flow. *Energy Conversion and Management*, 65:308–321. 4

Muzaferija, S. and Peric, M. (1997). Computation of Free-Surface Flows Using the Finite-Volume Method and Moving Grids. *Numerical Heat Transfer B*, 32:369–384. 15, 16

Newnham, R., Skinner, D., and Cross, L. (1978). Connectivity and piezoelectric-pyroelectric composites. *Materials Research Bulletin*, 13:525–536. 2

Nghiem, L. D., Mornane, P., Potter, I. D., Perera, J. M., Cattrall, R. W., and Kolev, S. D. (2006). Extraction and transport of metal ions and small organic compounds using polymer inclusion membranes (PIMs). *Journal of Membrane Science*, 281:7–41. 4

Olevsky, E. A. (1998). Theory of sintering: from discrete to continuum. *Materials Science and Engineering R*, 23:41–100. 41

Pagnoux, C., Chartier, T., de F. Granja, M., Doreau, F., Ferreira, J. M., and Baumard, J. F. (1998). Aqueous suspensions for tape-casting based on acrylic binders. *Journal of the European Ceramic Society*, 18:241–247. 17

Panahi, R., Jahanbakhsh, E., and Seif, M. S. (2006). Development of a VoF-fractional step solver for floating body motion simulation. *Applied Ocean Research*, 28:171–181. 15

Phillips, R. J., Armstrong, R. C., Brown, R. A., Graham, A. L., and Abbott, J. R. (1992). A constitutive equation for concentrated suspensions that accounts for shearinduced particle migration. *Physics of Fluids A*, 4:30–40. 18

Pitchumani, R. and Karbhari, V. M. (1995). Generalized Fluid Flow Model for Ceramic Tape Casting. *Journal of American Ceramic Society*, 78:2497–2503. xvii, 5, 12, 23, 24, 25, 27, 32, 35, 62, 63

Queutey, P. and Visonneau, M. (2007). An interface capturing method for free-surface hydrodynamic flows. *Computers & Fluids*, 36:1481–1510. 15

Riley, B. (1990). Solid oxide fuel cells - the next stage. *Journal of Power Sources*, 29:223–237. 2

Ring, T. A. (1989). A Model of Tape Casting Bingham Plastic and Newtonian Fluids. *Advanced Ceramics*, 26:569–576. 5, 14, 62, 63

Scherer, G. W. (1990). Theory of Drying. *Journal of American Ceramic Society*, 73:3–14. 42, 45, 53

Schwartz, B. (1984). Review of multilayer ceramics for microelectronic packaging. *Journal of Physics and Chemistry of Solids*, 45:1051–1068. 2

Schwartz, B. N. and Kirkpatrick, W. R. (1967). Switch for Selective Coupling a Sensor or Calibration Elemnt to aTerminal Block. US Patents No. 6045260. 1

Shanti, N. O., Bierschenk, D. M., Barnett, S. A., and Faber, K. T. (2012). Direct lamination of solid oxide fuel cell anode support, anode, and electrolyte by sequential tape casting of thermoreversible gel slips. *Journal of Power Source*, 212:43–46. xvii, 3

Shen, M. and Bever, M. B. (1972). Gradients in polymeric materials. *Journal of Materials Science*, 7:741–746. 3, 33

Shin, S., Yoon, I., and Juric, D. (2011). The Local Front Reconstruction Method for direct simulation of two- and three-dimensional multiphase flows. *Journal of Computational Physics*, 230:6605–6646. 14

Simwonis, D., Thulen, H., Dias, F. J., Naoumidis, A., and Stover, D. (1999). Properties of Ni/YSZ porous cermets for SOFC anode substrates prepared by tape casting and coat-mix process. *Journal of Materials Processing Technology*, 92-93:107–111. 17

Sjoblom, J., Skodvin, T., ystein Holt, and Nilsen, F. P. (1997). Colloid chemistry and modern instrumentation in offshore petroleum production and transport. *Colloids and Surfaces A: Physicochemical and Engineering Aspects*, 124:593–607. 4

Smith, A., Bahl, C. R. H., Bjrk, R., Engelbrecht, K., Nielsen, K. K., and Pryds, N. (2012). Materials Challenges for High Performance Magnetocaloric Refrigeration Devices. *Advanced Energy Materials*, 2:1288–1318. 34

Spangenberg, J., Roussel, N., Hattel, J. H., Sarmiento, E. V., and Geiker, G. Z. M. R. (2012a). Patterns of gravity induced aggregate migration during casting of fluid concretes. *Cement and Concrete Research*, 42:1571–1578. 18

Spangenberg, J., Roussel, N., Hattel, J. H., Stang, H., Skocek, J., and Geiker, M. R. (2012b). Flow induced particle migration in fresh concrete: Theoretical frame, numerical simulations and experimental results on model fluids. *Cement and Concrete Research*, 42:633–641. 18

Stetson, H. W. and Gyurk, W. J. (1967). Alumina Substrates. US Patents No. 3698923. 1

Stver, D., Buchkremer, H. P., and Uhlenbruck, S. (2004). Processing and properties of the ceramic conductive multilayer device solid oxide fuel cell (SOFC). *Ceramics International*, 30:1107–1113. 3

Tang, H., Wrobel, L. C., and Fan, Z. (2004). Tracking of immiscible interfaces in multiple-material mixing processes. *Computational Materials Science*, 29:103–118. 14

Tavakoli, R., Babaei, R., Varahram, N., and Davami, P. (2006). Numerical simulation of liquid/gas phase flow during mold filling. *Computer Methods in Applied Mechanics and Engineering*, 196:697–713. 14

Terrones, G., Smith, P. A., Armstrong, T. R., and Soltesz, T. J. (1997). Application of the Carreau Model to Tape-Casting Fluid Mechanics. *Journal of American Ceramic Society*, 80:3151–3156. 5, 13, 62

Tok, A. I. Y., Boey, F. Y. C., and Lam, Y. C. (2000). Non-Newtonian fluid flow model for ceramic tape casting. *Materials Science and Engineering A*, 280:282–288. 5, 12, 22, 23, 24, 27, 32, 62, 63

Ubbink, O. and Issa, R. I. (1999). A Method for Capturing Sharp Fluid Interfaces on Arbitrary Meshes. *Journal of Computational Physics*, 153:26–50. 15, 16

Vasconcelos, P. V., Labrincha, J. A., and Ferreira, J. M. F. (1998). Porosity development of diatomite layers processed by tape casting. *Ceramics International*, 24:447–454. 2, 17

Waclawczyk, T. and Koronowicz, T. (2008). Comparison of CICSAM and HRIC High-Resolution Schemes for Interface Capturing. *Journal of Theoretical And Applied Mechanics*, 46:325–345. 16

Wang, J. P., Bortwick, A. G. L., and Taylor, R. E. (2004). Finite-volume type VOF method on dynamically adaptive quadtree grids. *International Journal for Numerical Methods in Fluids*, 45:485–508. 14

Wonisch, A., Polfer, P., Kraft, T., Dellert, A., Heunisch, A., and Roosen, A. (2011). A Comprehensive Simulation Scheme for Tape Casting: From Flow Behavior to Anisotropy Development. *Journal of American Ceramic Society*, 94:2053–2060. 9, 13, 31

Yamamoto, J. K. (1989). Fabrication of controlled porosity in a tape cast glass ceramic substrate material. *Materials Letters*, 8:278–282. 2

Yeo, J.-G., Jung, Y.-G., and Choi, S.-C. (1998). Design and microstructure of ZrO2/SUS316 functionally graded materials by tape casting. *Materials Letters*, 37:304–311. 4, 34

Yuping, Z., Dongliang, J., and Greil, P. (2000). Tape casting of aqueous $Al_2O_3$ slurries. *Journal of the European Ceramic Society*, 20:1691–1697. 3

Zhang, G., Wang, Y., and Ma, J. (2002). Bingham Plastic Fluid Flow Model for Ceramic Tape Casting. *Materials Science and Engineering A*, 337:274–280. 5, 14, 22, 23, 24, 27, 32, 62

Zhao, C., Xue, J., Ran, F., and Sun, S. (2013). Modification of polyethersulfone membranes - A review of methods. *Progress in Materials Science*, 58:76–150. 4

# Appdx A

M. Jabbari, R. Bulatova, J. Hattel, C. R. H. Bahl, "Quasi-steady State Power Law Model for the Flow of $(La_{0.85}Sr_{0.15})_{0.9}MnO_3$ Ceramic Slurry in Tape Casting", *Materials Science & Technology* 29 (2013) 1080-1087.

# Quasi-steady state power law model for flow of $(La_{0\cdot85}Sr_{0\cdot15})_{0\cdot9}MnO_3$ ceramic slurry in tape casting

**M. Jabbari*[1], R. Bulatova[2], J. H. Hattel[1] and C. R. H. Bahl[2]**

One of the most common ways used to produce multilayer ceramics is tape casting. In this process, the wet tape thickness is one of the single most determining parameters affecting the final properties of the product, and it is therefore of great interest to be able to control it. In the present work, the flow in the doctor blade region of a slurry containing $(La_{0\cdot85}Sr_{0\cdot15})_{0\cdot9}MnO_3$ (LSM) material is described with a simple quasi-steady momentum equation in combination with an Ostwald–de Waele power law constitutive equation. Based on rheometer experiments, the constants in the Ostwald–de Waele power law are identified for the considered LSM material and applied in the analytical solution for the tape thickness. This solution is then used for different values of substrate velocity and doctor blade height and compared with experimental findings of the wet tape thickness, and good agreement is found.

**Keywords:** Tape casting, Doctor blade, Fluid flow, Non-Newtonian, Power law

## Introduction

Tape casting is an important process for producing large area, thin, flat ceramics, which can be patterned, stacked and laminated to form three-dimensional structures.[1] The method was originally developed for producing electronic ceramics (insulating substrates and packages and multilayer capacitors) and is still mainly used for this. Structural laminates, knives, membranes and solid oxide fuel cells are examples of other applications for thin ceramics formed by tape casting. The tape thickness that can be achieved is generally in the range of 25 up to 1 mm, but it is possible to produce tapes with thicknesses of $<5$ μm.

The parallel (doctor) blade process was first used in preparing ceramic tapes in the 1940s, and it has a key role in producing thin and flat ceramic tapes.[2,3] Thickness control is of critical importance in tape casting, since it affects the final properties of the tape. Different parameters such as powder distribution, slurry composition, flow field and sintering affect the thickness of the final tape.[4–6] In addition to this, the geometry of the process set-up itself has different effects on the related final properties of the manufactured product.[7]

In the tape casting process, a slurry is pumped into a reservoir and this slurry is then moved by the peeling belt. Since this technique is used to produce tapes with relatively small thicknesses, accurate control of the tape thickness which exits the doctor blade is a key factor determining the final properties.

One of the most challenging parts of modelling the flow of the ceramic slurry in the tape casting process is to conduct the modelling with the proper constitutive equation which governs the material's rheological behaviour. In general, this rheological behaviour can be classified by five different material types as shown in Fig. 1. For Newtonian fluids, the shear stress $\tau$ has a linear correlation with the shear rate $\dot{\gamma}$ in which the slope of the line is the constant Newtonian viscosity $\mu$. The second type is represented by pseudoplastic fluids that are often represented by the Ostwald–de Waele power law equation. The third one is named dilatant fluids, and they are characterised by an increasing slope of the shear stress–shear rate behaviour. The fourth is the Bingham plastic material which has a yield point $\tau_y$ below which no flow takes place, whereas above it, the behaviour is linear and characterised by the plastic viscosity. Finally, for viscoplastic materials, there is also a yield point like for the Bingham material, but above that, a polynomial behaviour can be seen.

The first model for predicting the tape thickness in tape casting was developed by Chou *et al.*[4] In their work, the Newtonian behaviour was used and they assumed that the flow in the parallel doctor blade region is a linear combination of pressure and drag flow. However, in the tape casting process of ceramics, the slurry seldom behaves like a Newtonian fluid. Pitchumdni and Karbhari[9] evaluated the effects of an imposed pressure gradient due to the height of the slurry in the casting head, as well as those of the drag due to the moving substrate on the slurry flow by modelling the slurry discharge as a generalised power law flow, i.e.

[1]Department of Mechanical Engineering, Technical University of Denmark, Nils Koppels Allé, Kgs. Lyngby 2800, Denmark
[2]Department of Energy Conversion and Storage, Technical University of Denmark, Frederiksborgvej 399, Building 779, Roskilde, Denmark

*Corresponding author, email mjab@mek.dtu.dk


Published by Maney on behalf of the Institute
Received 1 March 2013; accepted 20 March 2013
DOI 10.1179/1743284713Y.0000000255

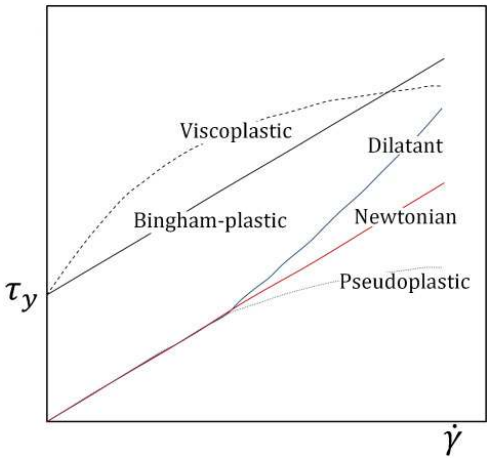


**1 Rheological classification of flow[8]**

$$\tau = k\dot{\gamma}^n \tag{1}$$

where $k$ and $n$ are the consistency of the fluid and deviation from a Newtonian fluid respectively, and both are constants for a specific slurry. However, in their work, the height of the ceramic slurry is assumed to be constant as opposed to the present work where it is allowed to vary.

Ring[10] modelled the tape casting slurry by applying the Bingham plastic constitutive law

$$\tau = \tau_0 + \mu\gamma \tag{2}$$

where $\tau_0$ is the Bingham yield stress, which is the finite stress required for flow initiation, and $\mu$ is the plastic viscosity. In this model, the material acts as a rigid body below the yield point, and above it, the ceramic slurry flows with the constant plastic viscosity. However, the $(La_{0\cdot85}Sr_{0\cdot15})_{0\cdot9}MnO_3$ (LSM) ceramic used in the present work did not show any yield point, which means that the slurry flows all the time. Recently, the Herschel–Bulkley model was used in the tape casting process for modelling the flow field by Huang *et al.*[11] This model is a combination of the Bingham plastic and power law models; however, again, they did not consider the transient behaviour of the ceramic slurry height.

Ceramics might be attractive materials for high temperature applications provided that both their reliability and toughness could be improved. The key factor improving the toughness of these materials is the presence of weak interfaces between fibres and the composite matrix or between the ceramic layers in multilayered structures. These interfaces allow for energy dissipation before fracture through mechanisms of crack deflection, crack bridging, fibre pullout and interface delamination. Multilayered ceramics are generally processed by tape casting and firing or hot pressing.[12] The presence of the different layers in multilayer materials controls the crack path, frequently avoiding completely brittle behaviour. When the layers are strongly bonded together, a crack in one layer can propagate readily into the adjacent layer, and then the material behaves as a conventional ceramic.[13] Most often, the graded structures are produced from laminating two or more single layers. In this respect, controlling the tape thickness and its uniformity along the casting direction becomes more important.

Moreover, the shape changes that happen during the sintering process due to the shrinkages in different directions will result in shape instability.[14] This shape instability is more important in the multilayer materials, since during the sintering process every layer has different thermal behaviour. However, even in the case of monolayer tape casting, it is of great importance to control the aforementioned shape instabilities. Raj and Cannon[14] proposed a formula to measure the percentage of anisotropic shrinkage in the tape casting process. They showed that the tape thickness and its variation have a great impact on the anisotropic shrinkage and the resultant mechanical properties, where an increase in the tape thickness causes a decrease in the anisotropic shrinkage. This emphasises the importance of the thickness control in the tape casting process.

Hence, in the present paper, an analytical model capable of predicting the final tape thickness is presented. It is based on a quasi-steady state description of the velocity and the pressure field in the doctor blade region, allowing the slurry height to drop during casting, and this is combined with a power law model for the fluid flow. Many of the affecting parameters in the process are embedded and they can easily be varied to evaluate their influence. The proposed models describe the flow characteristics of tape casting well. Results of the model are compared with experiments, and good agreement is obtained.

In the present paper, a quasi-steady state description of the velocity and the pressure field in the doctor blade region, allowing the slurry height to drop during casting, is combined with a power law model for the fluid flow. Many of the affecting parameters in the process are embedded, and they can easily be varied to evaluate their influence. The proposed models describe the flow characteristics of tape casting well. Results of the model are compared with experiments, and good agreement is obtained.

## Analysis

In order to express the volume flow and thus the tape thickness, the velocity field equation in the doctor blade region must be developed. Based on the number of doctor blades, there are two kinds of tape casters: a simple tape caster that has only one doctor blade (illustrated schematically in Fig. 2), and a double blade tape caster in which a front doctor blade is used to ensure a hydrostatic pressure in front of the rear one.[15]

As shown in Fig. 2, $\delta$ is the green tape thickness, $h$ is the doctor blade height, $W$ is the width of the doctor blade, $H_0$ is the height of the slurry in front of the doctor blade, $d$ is the depth of the reservoir, $l$ is the inclined length of the reservoir and $\theta$ is the angle of the reservoir.

The pressure gradient inside the channel below the doctor blade is constant, since there is a hydrostatic pressure in front of the doctor blade and it can be determined by the height of the slurry as shown below[15]

$$\frac{dp}{dx} = -A_0 = -\frac{\rho g H_0}{W} \tag{3}$$

where $\rho$ is the density of the slurry, and $g$ is the acceleration due to gravity.

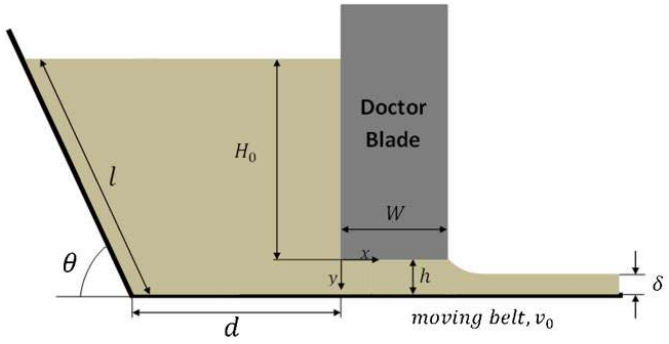


**2 Schematic geometry of tape casting machine**

By assuming an infinitely long and wide plate as compared to the thickness and combining with momentum conservation in the $x$ direction under steady state conditions, we obtain the following[15,16]

$$\frac{d\tau}{dy}=\frac{dp}{dx} \tag{4}$$

where $\tau$ is the shear stress. From equations (3) and (4), $\tau$ is found to be

$$\tau=-A_0y+A_1 \tag{5}$$

where $A_1$ is an integration constant.

For power law fluids, the shear stress $\tau$ is given by the constitutive equation[16]

$$\tau=k\left(\frac{\partial u}{\partial y}\right)^n \tag{6}$$

where it has been assumed that the only velocity component contributing to the shear rate is the velocity in the $x$ direction $u$.

Rewriting equations (5) and (6) and integrating along the channel height $h$

$$\int_0^h(-A_0y+A_1)dy=\int_0^h k\left(\frac{\partial u}{\partial y}\right)^n dy \tag{7}$$

and assuming that $k$ and $n$ are constants, we obtain

$$u=\left(-\frac{1}{A_0k\frac{1}{n}}\right)\left(\frac{1}{\frac{1}{n}+1}\right)(-A_0y+A_1)^{\frac{1}{n}+1}+A_2\ (0<y<h) \tag{8}$$

where $A_2$ is another integration constant.

The boundary conditions for equation (8) in the doctor blade region of tape casting are

$$\begin{cases}u(0)=0\\ u(h)=v_0\end{cases} \tag{9}$$

where $v_0$ is the velocity of the moving belt.

Applying these boundary conditions in equation (8), and introducing the expressions that $(1/n)+1=\chi$ and $-[1/A_0k(1/n)]=\psi$, we get

$$\begin{cases}0=\dfrac{\psi}{\chi}A_1^{\chi}+A_2\\ v_0=\dfrac{\psi}{\chi}(-A_0h+A_1)^{\chi}+A_2\end{cases} \tag{10}$$

which is rewriting into

$$\begin{cases}v_0=\dfrac{\psi}{\chi}\left[(-A_0h+A_1)^{\chi}+A_1^{\chi}\right]\\ A_2=-\dfrac{\psi}{\chi}A_1^{\chi}\end{cases} \tag{11}$$

In order to find the integration constant $A_1$, the Newton–Raphson method is used. To do so, the following equation originating from the upper expression in equation (11) is solved numerically to find the parameter $A_1$

$$F(A_1)=\frac{\psi}{\chi}\left[(-A_0h+A_1)^{\chi}+A_1^{\chi}\right]-v_0=0 \tag{12}$$

and consequently after finding $A_1$, the parameter $A_2$ is calculated from the lower expression in equation (11).

As a consequence of mass conservation, the thickness of the green tape $\delta$, can then be determined by integrating $u$ over the channel height and dividing by the tape velocity, i.e.

$$\delta=\frac{1}{v_0}\int_0^h u\,dy=\frac{-\left[(-A_0h+A_1)^{\chi+1}-A_1^{\chi+1}\right]}{v_0A_0\psi\chi(\chi+1)}+A_2h \tag{13}$$

Reaching to a constant tape thickness is not an impossible goal, since most of the manufacturing processes for tape casting are at the continuous form in which the reservoir at all times is fed by slurry. Moreover, using two doctor blades in the design of the machine will result in having almost constant hydrostatic pressure during the casting process. However, it is of great importance to control the tape thickness in the small tape casters especially in small scale production and laboratories, in which the slurry height is not constant in the reservoir but gradually decreasing with time. This phenomenon leads to the present modification of the standard steady state model,[2,4,9,15,16] making it dependent on the height variation.

Now, the proposed quasi-steady state formulation is developed based on the continuity equation. Assuming that the slurry is incompressible, the volume of the slurry which drops down in the reservoir is equal to the volume of the slurry which is conveyed out of the doctor blade region by the peeling belt. Assuming that during the time period equal to $\Delta t$, the height of the slurry will decrease from the initial value of $H_0$ to $H_1$, the aforementioned volume (equals area in the present

two-dimensional model) in the reservoir which is decreased will be given as

$$\Delta S_1 = \left[d + \frac{1}{2} l \cos\theta \left(1 + \frac{H_1 + h}{H_0 + h}\right)\right](H_0 - H_1) \qquad (14)$$

This area is moved out of the doctor blade region with the constant velocity of $v_0$ and the distance of $v_0 \times \Delta t$; hence, it is equal to $v_0 \times \Delta t \times \delta_1$. The new initial height in the next time step is now $H_1$ and the new $\Delta S_2$ is found from using $H_1$ as initial height in equation (14) and so forth.

In the tape casting process, when the flow exits the doctor blade region, the fluid starts to flow in a transverse direction also (here in the $z$ direction) and this is mostly named side flow. As the final tape is in general very wide in the $z$ direction compared to its thickness, this side flow will be relatively small. Moreover, after the drying stage, the tape thickness is decreased due to weight loss. Considering both these effects, the final thickness of the dried tape is

$$\delta_{tp} = \frac{\alpha\beta\rho}{\rho_{tp}}\delta \qquad (15)$$

where $\delta_{tp}$ is the thickness of the dried tape, $\alpha$ is the fraction loss for side flow, $\beta$ is the fraction loss for weight reduction due to drying, $\rho$ is the density of green tape and $\rho_{tp}$ is the density of dried tape, and $\delta$ is the thickness of the green tape.

## Experimental

The different constituents and their function for the LSM slurry used in the experiments are given in Table 1. A commercial LSM was calcined at 1000°C and used in the amount of 62·05 wt-% in the final slurry. The average particle size and specific surface area were 12·42 μm and 23·24 $m^2\ g^{-1}$ respectively. Moreover, the weight ratios between LSM and MEKET (solution of methylethylketone and ethanol with the weight ratios of 1 : 3) and PVB/LSM were 1 : 2·44 and 1 : 11·53 respectively. To remove air bubbles from the slurries, mechanical vacuum was enforced for 15 min. The mean particle size and density of the final slurries were accordingly equal to 2·20–2·73 μm and 1·91 g $mL^{-1}$. The particle size distributions were measured with a laser diffraction particle size analyser LS 13 320 from Beckman Coulter (USA). The rheological profiles were measured using a narrow gap parallel plate sensor system in Rheometer HAAKE Rheo Stress 600 (Haake, Germany).

Experiments were carried out using a one-doctor blade continuous type of tape casting bench, and the plastic carrier tape (Mylar in the present case) was driven by stainless steel rollers. The doctor blade gap distance was set by using etalon sticks and a micrometre screw with an accuracy of 0·01 mm. After the propulsion of the torque drum, whose speed was programmed in advance, the slurry was peeled out according to the carrier movement, forming a thin layer of tape. The cast tapes were dried in air for 5 days, and their thicknesses were measured using the micrometer screw. The thicknesses of the cast tapes were measured in every 10 cm from doctor blade exit.

**Table 1 Material content and their function for LSM slurry used in experiments**

| Material | Function |
|---|---|
| $(La_{0\cdot85}Sr_{0\cdot15})_{0\cdot9}MnO_3$ (LSM) | Ceramic substrate |
| Methylethylketone | Solvent |
| Ethanol | Solvent |
| Polyvinyl pyrrolidone (PVP) | Dispersant |
| Polyvinyl butyral (PVB) | Binder |
| Polyethylene glycol (PEG) | Plasticiser |
| Dibutyl phthalate (DBP) | Plasticiser |
| Additol | Deflocculant |

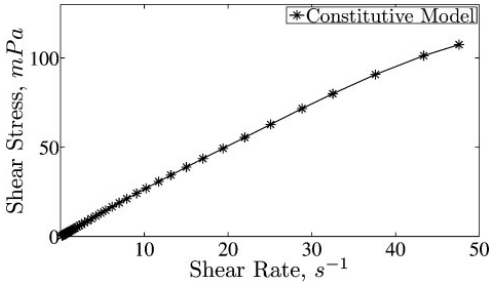


**3 Rheology behaviour of LSM slurry**

Experiments were conducted in three different cases, which are summarised in Table 2. For the first set of experiments, the same amount of ceramic slurry (constant $H_0$) was cast with three different substrate velocities. Then, in case 2, with constant velocity and slurry height, the amount of the doctor blade height was varied. In the last set of experiments during constant substrate velocity, the material load in the reservoir $H_0$ was varied. These experiments were carried out to investigate the effect of the three important parameters, i.e. drag forces related to substrate velocity, hydrostatic pressure and doctor blade height on the side flow amount.

## Results and discussion

Results from the rheology experiment showed that the LSM slurry follows the Ostwald–de Waele power law fluid behaviour. This is illustrated in Fig. 3, and the relationship for the shear rate and shear stress was found to be

$$\tau = 3{\cdot}31(\partial u/\partial y)^{0\cdot90} \qquad (16)$$

where the constant $k$, which is the consistency of fluid, is equal to 3·31 mPa $s^n$ (where $n$=0·90), and the constant $n$, which is the proximity to a Newtonian fluid, is equal to 0·90, quite close to the Newtonian fluid value of 1. The constant for the side flow $\alpha$ was obtained by a volumetric comparison of the tape which flowed outside

**Table 2 Summary of experimental studies**

| Parameter | Case 1 | Case 2 | Case 3 |
|---|---|---|---|
| $W$/mm | 6·4 | 6·4 | 6·4 |
| $h$/mm | 1 | 0·25, 0·4, 1 | 0·4 |
| $v_0$/mm $s^{-1}$ | 3·67, 10, 14·67 | 3·67 | 3·67 |
| $H_0$/mm | 1·2 | 10·6 | 3·1, 6·6, 20·8 |
| $d$/cm | 8·8 | 8·8 | 8·8 |
| $\alpha$/° | 45 | 45 | 45 |

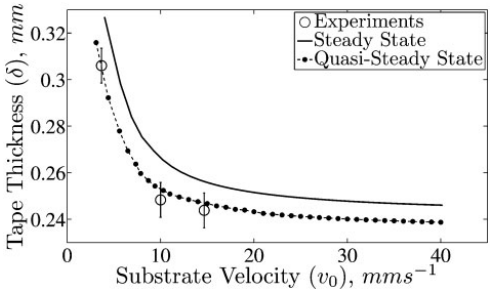


4 **Effect of substrate velocity on tape thickness with doctor blade height of 1 mm**

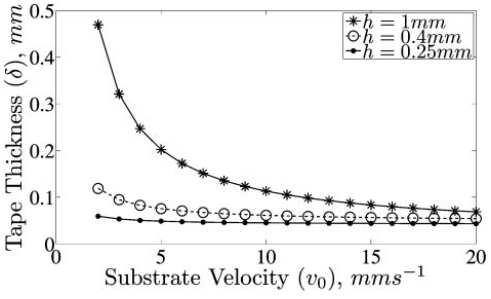


6 **Results of modelling for effect of doctor blade height on tape thickness**

the casting width to the tape within the casting width ($0{\cdot}8<\alpha<0{\cdot}9$). The drying weight loss factor $\beta$ was obtained from drying experiments, which measured the dried tape mass and compared it to the wet slurry mass ($0{\cdot}58<\beta<0{\cdot}64$).

## Effect of substrate velocity

Figure 4 shows the effect of the substrate velocity on the dried tape thickness for the experimental data, steady state and quasi-steady state model. As seen from the figure for all types of data, an increased substrate velocity results in decreasing of the tape thickness. By further increase in the substrate velocity, it is found that the tape thickness decreases hyperbolically,[4,9] which is also seen from equation (13). From previous works,[4,8,9] it was found that when the drag force is increased by increasing the substrate velocity, it becomes more dominant compared to the pressure force that results in more stretching of the slurry over the peeling belt. Figure 4 shows that the proposed quasi-steady state model is in better agreement with corresponding experiments as compared to the steady state model, since in the quasi-steady state model the effect of decreasing level of the slurry height was taken into account. It should be noted that the variation of the height in the slurry will change the parameter $A_0$ and the resultant values of $A_1$ and $A_2$ (which are calculated numerically); this of course is neglected in the steady state model.

Figure 5 depicts the velocity profiles below the doctor blade for three different tape velocities. It is seen that for the higher substrate velocity (of 14·67 mm $s^{-1}$), the distribution approaches a linear correlation, which corresponds to Couette flow conditions. For lower velocities, the hydrostatic pressure plays a more dominant role, resulting in a velocity peak ~0·25 mm above the peeling belt, which originates from the combination of Couette and Poiseuille flow conditions. These tendencies are also found in the analytical model for flow in tape casting originally proposed by Kim *et al.*[2] and further developed on dimensionless form by Jabbari and Hattel.[8]

## Effect of doctor blade height

The effect of the doctor blade height on the tape thickness is illustrated in Fig. 6. It is seen that increasing the doctor blade height leads to a higher tape thickness, which is expected. However, the difference between the curves in Fig. 6 is decreased by increasing the velocity. For a constant pressure height, increasing the doctor blade height results in more material being carried out of the doctor blade region. This means that the thickness of the tape will be increased. As mentioned before, for high casting velocities (substrate velocity), the drag force becomes more dominant. The increase in the tape thickness coming from a higher doctor blade gap is reduced as the velocity is increased.

The comparison between the proposed model, steady state model and experimental results is shown in Fig. 7. It can be seen that the new proposed model is in better agreement with experiments in comparison to the steady state model. The highest deviation between data was observed for the higher values of the doctor blade height. This could arise from some of the assumptions used in the equations for the proposed model. The main assumption in this regards is the use of constant side

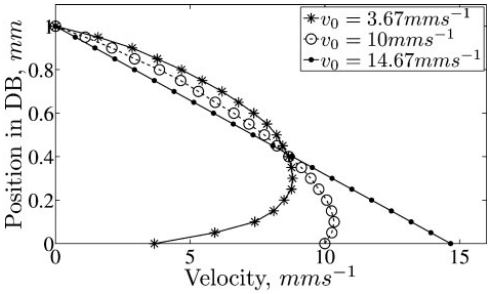


5 **Average velocity profile below doctor blade region with different substrate velocities**

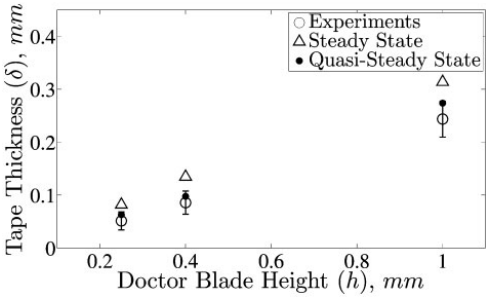


7 **Comparison of proposed quasi-steady state model with steady state model and experiments for $v_0$=3·67 mm $s^{-1}$**

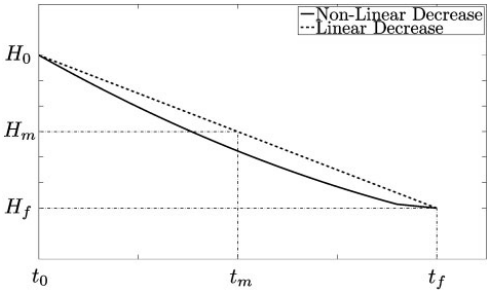


**8 Schematic illustration of slurry height change by time**

flow factor $\alpha$ for calculating the tape thickness based on equation (15). However, this factor is not constant based on the numerical investigation done by the authors,[17] and highly dependent on the geometry of the tape caster and the process parameter. On the other hand, in most cases, the desired thickness for the final tapes is in the range of $\leq$100 μm, in which the proposed model agrees well with the experimental data. The smaller deviation found in the experiment might be due to the effect of side flow, which obviously reduces the tape thickness as compared to the analytical solution.

## Effect of slurry load

It should be emphasised that for the comparisons shown in Figs. 4 and 7, the height of the slurry that was inserted in the steady state solution[15,16] was the initial height $H_0$. This of course overestimates the hydrostatic pressure and hence the tape thickness in cases where the slurry height is actually decreasing over time.

Thus, in order to make a more fair comparison between the analytical steady state model and the proposed quasi-steady state model, it was chosen to represent the slurry height (which is constant) in the steady state model by some reasonable average.

Now, consider Fig. 8 in which the decrease in the height of the slurry in the reservoir over time is represented schematically. Here, $H_0$ is the initial ceramic height and $H_f$ is the last point where the fluid experiences the hydrostatic pressure (equal to the doctor blade height $h$). Of course, the real trend for the decrease of the height is a non-linear behaviour, starting with high hydrostatic pressure and decreasing by time, but as a reasonable average, one could assume that there is a linear behaviour in the reduction of the slurry height by time, i.e.

$$H_m = \frac{H_0 + H_f}{2} \tag{17}$$

This mean value is used in the steady state model when comparing with the quasi-steady state model in Figs. 9 and 10.

By choosing fairly small time increments for the modelling, the results for different values of heights in the reservoir are shown in Fig. 9. As it seen from Fig. 9, the thickness of the tape in the end of a strip is higher than that in the beginning of a strip. This is due to the higher level of material in the reservoir in the beginning of the process. As time passes, the height of the slurry in the reservoir decreases, and consequently, the resultant height of the tape will decrease. This means that the hydrostatic pressure decreases by time and the drag forces start to show their dominance by making the tape thinner. However, this phenomenon cannot be detected by the steady state model, no matter which value of the slurry height (initial or average) is applied. Moreover, it can be seen that the higher level of slurry in the reservoir leads to a higher tape thickness in the strip. On the other

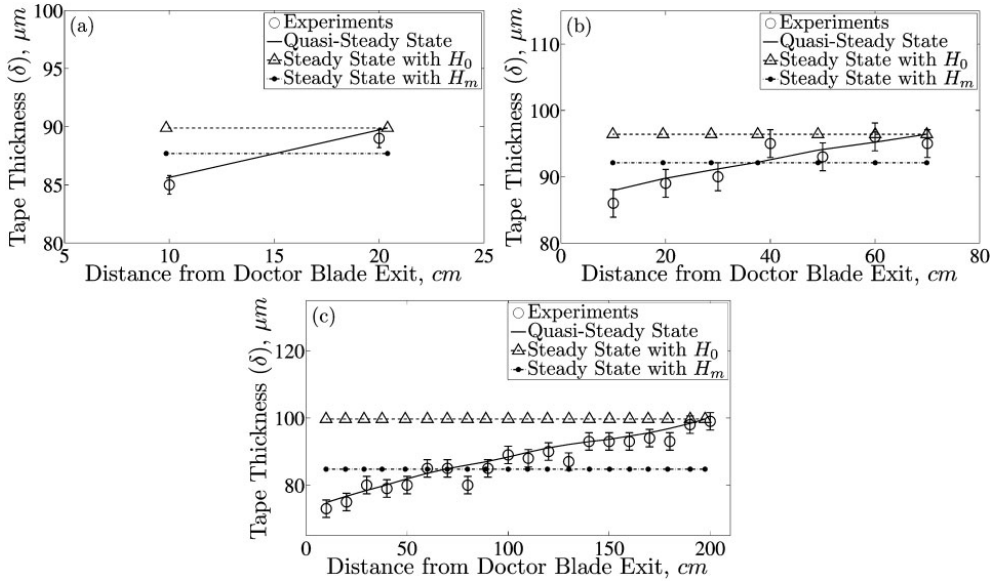


*a* $H_0$=3·1 mm; *b* $H_0$=6·6 mm; *c* $H_0$=20·8 mm

**9 Results of modelling and their comparison with experimental data for case 3**

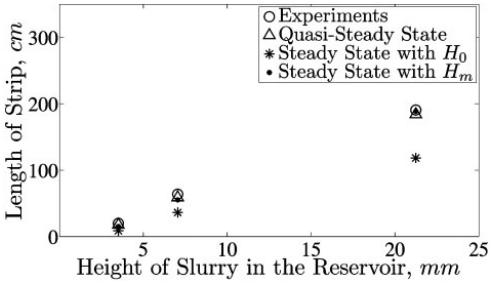


**10 Correlation between height of slurry and length of strip from model and experiments with substrate velocity of 3·67 mm $s^{-1}$**

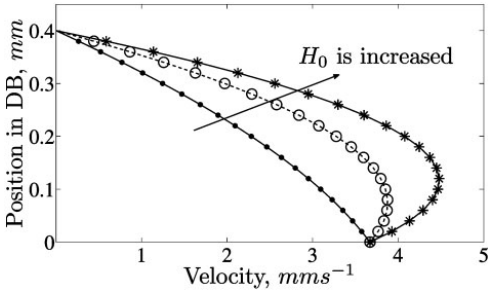


**11 Effect of variation in slurry height on velocity profile below doctor blade region with doctor blade size of $h$=0·4 mm**

hand, it is also seen that the mean assumption for the initial slurry height (steady state with $H_m$) in some points catches the experimental data better than the one with the initial height (steady state with $H_0$). However, it does not predict the transient behaviour of the slurry height, which is embedded in the quasi-steady state model.

Furthermore, the higher level of slurry will result in a longer final strip because of more material content in the process. The predicted values from the quasi-steady state, steady state model with initial height and steady state with the mean height assumption and the estimated data from experiments for the length of strip with the different heights of the slurry are shown in Fig. 10. The results of the quasi-steady state model are in very good agreement with the experimental data. The small differences between the experiments and the proposed model might be due to the influence of the side flow. However, it can also be seen that there is much more difference between the steady state model and the experimental data, which was expected. It is obvious that the steady state model with the initial height gives a constant value of the tape thickness, which only fits to the experimental and the quasi-steady state model in the beginning where the slurry height is actually $H_0$. Moreover, the results of the steady state model with the mean assumption for the initial slurry height are in good agreement with both the quasi-steady state and the experimental data; however, they are still constant and a more representative level is expected.

To get a better understanding of the effect of the variable slurry height on the tape thickness, the velocity profile was analysed below the doctor blade region for one of the tests in case 3 ($H_0$=20·8 mm, $h$=0·4 mm and $v_0$=3·67 mm) which is shown in Fig. 11. Here, the line with the asterisk marker represents the velocity profile for the initial slurry height ($H_0$=20·8 mm), the line with the 'o' marker is the representative of the velocity profile after some period of time and the line with the dot marker represents results even later in time. As seen, since the hydrostatic pressure decreases by time due to the reduction in level in the slurry height, the velocity profile is changed and the area under the velocity profile is decreased, which can be seen in Fig. 12, and consequently, the 'area' out of the blade is decreased. On the contrary, decreasing the pressure head for a constant velocity, the thickness of the tape is decreased in the exit and vice versa. This behaviour very much emphasises the importance of the proposed quasi-steady state model, in which the transient effect of the slurry height in the reservoir (which resembles the pressure head) is implemented. As already discussed, the variation in the velocity profile will cause a change in the tape thickness (Fig. 12). This phenomenon can easily be seen in Fig. 9, where the tape thickness decreases in the casting direction due to the transient decrease of the slurry height in the reservoir.

## Conclusions

A quasi-steady state power law model for the constitutive behaviour of the non-Newtonian slurry of LSM was proposed and used to analyse the effect of substrate velocity, doctor blade height and slurry height in the reservoir on the final tape thickness in tape casting. This proposed model was based on the continuity equation assuming incompressibility such that the decrease of the volume of the slurry in the reservoir is equal to the one that leaves the doctor blade region. The results show that increasing the substrate velocity (casting speed) causes a decrease in the tape thickness due to the dominance of drag force over hydrostatic pressure. On the other hand, increasing the doctor blade height with constant velocity, the thickness of the final tape will be increased, since the gap size for the slurry is high enough for it to be conveyed more out of the doctor blade region. In both cases, the developed quasi-steady state model has better agreement with the experiments compared to the well known steady state model. For both quasi-steady state model and experiments, it is observed that the height of tape at the end point of the strip is higher in comparison to the beginning of the

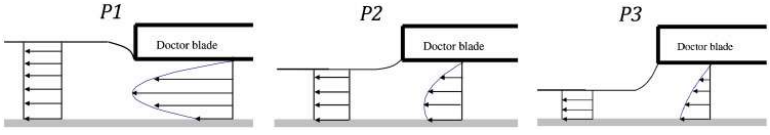


**12 Schematic illustration of effect of increased pressure head on tape thickness ($P_1$>$P_2$>$P_3$)[2]**

strip, which is not predictable by steady state solution. Moreover, by increasing the material load (the height of slurry in the reservoir), the aforementioned differences between the beginning and the end of strip and the length of strip will be increased. A new modified steady state model is also presented based on a linear correlation between the level in the slurry height and the time. Although the presented model does not have the full accuracy of the quasi-steady state model, it showed some good results compared to the conventional steady state calculations from the literature. Although the LSM ceramic used in the present study has a slightly non-Newtonian behaviour ($n$=0·90), the model contains all main parameters that influence the process, and it has the flexibility to be used for different slurries, which are more non-Newtonian, as well as different machine designs. Moreover, the results show that the classical steady state is not so well describing for the real process in which the ceramic height in the reservoir is not constant. However, the results of the proposed quasi-steady state model show that it has good agreement with the experimental data.

## Acknowledgements

The authors would like to acknowledge the support of the Scientific Research Councils on Technology and Production Sciences (FTP) (contract no. 09-072888, OPTIMAC), which is part of the Danish Council for Independent Research (DFF).

## References

1. G. S. Grader and L. Zuri: *J. Am. Ceram. Soc.*, 1993, **76**, 1809–1814.
2. H. J. Kim, M. J. M. Krane, K. P. Trumble and K. J. Bowman: *J. Am. Ceram. Soc.*, 2006, **89**, 2769–2775.
3. C. Pagnoux, T. Chartier, M. Granja, F. Doreau, J. M. Ferreira and J. F. Baumard: *J. Eur. Ceram. Soc.*, 1998, **18**, 241–247.
4. Y. T. Chou, Y. T. Ko and M. F. Yan: *J. Am. Ceram. Soc.*, 1987, **70**, 280–282.
5. Y. Tanimoto, T. Hayakawa and K. Nemoto: *Dent. Mater.*, 2007, **23**, 549–555.
6. M. P. Albano and L. B. Garrido: *Ceram. Int.*, 2005, **31**, 57–66.
7. P. H. Gaskell, B. Rand, J. L. Summers and H. M. Thompson: *J. Eur. Ceram. Soc.*, 1997, **17**, 1185–1192.
8. M. Jabbari and J. Hattel: AIP Proc. Int. Conf. on 'Numerical analysis and applied mathematics', Halkidiki, Greece, American Institute of Physics (AIP), September 2011, Vol. 1389, 143–146.
9. R. Pitchumdni and V. M. Karbhari: *J. Am. Ceram. Soc.*, 1995, **78**, 2497–2503.
10. T. A. Ring: *Adv. Ceram.*, 1989, **26**, 569–576.
11. X. Y. Huang, C. Y. Liu and H. Q. Gong: *Mater. Manuf. Processes*, 1997, **12**, 935–943.
12. C. Badinia, P. Fino, A. Ortona and C. Amelio: *J. Eur. Ceram. Soc.*, 2002, **22**, 2071–2079.
13. C. A. Folsom, F. W. Zok and F. F. Lang: *J. Am. Ceram. Soc.*, 1994, **77**, 689–696.
14. P. M. Raj and W. R. Cannon: *J. Am. Ceram. Soc.*, 1999, **82**, 2619–2625.
15. G. Zhang, Y. Wang and J. Ma: *Mater. Sci. Eng. A*, 2002, **A337**, 274–280.
16. A. I. Y. Tok, F. Y. C. Boey and Y. C. Lam: *Mater. Sci. Eng. A*, 2000, **A280**, 282–288.
17. M. Jabbari and J. H. Hattel: *J. Am. Ceram. Soc.*, 2013, **96**, 1414–1420.

# Appdx B

M. Jabbari, J. Hattel, "Numerical Modelling of the Side Flow in Tape Casting of a Non-Newtonian Fluid", *Journal of the American Ceramic Society* 96 (2013) 1414-1420.

journal

*J. Am. Ceram. Soc.*, **96** [5] 1414–1420 (2013)
DOI: 10.1111/jace.12295


# Numerical Modeling of the Side Flow in Tape Casting of a Non-Newtonian Fluid

M. Jabbari† and J. H. Hattel

Department of Mechanical Engineering, Technical University of Denmark, Nils Koppels Allé, 2800 Kgs Lyngby, Denmark

**One of the most common ways used to produce multilayer ceramics (MLC) is tape casting. In this process, the dried tape thickness is of great interest to control the desired products and applications. One of the parameters that influences the final tape thickness is the side flow factor (α) which is mostly measured at the end of the process by a volumetric comparison of the tape which flowed outside the casting width to the tape within the casting width. This phenomenon has not been predicted theoretically yet in the literature. In this study, the flow of $(La_{0.85}Sr_{0.15})_{0.9}MnO_3$ (LSM) slurry in the tape casting process is modeled numerically with ANSYS FLUENT in combination with an Ostwald-de Waele power law constitutive equation. Based on rheometer experiments, the constants in the Ostwald-de Waele power law are identified for the considered LSM material and applied in the numerical modeling. This model is then used for different values of substrate velocity, initial doctor blade height and material load in the reservoir, to investigate their effect on α. It is found that this factor mostly ranges between 0.8 and 0.9. Results of the modeling are compared with experimental findings and good agreement is found.**

## I. Introduction

The production of ceramics is growing as their usage is expanding, often requiring high quality and low geometry tolerance, like in capacitors, piezoelectric actuators, gas sensors, etc. The parallel (doctor) blade process was first used in preparing ceramic tapes in the 1940s and it plays a key role in producing thin ceramic tapes.[1,2] Tape casting is a forming method that has mainly been used in the electronics industry to produce multilayer capacitors and electronic substrates.[3,4] This technique is a well-established process which is used to produce ceramic layers and MLC. The general schematic of the process is illustrated in Fig. 1.

In the tape casting process, the ceramic slurry is mostly categorized as a non-Newtonian fluid with relatively high viscosity. A summary of work published regarding the rheological classification of non-Newtonian fluids and the existence of analytical/numerical models with focus on tape casting was well documented before by the authors (M. Jabbari, R. Bulatova, J. H. Hattel, and C. R. H. Bahl, under review).[5]

In general, the fluid flow in the doctor blade region and the subsequent outflow can be analyzed solving the momentum equation together with the continuity equation in two dimensions assuming that the flow is generated by both the viscous drag due to the peeling velocity of the substrate and the static hydraulic pressure in the slurry reservoir (M. Jabbari *et al.*, under review).[5] There are a few research articles in which the flow field and tape thickness were modeled analytically. Chou *et al.*[6] modeled the flow in the parallel blade region. Because of the low Reynolds number, they neglected the inertia forces by assuming Stokes flow for a Newtonian fluid. It is shown[5] that the most important parameters in the tape casting process are the hydrostatic pressure behind the flow in the doctor blade region and the velocity of the peeling belt. Depending on the dominance of these parameters one over another, the final thickness of the tape will vary. The transient behavior of the slurry height in the reservoir (i.e., the decreasing of the height in the casting chamber) has commonly been neglected in the literature,[5,6–8] even though it has an influence on the tape thickness and its uniformity along the casting direction. Hence, an analytical model for the transient behavior of the slurry height was proposed by the authors to overcome the mentioned problems (M. Jabbari *et al.*, under review).

The most important parameters determining the quality of the parts produced by tape casting are the tape thickness and the flatness of the tape. Although there are many parameters to check and control in the process, these two are the most important ones from a manufacturing view point. Reaching a constant tape thickness is not an unrealistic goal industrially, as most of the manufacturing processes for tape casting are in the continuous form in which the reservoir is continuously fed by the slurry. Moreover, using two doctor blades in the design of the machine will result in having an almost constant hydrostatic pressure during the casting process. However, in small tape casters, especially in small-scale production and laboratories, it is of great importance to control the tape thickness. Finally, another inherent phenomenon which affects the tape thickness is the side flow of the slurry when it leaves the doctor blade. Although this side flow in tape casting is of relatively limited magnitude, it is interestingly enough always being mentioned as an influencing parameter in the calculations of the tape thickness and always measured experimentally[5–8] by a volumetric comparison of the tape which flowed outside the casting width to the tape within the casting width. Hence, the side flow factor is measured by relating the width of the doctor blade to the width of the produced tape. To understand the nature of the side flow and the way it can be calculated, the three following stages are now introduced and corresponding expressions for the mass per length of the tape slurry are given:

1. Initial stage: side flow and drying has not taken place, $M_0 = \rho W h$.
2. Second stage: side flow has taken place but drying has not taken place, $M_1 = \rho W' h'$.
3. Third stage: both side flow and drying has taken place, $M_2 = \rho_{tp} W'' \delta_{tp}$.

where the different parameters are summarized in Table I and illustrated schematically in Fig. 2.

As there is no mass loss until stage 3, the masses in stages 1 and 2 are equal ($M_0 = M_1$), and due to the side flow the tape width is increased, hence decreasing the tape height (thickness). This results in the side flow factor to be defined as follows:

M. Menon—contributing editor

Manuscript No. 32217. Received October 27, 2012; approved February 22, 2013.
†Author to whom correspondence should be addressed. e-mail: mjab@mek.dtu.dk

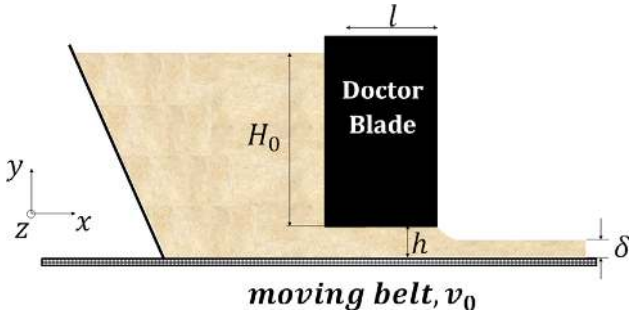


**Fig. 1.** Schematic of tape casting process.

**Table I. Parameters Definitions for the Three Stages of the Calculations**

| Stage | Side flow/drying | Tape width | Tape thickness | Density |
|---|---|---|---|---|
| 1 | No side flow no drying | $W$ | $h$ | ρ |
| 2 | With side flow no drying | $W'$ | $h'$ | ρ |
| 3 | With side flow with drying | $W''$ | $\delta_{tp}$ | $\rho_{tp}$ |

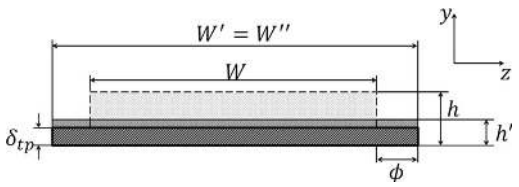


**Fig. 2.** Schematic illustration of side flow factor.

$$\alpha = \frac{W}{W'} = \frac{h'}{h} \tag{1}$$

Moreover, due to the drying process, the mass in stage 3 is different from the previous stages ($M_2 < M_1 = M_0$). In fact, the ratio of the mass in stage 3 and 2 ($\beta = M_2/M_1$) is typically denoted the drying factor, which is the fraction loss for weight reduction due to drying:

$$\beta = \frac{\rho_{tp} W'' \delta_{tp}}{\rho W' h'} \tag{2}$$

Assuming in the above equation the drying does only affect the tape height (thickness) whereas its influence on the width is negligible, we get $W' \approx W''$. By combining Eq. (1) with Eq. (2), the side flow factor becomes:

$$\alpha = \frac{W}{W'} = \frac{1}{\beta} \cdot \left( \frac{\delta_{tp} \cdot \rho_{tp}}{h \cdot \rho} \right) \tag{3}$$

thus yielding the well-known expression that is typically used to describe the side flow factor (α) in the literature.[5–8]

By assuming symmetrical flow in the sides, the final tape width becomes $W' = W + 2\phi$, and the side flow factor can be calculated by the simple relationship:

$$\alpha = \frac{W}{W'} = \frac{W}{W + 2\phi} \tag{4}$$

which is the expression used henceforth in the numerical calculations in the present work. Equation (4) shows that by increasing the amount of the flow in the sides (ϕ), the side flow factor (α) decreases, and vice versa.

In the present work, the flow of the weakly non-Newtonian ceramic fluid ($(La_{0.85}Sr_{0.15})_{0.9}MnO_3$ - LSM) described with the Ostwald-de Waele constitutive model in the tape casting process is investigated using the finite volume-based commercial code (ANSYS FLUENT). The flow of the slurry in the sides after leaving the doctor blade and when stretching over the peeling belt was evaluated to predict the side flow effect in the tape casting process. The effect of the hydrostatic pressure on the side flow was modeled by choosing three different initial slurry heights inside the reservoir. Moreover, the effect of the substrate velocity as well as the doctor blade height on the side flow was studied. For all these investigations, the results of the numerical modeling are compared with corresponding experimental findings.

## II. Governing Equations and Boundary Conditions

When dealing with flow problems, the momentum and continuity equations should be solved:

$$\rho\left(\frac{\partial u}{\partial t} + u \cdot \nabla u\right) = -\nabla p + \nabla \cdot T + F \tag{5}$$

$$\frac{\partial \rho}{\partial t} + \nabla \cdot (\rho u) = 0 \tag{6}$$

where ρ is density, $u$ is velocity vector, $p$ is pressure, $T$ is viscous stress tensor, and $F$ is the contribution from external forces. Here, the momentum Eq. (5) is equivalent to Newton's second law of motion, and the continuity Eq. (6) ensures conservation of mass.

The non-Newtonian behavior of the slurry is described by the Ostwald-de Waele power law, i.e.:

$$\tau = k\dot{\gamma}^n \tag{7}$$

in which $k$ is the consistency of the fluid and the exponent $n$ characterizes the flow type, respectively. The deviation of n from unity denotes the amount of deviation from a Newtonian fluid.

To describe and model the side flow properly, apart from solving the momentum and continuity equations with the

relevant constitutive law, the tracking of the free surface as well as the effect of surface tension should be sufficiently addressed.

The volume of fluid (VOF) model[9] which is such a surface-tracking technique applied to a fixed Eulerian mesh is used in the present work. It is designed for two or more immiscible fluids where the position of the interface between the fluids is of interest and it relies on the fact that the two or more fluids (or phases) are not interpenetrating. For this study the two phases are the ceramic slurry and the air. For each additional phase which is added to the model, a variable is introduced: the volume fraction of the phase in the computational cell. In each control volume, the volume fractions of all phases sum to unity. The fields for all variables and properties are shared by the phases and represent volume-averaged values, as long as the volume fraction of each of the phases is known at each location.

The properties appearing in the transport equation are determined by the presence of the component phases in each control volume. In a two-phase system, for example, if the phases are represented by the subscripts 1 and 2, and if the volume fraction of the second of these is being tracked, the density in each cell is given by the following equation:

$$\rho = f_2\rho_2 + (1 - f_2)\rho_1 \tag{8}$$

The evolution of scalar $f$ (volume fraction of fluid) is governed by the simple advection equation:

$$\frac{\partial f}{\partial t} + \frac{\partial u_i f}{\partial x_i} = 0 \tag{9}$$

The VOF model can also include the effect of surface tension along the interface between each pair of phases. In ANSYS FLUENT, the model can be augmented by the additional specification of the contact angles between the phases and the walls, and the solver will include the additional tangential stress terms that arise due to the variation in surface tension coefficient. The surface tension is modeled by means of the continuum surface force (CSF) model proposed by Brackbill *et al.*[10] With this model, the addition of surface tension to the VOF calculation results in a source term in the momentum equation. In the case of constant surface tension along the surface and considering only the forces normal to the interface, the pressure drop across the surface depends on the surface tension coefficient, $\sigma$, and the surface curvature as measured by two radii in orthogonal directions, $R_1$ and $R_2$, as expressed in Eq. (10).

$$p_2 - p_1 = \sigma\left(\frac{1}{R_1} + \frac{1}{R_2}\right) \tag{10}$$

where $p_2$ and $p_1$ are the pressure in the two fluids on either side of the interface. In the formulation of the CSF model, the surface curvature is computed from local gradients in the surface normal at the interface. The surface normal $n$ is then, defined via Eq. (11) as the gradient of $\alpha_q$, the volume fraction of the $q$ th phase, the following way:

$$n = \nabla\alpha_q \tag{11}$$

The curvature, $\kappa$, to be used in Eq. (10) ($\kappa = 1/R$) is defined in Eq. (12) in terms of the divergence of the unit normal,[10] $\hat{n}$:

$$\kappa = \nabla \cdot \hat{n} \tag{12}$$

where

$$\hat{n} = \frac{n}{|n|} \tag{13}$$

The surface tension is expressed in terms of the pressure jump across the surface. The force at the surface can be expressed as a volume force using the divergence theorem. It is this volume force that is the source term which is added to the momentum equation and has the following form:

$$F_{vol} = \Sigma\sigma_{ij}\frac{\alpha_i\rho_i\kappa_j\nabla\alpha_j + \alpha_j\rho_j\kappa_i\nabla\alpha_i}{\frac{1}{2}(\rho_i + \rho_j)} \tag{14}$$

Equation (8) allows for a smooth superposition of forces near cells where more than two phases are present. If only two phases are present in a cell, then $\kappa_i = -\kappa_j$ and $\nabla\alpha_i = -\nabla\alpha_j$, then Eq. (14) simplifies to Eq. (15)

$$F_{vol} = \sigma_{ij}\frac{\rho\kappa_i\nabla\alpha_i}{\frac{1}{2}(\rho_i + \rho_j)} \tag{15}$$

where $\rho$ is the volume-averaged density computed using the following equation:

$$\rho = \Sigma\alpha_q\rho_q.$$

A schematic illustration of the 3D computational domain is shown in Fig. 3. The dimensions are chosen relevant to the machine design of the tape caster and according to the experimental setup applied in the present work. The domain was discretized with a relatively fine mesh (cell side lengths in the order of 10 μm).

To reduce the computation time, the reservoir region was not included in the model instead pressure boundary condition was implemented in the inlet face as shown in Fig. 3. The analytical equation for calculating the pressure gradient in the doctor blade region is given below (M. Jabbari *et al.*, under review)[11]

$$\frac{dp}{dx} = -\frac{\rho g H_0}{wl} \tag{16}$$

where $\rho$ is density, $g$ is body acceleration due to gravity, $H_0$ is the initial height of the slurry in the reservoir, and $w$ is the length of the doctor blade region.

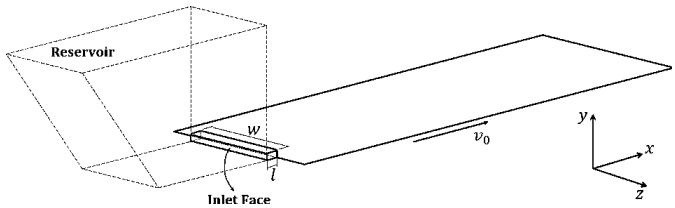


**Fig. 3.** Schematic illustration of computational domain for numerical analysis.

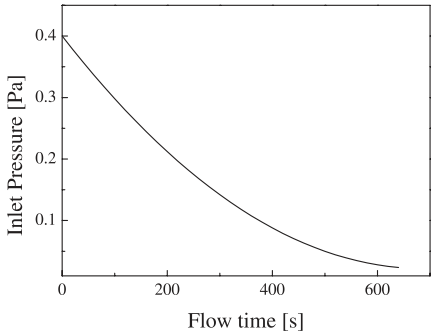


**Fig. 4.** Example of implemented inlet boundary condition for $H_0$ = 20.8 mm.

As seen from Eq. (16) the pressure gradient inside the channel below the doctor blade is assumed constant, and it can be determined by the height of the slurry in the reservoir. However, this height is not constant for the setup considered in the present work, but decreasing with time. To simulate this transient behavior of the slurry height, a user defined function (UDF) based on Eq. (16) was coded in the programming language C and linked to ANSYS FLUENT. This UDF was treated as a variable pressure boundary condition which is changed by the actual flow time and updated every time step. An example of such boundary condition is illustrated in Fig. 4. A fixed velocity in the $x$-direction ($v_0$) is implemented on the substrate as the velocity of the peeling belt with no slip condition. A zero gradient is assumed for all flow properties in the outlet boundary condition. All other boundaries are implemented as wall boundaries with no slip condition. The initial conditions are the inlet pressure boundary condition at the "Inlet Face" based on Eq. (16), no fluid is yet present in the calculation domain and the peeling belt velocity is $v_0$.

## III. Numerical Analysis

For the present transient calculations, the noniterative time-advancement (NITA) scheme[12] is used to reduce the amount of computations. The idea underlying the NITA scheme is that, to preserve overall time accuracy, there is no need to reduce the splitting error to zero, but only have to make it the same order as the truncation error. The NITA does not need any outer iterations and hence there is only a single outer iteration per time step, which significantly speeds up transient simulations. The NITA is used with the fractional-step method, which offers the possibility of considerable increase in efficiency.[13] The Compressive interface capturing scheme for arbitrary meshes (CICSAM) method was used for interpolation of the interface, as it was already evaluated and found to be suitable for the tape casting process by the authors (M. Jabbari and J. H. Hattel, under review). The CICSAM, based on Ubbink and Issa's work,[14] is a high-resolution differencing scheme. It is particularly suitable for flows with high ratios of viscosities between the phases. CICSAM is implemented in ANSYS FLUENT as an explicit scheme and offers the advantage of producing an interface that is almost as sharp as the geometric reconstruction scheme.

## IV. Experiments

The different ingredients and their function for the LSM slurry used in the experiments are given in Table II. A commercial LSM was calcined at 1000°C, and used in the amount of 62.05 wt% in the final slurry. The average particle size and specific surface area were 12.42 μm and 23.24 $m^2/g$, respectively. Moreover, the weight ratio between LSM:MEKET (solution of methyl ethyl ketone and ethanol with the weight ratio of 1:3) and PVB:LSM was 1:2.44 and 1:11.53, respectively. To remove air bubbles from slurries, mechanical vacuum was enforced for 15 min. The mean particle size and density of the final slurries were accordingly equal to 2.20–2.73 μm and 1.91 g/mL. The particle size and distribution were measured by a Laser Diffraction Particle Size Analyzer LS 13 320 from BECKMAN COULTER (Beckman Coulter Danmark ApS, København, Denmark). The rheological profiles were measured using a narrow-gap parallel plate sensor system in Rheometer HAAKE Rheo Stress 600 (Thermo Scientific, Odense C Denmark).

**Table II. Material Content and Their Function for Non-Newtonian LSM Slurry used in Experiments**

| Material | Function |
|---|---|
| $(La_{0.85}Sr_{0.15})_{0.9}MnO_3$ (LSM) | Ceramic substrate |
| Methyl ethyl ketone | Solvent |
| Ethanol | Solvent |
| Polyvinyl pyrrolidone (PVP) | Dispersant |
| Polyvinyl butyral (PVB) | Binder |
| Polyethylene glycol (PEG) | Plasticizer |
| Dibutyl phthalate (DBP) | Plasticizer |
| Additol | Deflocculant |

The experiments were carried out using a one-doctor blade continuous type of casting bench, and the plastic carrier (Mylar in the present case) was driven by a stainless steel roller. The doctor blade gap distance was set using etalon sticks and a micrometer screw with an accuracy of 0.01 mm. After the propulsion of a torque drum, whose speed was programmed in advance, the slurry was peeling out along the carrier movement, forming a thin layer of tape. The casted tapes were dried in air for 5 days, and their thickness was measured using a micrometer screw.

Experiments were conducted in three different cases, which are summarized in Table III. For the first set of experiments, the same amount of ceramic slurry (constant $H_0$) was casted with three different substrate velocities. Then in case two, during a constant substrate velocity ($v_0$) the material load in the reservoir ($H_0$) was varied. Finally, in the last set of experiments with a constant velocity and slurry height, the doctor blade height was varied. These experiments were carried out to investigate the effect of the following three important parameters, i.e.,: drag forces related to substrate velocity as well as hydrostatic pressure and doctor blade height on the side flow factor (α).

## V. Results and Discussion

### *(1) Material Constants*

The results of the rheology experiment showed that the LSM slurry follows the Ostwald-de Waele power law fluid behavior. This is illustrated in Fig. 5 and the relationship between shear rate and shear stress is found to be:

$$\tau = 3.31 \cdot (du/dy)^{0.90} \tag{17}$$

Comparing Eqs (7) and (17), the constant $k$ which is the consistency of the fluid is found to be equal to

**Table III. Overview of the Experimental Studies Carried Out**

| Parameter | Case 1 | Case 2 | Case 3 |
|---|---|---|---|
| $w$ (cm) | 17.8 | 17.8 | 17.8 |
| $l$ (cm) | 0.6 | 0.6 | 0.6 |
| $h$ (cm) | 1 | 0.4 | 0.25, 0.4, 1 |
| $v_0$ (mm/s) | 3.67, 10, 14.67 | 3.67 | 3.67 |
| $H_0$ (mm) | 1.2 | 3.1, 6.6, 20.8 | 10.6 |

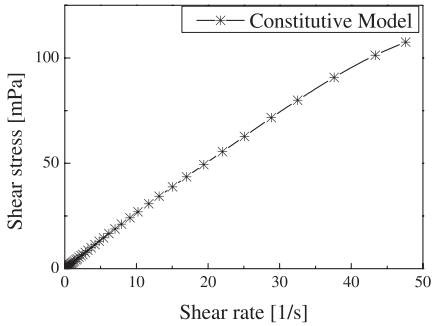


**Fig. 5.** Rheology behavior of LSM slurry.

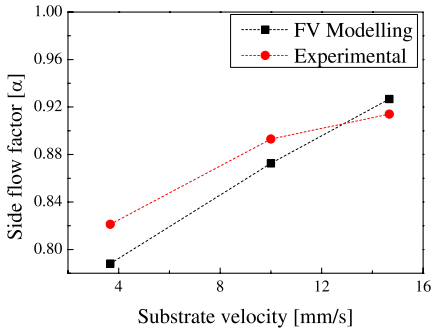


**Fig. 6.** Impact of the substrate velocity on the side flow factor ($H_0$ = 1.2 mm, $h$ = 1 mm). The lines are guides to the eye.

$k$ = 3.31 mPa.s$^n$. Moreover, the constant $n$ is equal to 0.90 which denotes a small deviation from a Newtonian fluid, indicating a closely Newtonian behavior. These parameters are implemented in the numerical calculations for the behavior of the non-Newtonian LSM ceramic.

### *(2) Impact of Substrate Velocity*

The effect of substrate velocity on the side flow factor is illustrated in Fig. 6. The results showed that by increasing the velocity of the peeling belt, the value of the side flow factor will be increased. It should be kept in mind that an increased value of the side flow factor means that the slurry flows less toward the sides. Moreover, for high values of the side flow factor and neglecting the drying factor, the dried tape thickness will be closer to that of the green tape. Increasing the substrate velocity increases the drag forces in the casting direction ($x$-direction) compared with the side direction ($z$-direction), and gives the slurry less possibility to flow toward the sides. It should be mentioned that the side flow factor expresses the mean value of the side flow along the tape. It should also be emphasized that for higher velocities, the side flow factor is near to one indicating almost no side flow. However, this does not mean that the tape thickness remains constant, as the actual tape thickness is proportional to the reverse of the velocity function ($\delta = 1/f(v)$), which means that by increasing the substrate velocity the final tape thickness will decrease. So, for high velocities the real tape thickness will decrease a little bit due to the combination of the elucidated reciprocal relationships as well as caused by the reduced flow of the slurry toward the sides. The minimum and maximum values for the side flow factor predicted by the numerical model are 0.79 and 0.93, respectively. This was in good agreement with the corresponding experimental values of 0.82 and 0.92.

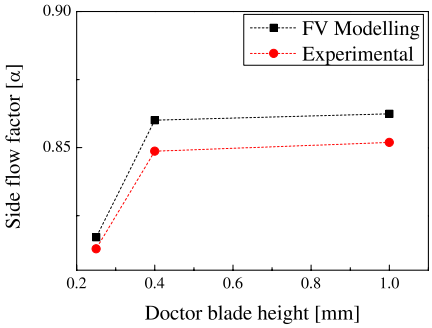


**Fig. 7.** Effect of the doctor blade height on the side flow factor ($H_0$ = 10.6 mm, $v_0$ = 3.67 mm/s). The lines are guides to the eye.

### *(3) Impact of Doctor Blade Height*

Figure 7 shows the influence of the variation in doctor blade height on the side flow factor. As the doctor blade height increases, the size of the side flow factor (α) increases for both numerical and experimental predictions. As discussed before, a higher side flow factor results into less flow of slurry toward the sides after leaving the doctor blade region. For the lower value of the doctor blade height, as the slurry height in the reservoir and the velocity of the peeling belt are constant, the hydrostatic pressure behind the flow is higher compared with the one with the bigger doctor blade height. Increasing the hydrostatic pressure will increase the flow to the sides and hence lead to a decrease in the resultant side flow factor (this will be discussed in more details in the next section). On the other hand, due to the low velocity used in these series of experiments, the ceramic slurry has much time to flow toward the sides after leaving the doctor blade region. These two phenomena obviously interact, but with the bigger doctor blade height, the effect of hydrostatic pressure decreases and leads to a decrease in the flow to the sides and hence an increase of the side flow factor. The minimum and maximum values for the side flow factor predicted by the numerical model are 0.82 and 0.86, respectively. This was in good agreement with the corresponding experimental values of 0.81 and 0.85.

Increasing the doctor blade height will increase the amount of the material (here the ceramic slurry) which is carried out, and consequently increases the initial tape thickness in the outlet region. This increase in the initial tape thickness over the peeling belt results in increasing the amount of flow to the sides, and consequently the side flow factor decreases. This phenomenon is illustrated in Fig. 8 for two different initial tape thicknesses for two different instants in time. It is seen that by increasing the initial tape thickness, the flow to the side increases for both instants. This can be caused by the surface tension forces which are predominant in the tape with the smaller thickness compared with the tape with larger thickness. As already discussed, the higher initial tape thickness is the result of the bigger doctor blade height. This means that for high values of the doctor blade height the side flow factor (α) decreases. This can be used as an explanation for the almost constant behavior of the right-hand part of the graph in Fig. 7 as opposed to the left part where the slope is relatively high.

### *(4) Impact of Slurry Height*

The effect of the initial slurry height on the side flow factor is illustrated in Fig. 9. As expected, increasing the initial slurry height in the reservoir will increase the tape thickness [Section V*(3)*], thereby promoting the flow toward the sides and hence decrease the resultant side flow factor. Furthermore, a higher hydrostatic pressure behind the flow (inside

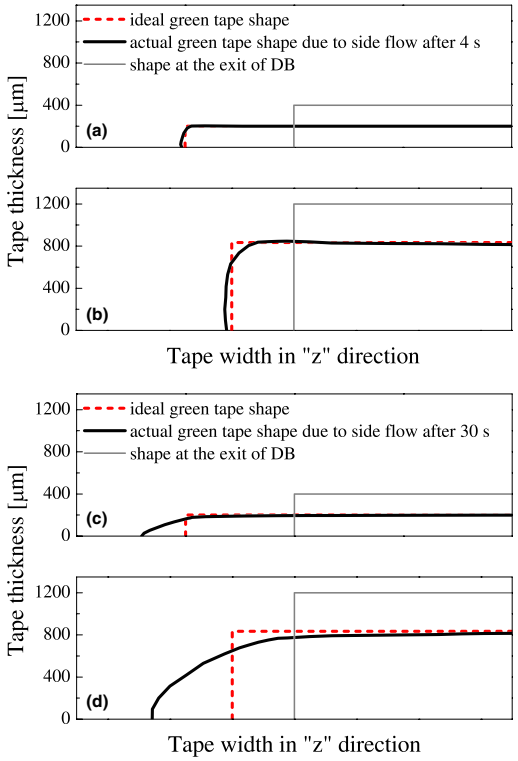


**Fig. 8.** Effect of initial tape thickness on the flow of slurry in the side obtained from the numerical model with (a) 200 μm and $t = 4$ s, (b) 834 μm and $t = 4$ s, (c) 200 μm and $t = 30$ s, and (d) 834 μm and $t = 30$ s.

the doctor blade region) will result in an increase in the ability to flow toward the sides. The minimum and maximum values for the side flow factor predicted by the numerical model are 0.80 and 0.91, respectively. This was in good agreement with the corresponding experimental values of 0.80 and 0.90.

For the highest value of the initial slurry height in the reservoir, it can be observed that the side flow in the beginning is considerably higher as compared with later stages in the process. This phenomenon is illustrated in Fig. 10, for both FVM modeling and experiments showing a "trumpet" shape

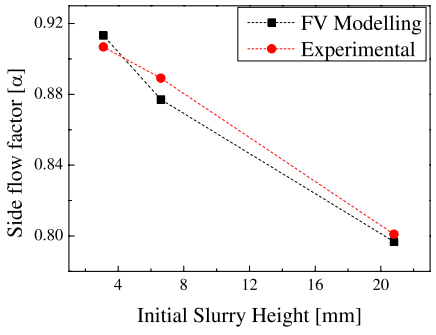


**Fig. 9.** Effect of the initial slurry height on the side flow factor. The lines are guides to the eye.


**Fig. 10.** Increased value of side flow in the beginning of the tape for the highest value of initial slurry height (20.8 mm) for (a) numerical prediction and (b) experimental tape casting.

to the right-hand side of the figure. This region which was the first to be carried out by the peeling belt will remain until the end of the process. This phenomenon is of course due to the high level of the hydrostatic pressure in combination with the free boundary being very close to the doctor blade region in the beginning of the process. As the time passes, the height of the slurry starts to decrease in the reservoir and the level of the pressure decreases (as it can be seen from Fig. 4), which will reduce the flow in the sides.

## VI. Conclusions

The effect of different process parameters (substrate velocity, doctor blade height, and initial slurry height in the reservoir) on the side flow behavior and resultant side flow factor was investigated in the tape casting process. A slightly non-Newtonian ceramic slurry was used for both modeling and experiments. The slurry, LSM, followed the Ostwald-de Waele power law ($\tau = k\dot{\gamma}^n$), in which the constant $k = 3.31$ mPa.s$^n$ and $n = 0.90$ was extracted from rheometer experiments. The material constants were implemented in the commercial CFD code ANSYS FLUENT which is capable of tracking the free surface using the conventional VOF method.

It is found that increasing the substrate velocity will reduce the flow toward the sides ($\phi$), which means that the side flow factor ($\alpha$) will increase. This is because when increasing the substrate velocity the drag forces in the casting direction ($x$-direction) also increase compared with the side direction ($z$-direction), and this gives the slurry less possibility to flow toward the sides. So, by increasing the substrate velocity one can reach a more uniform tape in terms of the thickness.

By increasing the doctor blade height, generally the side flow decreases, increasing the side flow factor. However, at some point due to the increase in the tape thickness after leaving the doctor blade, the side flow will increase, decreasing the side flow factor (see Fig. 8). The competition between these two phenomena is seen in Fig. 7 in which the increase in the side flow factor is reduced for higher values of the doctor blade height. This means that to control the tape uniformity along the casting direction as well as reaching the desired tape thickness (by minimizing the side flow), it is recommended to keep the doctor blade height as high as possible, however, without coming into the regime in Fig. 8, where the side flow factor becomes more or less constant as a function of the doctor blade height.

When the initial height of the slurry in the reservoir increases, the side flow factor decreases as a consequence of increased flow toward the sides coming from the higher hydrostatic pressure. And since the slurry height is decreasing

as the process progresses, this might lead to a tape with an unacceptable difference in green tape thickness between the front part of the tape as compared with the rear part.

The minimum and maximum values for the side flow factor ($\alpha$) predicted by the model are 0.78 and 0.93, respectively. This was in good agreement with the corresponding experimental values of 0.80 and 0.91.

## Acknowledgments

The authors would like to acknowledge the support of the Scientific Research Council on Technology and Production Sciences (FTP) (contract no. 09-072888, OPTIMAC), which is part of the Danish Council for Independent Research (DFF). Our thanks are also directed to Miss R. Bulatova and Dr. Christian R. H. Bahl from the DTU Energy Conversion and Storage for providing us with experimental data.

## References

[1]H. J. Kin, M. J. M. Krane, K. P. Trumble, and K. J. Bowman, "Analytical Fluid Flow Models for Tape Casting," *J. Am. Ceram. Soc.*, **89**, 2769–75 (2006).

[2]C. Pagnoux, T. Chartier, M. de. F. Granja, F. Doreau, J. M. Ferreira, and J. F. Baumard, "Aqueous Suspensions for Tape-Casting Based on Acrylic Binders," *J. Eur. Ceram. Soc.*, **18**, 241–7 (1998).

[3]A. Kristoffersson and E. Carlstrom, "Tape Casting of Alumina in Water With an Acrylic Latex Binder," *J. Eur. Ceram. Soc.*, **17**, 289–97 (1997).

[4]A. Gurauskis, S. -Herencia, and C. Baudin, "$Al_2O_3$/Y-TZP and YTZP Materials Fabricated by Stacking Layers Obtained by Aqueous Tape Casting," *J. Eur. Ceram. Soc.*, **26**, 1489–96 (2006).

[5]M. Jabbari and J. Hattel, "Numerical Modeling of Fluid Flow in the Tape Casting Process"; pp. 143–6 in *AIP Conference Proceedings Series*, Vol. **1389**, Numerical Analysis and Applied Mathematics: ICNAAM, Halkidiki, Greece, 2011.

[6]Y. T. Chou, Y. T. Ko, and M. F. Yan, "Fluid Flow Model for Ceramic tap Casting," *J. Am. Ceram. Soc.*, **70**, 280–2 (1987).

[7]A. I. Y. Tok, F. Y. C. Boey, and Y. C. Lam, "Non-Newtonian Fluid Flow Model for Ceramic Tape Casting," *Mater. Sci. Eng., A*, **280**, 282–8 (2000).

[8]S. C. Joshi, Y. C. Lam, F. Y. C. Boey, and A. I. Y. Tok, "Power law Fluids and Bingham Plastics Flow Models for Ceramic Tape Casting," *J. Mater. Process. Technol.*, **120**, 215–25 (2002).

[9]C. W. Hirt and B. D. Nichols, "Volume of Fluid (VOF) Method for the Dynamics of Free Boundaries," *J. Comput. Phys.*, **39**, 201–25 (1981).

[10]J. U. Brackbill, D. B. Kothe, and C. Zemach, "A Continuum Method for Modeling Surface Tension," *J. Comput. Phys.*, **100**, 335–54 (1992).

[11]G. Zhang, Y. Wang, and J. Ma, "Bingham Plastic Fluid Flow Model for Ceramic Tape Casting," *Mater. Sci. Eng., A*, **337**, 274–80 (2002).

[12]ANSYS Inc., *Fluent 12.0 Theory Guide*. 2009.

[13]S. Armfield and R. Street, "The Fractional-Step Method for the Navier-Stokes Equations on Staggered Grids: The Accuracy of Three Variations," *J. Comput. Phys.*, **153**, 660–5 (1999).

[14]O. Ubbink and R. I. Issa, "Method for Capturing Sharp Fluid Interfaces on Arbitrary Meshes," *J. Comput. Phys.*, **153**, 26–50 (1999). □

# Appdx C

M. Jabbari, J. Hattel, "Bingham-Plastic Fluid Flow Model in Tape Casting of Ceramics Using Two Doctor Blades - An Analytical Approach", *Materials Science & Technology* 30 (2014) 283-288.

# Bingham plastic fluid flow model in tape casting of ceramics using two doctor blades – analytical approach

**M. Jabbari* and J. Hattel**

One of the most common processes used in manufacturing of multilayer ceramic packages, multilayer capacitors and large scale integration circuits is tape casting. In this process, the wet tape thickness is one of the single most determining parameters affecting the final properties of the product, and it is therefore of great interest to be able to control it. One way to control the tape thickness is to use a two doctor blade configuration in the tape casting machine. In this case, it becomes important to fix the height of the slurry in front of both doctor blades according to the desired tape thickness and casting speed (belt velocity). In the present work, the flow in both doctor blade regions of a slurry is described with a steady state momentum equation in combination with a Bingham plastic constitutive equation, and this is integrated to a closed form analytical solution for both reservoirs based on the desired wet tape thickness and casting speed. The developed model is used to investigate the impact of different material parameters and machine designs on the required slurry height. The solution is compared with experimental findings from the literature, and good agreement is found.

**Keywords:** Tape casting, Two doctor blade, Bingham plastic, Fluid flow

## Introduction

Ceramics are growing in production and usage for numerous devices, like e.g. capacitors, piezoelectric actuators, gas sensors, etc., where high quality and low geometry tolerances are required. The parallel (doctor) blade process was first used in preparing ceramic tapes in the 1940s, and it has a key role in producing thin and flat ceramic tapes.[1] Tape casting is a forming method that has mainly been used in the electronics industry to produce multilayer capacitors and electronic substrates.[2] This technique is a well established process that is used to produce ceramic layers and multilayer ceramics. The general schematic of the process is illustrated in Fig. 1*a*. In the tape casting process, the ceramic slurry is mostly categorised as a non-Newtonian fluid with relatively high viscosity. A summary of work published regarding the rheological classification of non-Newtonian fluids and the existence of analytical/numerical models with focus on tape casting has been given before by the authors.[3] In the present study, the Bingham plastic constitutive model is used, where the material has a yield point ($\tau_y$=15 Pa in Fig. 1*b*), below which no flow takes place, whereas above it, the behaviour is linear and characterised by the plastic viscosity $k$

$$\tau = \tau_y + k\left(\frac{du}{dy}\right) \tag{1}$$

Generally, the fluid flow in the doctor blade region and the subsequent outflow can be analysed using Navier–Stokes equations in two dimensions assuming that flow is generated by both the viscous drag due to the peeling velocity of the substrate $v_0$ and the static hydraulic pressure due to the height of the slurry (either $H_1$ or $H_2$) in the reservoir.[3] There are a few research papers in which the flow field and tape thickness were modelled analytically.[4–8] However, all of them modelled the flow of the ceramic slurry for tape casting with one doctor blade only.

It should be emphasised that in the field of materials processing technology, there exists an inherent link between materials structure, processing conditions and final properties of the part. This is also very much the case for the present work. However, since we deal with a multistep processing route of manufacturing (tape casting followed by firing or drying and finally sintering), there exist some inherent constraints on the possibilities of varying the different materials and process parameters in the tape casting process, which will be elaborated in the following.

In general, the parameters influencing tape casting are related to either the material content (i.e. the ceramic powder, solvent, dispersant, binder, plasticiser and deflocculant) or the machine configuration (i.e. the slurry

Department of Mechanical Engineering, Technical University of Denmark, Nils Koppels Allé, Kgs. Lyngby 2800, Denmark

*Corresponding author, email mjab@mek.dtu.dk


Published by Maney on behalf of the Institute
Received 7 May 2013; accepted 24 May 2013
DOI 10.1179/1743284713Y.0000000313

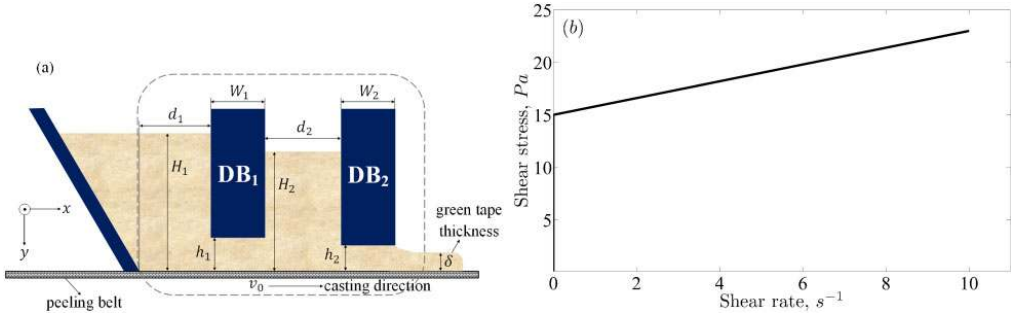


**1** ***a*** **two-dimensional illustration of tape casting process with two doctor blades and** ***b*** **example of Bingham plastic model**

height in the reservoir, the doctor blade height, substrate velocity, the doctor blade width and so forth).[2,8–10] It is moreover also well known that all these aforementioned parameters influence the tape structure and its thickness.[8] Albano and Garrido[9] investigated the influence of the slurry composition on the properties of the tapes based on the changes taking place in the rheological behaviour of the slurry. However, when it comes to the slurry composition, this is to a large extent already predetermined due to constraints from the subsequent sintering process because of the inherent relation between the material content and the final microstructures and properties of the sintered part. This means that most often, the same recipe is used for the material contents in tape casting, leaving this part of the influencing parameters relatively constrained. Thus, when trying to control important resulting parameters like tape thickness, etc. during the tape casting process itself, the main possibilities for that lie in the processing parameters rather than the slurry composition.

In general, the tape thickness is the most important parameter determining the quality of the parts produced by tape casting.[8,10–12] Reaching a constant tape thickness is normally achieved industrially either using a continuous form tape caster in which the reservoir all the time is fed by slurry or by applying two doctor blades in the design of the machine (Fig. 1*a*), which will result in having an almost constant hydrostatic pressure during the casting process. The latter type is investigated in the present work. More specifically, the aim is to model analytically the velocity and the pressure field in both doctor blade regions combined with the Bingham plastic model for the fluid flow. Then, this model is used to predict the height of the slurry in both doctor blades based on the desired tape thickness and the belt velocity. The model is based on an approach similar to the one presented by the authors in Ref. 8, however, for two doctor blades instead of one and a Bingham fluid instead of a power law fluid. Many of the affecting parameters in the process are embedded, and they can easily be varied to evaluate their influence. The proposed models describe the flow characteristics of tape casting well. Results of the model are compared with experiments from the work by Zhang *et al.*,[7] and good agreement is obtained.

## Fluid flow analysis

In order to express the volume flow and thus the tape thickness, the velocity field equation in the doctor blade region must be developed. The pressure gradient inside the channel below the doctor blade is constant, since there is a hydrostatic pressure in front of the doctor blade, and it can be determined by the height of the slurry as shown below

$$\frac{\mathrm{d}p}{\mathrm{d}x} = -A_{0\mathrm{i}} = -\frac{\rho g \Delta H}{W_{\mathrm{i}}} \tag{2}$$

where $\rho$ is the density of the slurry, $g$ is the acceleration due to gravity, $H_{\mathrm{i}}$ is the height of the slurry in front of the doctor blade, $W_{\mathrm{i}}$ is the width of doctor blade and the subscript i corresponds to each doctor blade. The values of $\Delta H_{\mathrm{i}}$ for the first doctor blade $DB_1$ and the second one $DB_2$ are equal to $\Delta H_1 = H_1 - H_2$ and $\Delta H_2 = H_2 - h_2$ respectively. By assuming an infinitely long and wide plate as compared to the thickness and combining with momentum conservation in the $x$ direction under steady state conditions, we obtain the following

$$\frac{\mathrm{d}\tau}{\mathrm{d}y} = \frac{\mathrm{d}p}{\mathrm{d}x} \tag{3}$$

From equations (2) and (3), $\tau$ is found to be

$$\tau = -A_{0\mathrm{i}} y + A_{1\mathrm{i}} \tag{4}$$

where $A_{1\mathrm{i}}$ is an integration constant. Rewriting equations (1) and (4) for a Bingham plastic fluid and integrating along the channel height $h_{\mathrm{i}}$, we obtain

$$\int (-A_{0\mathrm{i}} y + A_{1\mathrm{i}}) \mathrm{d}y = \int \left[ \tau_{\mathrm{y}} + k \left( \frac{\mathrm{d}u}{\mathrm{d}y} \right) \right] \mathrm{d}y \tag{5}$$

### Sufficient belt velocity

When the velocity of the substrate is high enough to overcome the yield point, ($\tau = -A_{0\mathrm{i}} y + A_{1\mathrm{i}} > \tau_{\mathrm{y}}$ in $0 < y < h_{\mathrm{i}}$), the shear rates are always positive ($\mathrm{d}u/\mathrm{d}y > 0$), and the velocity profile below the doctor blade region can be found from equation (5)

$$u(y) = -\frac{A_{0\mathrm{i}}}{2k} y^2 + \frac{A_{1\mathrm{i}} - \tau_{\mathrm{y}}}{k} y + A_{2\mathrm{i}} \tag{6}$$

The integration constants $A_{1\mathrm{i}}$ and $A_{2\mathrm{i}}$ can be found by applying the boundary conditions [$u(y=0)=0$ and $u(y=h_{\mathrm{i}})=v_0$] as below

$$\begin{cases} A_{1\mathrm{i}} = \tau_{\mathrm{y}} + \dfrac{v_0 k}{h_{\mathrm{i}}} + \dfrac{A_{0\mathrm{i}} h_{\mathrm{i}}}{2} \\ A_{2\mathrm{i}} = 0 \end{cases} . \tag{7}$$

The critical belt velocity for flow can easily be found by combining the first equation of equation (7) with equation (4) and setting $v_0=v_{cr}$ as well as $y=h_i$ and $\tau=\tau_y$, which results in

$$v_{cr}=\frac{A_{0i}h_i^2}{2k} \tag{8}$$

The green tape thickness can also be found from the continuity equation as

$$\delta=\frac{1}{v_0}\int_0^{h_i}u(y)\mathrm{d}y=\frac{A_{0i}h_i^3}{12v_0k}+\frac{h_i}{2} \tag{9}$$

Using a similar approach upstream (i.e. for the first doctor blade region), combining equations (2) and (9) and using that $\Delta H_2=H_2-h_2$, the height of the slurry behind the second doctor blade can be determined as follows

$$H_2=\frac{6v_0kW_2}{\rho gh_2^3}(2\delta-h_2)+h_2 \tag{10}$$

Based on the calculated value of $H_2$, and using a similar approach upstream (i.e. for the first doctor blade region) and that $\Delta H_1=H_1-H_2$, the value of the height behind the first doctor blade region can be expressed by

$$H_1=\frac{6v_0kW_1}{\rho gh_1^3}(2\delta-h_1)+H_2 \tag{11}$$

### Insufficient belt velocity

When the velocity of the peeling belt is not sufficient to overcome the yield point, i.e. $v_0\leq v_{cr}$, the doctor blade region will divide into two regions with a critical value of $y$, $y_{cr}$, where below $y_{cr}$ the shear rates are always positive ($\mathrm{d}u/\mathrm{d}y>0$), and above that are equal to zero ($\mathrm{d}u/\mathrm{d}y=0$). Consequently, the velocity profile below the doctor blade region becomes

$$u(y)=\begin{cases}-\dfrac{A_{0i}}{2k}y^2+\dfrac{A'_{1i}-\tau_y}{k}y+A'_{2i} & 0<y\leq y_{cr}\\ v_0 & y_{cr}<y<h_i\end{cases} \tag{12}$$

Applying the boundary conditions in momentum and constitutive equations (equations (3) and (4)), the value of $y_{cr}$ and the integration constants can be determined as follows

$$B.C.:\begin{cases}\tau(y=y_{cr})=\tau_y\\ u(y=0)=0\\ u(y=y_{cr})=v_0\end{cases}\Rightarrow\begin{matrix}A'_{1i}=(2v_0kA_{0i})^{1/2}+\tau_y\\ A'_{2i}=0\\ y_{cr}=\left(\dfrac{2v_0k}{A_{0i}}\right)^{1/2}\end{matrix} \tag{13}$$

In addition, finally, the green tape thickness can be determined by solving the continuity equation as follows

$$\delta=\frac{1}{v_0}\left[\int_0^{y_{cr}}u(y)\mathrm{d}y+\int_{y_{cr}}^{h_i}u(y)\mathrm{d}y\right]=h_i-\frac{1}{3}\left(\frac{2v_0k}{A_{0i}}\right)^{1/2} \tag{14}$$

Assuming that the tape thickness and the belt velocity are known parameters, the value of the height behind the second doctor blade and consequently the first doctor blade can be determined as below

$$\begin{cases}H_2=h_2+\dfrac{w_2}{\rho g}\left\{\dfrac{-18v_0k+\left[(-18v_0k)^2+\dfrac{4(6k\delta v_0)^2}{k_2^2}\right]^{1/2}}{2h_2^2}\right\}\\ H_1=H_2+\dfrac{w_1}{\rho g}\left\{\dfrac{-18v_0k+\left[(-18v_0k)^2+\dfrac{4(6k\delta v_0)^2}{k_1^2}\right]^{1/2}}{2h_1^2}\right\}\end{cases} \tag{15}$$

### Model validation

To test the proposed model, results of modelling were compared with the experimental data from Zhang *et al.*[7] Based on each tape thickness, the values for the height in the second reservoir obtained from the present model in the form of $A_{02}$ ($A_{02}=\rho gH_2/W_2$), compared to that of the data from Zhang *et al.*,[7] and summarised in Table 1. As seen, a very good agreement is found.

## Results and discussion

### Thickness versus velocity

Figure 2 shows the effect of the substrate velocity on the green tape thickness for two different values of the second doctor blade height ($h_2$). As seen from the figure, an increased substrate velocity results in decreasing of the tape thickness. From previous works,[3–5] it was found that when the drag force is increased by increasing the substrate velocity, it becomes more dominant compared to the pressure force, which results in more stretching of the slurry over the peeling belt. Moreover, it is seen that there are two zones in both figures (separated with a dashed line), which correspond to the sufficient and insufficient belt velocity. It was found that the insufficient zone shifts to higher velocities by increasing the height of the doctor blade, which is also seen from equation (8). The other point that can be understood from the figures is that the tape thickness is always higher than the half of the doctor blade height ($\delta>h_i/2$). This can also be seen from equations (10) and (11), in which $\delta\leq h_i/2$ results in zero or negative pressure gradient ($H_i\leq h_i$). Furthermore, based on equation (8),

**Table 1 Comparison of present model with experimental data from Zhang *et al.*[7]**

| | | | | | $A_{02}$/Pa m$^{-1}$ | $A_{02}$/Pa m$^{-1}$ | |
|---|---|---|---|---|---|---|---|
| $\tau_y$/Pa[7] | $k$/Pa s[7] | $h_2$/mm[7] | $v_0$/mm s$^{-1}$,[7] | $\delta$/mm[7] | Zhang et al.[7] | Present model | Relative error/% |
| 18·28 | 8·16 | 1·5 | 2 | 0·653 | 3347·86 | 3493·20 | 4·16 |
| 39·14 | 39·42 | 2 | 2 | 0·744 | 6584·31 | 6710·65 | 1·88 |
| 31·11 | 8·81 | 2·5 | 2 | 1·327 | 3324·81 | 3421·87 | 2·83 |
| 27·27 | 4·08 | 3 | 2 | 1·4873 | 3363·15 | 3452·13 | 2·57 |

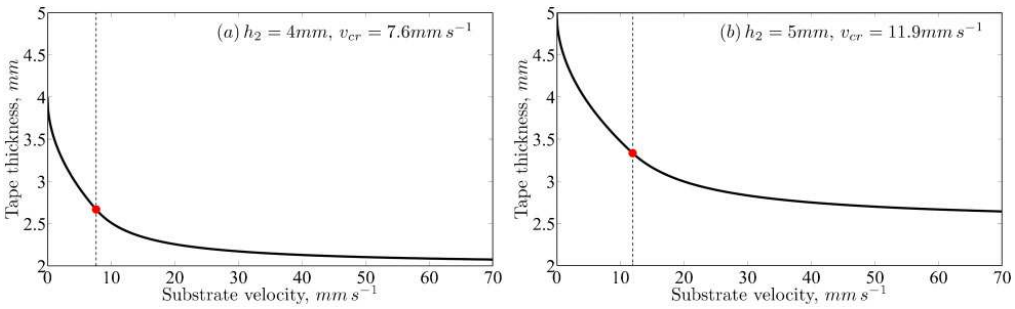


**2 Variation of tape thickness by substrate velocity for *a* $h_2$=4 mm and *b* $h_2$=5 mm**

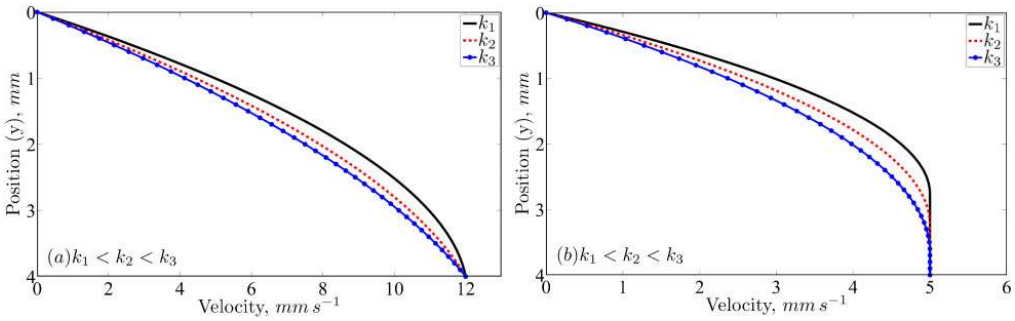


**3 Velocity profiles in doctor blade region for *a* $v_0 > v_{cr}$ and different *k* and *b* $v_0 \leq v_{cr}$ and different *k*; value of critical velocity in these special tests is equal to 10·5**

it can be found that the insufficient region will shift toward the higher velocities when increasing the slurry height, decreasing the doctor blade width and decreasing the plastic viscosity.

## Velocity profiles in doctor blade region

As already discussed, the flow behaviour based on the critical velocity for the belt can be categorised into two groups, i.e. sufficient and insufficient. The velocity profiles for two categories are illustrated in Fig. 3 for $h_2$=4 mm and different $k$ values. It can be seen that, when the velocity in the substrate is smaller than the critical velocity, the flow experiences the needed shear rate in some point above the belt. The aforementioned point in the velocity profile gets closer to the peeling belt by increasing the plastic viscosity $k$. This phenomenon can be better seen in Fig. 4, where a region with zero shear rate can be found with the belt velocities below the critical velocity. Moreover, it can be seen that for the belt velocities above the critical velocity, the shear rate values are always >0.

**Table 2 Geometrical parameters used for modelling represented in Fig. 5**

| Parameter | Value/mm |
|---|---|
| $\delta$ | 2·7 |
| $W_1$ | 6·38 |
| $W_2$ | 6·38 |
| $d_1$ | 9 |
| $d_2$ | 9 |
| $h_1$ | 4·2 |
| $h_2$ | 4 |

## Slurry heights

As already discussed, the main aim of the present study is to find the slurry height behind both the doctor blades when knowing the desired tape thickness and belt velocity. When solving the equations to find the aforementioned heights, one should consider whether the belt velocity is sufficient. Moreover, the momentum and continuity equations should be solved in both doctor blade regions. Figure 5 represents the height of the slurry behind the both doctor blades for the domain presented in the box in the Fig. 1*a* with a dashed line. The geometrical parameters used for the data shown in Fig. 5 are summarised in Table 2. As it seen, for the constant tape thickness, if the belt velocity cannot overcome the yield point (Fig. 5*b*), the slurry height behind both doctor blades should be increased.

The effect of the desired tape thickness on the required slurry height behind both doctor blades is shown in Fig. 6 for both the sufficient and the insufficient condition. As seen, the slurry height behind the first doctor blade is always greater than that of the second doctor blade ($H_1 > H_2$). As previously mentioned, the slurry heights for both doctor blades are higher for the insufficient condition. Moreover, it can be seen that in the case of sufficient belt velocity, the relation between the variation of the tape thickness and required slurry heights are linear.

The effect of changes in the second doctor blade width $W_2$ on the desired tape thickness is illustrated in Fig. 7*a* and *b*. Increased value of the width results in increase in the required value of the slurry height. This can be easily understood from equations (10), (11) and (15), where a

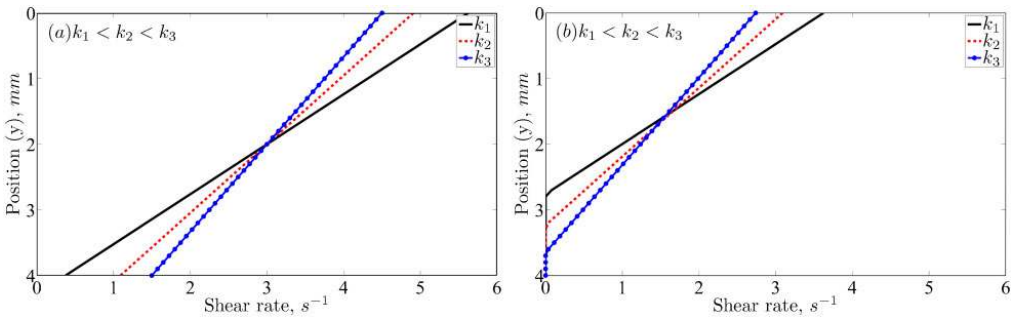


**4 Shear rates below doctor blade region for *a* $v_0 > v_{cr}$ and different *k* and *b* $v_0 \leq v_{cr}$ and different *k*; value of critical velocity in these special tests is equal to 10·5**

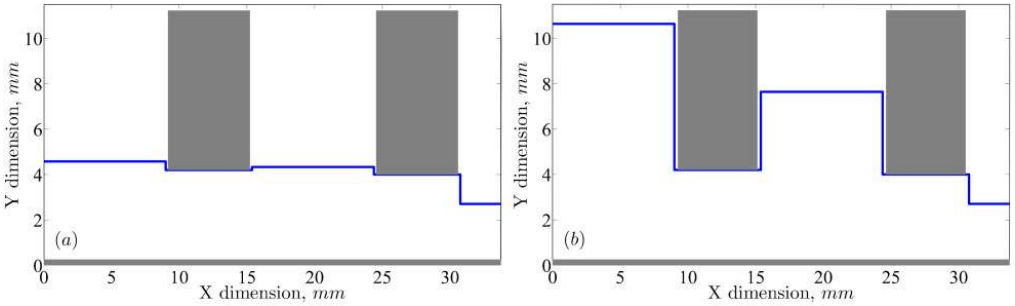


**5 Height of slurry behind both doctor blade with *a* sufficient belt velocity ($v_0$=12 mm $s^{-1}$) and *b* insufficient belt velocity ($v_0$=5 mm $s^{-1}$)**

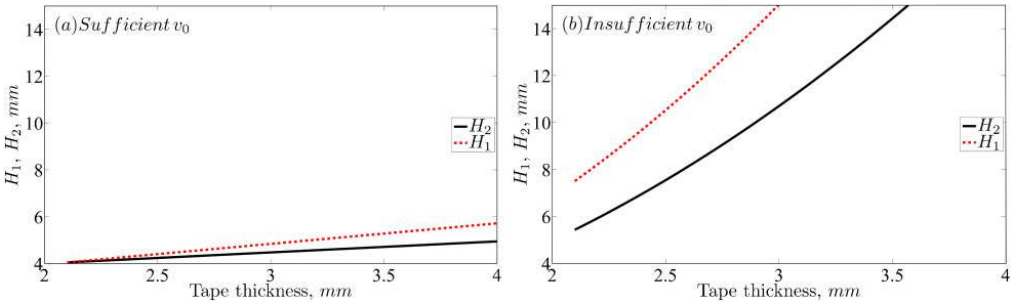


**6 Impact of increasing value of tape thickness on required height of slurry behind both doctor blades with *a* sufficient and *b* insufficient belt velocity**

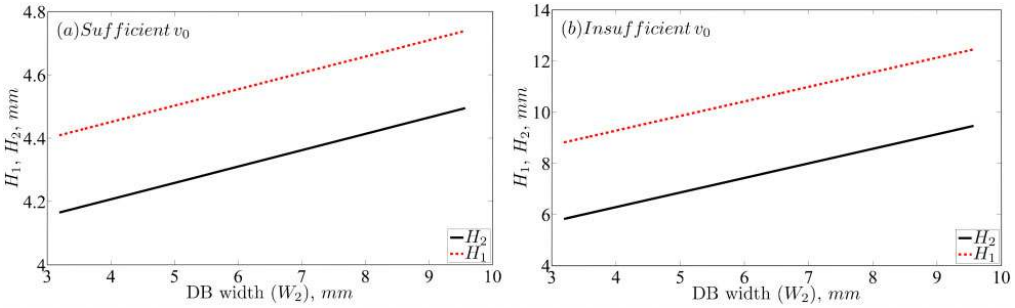


**7 Effect of second doctor blade width on both slurry heights for *a* sufficient and *b* insufficient belt velocity**

higher value of the doctor blade width leads to a higher value of $H_2$ and the resultant $H_1$. By assuming that the value of $d_2+W_2$ is constant, then the variation in the value of $W_2$ resembles the impact of the second reservoir size $d_2$ on the slurry height.

## Conclusions

A steady state model for the Bingham plastic constitutive behaviour of a non-Newtonian slurry was proposed and used to analyse the flow field below the doctor blade region in tape casting using two doctor blades. This proposed model was based on the continuity equation assuming incompressibility such that the decrease in the volume of the slurry in the reservoir is equal to the one that leaves the doctor blade region. The results show that based on the ability of the flow to overcome the yield stress, there are two different zones, i.e. a sufficient one and an insufficient one, in which the predicted values for the slurry height and velocity profiles are totally different. The region with the insufficient belt velocity shifts toward the higher velocities by increasing the value of the critical velocity, i.e. increasing the doctor blade $h_i$, increasing the slurry height behind the doctor blade $H_i$, decreasing the doctor blade width $W_i$ and the plastic viscosity $k$). Moreover, the tape thickness is always smaller than the half of the doctor blade height ($\delta > h_i/2$), no matter what belt velocity is used.

The results show that when the belt velocity is not high enough to overcome the Bingham yield point (insufficient belt velocity), there is always a region with a zero shear rate below the doctor blade, and this region decreases its width by increasing the plastic viscosity $k$. The required slurry height based on the desired tape thickness and the belt velocity predicted by the proposed model and the results show that in the insufficient condition, the slurry height behind the both doctor blades will increase in comparison to the sufficient condition. Moreover, the variations of the aforementioned heights are different in the sufficient and insufficient condition, showing a linear increase for the sufficient condition. On the other hand, increasing the doctor blade width $W_i$ (or decreasing the reservoir size $d_i$) with constant velocity and tape thickness, the required slurry height behind both doctor blades will be increased. The model contains all main parameters that influence the process, and it has the flexibility to be used for different slurries, which they have different constitutive behaviour as well as different machine design.

## Acknowledgement

The authors would like to acknowledge the support of the Scientific Research Council on Technology and Production Sciences (FTP) (contract no. 09-072888, OPTIMAC), which is part of the Danish Council for Independent Research (DFF).

## References

1. H. J. Kim, M. J. M. Krane, K. P. Trumble and K. J. Bowman: *J. Am. Ceram. Soc.*, 2006, **89**, 2769–2775.
2. A. Kristoffersson and E. Carlstrom: *J. Eur. Ceram. Soc.*, 1997, **17**, 289–297.
3. M. Jabbari and J. Hattel: AIP Proc. Int. Conf. on 'Numerical analysis and applied mathematics', American Institute of Physics (AIP), Halkidiki, Greece, September 2011, 143–146.
4. Y. T. Chou, Y. T. Ko and M. F. YAN: *J. Am. Ceram. Soc.*, 1987, **70**, 280–282.
5. R. Pitchumani and V. M. Karbhari: *J. Am. Ceram. Soc.*, 1995, **78**, 2497–2503.
6. A. I. Y. Tok, F. Y. C. Boey and Y. C. Lam: *Mater. Sci. Eng. A*, 2000, **A280**, 282–288.
7. G. Zhang, Y. Wang and J. Ma: *Mater. Sci. Eng. A*, 2002, **A337**, 274–280.
8. M. Jabbari, R. Bulatova, J. H. Hattel and C. R. H. Bahl: *Mater. Sci. Technol.*, **29**, 1080–1087.
9. M. P. Albano and L. B. Garrido: *Ceram. Int.*, 2005, **31**, 57–66.
10. C. Badinia, P. Fino, A. Ortona and C. Amelio: *J. Eur. Ceram. Soc.*, 2002, **22**, 2071–2079.
11. C. A. Folsom, F. W. Zok and F. F. Lang: *J. Am. Ceram. Soc.*, 1994, **77**, 689–696.
12. P. M. Raj and W. R. Cannon: *J. Am. Ceram. Soc.*, 1999, **82**, 2619–2625.

# Appdx D

M. Jabbari, J. Spangenberg, J. Hattel, "Modeling of the Interface Behavior in Tape Casting of Functionally Graded Ceramics for Magnetic Refrigeration Parts", *International Journal of Refrigeration* 36 (2013) 2403-2409.

INTERNATIONAL JOURNAL OF REFRIGERATION 36 (2013) 2403–2409

Available online at www.sciencedirect.com

SciVerse ScienceDirect

journal homepage: www.elsevier.com/locate/ijrefrig

# Modeling of the interface behavior in tape casting of functionally graded ceramics for magnetic refrigeration parts

*Masoud Jabbari**, *Jon Spangenberg*, *Jesper Hattel*

*Department of Mechanical Engineering, Technical University of Denmark, Nils Koppels Allé, 2800 Kgs., Lyngby, Denmark*

ARTICLE INFO

*Article history:*
Received 11 February 2013
Received in revised form
11 May 2013
Accepted 13 May 2013
Available online 30 May 2013

*Keywords:*
Magnetic refrigeration
Functionally graded ceramics
Tape casting
Fluid flow

ABSTRACT

The main goal of this work is to study the multiple material flows in side-by-side (SBS) tape casting and analyze the influence of the different material properties, i.e. the density and the viscosity, on the interface between the fluids, since this is highly important for the efficiency of a graded configuration of the magnetocaloric materials. The Newtonian flow behavior with relatively high viscosity is assumed for each fluid and used in the simulation with a commercial CFD code (ANSYS FLUENT). The results show that the density difference does not affect the interface between the adjacent fluids, whereas the viscosity of the fluids plays the most important role in the behavior of the interface. Moreover, increasing the viscosity difference of the adjacent fluids, $\Delta\mu$, leads to increasing the diffusive region between them. However, this can be counteracted by decreasing the velocity by the substrate.



# Modélisation du comportement de l'interface lors du coulage en bande des céramiques calibrées pour les composants utilisés dans le froid magnétique

*Mots clés* : froid magnétique ; céramiques calibrées sur le plan fonctionnel ; coulage en bande ; écoulement du fluide

## 1. Introduction

The concept of graded materials was first established by Bever and Duwez (1972) for composite materials, and then further developed for polymeric materials (Shen and Bever, 1972). Functionally graded materials (FGMs) are materials that have a gradual variation of material properties from one end to another. The FGMs were originally developed as special materials which could sustain long-term exposure to high temperature and large differences of temperature. Nowadays, FGMs offer great promise in applications where the operating conditions are severe. For example, wear-resistant linings for

* *Corresponding author*. Tel.: +45 45254734; fax: +45 45930190.
E-mail addresses: mjab@mek.dtu.dk, jabbaribehnam@gmail.com (M. Jabbari).
0140-7007/$ – see front matter © 2013 Elsevier Ltd and IIR. All rights reserved.
http://dx.doi.org/10.1016/j.ijrefrig.2013.05.002

**Nomenclature**

| | |
|---|---|
| $a,b$ | separator position in reservoir |
| $f_1 f_2$ | fluid one/two |
| $\vec{F}$ | external forces (kg m s$^{-2}$) |
| $g$ | gravitational acceleration (m s$^{-2}$) |
| $H_0$ | initial height of slurry (m) |
| $l$ | length of doctor blade (m) |
| $L_y$ | length of calculation domain (m) |
| $n$ | number of phases |
| $p$ | pressure (Pa) |
| $v_0$ | substrate velocity (m s$^{-1}$) |
| $\vec{v}_m$ | mass-averaged velocity (m s$^{-1}$) |
| $\vec{v}_{dr,k}$ | drift velocity of secondary phase (m s$^{-1}$) |
| $w$ | width of doctor blade (m) |
| $w_x$ | tape width (m) |
| $W_x$ | width of calculation domain (m) |
| x, y, z | spatial coordinates |

*Greek symbols*

| | |
|---|---|
| $\alpha_1, \alpha_2$ | angle between the interface and the substrate (degree) |
| $\dot{\gamma}$ | strain rate (s$^{-1}$) |
| $\underline{\dot{\gamma}}$ | strain rate tensor |
| $\delta_z$ | tape thickness (m) |
| $\zeta_k$ | volume fraction |
| $\lambda$ | distance from inlet (cm) |
| $\mu_1, \mu_2$ | dynamic viscosity (Pa s) |
| $\mu_m$ | dynamic viscosity of mixture (Pa s) |
| $\rho, \rho_1, \rho_2$ | density (kg m$^{-3}$) |
| $\rho_m$ | density of mixture (kg m$^{-3}$) |
| $\tau$ | viscous stress (Pa) |
| $\underline{\tau}$ | viscous stress tensor |
| $\Phi$ | interface between two fluids |
| $\chi$ | constant ratio |

*Symbols*

| | |
|---|---|
| $\Pi$ | second invariant |

*Superscripts*

| | |
|---|---|
| $\top$ | transpose |

*Subscripts*

| | |
|---|---|
| $dr$ | drift |
| $k$ | phase |
| $m$ | mixture |
| x, z | direction |

handling large heavy abrasive ore particles, rocket heat shields, heat exchanger tubes, thermoelectric generators, heat-engine components, plasma facings for fusion reactors, and electrically insulating metal/ceramic joints. They are also ideal for minimizing thermo-mechanical mismatch in metal-ceramic bonding. There are different techniques to produce FGMs which is well summarized by Kieback et al. (2003). Among them tape casting is reported extensively in literature (Yeo et al., 1998; Acikbas et al., 2006) due to producing large-area, thin, flat ceramics, which can be patterned, stacked, and laminated to form three-dimensional structures (Grader and Zuri, 1993). The method was originally developed for producing electronic ceramics (insulating substrates and packages and multilayer capacitors) and is still mainly used for this.

Magnetic refrigeration is a cooling technology based on the magnetocaloric effect, which can be used to attain extremely low temperatures, as well as the ranges used in room-temperature refrigerators, depending on the design of the system. The magnetocaloric effect (MCE) was originally discovered by Warburg as reported by Pecharsky and Gschneidner (1999). There are several examples in literature in the field of magnetic refrigeration regarding the process (Brück et al., 2003; Okamura et al., 2006), material selection (Engelbrecht et al., 2011; Bahl et al., 2012a) as well as numerical modeling (Nielsen et al., 2009, 2011). However, so far nothing has been reported in literature regarding modeling magnetic refrigeration parts which are produced by tape casting.

Normally the temperature change of the magnetocaloric effect is too small to be utilized without any amplification measures. Therefore application of the magnetocaloric effect for actual cooling (or heating) purposes relies on the creation of a temperature span that is significantly larger than the temperature change itself. This leads to the establishing of active magnetic regeneration (AMR), which combines repeated magnetization and demagnetization of the magnetocaloric material. However, having one temperature at one end of the plate of magnetocaloric material and another temperature at the other end means that only part of the plate is actually at the Curie temperature, i.e. is operating optimally. Having a material with a varying Curie temperature would thus be advantageous (Bahl et al., 2012b). Being an intrinsic property of a material, the Curie temperature cannot be changed without chemical modification. Such a modification often consists of doping small amount of impurities into the material. The other method of changing the Curie temperature is to use multi-material layered AMRs as originally proposed by Rowe and Tura (2006). Moreover, multilayer regenerators produce a

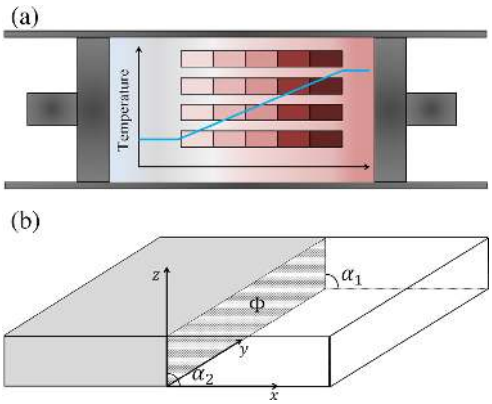


**Fig. 1 – (a) Schematic example of FGCs used in magnetic refrigeration, and (b) Schematic representation of the interface between the two adjacent layers.**

larger temperature span and cooling power as compared to single material regenerators of equivalent mass and geometry (Richard et al., 2004; Arnold et al., 2011; Engelbrecht et al., 2011).

As explained by Reves et al. (2012), in the recently developed technique of side-by-side (SBS) tape casting, multiple slurries are tape casted adjacently forming a single tape to produce functionally graded ceramics (FGCs). Then, these FGCs are used in the magnetic refrigeration process in which there is a temperature gradient along the part (see Fig. 1(a)).

One of the most important parameters which has a significant effect on the final properties of the SBS ceramics, is the behavior of the interface ($\Phi$) between the adjacent layers (see Fig. 1(b)). The aforementioned interface in the FGCs used for magnetic refrigeration are supposed to be close in shape to its ideal form of a 2D in-plane surface (in the $y-z$ plane), which is perpendicular to the substrate plane ($x-y$ plane). In this manner, the graded behavior can be used most efficiently. However, based on the slurry properties (i.e. the density and the viscosity) and the process conditions (i.e. the initial slurry height in the reservoir and the velocity of peeling belt), the interface between the two adjacent layers can vary from its ideal shape to have different shapes as follows:

1. $\alpha_1 = \alpha_2 \neq 90$: $\Phi$ is a planar surface.
2. $\alpha_1 \neq \alpha_2 \neq 90$: $\Phi$ is a twisted, non-planar surface.

In the present work the numerical modeling of the SBS tape casting with two slurry inlets will be presented. The model is implemented and developed in the commercial CFD package ANSYS FLUENT and used to analyze the interface between two adjacent fluids. Based on this, the influence of the material parameters of the two adjacent fluids, i.e. the density and the viscosity, and the important process parameter of substrate velocity on the predicted interface are also investigated.

## 2. Mathematical model

A large number of flows encountered in nature and technology are a mixture of phases. Physical phases of matter are gas, liquid, and solid, but the concept of phase in a multiphase flow system is applied in a broader sense. In multiphase flow, a phase can be defined as an identifiable class of material that has a particular inertial response to and interaction with the flow and the potential field in which it is immersed. Advances in computational fluid mechanics have provided the basis for further insight into the dynamics of multiphase flows. Currently there are two approaches for the numerical calculation of multiphase flows which are available in ANSYS FLUENT (ANSYS Inc., 2009): the Euler-Lagrange approach and Euler–Euler approach. The mixture model which is of the latter type was used in the present study, because it has better accuracy for the slurry flow of ceramics (ANSYS Inc., 2009). Moreover, a second-order time integration scheme is available together with the Mixture (and Eulerian) multiphase models, which is not the case for the conventional VOF Explicit Scheme.

The mixture model is a simplified multiphase model that can be used in different ways. It can be used to model multiphase flows where the phases move at different velocities, but assuming local equilibrium over short spatial length scales. It can be used to model homogenous multiphase flow with very strong coupling and phases moving at the same velocity and lastly, the mixture model are recommended to use for flows with high viscosity and non-Newtonian viscosity (ANSYS Inc., 2009). The mixture model solves the continuity equation, the momentum equation and the energy equation for the mixture, and the volume fraction equation for the secondary phases, as well as algebraic expressions for the relative velocities (if the phases are moving at different velocities).

### 2.1. Continuity equation

The continuity equation for the mixture is

$$\frac{\partial}{\partial t}(\rho_m) + \nabla\cdot(\rho_m \vec{v}_m) = 0 \tag{1}$$

where $\vec{v}_m$ is the mass-averaged velocity

$$\vec{v}_m = \frac{\sum_{k=1}^{n}\zeta_k\rho_k\vec{v}_k}{\rho_m} \tag{2}$$

and $\rho_m$ is the mixture density

$$\rho_m = \sum_{k=1}^{n}\zeta_k\rho_k \tag{3}$$

in which $\zeta_k$ is the volume fraction of phase $k$.

### 2.2. Momentum equation

The momentum equation for the mixture can be obtained by combining the individual momentum equations for all phases leading to

$$\frac{\partial}{\partial t}(\rho_m\vec{v}_m) + \nabla\cdot(\rho_m\vec{v}_m\vec{v}_m) = -\nabla\cdot\left[\mu_m\left(\nabla\vec{v}_m + \nabla\vec{v}_m^{T}\right)\right] + \rho_m\vec{g} + \vec{F} + \nabla\cdot\left(\sum_{k=1}^{n}\zeta_k\rho_k\vec{v}_{dr,k}\vec{v}_{dr,k}\right) \tag{4}$$

where $n$ is the number of phases, $\vec{F}$ is the contribution from external forces, and $\mu_m$ is the viscosity of the mixture given by:

$$\mu_m = \sum_{k=1}^{n}\zeta_k\mu_k \tag{5}$$

and $\vec{v}_{dr,k}$ is the drift velocity for the secondary phase $k$:

$$\vec{v}_{dr,k} = \vec{v}_k - \vec{v}_m \tag{6}$$

which in the case of two fluids will be zero. The drift velocity only becomes active when one of the phases is in particle form.

### 2.3. Constitutive model

We now consider the viscous stress tensor $\underline{\underline{\tau}}$ as well as the strain rate tensor which is given as:

$$\underline{\underline{\dot{\gamma}}} = \nabla\vec{v} + (\nabla\vec{v})^{\top} \tag{7}$$

where $\vec{v}$ is the velocity vector, $\nabla\vec{v}$ is the velocity-gradient tensor and the superscript $\top$ denotes its transpose. The magnitudes of $\underline{\underline{\dot{\gamma}}}$ and $\underline{\underline{\tau}}$, denoted respectively by $\dot{\gamma}$ and $\tau$, are defined by

$$\dot{\gamma} = \sqrt{\frac{1}{2}\prod_{\dot{\gamma}}} = \sqrt{\frac{1}{2}\underline{\underline{\dot{\gamma}}} : \underline{\underline{\dot{\gamma}}}} \quad \text{and} \quad \tau = \sqrt{\frac{1}{2}\prod_{\tau}} = \sqrt{\frac{1}{2}\underline{\underline{\tau}} : \underline{\underline{\tau}}} \tag{8}$$

where $\prod$ stands for the second invariant of a tensor. For the Newtonian behavior of a fluid the constitutive behavior is described by

$$\underline{\underline{\tau}} = \mu\underline{\underline{\dot{\gamma}}} \tag{9}$$

in which $\mu$ is the dynamic viscosity of the fluid. Most of the ceramics and polymeric fluids show some non-Newtonian behavior (Jabbari and Hattel, 2011, 2012). However, in the present study the fluids are assumed to behave as a Newtonian fluid with relatively high viscosity, which is a reasonable assumption for many slurries (Jabbari and Hattel, 2012, 2013; Jabbari et al., 2013).

### 2.4. *Boundary conditions*

A schematic illustration of the SBS tape casting process with the separator plane in the reservoir is shown in Fig. 2(a). The dimensions are chosen relevant to the machine design of the tape caster (Jabbari and Hattel, 2011, 2012; Jabbari et al., 2013). The domain was discretized with a relatively fine mesh ($dx = dy = dz = 1\ \mu m$). In order to get a better accuracy in the region between the two inlets (the notch region) where the two fluids meet, the domain is refined with a finer mesh ($dx = dy = dz = 0.5\mu m$). The analytical equation for calculating the pressure gradient in the doctor blade region is given below (Jabbari and Hattel, 2011; Kim et al., 2006):

$$\frac{dp}{dy} = \frac{\rho g H_0}{wl} \tag{10}$$

where $\rho$ is density, $g$ is body acceleration due to gravity, $H_0$ is the initial height of the slurry in the reservoir, $l$ is the length of the doctor blade region, and $w$ is the width of the doctor blade region. Based on the position of the separator plane in the reservoir (different values of $a$ and $b$, where $a+b = w$), Eq. (10) is hence modified for each of the fluids in the SBS tape casting process. In the present study it is assumed that $a = b$, hence for each fluid the relevant width becomes half of the total width and in the reservoir the pressure gradient in the doctor blade region becomes:

$$\frac{dp}{dy} = \frac{2\rho g H_0}{wl} \tag{11}$$

In order to reduce the computational domain (and hence the computational time), the reservoir region was neglected by creating a user defined function (UDF) code written in C programming language based on Eq. (11) and linked to the CFD code. This UDF was treated as a constant pressure boundary condition in the "Inlet Face" (see Fig. 2(a)), which is applied every time step. A fixed velocity in the $(-y)$-direction ($v_0$) is implemented on the substrate as the velocity of the peeling belt with no slip condition. A zero gradient is assumed for all flow properties in the outlet boundary condition.

Since the width of the produced graded tape ($w_x$) is much bigger than the tape thickness ($\delta_z$), where their ratio ($\chi = w_x/\delta_z$) can vary between $10 < \chi < 1 \times 10^3$, the computational domain in both sides of the separator plane is reduced to reach the ratio of $\chi = 10$ with a symmetry plane on each side. An example of the computational domain is illustrated in Fig. 2(b). As seen, there is a movable cross-sectional plane (MCP) at the distance of $\lambda$ from the inlet, which will be used later on for the investigation of the interface behavior in different distances from the doctor blade exit. All other boundaries in the doctor blade region and the notch between the two inlets are implemented as wall boundaries with no slip condition.

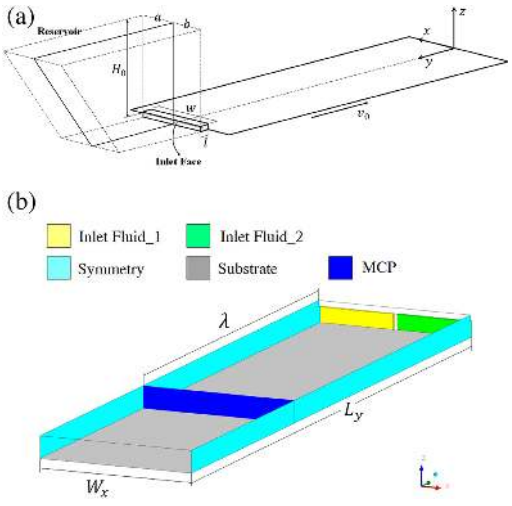


**Fig. 2 – (a) Schematic illustration of computational domain for numerical analysis of SBS tape casting, (b) Reduced computational domain used in the present study.**

## 3. Case studies

To evaluate the impact of different parameters on the behavior of the interface between the two fluids, different cases were investigated, which are summarized in Table 1. The numbers in this table are chosen based on the typical slurries used in the process. Case 1 was simulated to investigate the impact of the width of the domain. In order to find out which material parameter, either the density or the viscosity, is affecting the interface between the adjacent fluids the most, both case 2 and case 3 were defined and evaluated. Case 4 was created to investigate the influence of the viscosity difference ($\Delta\mu$) of the adjacent fluids on the interface between them. And finally, case 5 and case 6 were introduced to evaluate the effect of the substrate velocity (process parameter) on the interface of the adjacent fluids, with the increased (double) value of the substrate velocity as compared to the Base case and case 2, respectively.

## 4. Results and discussion

### 4.1. *Domain size effect*

Before evaluating further about the impact of the material properties and process parameters on the interface behavior, the reliability of the chosen reduced calculation domain

**Table 1 – Summary of the parameters used in different cases.**

| Cases | $L_y$ (m) | $W_x$ (m) | $v_0$ (m s$^{-1}$) | Fluid 1 ($f_1$) | | Fluid 2 ($f_2$) | |
|---|---|---|---|---|---|---|---|
| | | | | $\rho_1$ (kg m$^{-3}$) | $\mu_1$ (Pa.s) | $\rho_2$ (kg m$^{-3}$) | $\mu_2$ (Pa.s) |
| Base | 0.4 | 0.002 | 0.00367 | 2 | 3 | 4 | 6 |
| Case 1 | 0.4 | 0.02 | 0.00367 | 2 | 3 | 4 | 6 |
| Case 2 | 0.4 | 0.002 | 0.00367 | 2 | 3 | 4 | 3 |
| Case 3 | 0.4 | 0.002 | 0.00367 | 2 | 3 | 2 | 6 |
| Case 4 | 0.4 | 0.002 | 0.00367 | 2 | 2 | 2 | 8 |
| Case 5 | 0.4 | 0.002 | 0.00734 | 2 | 3 | 4 | 6 |
| Case 6 | 0.4 | 0.002 | 0.00734 | 2 | 3 | 4 | 3 |

should be checked. This means that the solution should be checked to see whether it is affected by the domain size in terms of the width. To do so, the base case was compared with Case 1. To get a better idea of the interface behavior, a closer look at the first fluid inlet ($x < -10$), the notch between the two flow inlets ($-10 < x < 10$), and the second fluid inlet ($x > 10$) together with the "z" axis position are shown in Fig. 3(a). The results of the simulations at the location of the MCP are illustrated in Fig. 3(b). As seen, the predicted interfaces for the two mentioned cases are the same, providing that the reduction in the width ($W_x$) for the enhanced computational domain is reliable and efficient for the rest of the calculations.

The variation of the predicted interface between the adjacent fluids in the casting direction ($-y$) was investigated by analyzing the interface in the different MCPs (by changing $\lambda$). Since the width of the domain has no influence on the

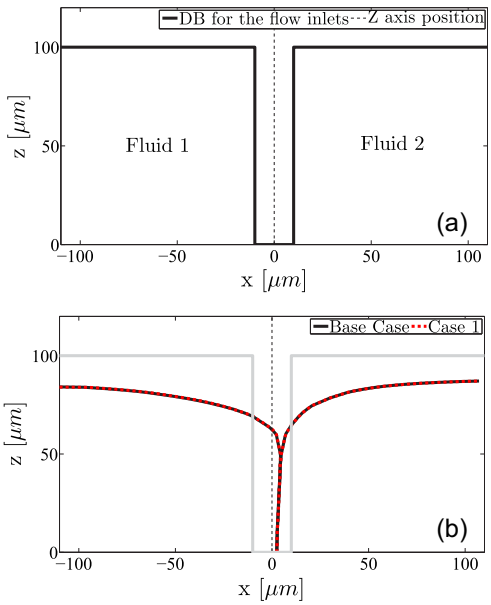


**Fig. 3 – (a) Doctor blade (DB) region in the notch together with the MCP for $\lambda = 0$ ($y = 40$ cm), and (b) Comparison of the predicted interfaces for fluid $f_1$ for the two different cases of different domain width and at the MCP for $\lambda = 20$ cm.**

interface behavior, it was decided to use the Base case for this investigation, with four different values for the MCP, i.e. $\lambda_1 = 0.2$ cm, $\lambda_2 = 2$ cm, $\lambda_3 = 20$ cm and $\lambda_4 = 30$ cm. As seen from the results shown in Fig. 4, the interface behavior in the MCP shortly after the doctor blade exit ($\lambda_1 = 0.2$ cm) is changing along the casting direction. In the beginning, the fluid with the lower viscosity diffuses toward the fluid with higher viscosity, creating a tendency toward the lower viscosity one goes beneath the higher viscosity one. However, in the next MCPs the tendency changes by pushing the higher viscosity one beneath the lower viscosity one. This results in creating a twisted non-planar interface between the adjacent fluids. Moreover, it is seen that after some point, the interface does not change anymore (compare the results for $\lambda_3 = 20$ cm and $\lambda_4 = 30$ cm).

### 4.2. *Impact of the density*

The effect of the densities of the two adjacent fluids on the interface behavior is evaluated by comparing three cases, i.e. the base case, case 2 and case 3. The results of the comparison are shown in Fig.5. It can be seen that for the base case and case 3, where the viscosity for the two fluids in the two cases are not changed (although their values are not the same), the interfaces between the adjacent flows are the same. In both the base case and case 3, the fluid with the lower viscosity diffuses toward the fluid with higher viscosity, creating a tendency towards the higher viscosity one goes beneath the lower viscosity one. Moreover, it is seen that when the viscosities of the two fluids are the same (case 2), the interface between the two fluids does not move and stays in the middle

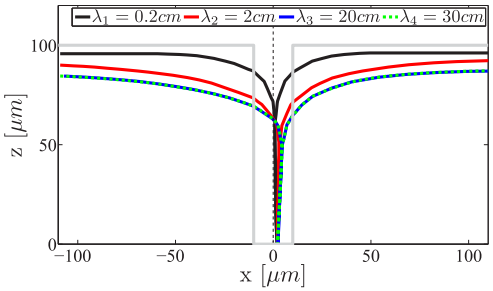


**Fig. 4 – Variation of the predicted interface for different distances from the flow inlets ($\lambda$) for the base case.**

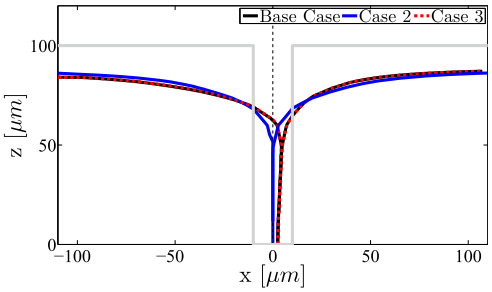


**Fig. 5 – Comparison of the predicted interface between the adjacent fluids for the three different cases (Base case, case 2 and case 3) in the MCP with $\lambda = 20$ cm for evaluation of the density effect.**

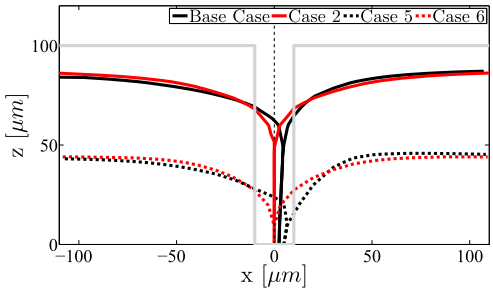


**Fig. 7 – The effect of the change in the substrate velocity on the predicted interface in the MCP with $\lambda = 20$ cm.**

point ($x = 0$). This indicates that the density does not play a role in the behavior of the interface between the two adjacent fluids; and that the viscosity is the affecting parameter.

### 4.3. *Impact of the viscosity*

Knowing that the interface between two fluids is mainly affected by the viscosity of the fluids, one additional analysis was carried out to evaluate the effect of the viscosity difference. This difference ($\Delta\mu$) of the two adjacent fluids was increased from 3*Pa s* (case 3) to 4*Pa s* (case 4). The results of this investigation are illustrated in Fig. 6. As seen, by increasing the viscosity difference the interface between the fluids is moved more toward the fluid with the higher viscosity.

### 4.4. *Effect of the substrate velocity*

The effect of the substrate velocity on the predicted interface between the adjacent fluids is illustrated in Fig. 7, comparing the Base case and case 2 with case 5 and case 6, respectively. The results show that by increasing the substrate velocity, the level of both fluids decreased (case 5 and case 6). This is due to increase of the drag force by increasing the substrate velocity,

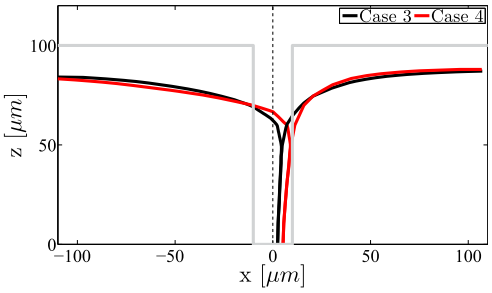


**Fig. 6 – Impact of the viscosity difference ($\Delta\mu$) on the interface between the adjacent fluids in the MCP with $\lambda = 20$ cm. Case 4 has a higher viscosity difference.**

which makes it more dominant compared to the pressure force, and results in more stretching of the slurry over the peeling belt (Jabbari and Hattel, 2011, 2012, 2013). It should be noted that the mas flow is constant during this case, whereas the substrate velocity is doubled, leading to thin but long tapes. Confirming the previous results, it is the viscosity that influences the interface behavior. It can be seen that the only change for case 6, where the viscosities of the adjacent fluids are the same, is the reduction in the height. However, comparing the Base case and case 5, not only the height is decreased, the behavior of the interface is changed. It is seen that by increasing the substrate velocity, the interface between the fluids is moved more toward the fluid with the higher viscosity.

## 5. Conclusions

Numerical modeling of the side-by-side (SBS) tape casting process with two fluid entries was conducted with the finite volume (FV) based commercial CFD package ANSYS FLUENT. The interface between the adjacent flows was modeled using the CFD code together with a UDF (user defined function) for the pressure boundary condition. The effect of the flow in the width direction ($x$) and the casting direction ($-y$) on the interface region was investigated. It is seen that the interface behavior is not affected by the width of the tapes, and this can be used to reduce the simulation domain resulting in less computational efforts. Moreover, as we proceed along the casting direction the angle of the intersection between the interface and the MCP changing creating a twisting and hence a non-planar interface.

The predicted interface was investigated to understand the influence of the material parameters of the two adjacent fluids, i.e. the density and the viscosity, on the position of the interface. It was observed that the densities of the fluids do not influence the interface between the adjacent fluids, whereas the viscosity of the fluids plays a key role in the interface behavior. Specifically, it is seen that the viscosity difference ($\Delta\mu$) causes the fluid with lower viscosity to move toward the one with the higher viscosity. Moreover, increasing the aforementioned difference leads to further movement of the interface toward the fluid with the higher viscosity.

The impact of the substrate velocity was also investigated. As expected, it is found that by increasing the substrate velocity the height of both fluids decreased. Moreover, in the presence of the viscosity difference for the adjacent fluids, by increasing the substrate velocity the interface moved more toward the fluid with the higher viscosity.

Finally, it can be concluded that for the magnetic refrigeration applications with the objective of an ideal (totally perpendicular) interface between the adjacent fluids, the viscosities of the fluids should be kept as close as possible. Moreover, in the presence of a viscosity difference ($\Delta\mu$), to decrease the diffusive region, as low velocities as possible for the substrate should be used.

## Acknowledgment

The authors would like to acknowledge the support of the Scientific Research Councils on Technology and Production Sciences (FTP) (Contract No. 09-072888, OPTIMAC), which is part of the Danish Council for Independent Research (DFF).

## REFERENCES

Acikbas, N.C., Suvaci, E., Mandal, H., 2006. Fabrication of functionally graded SiAlON ceramics by tape casting. J. Am. Ceram. Soc. 89, 3255–3257.

ANSYS Inc, 2009. FLUENT 12.0 Theory Guide.

Arnold, D.S., Tura, A., Rowe, A., 2011. Experimental analysis of a two-material active magnetic regenerator. Int. J. Refrigeration 34, 178–191.

Bahl, C.R.H., Velazquez, D., Nielsen, K.K., Engelbrecht, K., Andersen, K.B., Bulatova, R., Pryds, N., 2012a. High performance magnetocaloric perovskites for magnetic refrigeration. App. Phys. 100, 121905.

Bahl, C.R.H., Bjørk, R., Smith, A., Nielsen, K.K., 2012b. Properties of magnetocaloric materials with a distribution of Curie temperatures. J. Magnet. Magnet. Mater. 324, 564–568.

Bever, M.B., Duwez, P.E., 1972. Gradients in composite materials. Mater. Sci. Eng. 10, 1–8.

Brück, E., Tegus, O., Li, X.W., Boer, F.R., Buschow, K.H.J., 2003. Magnetic refrigeration – towards room-temperature applications. Physica B 327, 431–437.

Engelbrecht, K., Bahl, C.R.H., Nielsen, K.K., 2011. Experimental results for a magnetic refrigerator using three different types of magnetocaloric material regenerators. Int. J. Refrigeration 34, 1132–1140.

Grader, G.S., Zuri, L., 1993. Tape casting slip preparation by in situ polymerization. J. Am. Ceram. Soc. 76, 1809–1814.

Jabbari, M., Bulatova, R., Hattel, J., Bahl, C.R.H., 2013. Quasi-steady state power law model for the flow of $(La_{0.85}Sr_{0.15})_{0.9}MnO_3$ ceramic slurry in tape casting. Mater. Sci. Technol. http://dx.doi.org/10.1179/1743284713Y.0000000255.

Jabbari, M., Hattel, J., 2011. Numerical modeling of fluid flow in the tape casting process. A I P Conf. Proc. 1389, 143–146.

Jabbari, M., Hattel, J., 2012. Numerical modeling of the flow of a power law ceramic slurry in the tape casting process. In: Tenth International Conference on Advances and Trends in Engineering Materials and Their Applications, pp. 151–157. AES-ATEMA INTERNATIONAL CONFERENCE.

Jabbari, M., Hattel, J., 2013. Numerical modeling of the side flow in tape casting of a non-Newtonian fluid. J. Am. Ceram. Soc. 96, 1414–1420.

Kieback, B., Neubrand, A., Riedel, H., 2003. Processing techniques for functionally graded materials. Mater. Sci. Eng. A 362, 81–105.

Kim, H.J., Krane, M.J.M., Trumble, K.P., Bowman, K.J., 2006. Analytical fluid flow models for tape casting. J. Am. Ceram. Soc. 89, 2769–2775.

Nielsen, K.K., Bahl, C.R.H., Smith, A., Bjørk, R., Pryds, N., Hattel, J., 2009. Detailed numerical modeling of a linear parallel-plate active magnetic regenerator. Int. J. Refrigeration 32, 1478–1486.

Nielsen, K.K., Tusek, J., Engelbrecht, K., Schopfer, S., Kitanovski, A., Bahl, C.R.H., Smith, A., Pryds, N., Poredo, A., 2011. Review on numerical modeling of active magnetic regenerators for room temperature applications. Int. J. Refrigeration 34, 603–616.

Okamura, T., Yamada, K., Hiranob, N., Nagaya, S., 2006. Performance of a room – temperature rotary magnetic refrigerator. Int. J. Refrigeration 29, 1327–1331.

Pecharsky, V.K., Gschneidner, K.A., 1999. Magnetocaloric effect and magnetic refrigeration. J. Magnet. Magnet. Mater. 200, 44–56.

Reves, A., Linderoth, S., Pryds, N., Smith, A., 2012. Magnetic regenerator, a method of making a magnetic regenerator, a method of making an active magnetic refrigerator and an active magnetic refrigerator. US Patent, No. 2012/0079834 A1.

Richard, M.A., Rowe, A.M., Chahine, R., 2004. Magnetic refrigeration: single and multimaterial active magnetic regenerator experiments. J. Appl. Phys. 94, 2146.

Rowe, A., Tura, A., 2006. Experimental investigation of a three-material layered active magnetic regenerator. Int. J. Refrigeration 29, 1286–1293.

Shen, M., Bever, M.B., 1972. Gradients in polymeric materials. J. Mater. Sci. 7, 741–746.

Yeo, J., Jung, Y., Choi, S., 1998. Design and microstructure of ZrO2/SUS316 functionally graded materials by tape casting. Mater. Lett. 37, 304–311.

# Appdx E

M. Jabbari, R. Bulatova, J. Hattel, C. R. H. Bahl, "An Evaluation of Interface Capturing Methods in a VOF Based Model for Multiphase Flow of a Non-Newtonian Ceramic in Tape Casting", *Applied Mathematical Modelling* 38 (2014) 3222-3232.

Applied Mathematical Modelling 38 (2014) 3222–3232

Contents lists available at ScienceDirect

Applied Mathematical Modelling

journal homepage: www.elsevier.com/locate/apm

# An evaluation of interface capturing methods in a VOF based model for multiphase flow of a non-Newtonian ceramic in tape casting

M. Jabbari [a,*], R. Bulatova [b], J.H. Hattel [a], C.R.H. Bahl [b]

[a] Department of Mechanical Engineering, Technical University of Denmark, Nils Koppels Allé, 2800 Kgs, Lyngby, Denmark
[b] Department of Energy Conversion and Storage, Technical University of Denmark, Frederiksborgvej 399, Building 779, Roskilde, Denmark

ARTICLE INFO

*Article history:*
Received 21 August 2012
Received in revised form 11 November 2013
Accepted 26 November 2013
Available online 21 December 2013

*Keywords:*
VOF method
Tape casting
Non-Newtonian
Power law

ABSTRACT

The aim of the present study is to evaluate the different interface capturing methods as well as to find the best approach for flow modeling of the ceramic slurry in the tape casting process. The conventional volume of fluid (VOF) method with three different interpolation methods for interface capturing, i.e. the Geometric Reconstruction Scheme (GRS), High Resolution Interface Capturing (HRIC) and Compressive Interface Capturing Scheme for Arbitrary Meshes (CICSAM), are investigated for the advection of the VOF, both for Newtonian and non-Newtonian cases. The main purpose is to find the best method for the free surface capturing during the flow of a ceramic slurry described by a constitutive power law equation in the tape casting process. First the developed model is tested against well-documented and relevant solutions from literature involving free surface tracking and subsequently it is used to investigate the flow of a $La_{0.85}Sr_{0.15}MnO_3$ (LSM) ceramic slurry modeled with the Ostwald de Waele power law. Results of the modeling are compared with corresponding experimental data and good agreement is found.



## 1. Introduction

Tape casting is a forming method that has mainly been used in the electronics industry to produce multi-layer capacitors and electronic substrates [1,2]. This method basically starts with a specially designed slurry which can be cast by a blade to a flat sheet or layer, then dried into a flexible solid tape which can be sintered subsequently into a hard ceramic substrate layer [3]. This technique is a well-established process which is used to produce ceramic layers and multi-layered ceramics (MLC). The parallel (doctor) blade process was first used in preparing ceramic tapes in the 1940s and today it plays a key role in producing thin and flat ceramic tapes [4,5].

Generally, the fluid flow in the doctor blade region and the subsequent outflow can be analyzed using Navier–Stokes equations in two dimensions assuming that flow is generated by both viscous drag due to the peeling velocity of the substrate and the static hydraulic pressure in the slurry reservoir. There are a few research papers in which the flow field and the resulting tape thickness were modeled analytically. Chou et al. [6] modeled the flow in the parallel blade region and due to the low Reynolds number, they neglected the inertia forces by assuming Newtonian-Stokes flow.

* Corresponding author. Tel.: +45 45254734; fax: +45 45930190.
*E-mail address:* mjab@mek.dtu.dk (M. Jabbari).

0307-904X/$ - see front matter © 2013 Elsevier Inc. All rights reserved.
http://dx.doi.org/10.1016/j.apm.2013.11.046

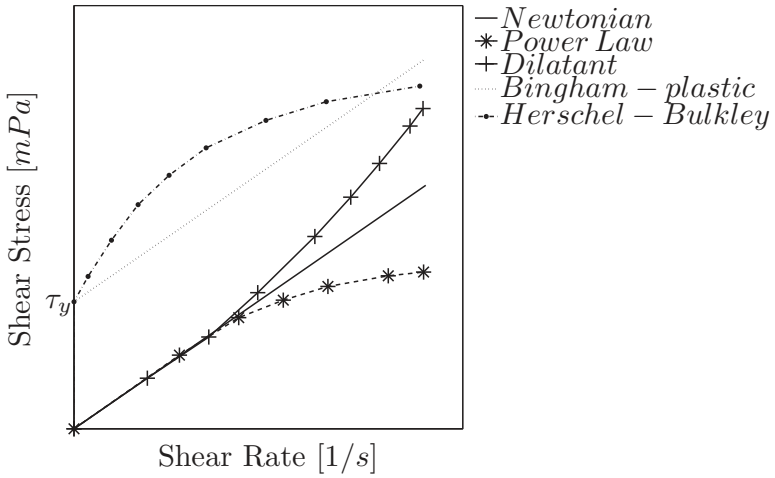


**Fig. 1.** Rheological classification of fluids.

In a general sense, fluids that exhibit characteristics not covered by the Newtonian constitutive equation are non-Newtonian. The exceptions to the Newtonian fluids are not of rare occurrence, and in fact many common fluids are non-Newtonian. Fig. 1 shows the rheological classification of the non-Newtonian fluids.

In the tape casting process, the ceramic slurry is mostly categorized as a non-Newtonian flow with relatively high viscosity. The viscoplastic description was used by Huang et al. [7] to model the flow field in the tape casting process. In their 2D analytical model the effects of pressure gradient, substrate velocity and resultant tape thickness were evaluated. The effect of different rheological behaviors of the tape slurry (Newtonian, power law and Bingham plasticity) for a generalized pressure flow in tape casting was investigated by Joshi and et al. [8]. They estimated the tape thickness analytically and controlled the size of the parallel channel in tape casting accordingly.

The flow of Bingham fluids are evaluated and investigated in different areas of the engineering sciences [9,10]. The ideal Bingham material model is characterized by a shear stress ($\tau$) which is a linear function of shear rate ($\dot{\gamma}$). The yield stress ($\tau_y$ in Fig. 1) is the finite stress which is required for flow initiation (Fig. 1). The main mathematical difficulty when solving ideal Bingham flows is the non-differentiability of the constitutive law at the yield point. The most straightforward and convenient way to circumvent this difficulty is to approximate the material behavior by a bi-viscosity model, in which the material has no true yielding point but flows with a very high viscosity below the yield stress and with the plastic viscosity above it [11]. In most engineering applications, flow of non-Newtonian fluids are characterized by the Bingham, Herschel-Bulkley or Ostwald de Waele power law constitutive models which are shown in Fig. 1 [8,12–16]. A summary of work published regarding the rheological classification of non-Newtonian fluids and the existence of analytical/numerical models with focus on tape casting have been given previously by the authors [17].

Flow processes often involve the presence of free surfaces, the tracking of which has significant impact on the manufacturing and the final quality of the product. Examples abound, e.g., casting processes, mold filling, thin film processes, extrusion, coatings, spray deposition, fluid jetting devices in which material interfaces are inherently present. This phenomenon is also considered in multi-material flows with sharp immiscible interfaces [18]. Several CFD methods have been developed in the last decades with the aim of simulating such complex flows with free surfaces. Two very well-known example of this is the volume of fluid (VOF) and level set methods. In general, there are a lot of different research papers which are dedicated to free surface modeling, different interpolation schemes, liquid/gas phase flow, multi fluid flow, multiphase flow and different numerical methods to simulate the flow field with the presence of an interface [18–26].

A proper discretization of the convective term in the equation for transport of the VOF is crucial for simulation of a multiphase flow. It is well-known that numerical schemes, commonly used for discretization of the convection term, introduce numerical diffusion or numerical dispersion phenomena [27]. For this reason, some additional techniques are needed, i.e. high-resolution schemes. Examples of these can be found in [28–31] with special focus on capturing sharp interfaces.

The aim of this paper is to evaluate the different interface capturing methods and to find the best approach for flow modeling of the ceramic slurry in the tape casting process using the commercial software ANSYS FLUENT. The conventional VOF method will be used with three discretization schemes for the convection of the VOF: Geometric Reconstruction Scheme (GRS), High Resolution Interface Capturing (HRIC) and Compressive Interface Capturing Scheme for Arbitrary Meshes (CICSAM), which all will be discussed in detail. The main purpose is to find the best method for capturing the free surface in the flow of a non-Newtonian ceramic slurry described by the constitutive power law equation in the tape casting process. To do so, two different test cases will be investigated and compared with data in literature. One of the cases is the

flow of water (as a Newtonian fluid) in a box with a small obstacle in its path. In the other case, the flow of a power law ceramic fluid on an inclined plate will be tested. The aim of these cases is to serve as validation for the developed model and to investigate the influence of material behavior, i.e. a Newtonian fluid with $n = 1$ and a highly non-Newtonian fluid with $n = 0.5294$, on the different schemes for interface interpolation. Moreover, these cases are chosen because they are relatively simple modeling-wise in combination with being very well documented in literature [30,32]. After testing the developed model, it will be used to investigate the flow of a $La_{0.85}Sr_{0.15}MnO_3$ (LSM) ceramic slurry with the Ostwald de Waele power law constitutive behavior in tape casting. Results of the modeling will be compared with corresponding experimentally obtained data.

## 2. Governing equations

When dealing with flow problems, the coupled momentum and continuity equations should be solved:

$$\rho\left(\frac{\partial u}{\partial t} + u \cdot \nabla u\right) = -\nabla p + \nabla \cdot T + F \tag{2.1}$$

$$\frac{\partial \rho}{\partial t} + \nabla \cdot (\rho u) = 0 \tag{2.2}$$

where $\rho$ is density, $u$ is velocity, $p$ is pressure, $T$ is stress tensor and $F$ is the contribution from external forces. Here, the momentum Eq. (2.1) expresses Newton's second law of motion, and the continuity Eq. (2.2) ensures conservation of mass. The momentum equation is dependent on the volume fraction of all phases through the properties $\rho$ and $\mu$ (viscosity in the term $T$) via volume-fraction averaging as shown in Eq. (2.4)

The non-Newtonian Ostwald-de Waele constitutive law states that the shearing force (per unit area)) $\tau$ is proportional to the shear rates (the rate of shear strain $\dot{\gamma} = \partial u/\partial y$) as given below:

$$\tau = k\dot{\gamma}^n \tag{2.3}$$

in which $k$ and $n$ are the consistency of the fluid and amount of deviation from a Newtonian fluid, respectively.

The volume of fluid (VOF) model is a surface-tracking technique applied to a fixed Eulerian mesh. It is designed for two or more immiscible fluids where the position of the interface between the fluids is of interest. In the VOF model, a single set of momentum equations is shared by the fluids, and the volume fraction of each of the fluids in each computational cell is tracked throughout the domain [33].

The properties appearing in the transport equation are determined by the presence of the component phases in each control volume. In a two-phase system, for example, if the phases are represented by the subscripts 1 and 2, and if the volume fraction of the second of these is being tracked, the density in each cell is given by

$$\rho = f_2\rho_2 + (1 - f_2)\rho_1 \tag{2.4}$$

The evolution of scalar $f$ (volume fraction) is governed by the simple advection equation:

$$\frac{\partial f}{\partial t} + \frac{\partial u_i f}{\partial x_i} = 0 \tag{2.5}$$

More information on the VOF method can be found in the original work by Hirts and Nichols [33].

When coupled with the Navier–Stokes equations, the volume fraction is treated as an active scalar (it has influence on the velocity field). The main numerical difficulties connected with discretization of the transport equation for the volume fraction are: keeping constant width of the interface, i.e. avoiding artificial diffusion of the step interface profile and assuring a monotonic change of the variables. This last condition is also known as the boundedness criterion [33]. In order to overcome the aforementioned problems different methods were proposed. For instance, in Hirt and Nicholls [33] a Donor–Acceptor Scheme (DAS), based on the availability criterion, was introduced. Problems that arose when using this scheme provoked other proposals that follow the idea of geometric interface reconstruction; examples are SLIC (Simple Line Interface Calculation) method, PLIC (Piecewise Linear Interface Construction) method or more recent methods that use the least-square procedure or splines [23]. Methods that employ these ideas give good approximation of the shape of the interface and they allow for proper calculation of the fluxes through faces of the control volumes. However, their application is often restricted to structured grids with simple shapes of the control volumes. Moreover, since estimation of a spatial orientation of the interface from the distribution of the volume fraction needs a substantial number of numerical operations, interface reconstruction methods increase the computational effort [34].

Unlike geometric interface reconstruction methods, the high-resolution schemes, i.e. Compressive Interface Capturing Scheme for Arbitrary Meshes (CICSAM) [27] and High Resolution Interface Capturing (HRIC) [28], do not introduce geometrical representation of the interface but try to satisfy the aforementioned conditions by properly chosen discretization scheme [34]. The different VOF differencing schemes of volume fraction equation, i.e. geometrical reconstruction, donor–acceptor, CICSAM and HRIC, and their definitions are well summarized by Lopez and Quinta-Ferreira [35].

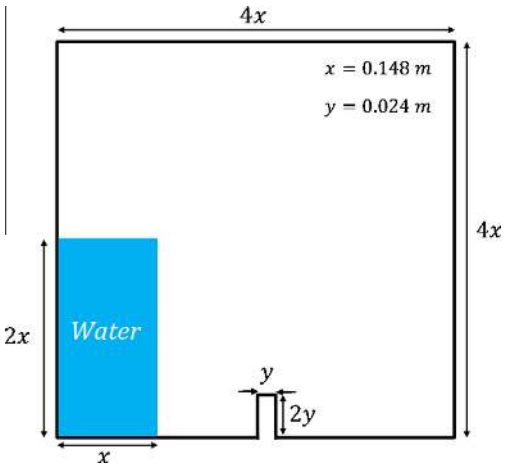


**Fig. 2.** Computational domain used for calculation of the flow for Newtonian (water) fluid.

## 3. Test case1: dam breaking with obstacle

In this case flow of water (Newtonian fluid) inside a box was investigated. The computational domain used for this calculation is illustrated in Fig. 2. The no-slip boundary condition was used for the wall and the thermal effect (energy equation) was neglected. The results of numerical modeling with different interface capturing methods are illustrated in Fig. 3a. It is seen that both the CICSAM and HRIC methods show the same profile, whereas the GRS is substantially different. Moreover, the numerical results of the present study were compared with the numerical and experimental data by Panahi et al. and shown in Fig. 3b and c [30]. It is obvious that the GRS scheme deviates from all other numerically obtained results, but it seems that it does not deviate a lot from the experimental data. Furthermore, the CPU times for the three methods are shown in Fig. 4. It is seen that the computational efforts are almost similar for the three schemes, however with a slightly higher value for the GRS scheme as compared to the others.

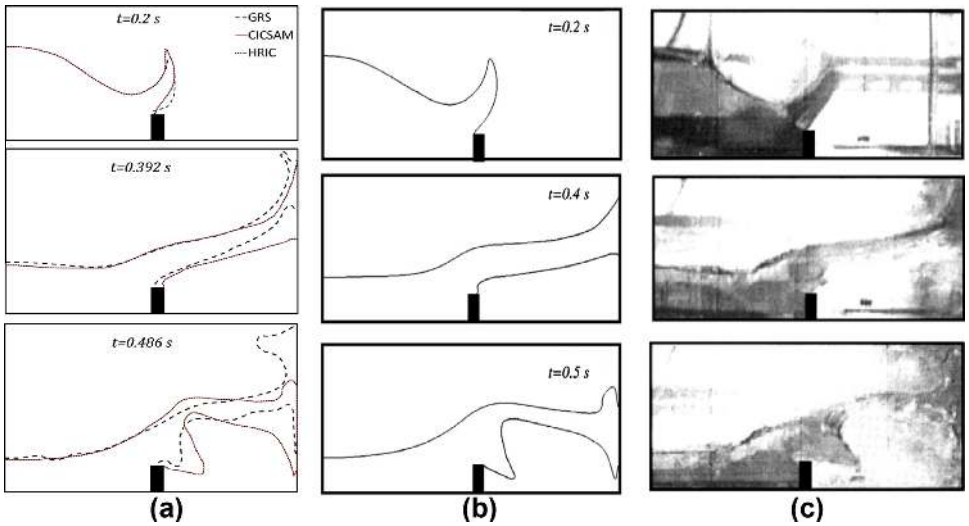


**Fig. 3.** Results and comparison of dam break for; (a) present study for different surface capturing methods, (b) numerical simulation by Panahi et al., and (c) experimental visualization by Koshizuka et al. [30].

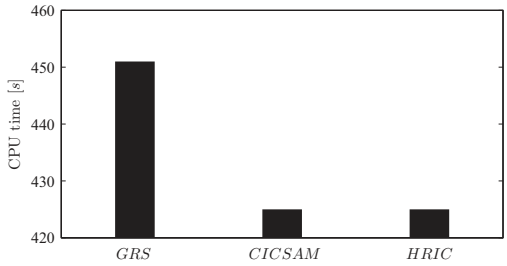


**Fig. 4.** CPU time comparison for different interface capturing method.

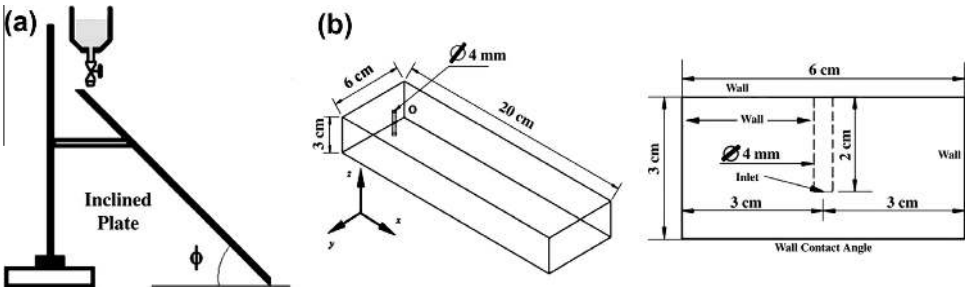


**Fig. 5.** Schematic of (a) experimental and (b) 3D computational domain used in the present case and taken from Haeri et al. [32].

## 4. Test case2: falling film on an inclined plate

The falling film of a non-Newtonian fluid on an inclined plate was investigated in this case. The geometry and the boundary conditions were used from the work by Haeri et al. [32] and are shown in Fig. 5. Full details of the modeling procedure can be found in Haeri et al. The constitutive model used for the material behavior is the power law equation with the constants shown below:

$$\tau = k\dot{\gamma}^n, (k = 11.007, n = 0.5294) \tag{4.1}$$

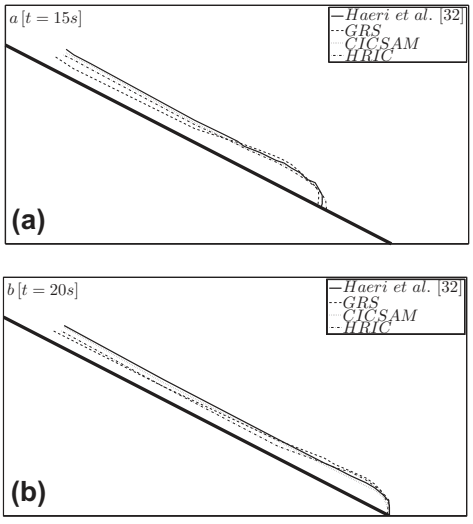


**Fig. 6.** Comparison of different interface capturing methods at different times of (a) $t$ = 15 s and (b) $t$ = 20 s.

The main purpose of this case is to test the model implemented in ANSYS FLUENT for the three different interface capturing methods and validate it for the case of a highly non-Newtonian fluid. The position of the resultant film thickness was extracted from the aforementioned work by Haeri et al. [32] and compared with the model developed in this study, see Fig. 6. The results reveal that the CICSAM method shows the best agreement. However it should be noted that the interpolation method that was used in Haeri et al. [32] was also the CICSAM method. Moreover, it is seen that the GRS again has the highest deviation from the other schemes. Moreover, in comparison to the Newtonian fluid (Test case1), the non-Newtonian fluid showed more instability in the interface. This was concluded from investigating the interface obtained by the HRIC method in more detail. Although the mentioned scheme has the highest accuracy as compared to the other methods, it still showed some oscillations in the interface.

The CPU times for the simulation of the falling film on a plate with different schemes are shown in Fig. 7. As seen, the computational time for the GRS method is again the highest. Moreover, for this special case there is a noticeable difference in the computational time between the CICSAM and the HRIC methods.

From the two test cases it can be concluded that for capturing the free surface, for both Newtonian and non-Newtonian fluids, the CICSAM scheme has less computational time as compared to the other interpolation schemes. More importantly, the CICSAM scheme showed less instability in the interface as well as a good prediction of the free surface for both the Newtonian and the non-Newtonian case.

## 5. Modeling of tape casting

### 5.1. Numerical procedure

A schematic illustration of the computational domain is shown in Fig. 8. The calculation domain is designed in 2D, and the side effect of flow outside the doctor blade region which to some extent affects the tape thickness is neglected. However, the mentioned effect is mimicked using extra parameters which were measured experimentally. The dimensions are chosen according to the machine design of the tape caster which was used in the experiments. The domain is discretized with a relatively fine mesh.

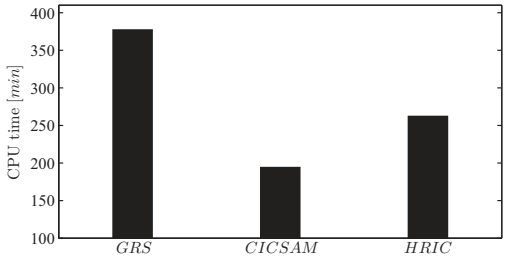


**Fig. 7.** CPU time comparison for different interface capturing methods.

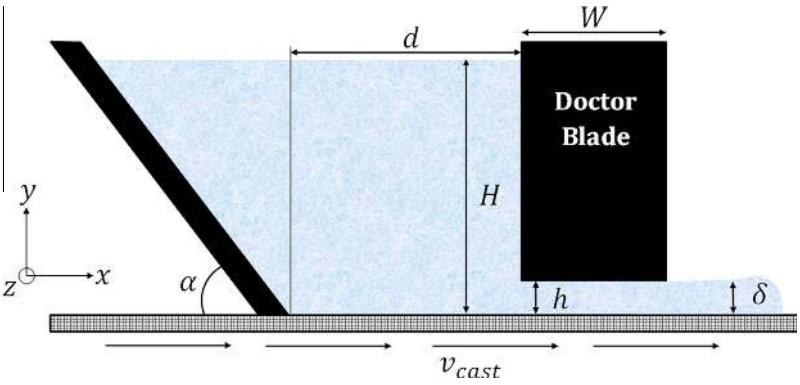


**Fig. 8.** Computational domain for modeling of tape casting.

For the inlet boundary condition the velocity is set to a very small value ($10^{-8}$m/s), just to avoid the initial zero boundary condition. A fixed velocity in the $x$ -direction ($v_0$) is implemented on the substrate expressing the velocity of the peeling belt with no slip condition. A zero gradient is assumed for all flow properties in the outlet boundary condition. All other boundaries are implemented as wall boundaries with no slip condition.

For the transient calculations the non-iterative time-advancement (NITA) scheme is used to reduce the amount of computations. The idea underlying the NITA scheme is that, in order to preserve overall time accuracy, there is no need for reducing the splitting error to zero, but only having to make it the same order as the truncation error. The NITA does not need outer iterations and hence there is only one single "outer iteration" per time-step, which significantly speeds up transient simulations. The NITA is used with the fractional-step method, which offers the possibility of a considerable increase in efficiency [36].

The illustrated domain in Fig. 8 is discretized with a structured mesh. The general cell size is chosen to be 10 μm. However, in order to check the dependency of the solution on the mesh size, two other different mesh sizes were also tested. As shown in Fig. 9, the convergence history of the wall shear stress in the substrate (where the casting velocity is implemented) is evaluated by three different mesh sizes of 10, 5 and 1 μm. The results show that the simulation is reasonably independent of the mesh size where elements smaller than 10 μm are used. For the mesh and the velocity of the substrate used in this paper, the time step size is set in the range of 0.0005–0.002 s.

### 5.2. Experiments

The different materials used as well as their function for the $La_{0.85}Sr_{0.15}MnO_3$ (LSM) slurry are given in Table 1. A commercial LSM was calcined at 1000 °C, and used in the amount of 62.05 wt.% in the final slurry. The average particle size and specific surface area were 12.42 μm and 23.24 $m^2$/g, respectively. Moreover, the weight ratio between LSM:MEKET (solution of methylethylketone and ethanol) and PVB:LSM were 1:2.44 and 1:11.53, respectively. To remove air bubbles from slurries, the mechanical vacuum was enforced for 15 min. The mean particle size and density of the final slurries were accordingly equal to 2.20–2.73 μm and 1.91 g/ml. The particle size and particle size distribution were measured by the Laser Diffraction Particle Size Analyzer LS 13 320 from BECKMAN COULTER (USA). The rheological profiles were measured using a narrow-gap parallel plate sensor system in Rheometer HAAKE Rheo Stress 600 (Haake, Germany).

Experiments were carried out using a one-doctor blade continuous type of casting bench, and the plastic carrier (in the present case Mylar) was driven by a stainless steel roller. The doctor blade gap distance was set by using etalon sticks and a micrometer screw with an accuracy of 0.01 mm. After the propulsion of a torque drum, whose speed was programmed in

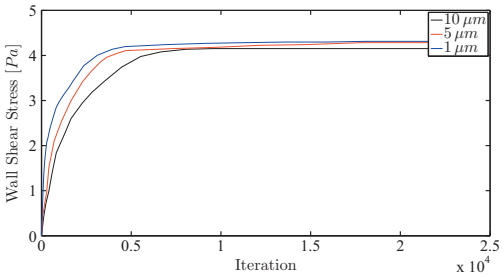


**Fig. 9.** Convergence history of the wall shear stress for numerical sanity of mesh dependency.

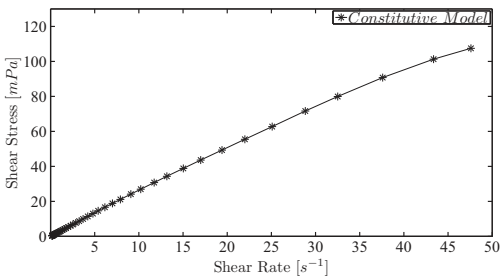


**Fig. 10.** Rheology behavior of LSM ceramic.

**Table 1**
The different materials used and their function for the non-Newtonian LSM slurry.

| Material | Function |
|---|---|
| $La_{0.85}Sr_{0.15}MnO_3$ (LSM) | Ceramic substrate |
| Methyl ethyl ketone | Solvent |
| Ethanol | Solvent |
| Polyvinyl pyrrolidone (PVP) | Dispersant |
| Polyvinyl butyral (PVB) | Binder |
| Polyethylene glycol (PEG) | Plasticizer |
| Dibutyl phthalate (DBP) | Plasticizer |
| Additol | Deflocculant |

**Table 2**
Summary of parameter settings during the two experimental studies.

| Parameter | Case 1 | Case 2 |
|---|---|---|
| $W$ (μm) | 6000 | 6000 |
| $h$ (μm) | 1000 | 400 |
| $v_0$ (mm/s) | 3.67, 10, 14.67 | 3.67 |
| $H_0$ (μm) | 1200 | 3536, 7074, 21222 |
| $d$ (cm) | 8.8 | 8.8 |
| $\alpha$ (deg) | 45 | 45 |

advance, the slurry was peeling out along the carrier movement, forming a thin layer of tape. The cast tapes were dried in air for 5 days, and finally their thicknesses were measured using a micrometer screw.

Experiments were conducted in two different cases, which are summarized in Table 2. For the first set of experiments, the same amount of ceramic slurry (constant $H_0$) were cast with three different substrate velocities. Then in case 2, during constant substrate velocity the material load in the reservoir ($H_0$) was varied. These experiments were carried out to investigate the effect of the two important parameters, i.e. drag forces related to substrate velocity and hydrostatic pressure, on the tape thickness ($\delta$).

## 6. Results and discussion

### 6.1. Material constants

The results of the rheology experiment showed that the LSM slurry follows the Ostwald power law fluid behavior. This is illustrated in Fig. 10 and the relationship between shear rate and shear stress is found to be:

$$\tau = 3.31 \cdot (\partial u/\partial y)^{0.90} \tag{6.1}$$

From Eq. (6.1) the constant $k$ which is the consistency of the fluid is found to be equal to $k = 3.31\ mPa \cdot s^n$. Moreover, the constant $n$ which is the amount of deviation from a Newtonian fluid is equal to 0.90 (indicating close to Newtonian behavior). These parameters are implemented in the numerical calculations for the behavior of the non-Newtonian LSM ceramic.

In the tape casting process, when the flow exits the doctor blade region, the fluid starts to flow in the transverse direction also (here the $z$ direction which was neglected in the numerical model) and this is typically named side-flow. However, since the final tape in general is very wide in the $z$ direction compared to its thickness, this side-flow will be relatively small. Moreover, after the drying stage, the tape thickness is decreased due to weight loss. Considering both these effects, the final thickness of the dried tape can be expressed as [37]:

$$\delta_{tp} = \alpha\beta(\rho/\rho_{tp}) \cdot \delta \tag{6.2}$$

where $\delta_{tp}$ is the thickness of the dried tape, $\alpha$ is the fraction loss for side-flow, $\beta$ is the fraction loss for weight reduction due to drying, $\rho$ is the density of green tape and $\rho_{\mathrm{tp}}$ is the density of dried tape. The constant for the side flow ($\alpha$) was obtained by a volumetric comparison of the tape which flowed outside the casting width to the tape within the casting width leading to $0.8 < \alpha < 0.92$ [37]. The drying weight loss factor ($\beta$) was obtained from drying experiments which measured the dried tape mass and compared it to the wet slurry mass resulting in $0.58 < \beta < 0.65$.

### 6.2. Effect of velocity on thickness

The aim of this case study is to evaluate the effect of velocity changes in the peeling substrate on the tape thickness both experimentally and numerically. The results of the numerical modeling and the experiments are shown in Fig. 11. As seen, an increased substrate velocity results in decreasing of the tape thickness. By further increase of the substrate velocity it is

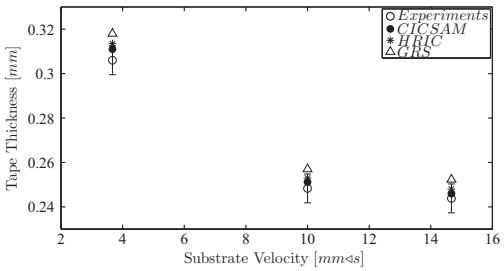


**Fig. 11.** Comparison of the numerical predictions and experiments for the effect of the substrate velocity on the tape thickness (doctor blade height is equal to 1000 μm).

found that the reduction in tape thickness decreases and it seems to become constant. The drag force is increased by increasing the substrate velocity and it becomes more dominant compared to the pressure force which results in more stretching of the slurry over the peeling belt. On the contrary, increasing the substrate velocity for a constant pressure force, the thickness of tape is decreased in the exit and vice versa. Moreover, it can be seen that the CICSAM method has the best prediction as compared to the other schemes. Moreover, a small difference can be detected between the two high resolution schemes, the CICSAM and the HRIC, which is due to the non-Newtonian behavior of the fluid. However, since the deviation from Newtonian behavior for the studied flow is small ($n = 0.90$), the difference between the aforementioned schemes is relatively limited, even when considering the GRS scheme. So, the only key factor that makes the CICSAM method more desirable for the tape casting process is the computational time, which is illustrated in Fig. 12.

### 6.3. Effect of slurry height

The effect of the material load (slurry height) in the reservoir ($H_0$) on the tape thickness is investigated with different interface capturing methods. Results of both numerical simulations and experiments are illustrated in Fig. 13. As the slurry height increases in the reservoir the hydrostatic pressure on the doctor blade region will be increased. Consequently, the tape thickness increases when it is conveyed out of the doctor blade region. The further increase in the numerical result

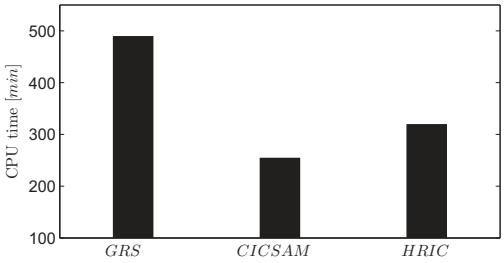


**Fig. 12.** CPU time comparison for different interface capturing method in the tape casting process.

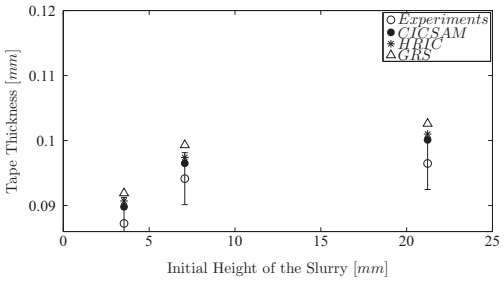


**Fig. 13.** Comparison of the numerical predictions and experiments for the effect of the slurry height on the tape thickness (the doctor blade height is equal to 400 μm).

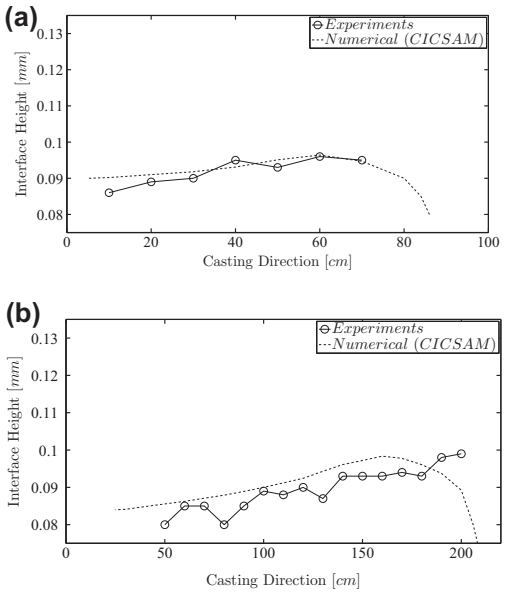


**Fig. 14.** Oscillations in the tape interface in the casting direction with the initial slurry height of (a) 7074 μm and (b) 21222 μm.

for $H_0$ = 21222 μm as compared to the experiment may be caused by the neglecting of the side effect flow which can decrease the final height of the tape especially for higher pressures. Again it is obvious that the CICSAM method has a somewhat better correlation with experimental data in comparison to the other methods. Based on the findings presented in Figs. 11–13, it was decided to use the CICSAM method for the final analysis in which a comparison with experiments was carried out. These experiments did show the non-constant tape height as well as the oscillation detected at the interface which arises from the decreasing slurry height in the reservoir over time. These variations in the tape thickness are recorded along the casting direction both experimentally and numerically (using the CICSAM scheme as mentioned before). Results of the measurements are shown in Fig. 14a and b for the slurry height of 7074 and 21222 μm, respectively.

Two types of information can be observed from Fig. 14. In the early stage of the process, the tape thickness is higher than that of the end due to the decrease in the slurry height in the reservoir over time. Moreover, this difference between the two ends of the strip gets higher as the initial slurry height is increased. On the other hand the more the height in the reservoir, the longer the strip which will be produced in the process.

As earlier mentioned, the increased level of material in the reservoir forces the ceramic to flow in the $z$-direction (and $-z$, side flow, see Fig. 8) which is neglected in the numerical modeling in both sides of the tape. Increasing the slurry height will therefore increase this side flow and decrease the tape thickness. However, increasing the slurry height will also increase the tape thickness due to the increased pressure. These two competing phenomena obviously work against each other, but the latter will be most predominant.

## 7. Conclusions

A multiphase flow model based on the volume of fluid (VOF) method was implemented in ANSYS FLUENT. Three different interpolation schemes, the Geometric Reconstruction Scheme (GRS), High Resolution Interface Capturing (HRIC) and Compressive Interface Capturing Scheme for Arbitrary Meshes (CICSAM), were investigated to find the optimum one for capturing of the free surface. The aforementioned methods were tested both for Newtonian and non-Newtonian fluids with two cases from literature regarding interface position as well as computational time. The results show that the CICSAM method has the best combination of accuracy of predicting the free surface and low cost of computation, especially for the non-Newtonian fluid. Moreover, the results of the validation show that in the fluids with Newtonian behavior, the high resolution interface capturing methods (both the CICSAM and the HRIC) give the same results. However, the higher deviation from a Newtonian fluid, the higher the difference between the two methods.

After testing the implemented model, numerical modeling of the non-Newtonian slurry of $La_{0.85}Sr_{0.15}MnO_3$ (LSM) was conducted by ANSYS FLUENT with the three different interpolation schemes, and the effects of substrate velocity and slurry height in the reservoir on the final tape thickness were evaluated. It was observed that the CICSAM method gave the closest

prediction to the experimental cases. Moreover, the results show that increasing the substrate velocity (casting speed) causes a decrease in the tape thickness due to the dominance of drag force over hydrostatic pressure. On the other hand, an increased value of the slurry height in the reservoir, results in increasing the final tape thickness. This is also the reason for the height of the tape in the end point of the strip being higher as compared to the beginning of the strip. Moreover, by increasing the material load (the initial height of the slurry in the reservoir) the aforementioned differences between the beginning and the end of strip and the length of the strip were increased.

## Acknowledgment

The authors would like to acknowledge the support of the Scientific Research Councils on Technology and Production Sciences (FTP) (Contract No. 09-072888, OPTIMAC), which is part of the Danish Council for Independent Research (DFF).

## References

[1] A. Kristoffersson, Elis Carlstrom, in: Tape casting of alumina in water with an acrylic latex binder, J. Eur. Ceram. Soc. 17 (1997) 289–297.
[2] A.J. Gurauskis, Sanchez-Herencia, C. Baudin, Al2o3/y-tzp and y-tzp materials fabricated by stacking layers obtained by aqueous tape casting, J. Eur. Ceram. Soc. 26 (2006) 1489–1496.
[3] Alfred I.Y. Tok, Freddy Y.C. Boey, K.A. Khor, Tape casting of high dielectric ceramic composite substrates for microelectronics application, J. Mater. Process. Technol. 89 (1999) 508–512. 90.
[4] Hyun Jun Kin, Matthe John M. Krane, Kevin P. Trumble, Keith J. Bowman, Analytical fluid flow models for tape casting, J. Am. Ceram. Soc. 89 (2006) 2769–2775.
[5] C. Pagnoux, T. Chartier, M. de F. Granja, F. Doreau, J.M. Ferreira, J.F. Baumard, Aqueous suspensions for tape-casting based on acrylic binders, J. Eur. Ceram. Soc. 18 (1998) 241–247.
[6] YE T. Chou, YA T. Ko, MAN F. Yan, Fluid flow model for ceramic tap casting, J. Am. Ceram. Soc. 70 (1987) 280–282.
[7] X.Y. Huang, C.Y. Liu, H.Q. Gong, A viscoplastic flow modeling of ceramic tape casting, Mater. Manufac. Proc. 12 (1997) 935–943.
[8] Sunil C. Joshi, Y.C. Lam, F.Y.C. Boey, A.I.Y. Tok, Power law fluids and bingham plastics flow models for ceramic tape casting, J. Mater. Process. Technol. 120 (2002) 215–225.
[9] G.G. Lipscomb, M.M. Denn, Flow of bingham fluids in complex geometries, J. Nonnewtonian Fluid Mech. 14 (1984) 337–346.
[10] Guillaume Vinay, Anthony Wachs, Jean-Francois Agassant, Numerical simulation of weakly compressible bingham flows: the restart of pipeline flows of waxy crude oils, J. Nonnewtonian Fluid Mech. 136 (2006) 93–105.
[11] P.G. Ciarlet, Handbook of Numerical Analysis, 16, Elsevier, 2011.
[12] C.R. Beverly, R.I. Tanner, Numerical analysis of three-dimensional bingham plastic flow, J. Nonnewtonian Fluid Mech. 42 (1992) 85–115.
[13] R.R. Huilgol, Z. You, Application of the augmented lagrangian method to steady pipe flows of bingham, casson and herschel-bulkley fluids, J. Nonnewtonian Fluid Mech. 128 (2005) 126–143.
[14] Alfred I.Y. Tok, Freddy Y.C. Boey, Y.C. Lam, Non-newtonian fluid flow model for ceramic tape casting, Mater. Sci. Eng. A 280 (2000) 282–288.
[15] T.G. Howell, D.R. Jeng, K.J. Dewitt, Momentum and heat transfer on a continuous moving surface in a power law fluid, Int. J. Heat. Mass. Transfer 40 (1996) 1853–1861.
[16] W. Kelly, B. Gigas, Using CFD to predict the behavior of power law fluids near axial-flow impellers operating in the transitional flow regime, Chem. Eng. Sci. 58 (2003) 2141–2152.
[17] M. Jabbari, R. Bulatova, J.H. Hattel, C.R.H. Bahl, Quasi-steady state power law model for flow of (La0.85Sr0.15)0.9MnO3 ceramic slurry in tape casting, Mater. Sci. Eng. 29 (2013) 1080–1087.
[18] Hao Tang, L.C. Wrobel, Z. Fan, Tracking of immiscible interfaces in multiple-material mixing processes, Comput. Mater. Sci. 29 (2004) 103–118.
[19] James M. Hyman, Numerical methods for tracking interfaces, Phys. 12D (1984) 396–407.
[20] A. Huerta, K.L.I.U. Wing, Viscous flow with large free surface motion, Comput. Methods Appl. Mech. Eng. 69 (1988) 277–324.
[21] Denis Gueyffier, Jie Li, Ali Nadim, Ruben Scardovelli, Stephane Zaleski, Volume-of-fluid interface tracking with smoothed surface stress methods for three-dimensional flows, J. Comput. Phys. 152 (1999) 423–456.
[22] J.P. Wang, A.G.L. Bortwick, R. Eatock Taylor, Finite-volume type vof method on dynamically adaptive quadtree grids, Int. J. Num. Methods Fluids 45 (2004) 485–508.
[23] James E. Pilliod Jr, Elbridge G. Puckett, Second-order accurate volume-of-fluid algorithms for tracking materials interfaces, J. Comput. Phys. 199 (2004) 465–502.
[24] E. Aulisa, S. Manservisi, R. Scardovelli, A surface marker algorithm coupled to an area-preserving marker redistribution method for three-dimensional interface tracking, J. Comput. Phys. 197 (2004) 555–584.
[25] R. Tavakoli, R. Babaei, N. Varahram, P. Davami, Numerical simulation of liquid/gas phase flow during mold filling, Comput. Methods Appl. Mech. Eng. 196 (2006) 697–713.
[26] S. Shin, I. Yoon, D. Juric, The local front reconstruction method for direct simulation of two- and three-dimensional multiphase flows, J. Comput. Phys. 230 (2011) 6605–6646.
[27] O. Ubbink, R.I. Issa, A method for capturing sharp fluid interfaces on arbitrary meshes, J. Comput. Phys. 153 (1999) 26–50.
[28] S. Muzaferija, M. Peric, Computation of free-surface flows using the finite-volume method and moving grids, Num. Heat Transfer B 32 (1997) 369–384.
[29] E.D. Dendy, N.T. Padial-Collins, W.B. VanderHeyden, A general purpose finite-volume advection scheme for continuous and discontinuous fields on unstructured grids, J. Comput. Phys. 180 (2002) 559–583.
[30] R. Panahi, E. Jahanbakhsh, M.S. Seif, Development of a vof-fractional step solver for floating body motion simulation, Appl. Ocean Res. 28 (2006) 171–181.
[31] P. Queutey, M. Visonneau, An interface capturing method for free-surface hydrodynamic flows, Comput. Fluid 36 (2007) 1481–1510.
[32] S. Haeri, S.H. Hashemabadi, Three dimensional CFD simulation and experimental study of power law fluid spreading on inclined plates, Int. J. Heat Mass Transfer 35 (2008) 1041–1047.
[33] C.W. Hirt, B.D. Nichols, Volume of fluid (VOF) method for the dynamics of free boundaries, J. Comput. Phys. 39 (1981) 201–225.
[34] T. Waclawczyk, T. Koronowicz, Comparison of CICSAM and HRIC high-resolution schemes for interface capturing, J. Theor. Appl. Mech. 46 (2008) 325–345.
[35] R.J.G. Lopez, R.M. Quinta-Ferreira, Volume-of-Fluid-based model for multiphase flow in high-pressure Trickle-Bed reactor: optimization of numerical parameters, AIChE J. 55 (2009) 2920–2933.
[36] S. Armfield, R. Street, The fractional-step method for the Navier-Stokes equations on staggered grids: the accuracy of three variations, J. Comput. Phys. 153 (1999) 660–665.
[37] M. Jabbari, J.H. Hattel, Numerical modeling of the side flow in tape casting of a non-newtonian fluid, J. Am. Ceram. Soc. 96 (2013) 1414–1420.

# Appdx F

M. Jabbari, J. Spangenberg, J. Hattel, "Particle Migration Using Local Variation of the Viscosity (LVOV) Model in Tape Casting of Ceramics", *Applied Mathematical Modelling*, 2013 (under review).

Elsevier Editorial System(tm) for Applied Mathematical Modelling
Manuscript Draft

Manuscript Number: APM-D-14-00183

Title: Particle Migration Using A Local Variation of the Viscosity (LVOV) Model in Tape Casting of Ceramics

Article Type: Research Paper

Keywords: Particle migration; viscosity; non-Newtonian; tape casting; fluid flow

Corresponding Author: Mr. Masoud Jabbari,

Corresponding Author's Institution: Technical University of Denmark

First Author: Masoud Jabbari

Order of Authors: Masoud Jabbari; Jon Spangenberg; Jesper Hattel

Abstract: In this paper, the migration of secondary particles in a non-Newtonian ceramic slurry in the tape casting process is investigated with the purpose of understanding the particle distribution patterns along the casting direction. The Ostwald-de Waele power law model for the non-Newtonian flow behavior is assumed in the simulation of the ceramic slurry flow. A local variation of the viscosity (LVOV) model as a function of the particle volume fraction is introduced and taken into account in the advection and the settling of the particles in the flow field. The results show that using the LVOV model changes the particle distribution pattern from being a constant distribution to a semi-layered one. The presence of such layered structure is highly affecting the subsequent sintering process, which in turn causes an anisotropic shrinkage behavior of the dried tapes. It is also found that increasing the substrate velocity (casting speed) leads to a more uniform distribution of the particles inside the ceramic slurry, in which case the shear induced particle migration is dominating over the gravity induced one.

# Particle Migration Using A Local Variation of the Viscosity (LVOV) Model in Tape Casting of Ceramics

**M. Jabbari [1,a], J. Spangenberg [b], J. H. Hattel [a]**

*a- Department of Mechanical Engineering, Technical University of Denmark, Nils Koppels Allé, 2800 Kgs. Lyngby, Denmark.*

*b- Department of Civil and Environmental Engineering, Princeton University, Princeton, NJ 08540, USA.*

**Abstract**

In this paper, the migration of secondary particles in a non-Newtonian ceramic slurry in the tape casting process is investigated with the purpose of understanding the particle distribution patterns along the casting direction. The Ostwald-de Waele power law model for the non-Newtonian flow behavior is assumed in the simulation of the ceramic slurry flow. A local variation of the viscosity (LVOV) model as a function of the particle volume fraction is introduced and taken into account in the advection and the settling of the particles in the flow field. The results show that using the LVOV model changes the particle distribution pattern from being a constant distribution to a semi-layered one. The presence of such layered structure is highly affecting the subsequent sintering process, which in turn causes an anisotropic shrinkage behavior of the dried tapes. It is also found that increasing the substrate velocity (casting speed) leads to a more uniform distribution of the particles inside the ceramic slurry, in which case the shear induced particle migration is dominating over the gravity induced one.

Keywords: particle migration, viscosity, non-Newtonian, tape casting, fluid flow

## 1. Introduction

Particle migration in fluids is found in many industrial applications such as transport and refining petroleum, paper manufacturing, environmental waste treatment and ceramic processing. The motion of small particles, drops, and bubbles in a viscous fluid at low Reynolds number is one of the oldest classes of problems in theoretical fluid mechanics [1]. A series of investigations conducted in literature have described the behavior of rigid and deformable particles suspended in very low Reynolds Newtonian liquids undergoing Couette and Poiseuille flow [2,3]. Although some of the work made in this area is based on the flow equations for a non-Newtonian fluid [1,4,5], most of the investigations are based on experimental findings [2,3,6].

1 Corresponding author: Tel.: +45-45254734; fax: +45-45930190; E-mail address: mjab@mek.dtu.dk (Masoud Jabbari).

Being mainly used in the electronics industry as a forming method of ceramics, tape casting is growing in production of numerous multilayer applications and electronic substrates, like e.g. capacitors, piezoelectric actuators, gas sensors, etc., where high quality and low geometry tolerances are required [7,8]. In the tape casting process, the ceramic slurry is mostly categorized as a non-Newtonian fluid with relatively high viscosity [8-11]. A summary of work published regarding the rheological classification of non-Newtonian fluids and the existence of analytical/numerical models with focus on tape casting has been given previously by the authors [8].

The ceramic slurry used in the tape casting process contains different ingredients, i.e. solvent, dispersant, binder, plasticizer and deflocculant, each of them having a specific influence on the final properties of the part [12,13]. The presence of these secondary phases inside the ceramic slurry results in the packing structure, which can be tracked in the final tapes after the sintering process [14,15]. The art of making dense ceramics has been practiced and developed for decades. The ability to produce porous ceramics with specific pore size and porosity is less well documented. Recently, efforts have been directed towards the development of ceramic filter systems in which the microstructure is tailored to the application [16,17]. Moreover, the field of porous ceramics is growing in different areas with different applications like membranes, flue gas purification, piezoelectric materials and solid oxide fuel cell (SOFC) anode substrates [17-20]. The main concern in the aforementioned products is to have a relatively homogenous distribution of position of the pores together with a uniform size distribution. This issue emphasizes the importance of the particle (i.e. binders or pore-formers) migration inside the ceramic slurry during the tape casting process.

The migration of the particles inside the ceramic slurry is the main topic of the present work and this will be addressed with a numerical model in the following. The model is based on a general fluid flow model capable of tracking the interface of the ceramic slurry and implemented in the commercial CFD package ANSYS Fluent, and validated with experimental results for the tape casting process [21]. The flow of the slurry is described as a non-Newtonian fluid with the Ostwald-de Waele power law. In the present work, the model is further developed and subsequently used to analyze the particle distribution patterns. Focus is put on the effect of a variation in the particle distribution on the rheological behavior as well as the settling velocity for the particles and this is analyzed using a new developed model called “local variation of the viscosity” (LVOV) proposed by the authors. The LVOV model is implemented and linked to the program in the CFD code as a user subroutine.

## 2. Particle Migration Induced by the Flow Field

In general, the particles in a non-homogeneous shear flow will migrate from regions of higher shear rate to regions of lower shear rate [22]. The migration takes place at particle Reynolds numbers small enough ($\sim 10^{-4}$) to preclude the importance of inertia effects. Phillips et al. [22] developed the modified version of the model proposed by Leighton and Acrivos [23] of the complex diffusion process associated with shear induced particle migration. They showed that the viscosity $\mu = \mu(\phi)$ of concentrated suspensions at Peclet number of $Pe >> 1$ can be approximated by

$$\frac{\mu}{\mu_c} = \left(1 - \frac{\phi}{\phi_m}\right)^{-1.82} \tag{1}$$

where $\mu/\mu_c$ is the relative viscosity, $\mu_c$ is the solvent viscosity, $\phi$ is the volume fraction of particles, and $\phi_m$ is the volume fraction at which $\mu/\mu_c$ tends to infinity, which was reported [22] to be equal to 0.68 with volume fractions in the range $0.01 < \phi < 0.5$. The change in the viscosity versus the volume fraction based on equation (1) is illustrated in Figure 1a.

In addition to the shear effects the migration of particles inside a fluid is influenced by gravity. This effect in essence results from the competition between the difference in density of the mixture components that forces them to separate and the viscous drag of the flowing suspending fluid that slows down the phenomenon, leading to an advection governed flow. A comprehensive review of the shear induced as well as the gravity induced migration of the particles inside a non-Newtonian fluid has been reported by Spangenberg et al. [24,25]. They showed that for a spherical, solid particle inside a fluid the settling velocity, $V_s$, is equal to $V_s = g\Delta\rho a^2/18\mu_s$, where $a$ is the diameter of the particle, $\Delta\rho$ is the density difference between the particle and the surrounding material, and $\mu_s$ is the viscosity of the suspending material. However, the nature of the fluid used in their research (concrete) and the process dimensions were considerably different from the ones in this research. Moreover, the rheological behavior used by Spangenberg et al. [24,25] is also different from the one considered in the present work, i.e. they used Bingham plasticity whereas the Ostwald-de Waele power law is used here.

Although, the settling velocity ($V_s$) has been taken into account for the migration of the particles, in the work by Spangenberg et al. [24,25] the impact of the particles and the volume fraction was not mentioned in their simulations. Buscall et al. [26] showed that the rate of settling, $V$, for a dilute suspension of particles, which is not grossly aggregated can be expressed by an equation of the form

$$\frac{V}{V_s} = \left(1 - \frac{\phi}{\eta}\right)^{k\eta} \tag{2}$$

in which $\phi$ is the volume fraction of the particles, $\eta$ is the volume fraction when the particles approach the close packing region, and $k$ is a constant. Buscall et al. [26] also showed that for polymeric and ceramic fluids the values for $\eta$ and $k$ would be 0.58 and 5.4, respectively. The variation of the settling rates versus the volume fraction is illustrated in Figure 1b. In the present study both equations (1) and (2) are used in the developed local variation of the viscosity (LVOV) model as a function of the particle volume fraction.

Figure 1: The influence of the particle volume fraction on (a) the viscosity based on equation (1) and (b) the settling rate of the particles based on equation (2).

## 3. Mathematical model

Advances in computational fluid mechanics have provided the basis for further insight into the dynamics of multiphase flows. Thus, today several commercial software packages are able to model this type of flow. Currently there are two approaches for the numerical calculation of multiphase flows which are available in ANSYS FLUENT [27]: the Euler-Lagrange approach and Euler-Euler approach. The mixture model which is of the latter type was used in the present study, because it has better accuracy for the slurry flow of ceramics [27]. Moreover, a second-order time integration scheme is available together with the Mixture (and Eulerian) multiphase models, which is not the case for the conventional VOF Explicit Scheme.

The mixture model is a simplified multiphase model that can be used in different ways. It can be used to model multiphase flows where the phases move at different velocities, but assuming local equilibrium over short spatial length scales. Moreover, it can be used to model homogeneous multiphase flow with very strong coupling and phases moving at the same velocity and lastly, the mixture model is recommended to use for flows with high viscosity and non-Newtonian viscosity [27]. The mixture model solves the continuity equation, the momentum equation and the energy equation for the mixture, and the volume fraction equation for the secondary phases, as well as algebraic expressions for the relative velocities (if the phases are moving at different velocities).

### 3.1 Continuity equation

The continuity equation for the mixture is

$$\frac{\partial}{\partial t}\left(\rho_m\right)+\nabla\cdot\left(\rho_m\vec{v}_m\right)=0 \tag{3}$$

where $\vec{v}_m$ is the mass-averaged velocity

$$\vec{v}_m=\frac{\sum_{k=1}^{n}\zeta_k\rho_k\vec{v}_k}{\rho_m} \tag{4}$$

and $\rho_m$ is the mixture density

$$\rho_m=\sum_{k=1}^{n}\zeta_k\rho_k \tag{5}$$

in which $\zeta_k$ is the volume fraction of phase $k$.

### 3.2 Momentum equation

The momentum equation for the mixture can be obtained by combining the individual momentum equations for all phases leading to

$$\frac{\partial}{\partial t}\left(\rho_m \vec{v}_m\right)+\nabla\cdot\left(\rho_m \vec{v}_m \vec{v}_m\right)=-\nabla p+\nabla\cdot\left[\mu_m\left(\nabla\vec{v}_m+\nabla\vec{v}_m{}^T\right)\right]+\rho_m\vec{g}+\vec{F}+\nabla\cdot\left(\sum_{k=1}^{n}\zeta_k\rho_k\vec{v}_{dr,k}\vec{v}_{dr,k}\right) \quad (6)$$

where $n$ is the number of phases, $\vec{F}$ is the contribution from external forces, and $\mu_m$ is the viscosity of the mixture given by:

$$\mu_m=\sum_{k=1}^{n}\zeta_k\mu_k \quad (7)$$

and $\vec{v}_{dr,k}$ is the drift velocity for the secondary phase $k$:

$$\vec{v}_{dr,k}=\vec{v}_k-\vec{v}_m \quad (8)$$

which in the case of two fluids will be zero. The drift velocity only becomes active when one of the phases is in particle form.

### 3.3 Constitutive model

We now consider the viscous stress tensor $\underline{\underline{\tau}}$ as well as the strain rate tensor $\underline{\underline{\dot{\gamma}}}$. The latter is given as:

$$\underline{\underline{\dot{\gamma}}}=\nabla\vec{v}+\left(\nabla\vec{v}\right)^{\mathrm{T}} \quad (9)$$

where $\vec{v}$ is the velocity vector, $\nabla\vec{v}$ is the velocity-gradient tensor and the superscript $\mathrm{T}$ denotes its transpose. The magnitudes of $\underline{\underline{\dot{\gamma}}}$ and $\underline{\underline{\tau}}$, denoted respectively by $\dot{\gamma}$ and $\tau$, are defined by

$$\dot{\gamma}=\sqrt{\frac{1}{2}\prod\dot{\gamma}}=\sqrt{\frac{1}{2}\underline{\underline{\dot{\gamma}}}:\underline{\underline{\dot{\gamma}}}} \quad \text{and} \quad \tau=\sqrt{\frac{1}{2}\prod\tau}=\sqrt{\frac{1}{2}\underline{\underline{\tau}}:\underline{\underline{\tau}}} \quad (10)$$

where $\prod$ stands for the second invariant of a tensor. For the Newtonian behavior of a fluid the constitutive behavior is described by

$$\tau=\mu\dot{\gamma} \quad (11)$$

in which $\mu$ is the dynamic viscosity of the fluid. Most of the ceramics and polymeric fluids show non-Newtonian behavior with different rheological constitutive models [7-11]. However, the one which is relevant and was used in the current work is the Ostwald-de Waele power law

$$\tau = m\dot{\gamma}^{n} \tag{12}$$

where $m$ and $n$ are the consistency of the fluid and deviation from a Newtonian fluid, respectively and both are constants for a specific slurry. This leads to the standard expression for the effective viscosity

$$\mu = m\dot{\gamma}^{n-1} \tag{13}$$

It should be noted that the effective viscosity is updated using the LVOV model (equation (1)).

**3.4 Advection of the particles**

The model used to simulate the migration of the particles is based on the work made by Spangenberg et al. [24,25] together with further development of updating the settling velocity based on the LVOV model. The particle migration, which is calculated through an advection and settling procedure, is given by

$$\frac{\partial \phi}{\partial t} + \nabla(\phi V) = 0 \tag{14}$$

where $V$ is the settling velocity vector which is updated in the LVOV model with equation (2). It should be noted that having particles of very small size, results in reducing the variation in the settling velocity.

**3.5 Boundary conditions**

A 2D schematic illustration of the tape casting process with the reservoir is shown in Figure 2. The dimensions are chosen relevant to a typical machine design of a tape caster [8-10]. The domain was discretized with a relatively fine mesh ($dx = dy = dz = 0.1\mu m$). In order to reduce the computational domain (and hence the computational time), the reservoir region was neglected by creating a user defined function (UDF) code written in C programming language and linked to the CFD code. This UDF was treated as a time-dependent pressure gradient boundary condition at the "Inlet Boundary" (see Figure 2), as originally proposed by Zhang et al. [28], and applied every time step [10].

$$\frac{dp}{dx} = \frac{\rho g H_0}{W} \tag{15}$$

where $\rho$ is density, $g$ is body acceleration due to gravity, $H_0$ is the initial height of the slurry in the reservoir, and $W$ is the width of the doctor blade region. This expression was later on modified by the authors [8,10] to include varying slurry height as well as two doctor blades [11]. A fixed velocity in the $x$-direction ($v_0$) is implemented on the substrate as the velocity of the peeling belt with no slip condition. A zero gradient is assumed for all flow properties as the outlet boundary condition.

Figure 2: 2D schematic illustration of the tape casting process.

**4. Results and discussion**

When dealing with the flow of a non-Newtonian fluid, the rheological behavior becomes very important. Characterization of the rheology of a specific fluid is mostly done by experimental evaluation under different shear rates. The ceramic slurry considered in this work, is the same as the one previously studied by the authors [8-10], namely $La_{0.85}Sr_{0.15}MnO_3$ (LSM) which is a common fluid used in producing thin substrates for fuel cells applications. Results from rheology experiments [8-10,21] showed that the LSM slurry follows the Ostwald-de Waele power law fluid behavior as shown in Figure 3.

Figure 3: Rheological behavior of the fluid (LSM) used in the current study based on the experiment from [8-10,21].

where the constant $m$ is equal to $3.31\, mPa \cdot s^n$ and the constant $n$ is equal to 0.90, quite close to the Newtonian fluid value of 1. The dimensions for the machine configuration shown in Figure 2 are also taken from previous works conducted by the authors [8-10,21], in which the doctor blade height is equal to $h = 0.4mm$. The density of the ceramic slurry is $\rho_c = 2\, g/ml$ [8-10], and for the particles inside the slurry it is equal to $\rho_p = 10\, g/ml$ ($\kappa = \rho_p/\rho_c = 5$). The particle size ($a$) is assumed to be $0.1\mu m$, and moreover the initial particle load (the volume fraction of the particles in the inlet boundary) inside the slurry is assumed to be 0.35.

The particle distribution inside the ceramic slurry is shown in Figure 4 for two sets of simulations, with and without applying the LVOV model. As seen, the results are totally different from the constant distribution to the spatially varying one. Using the LVOV model, it is seen that there are some parts inside the ceramic in which the concentration of the particles is higher compared to other parts, creating the resulting packing structure [14]. This will now be discussed in the view of the actual velocity distribution and corresponding shear rates for both cases in the doctor blade region. As illustrated in Figure 5(a) and (b), there are two high shear rate zones when using the LVOV model. These zones cause a ceramic slurry flow with higher concentrations of particles. The high shear rate zones below the doctor blade (just before the exit) will drive the particles inside the flow in the horizontal direction ( $x$ ). Moreover, due to relatively high shear rates at the bottom boundary, particles tend to swirl and create some regions with high concentrations (see the right hand side of Figure 4(b)). The high concentration region which was the first to be carried out by the peeling belt will be pushed forward by the flow coming from behind. This means that in the real life process, one should cut off the aforementioned region due to its highly non-uniform distribution of particles. However, even the flow behind shows a somewhat layered structure (left hand side of Figure 4(b)) resulting in a heterogeneous particle distribution. This confirms the existence of a non-uniform distribution (or packing) of the particle in tape casting of ceramics, which was also found experimentally by Chantaramee et al. [14].

Figure 4: Distribution of the volume fraction for the particles inside the ceramic slurry, (a) without applying, and (b) with applying the proposed LVOV model.

Figure 5: (a) The velocity profile, and (b) the shear rate distribution in the doctor blade region.

The velocity of the substrate (the casting speed, $v_0$ ) is now increased in order to evaluate the influence of increasing the shear rates in the LVOV model. Comparing the results from Figure 6 with Figure 4(b) it is immediately noticed that the thickness of the tape is more or less halved, which was also expected. Moreover, it is seen that the region with the concentration of particles still exists (right hand side of Figure 6). As mentioned earlier this region will be moved by the material flowing from behind, and that part of the tape can be cut off at the end of process. However, the pattern of the produced layered structure in the case with the higher velocity (Figure 6) is different from the one with lower velocities tending to have more horizontal layers. Looking at the velocity and the

shear rate distribution below the doctor blade, Figure 7(a) and (b), shows that increasing the substrate velocity will increase the shear rates and also the regions with the high shear rate zones. The presence of these zones will promote the migration of the particles inside the ceramic slurry. Moreover, the higher the shear rates in the slurry, the less the gravity induced particle migration. This leads to less settlement of the particles inside the fluid.

Figure 6: Distribution of the volume fraction for the particles inside the ceramic slurry with an increased (doubled) substrate velocity.

Figure 7: (a) The velocity profile, and (b) the shear rate distribution in the doctor blade region.

As mentioned earlier, the region with the highest concentration of the particles (right hand side of the Figure 4 and 6) is being carried by the flow behind. It is of course interesting to see the particle distribution at the point of time at which steady state conditions are reached. To do so, two sensors are implemented in the flow domain with a reasonable distance (here 10 and 20 $cm$ from the doctor blade exit) to check the variation of the volume fraction with distance. Two different substrate velocities of $v_1 = 3.67\,mm/s$ and $v_2 = 2v_1 = 7.34\,mm/s$ as well as two different density ratios of $\kappa = 0.1$ and $\kappa = 10$ are investigated. It was found that, after some reasonable time in the simulation, the particle distribution inside the ceramic slurry at a certain distance from the doctor blade exit is not changing anymore. The particle volume fraction inside the ceramic slurry in the steady state condition is illustrated in Figure 8(a) and (b). As mentioned earlier, it should be noted that the tape thickness decreases with an increase in the substrate velocity [8-11,21], and therefore the comparison is made by dividing the "Y" position along the tape thickness with the tape thickness itself (corresponding to normalizing with the current tape thickness). Again, it is seen that for the case with the lower shear rates (slower speed), particles tend to settle more in the bottom resulting in a higher concentration. This confirms that, using higher velocities for casting increases the dominance of the shear induced particle migration, creating a relatively uniform distribution of the particles. However, with lower casting speed the particles have enough time to settle in the bottom of the tape forming two different layers containing different particle distributions. Based on this, one can also conclude that changing any of the process parameters, i.e. the doctor blade height or the slurry height in the reservoir, in a way that leads to higher shear rates in the flow domain, can lead to a similar result. As reported in previous work by the authors [8-11,21], decreasing the doctor blade height as well as the slurry height in the reservoir will increase the shear driven flow in the tape casting process.

Seen from Figure 8(a) and (b), it can moreover be concluded that for higher density ratio ( $\kappa = 10$ ) the gravity shows its dominance by making the particles settle at the bottom of the tape. However, for lower values of $\kappa$ the shear induced particle migration becomes dominant hence producing two regions with almost uniform distribution of the particles (one in the top and one at the bottom), whereas in the mid-zone the volume fraction is changing considerably. Comparing Figure 8(a) and (b), one can see that in the region closer to the doctor blade exit ( $d = 10cm$ ) all of the investigated cases are showing more or less the same behavior. This trend stays somewhat the same for the distances further from the doctor blade region ( $d = 20cm$ ), however not for the cases with the high value of the density ratio ( $\kappa = 10$ ). This means that the particles with higher density are moved by the shear forces in the beginning of the process more than the gravity forces. However, gravity forces show their influence mostly in the regions further from doctor blade region.

Figure 8: Distribution of the volume fraction in the thickness of the produced tapes at two different distances of doctor blade exit, (a) $d = 10cm$, and (b) $d = 20cm$, at the point in time when steady state has been reached at $d = 10cm$ and $d = 20cm$.

**5. Conclusions**

We have shown in this paper that applying the developed local variation of the viscosity (LVOV) model presents an improvement in predicting the distribution of particles inside a ceramic slurry while tape casting as compared to not using such a model. The results showed that there is a non-uniform distribution of the particles, and that this is affected by the shear induced migration. These anisotropic structures are very important to investigate and subsequently control since they highly affect the following sintering process of the tapes.

Based on the modelling findings, we have moreover suggested that in order to create a layered structure with a relatively uniform distribution of the particles, the shear induced migration should be increased. This can be done by increasing the substrate velocity (casting speed), or even by decreasing the doctor blade height as well as the slurry height in the reservoir.

**Acknowledgment**

The authors would like to acknowledge the support of the Research Council for Technology and Production Sciences (FTP) (Contract No. 09-072888, OPTIMAC), which is part of the Danish Council for Independent Research (DFF).

**References**

[1] L. G. Leal, Particle motions in a viscous fluid, Ann. Rev. Fluid Mech. 12 (1980) 435-476.

[2] F. Gauthier, H. L. Goldsmith, S. G. Mason, Particle motions in non-Newtonian media I: Couette flow, Rheol. Acta 10 (1971) 344-364.

[3] F. Gauthier, H. L. Goldsmith, S. G. Mason, Particle motions in non-Newtonian media. II. poiseuille flow, J. Rheol. 15 (1971) 297-330.

[4] B. P. Ho, L. G. Leal, Migration of rigid spheres in a two-dimensional unidirectional shear flow of a second-order fluid, J. Fluid Mech. 76 (1976) 783-799.

[5] M. Frank, D. Anderson, E. R. Weeks, J. F. Morris, Particle migration in pressure-driven flow of a Brownian suspension, J. Fluid Mech. 493 (2003) 363-378.

[6] J. R. Abbott, N. Tetlow, A. L. Graham, S. A. Altobelli, E. Fukushima, L. A. Mondy, T. S. Stephens, Experimental observations of particle migration in concentrated suspensions: Couette flow, J. Rheol. 35 (1991) 773-795.

[7] M. Jabbari, J. Hattel, Numerical modeling of fluid flow in the tape casting process, vol. 1389 of AIP Conference Proceedings Series, pp. 143–146, Numerical Analysis and Applied Mathematics: ICNAAM, 2011.

[8] M. Jabbari, R. Bulatova, J. H. Hattel, C. R. H. Bahl, Quasi-steady state power law model for the flow of $(La_{0.85}Sr_{0.15})_{0.9}MnO_3$ ceramic slurry in tape casting, J. Mater. Sci. Technol. 29 (2013) 1080-1088.

[9] M. Jabbari, J. Hattel, Numerical modeling of the flow of a power law ceramic slurry in the tape casting process, Tenth International Conference on Advances and Trends in Engineering Materials and their Applications, pp. 151–157, AES-ATEMA INTERNATIONAL CONFERENCE, 2012.

[10] M. Jabbari, J. Hattel, Numerical modeling of the side flow in tape casting of a non-Newtonian fluid, J. Am. Ceram. Soc. 96 (2013) 1414-1420.

[11] M. Jabbari, J. Hattel, Bingham-plastic fluid flow model in tape casting of ceramics using two doctor blades - an analytical approach, J. Mater. Sci. Technol. (In Print), DOI: 10.1179/1743284713Y.0000000313.

[12] T. Chartier, A. Bruneau, Aqueous tape casting of alumina substrates, J. Eur. Ceram. Soc. 12 (1993) 243-247.

[13] C. Pagnoux, T. Chartier, M. de F. Granja, F. Doreau, J. M. Ferreira, J. F. Baumard, Aqueous suspensions for tape-casting based on acrylic binders, J. Eur. Ceram. Soc. 18 (1998) 241-247.

[14] N. Chantaramee, S. Tanaka, K. Uematsu, Development of packing structure of powder particles in tape casting, J. Ceram. Soc. Jap. 15 (2007) 136-140.

[15] N. Chantaramee, S. Tanaka, T. Takahashi, K. Uematsu, Evolution of discontinuity in particle orientation in ceramic tape casting, J. Am. Ceram. Soc. 91 (2008) 3181-3184.

[16] P. V. Vasconcelos, J. A. Labrincha, J. M. F. Ferreira, Porosity development of diatomite layers processed by tape casting, Ceram. Int. 24 (1998) 447-454.

[17] B. L. Krasnyi, V. P. Tarasovskii, A. Y. Valdberg, T. O. Kaznacheeva, Porous permeable ceramics for filter elements cleaning hot gases from dust, Glass Ceram. 62 (2005) 134-138.

[18] D. Simwonis, H. Thulen, F. J. Dias, A. Naoumidis, D. Stover, Properties of Ni/YSZ porous cermets for SOFC anode substrates prepared by tape casting and coat-mix process, J. Mater. Process. Technol. 92 (1999) 107-111.

[19] C. Galassi, Processing of porous ceramics: Piezoelectric materials, J. Eur. Ceram. Soc. 26 (2006) 2951-2958.

[20] Z. He, K. B. Andersen, L. Keel, F. B. Nygaard, M. Menon, K. K. Hansen, Processing and characterization of porous electrochemical cells for flue gas purification, Ionics 15 (2009) 427-431.

[21] M. Jabbari, R. Bulatova, J. H. Hattel, C. R. H. Bahl, An Evaluation of Interface Capturing Methods in a VOF Based Model for Multiphase Flow of a Non-Newtonian Ceramic in Tape Casting, Appl. Math. Model. (In Press).

[22] R. J. Phillips, R. C. Armstrong, R. A. Brown, A. L. Graham, J. R. Abbott, A constitutive equation for concentrated suspensions that accounts for shear induced particle migration, Phys. Fluids A 4 (1992) 30-40.

[23] D. Leighton, A. Acrivos, The shear-induced migration of particles in concentrated suspensions, J. Fluid Mech. 181 (1987) 415-439.

[24] J. Spangenberg, N. Roussel, J. H. Hattel, H. Stang, J. Skocek, M. R. Geiker, Flow induced particle migration in fresh concrete: Theoretical frame, numerical simulations and experimental results on model fluids, Cem. Concr. Res. 42 (2012) 633-641.

[25] J. Spangenberg, N. Roussel, J. H. Hattel, E. V. Sarmiento, G. Zirgulis, M. R. Geiker, Patterns of gravity induced aggregate migration during casting of fluid concretes, Cem. Concr. Res. 42 (2012) 1571-1578.

[26] R. Buscall, J. W. Goodwin, R. H. Ottewill, The settling of particles through Newtonian and non-Newtonian media, J. Colloid Interface Sci. 85 (1982) 78-86.

[27] ANSYS Inc., FLUENT 12.0 Theory Guide. 2009

[28] G. Zhang, Y. Wang, J. Ma, Bingham plastic fluid flow model for ceramic tape casting, Mater. Sci. & Eng. A 337 (2002) 274-280.

**Figure 1a**

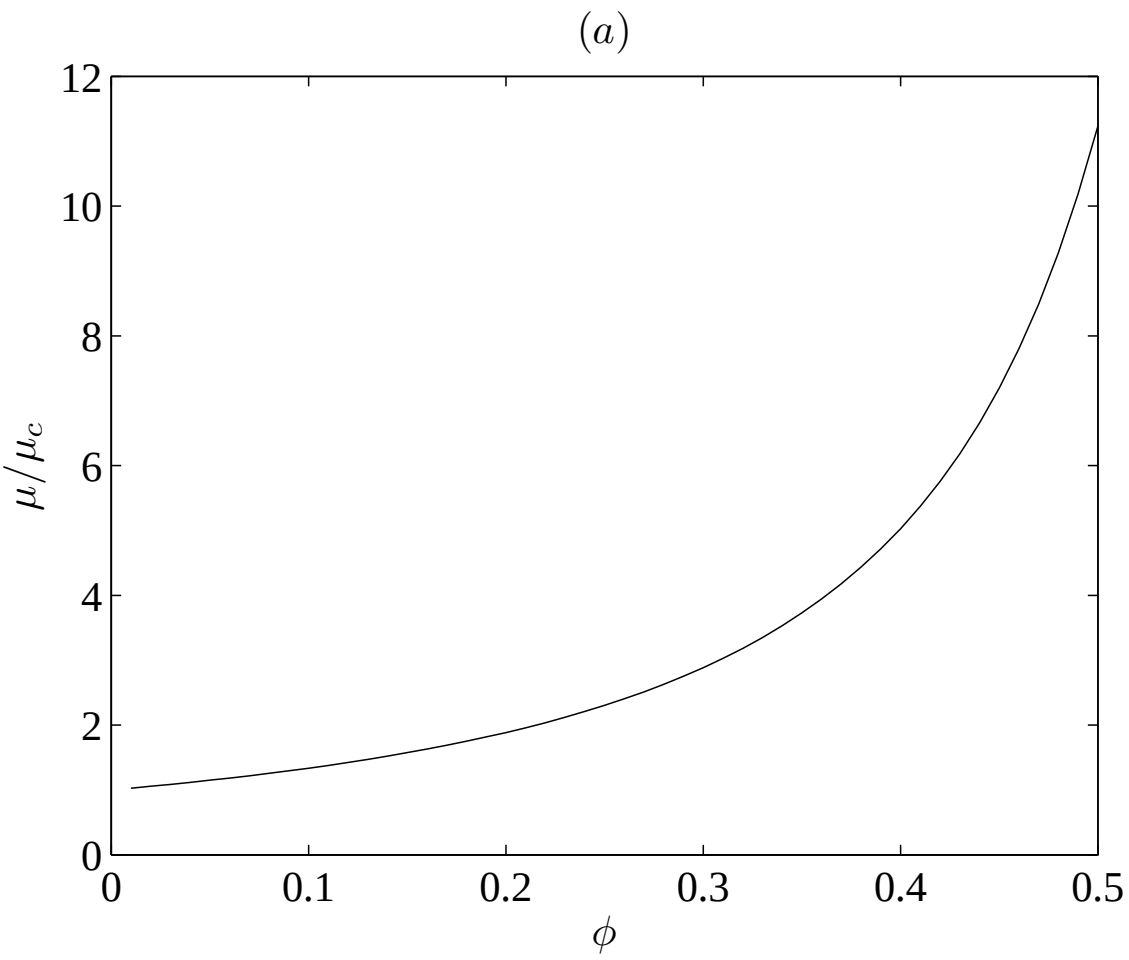

**Figure 1b**

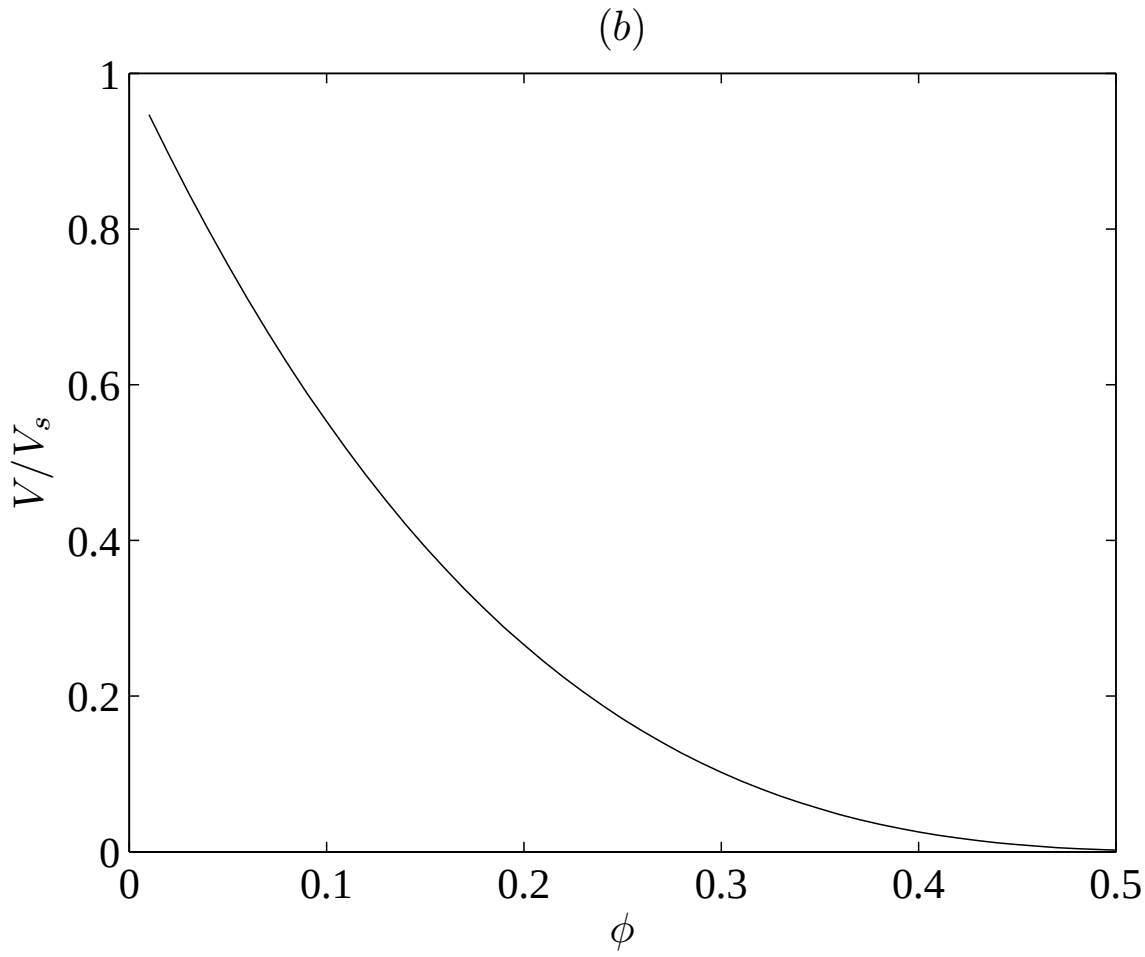

Figure 2
Click here to download high resolution image

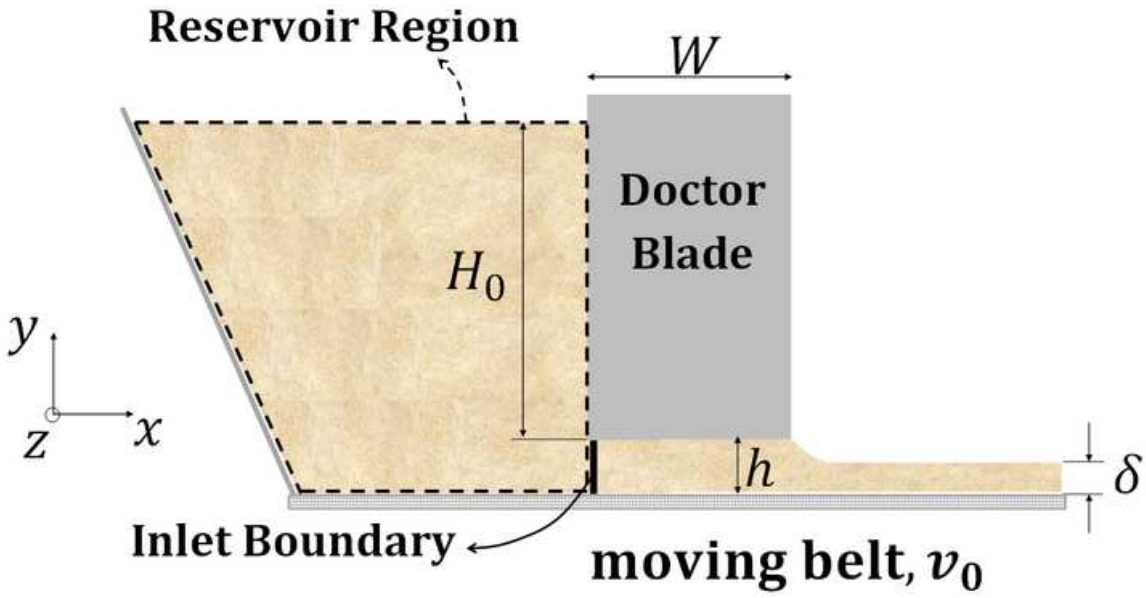

**Figure 3**

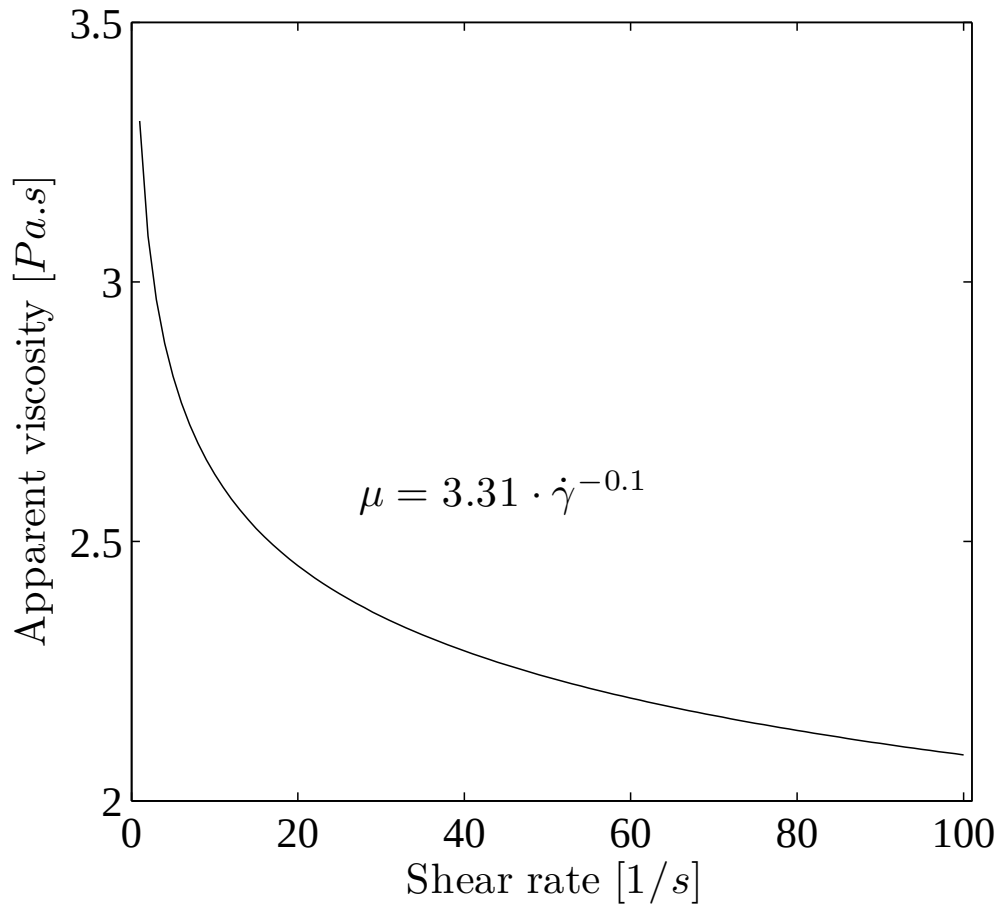
3.5
3
2.5
2
0
20
40
60
80
100
Apparent viscosity $[Pa.s]$
Shear rate $[1/s]$
$\mu = 3.31 \cdot \dot{\gamma}^{-0.1}$

**Figure 4a**

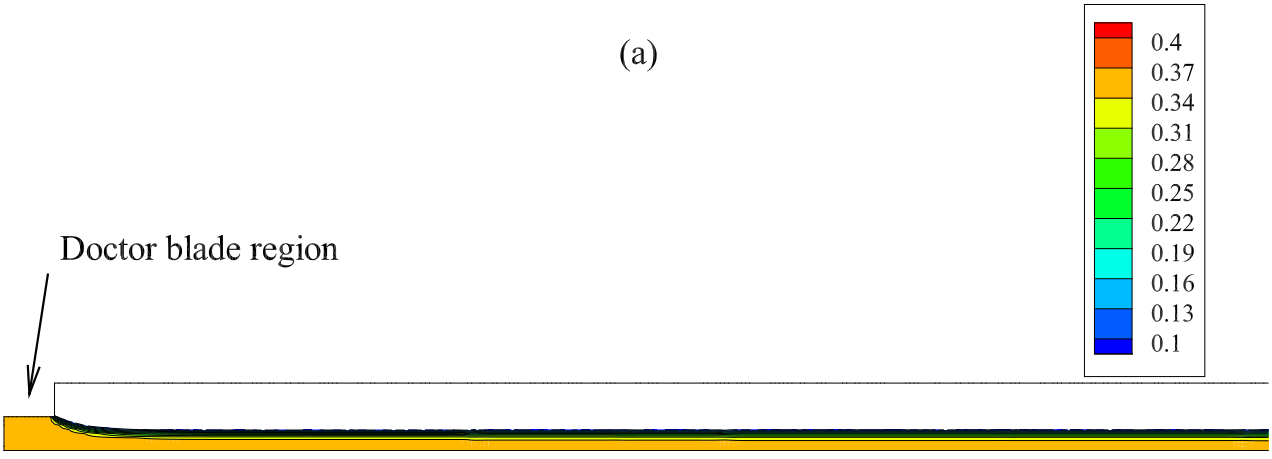

**Figure 4b**

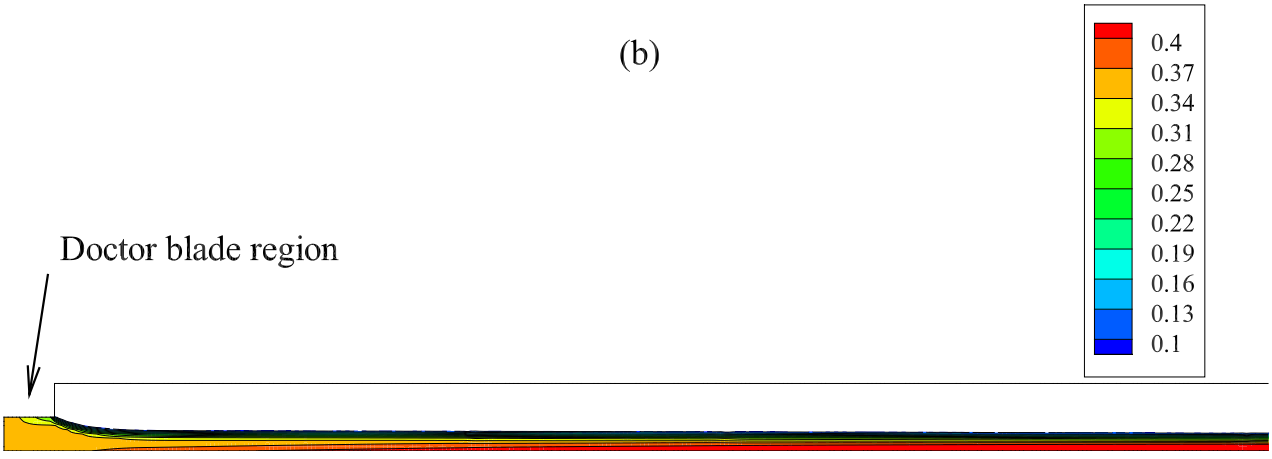

**Figure 5a**

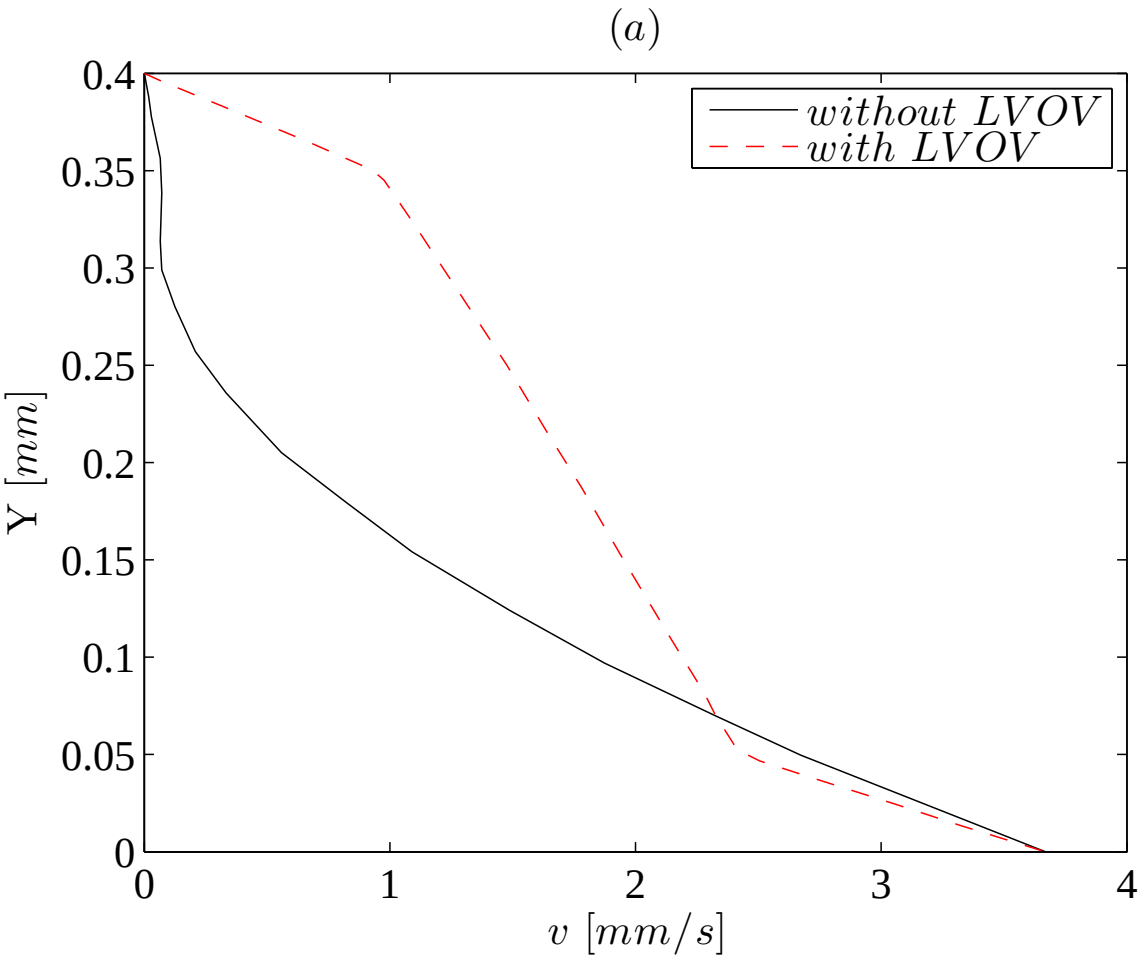
(a)
without LVOV
with LVOV
Y [mm]
v [mm/s]
0.4
0.35
0.3
0.25
0.2
0.15
0.1
0.05
0
0
1
2
3
4

**Figure 5b**

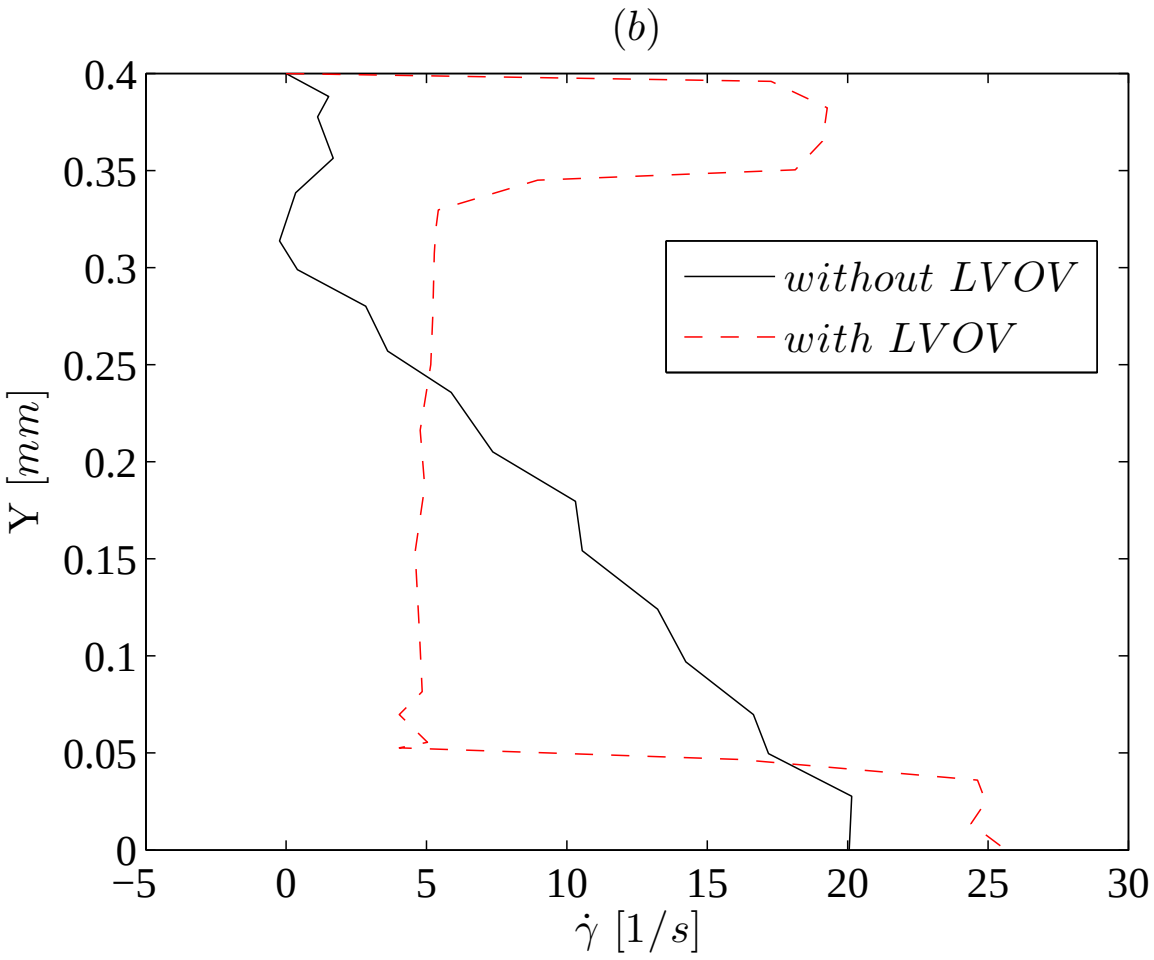
(b)
0.4
0.35
0.3
0.25
0.2
0.15
0.1
0.05
0
Y [mm]
−5
0
5
10
15
20
25
30
$\dot{\gamma}$ [1/s]
without LVOV
with LVOV

**Figure 6**

**Figure 7a**

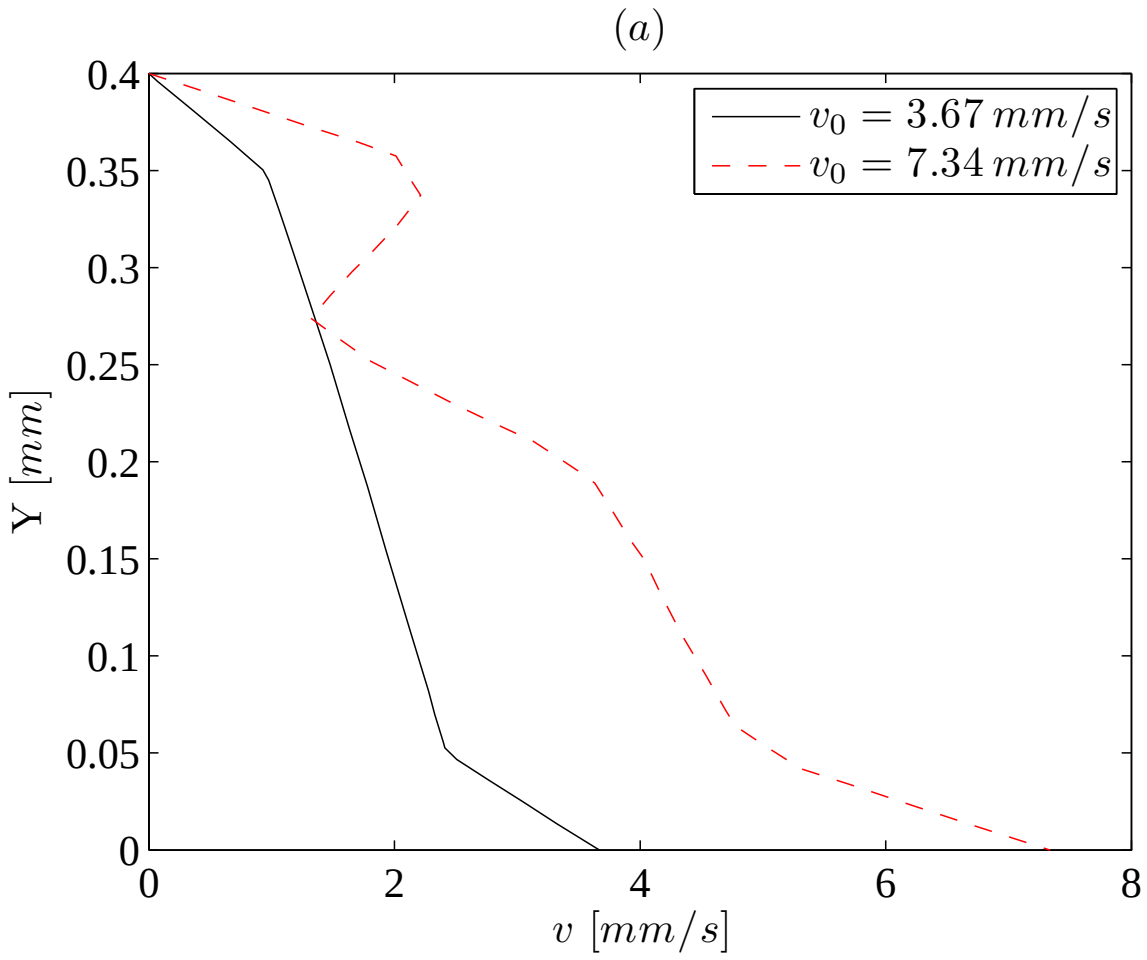
(a)
0.4
0.35
0.3
0.25
0.2
0.15
0.1
0.05
0
Y [mm]
0
2
4
6
8
v [mm/s]
v0 = 3.67 mm/s
v0 = 7.34 mm/s

**Figure 7b**

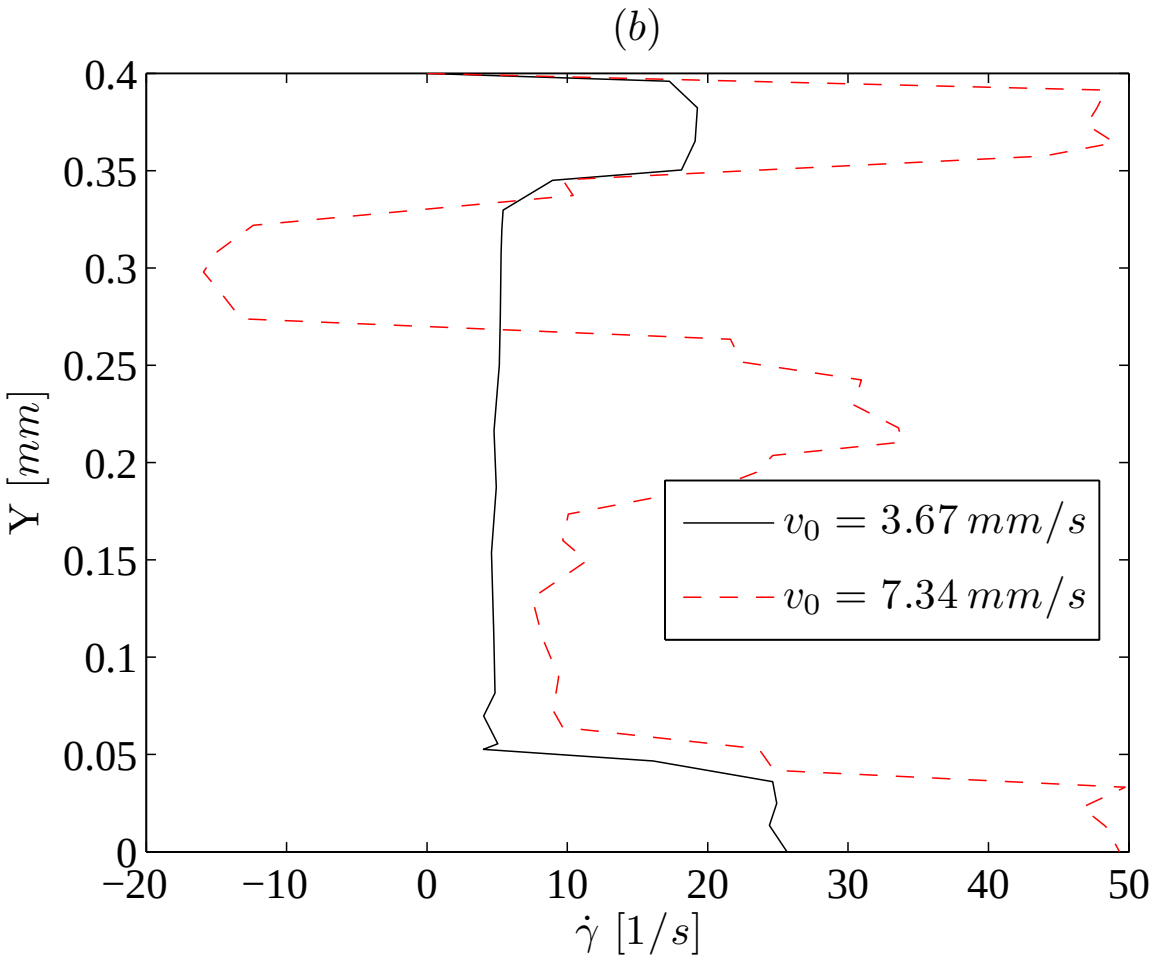
(b)
0.4
0.35
0.3
0.25
0.2
0.15
0.1
0.05
0
Y [mm]
−20
−10
0
10
20
30
40
50
$\dot{\gamma}$ [1/s]
$v_0 = 3.67\,mm/s$
$v_0 = 7.34\,mm/s$

**Figure 8a**

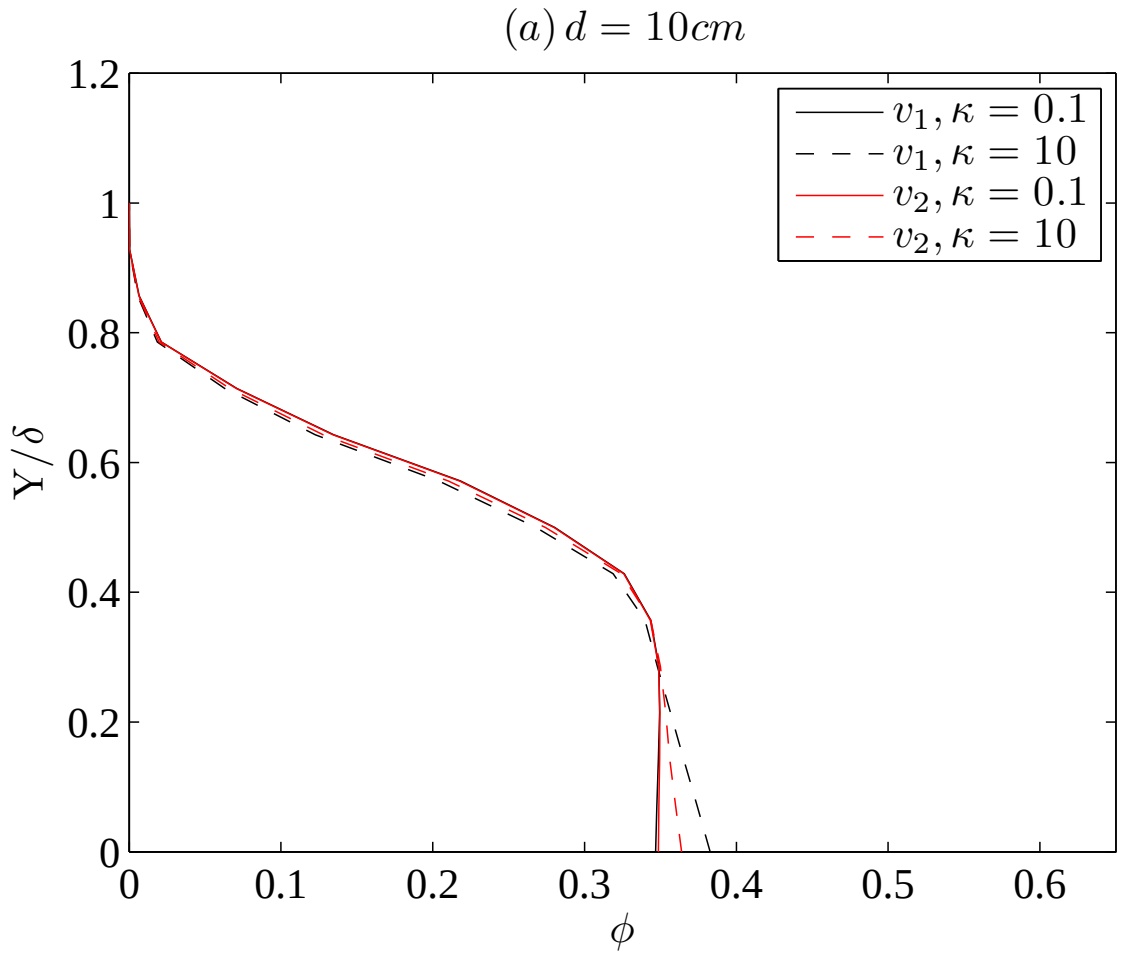
$(a)\, d = 10cm$
$v_1, \kappa = 0.1$
$v_1, \kappa = 10$
$v_2, \kappa = 0.1$
$v_2, \kappa = 10$
Y/δ
$\phi$
0
0.2
0.4
0.6
0.8
1
1.2
0.1
0.3
0.5

**Figure 8b**

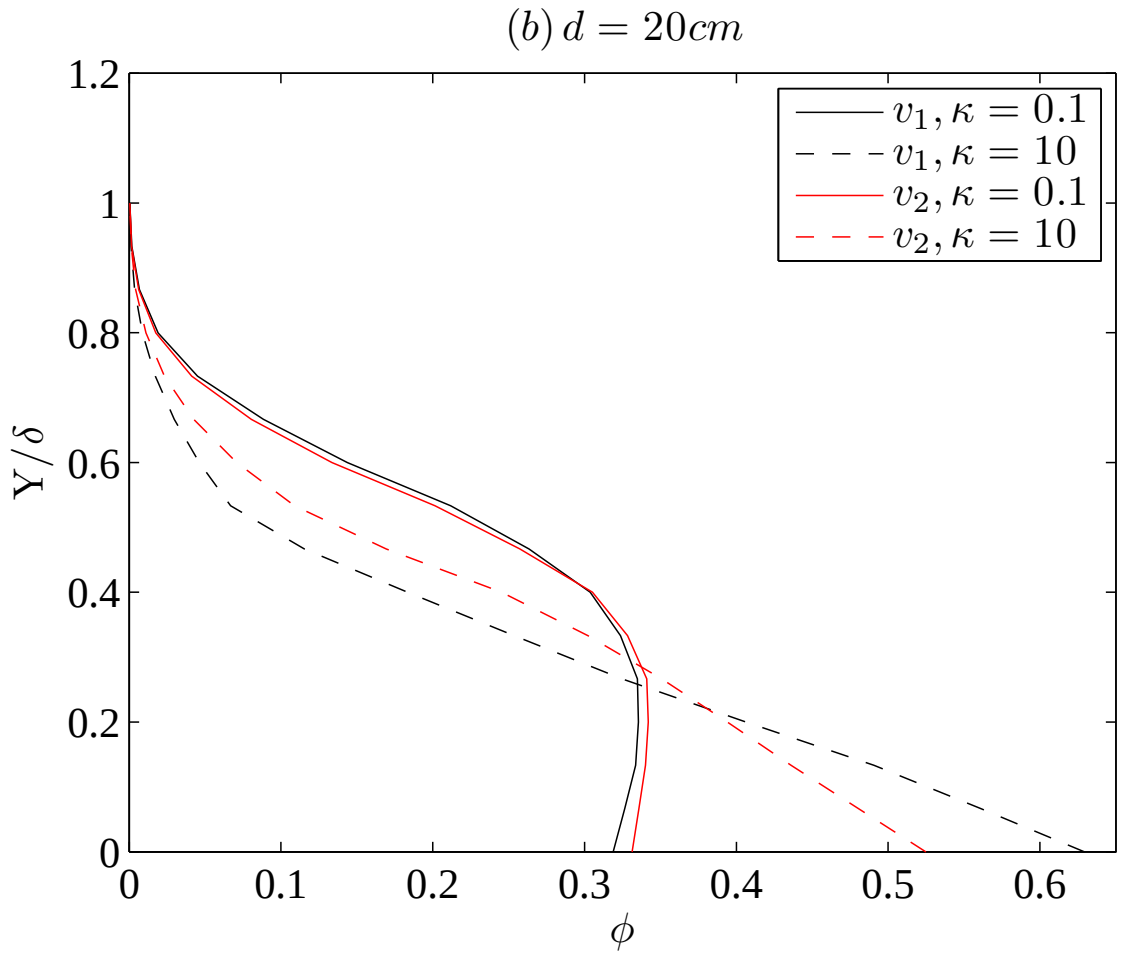
$(b)\, d = 20cm$
$v_1, \kappa = 0.1$
$v_1, \kappa = 10$
$v_2, \kappa = 0.1$
$v_2, \kappa = 10$
$Y/\delta$
$\phi$
0
0.2
0.4
0.6
0.8
1
1.2
0.1
0.3
0.5

# Appdx G

M. Jabbari, J. Hattel, "Modelling the drying process in tape casting with a simple ceramics-water system", *Continuum Mechanics and Thermodynamics*, 2014 (to be submitted).

# Modelling the drying process in tape casting with a simple ceramics–water system

M. Jabbari*, J. Hattel

September 17, 2014

*Process Modelling Group, Department of Mechanical Engineering, Technical University of Denmark, Nils Koppels Allé, 2800 Kgs. Lyngby, Denmark.*

**Abstract**

In this study, the evaporation of water from a ceramic-water mixture is investigated with the purpose of understanding the drying rate in the drying process of thin sheets produced by the tape casting process. The rate of mass loss in the drying process is a key factor which often is of interest, as it affects the final properties of the tapes. The 1D heat conduction equation is solved numerically to obtain the temperature field in a ceramic sheet. The change in the concentration of the water content is then used as the driving force for diffusive mass transport of the water. Mass-averaged thermal properties are assumed for the ceramic-water mixture in the initial stage, and as the water evaporates, the thermal properties of the solid ceramic become more dominant since the fraction of water approaches zero. The developed model is used to simulate a simple test for the drying process. The drying rate is simply calculated by examining the water content in each time step. It is found that the mass loss due to the evaporation is increasing close to linearly with the drying time corresponding to an almost constant drying rate. However, the rate starts to decrease after some time in the simulation.

Keywords: Evaporation, drying rate, heat conduction, Fick's law, ceramics

*Corresponding author: Tel. : +45-45254734; fax: +45-45930190; E-mail address: mjab@mek.dtu.dk (Masoud Jabbari).

## Nomenclature

| | |
|---|---|
| $\alpha$ Thermal diffusivity $[m^2/s]$ | $D$ Diffusion coefficient $[m^2/s]$ |
| $\alpha_{ceramic}$ Thermal diffusivity of ceramic $[m^2/s]$ | $f_{water}$ Fraction of water |
| $\alpha_{mix}$ Thermal diffusivity of mixture $[m^2/s]$ | $h$ Convective heat transfer coefficient $[W/m^2K]$ |
| $\alpha_{water}$ Thermal diffusivity of water $[m^2/s]$ | $k$ Thermal conductivity $[W/mK]$ |
| $\delta$ Tape thickness $[\mu m]$ | $N$ Number of control volumes |
| $\dot{Q}$ heat generation $[W/m^3]$ | $q$ Diffusive heat flux $[W]$ |
| $\phi$ Concentration of water $[mol/m^3]$ | $Q_a$ Activation energy for diffusion $[J/mol]$ |
| $\rho$ Density $[kg/m^3]$ | $R$ Gas constant $[J/molK]$ |
| $\sigma$ Stefan-Boltzmann constant $[W/m^2K^4]$ | $R_{th}^{cond}$ Conductive thermal resistance $[K/W]$ |
| $\varepsilon$ Surface emissivity | $R_{th}^{conv}$ Convective thermal resistance $[K/W]$ |
| $A$ Area $[m^2]$ | $R_{th}^{rad}$ Radiative thermal resistance $[K/W]$ |
| $c_p$ Specific heat $[J/kgK]$ | $T$ Temperature [°C] |
| | $T_\infty$ Cooling temperature [°C] |

# 1 Introduction to tape casting

Being mainly used in the electronics industry, tape casting as a forming method of ceramics is growing in production of numerous multilayer applications and electronic substrates, like e.g. capacitors, piezoelectric actuators, gas sensors, etc., where high quality and low geometry tolerances are required [1, 2]. In the tape casting process, the ceramic slurry is mostly categorized as a non-Newtonian fluid with relatively high viscosity [1–5]. A summary of work published regarding the rheological classification of non-Newtonian fluids and the existence of analytical/numerical models with focus on tape casting have been given previously by the authors [2, 5].

Tape casting consists of three major sub-processes which are (see Figure 1):

1. Tape casting of an aqueous (fluid) ceramic slurry in a doctor blade configuration
2. Drying of the green tape
3. Additional processing (which is often a sintering process).

Mostly the first and third stages have been investigated numerically [1–6] whereas the second has remained almost unexplored numerically. The sintering of the tape casted parts has been investigated in literature using continuum modelling [6]. The drying stage and the characterization of it in the form of final shrinkage is often measured experimentally, simply by the weight difference of the green and dried

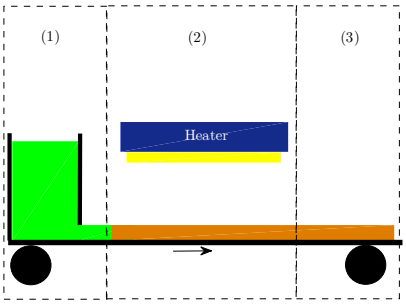


Figure 1: Schematic of the tape casting process with the three sub-processes: (1) tape casting of the ceramic slurry, (2) drying of the tape, and (3) extra processing.

tapes, without really noticing that the drying is one of the most important steps in the tape casting process. As the solvent is removed from the green sheet (or layer) via evaporation, the tape undergoes a transformation from its initial fluid-like state to a solid-like, composite layer. This leads to changes in the rheological behavior (mostly viscosity) of the ceramic slurry, and this is related to the amount of solvent (water in this study) evaporated during drying [7].

With many additives, and typically multiple solvents, drying of the tape as well as the behavior of the tape during the drying process can vary greatly from slip to slip. The tape casting process is somewhat unique among ceramic processes in the sense that a one-side drying process exists. After the slip is spread into a thin layer, all of the solvent is removed from a single side of the cast. Two things work together to cause the one-sided drying; a thin, essentially two-dimensional shape with no real height, and an impermeable carrier on the bottom. This single-sided drying is the cause of some very interesting phenomena within the tape matrix. Ideally, the chemical composition of the tape (primarily the solvent concentration) should stay uniform throughout the tape during the entire drying process. This, however, simply cannot occur, since all of the solvent must migrate to the top surface of the tape to evaporate. Hence, the two major mechanisms controlling the drying in the tape-cast layer are: (1) the rate of solvent evaporation from the surface of the cast and (2) the rate of solvent diffusion through the tape to the drying (top) surface. Of these two mechanisms, diffusion through the tape tends to be the rate-limiting factor [8].

The two aforementioned mechanisms can be adjusted by various means. The volatility of the solvent at the tape surface can be adjusted by adapting the types of solvent used, the concentration of solvent vapor in the local atmosphere, the local air temperature, and the solvent temperature. The diffusion rate through the tape layers can be adjusted by changing the binder concentration, altering particle size, adjusting the wet film temperature, and keeping an open pathway to the surface. Some of these control techniques, such as particle size and binder content, need to be addressed during the preparation of the slip and factored into the initial slip recipe. Other parameters like air temperature, slip temperature, and local vapor concentration are controlled by the drying equipment separate from the casting slip.

As the solvent on the top surface of the cast layer takes energy from the air and from the rest of the slip, it starts to evaporate into the surrounding atmosphere. The rate of evaporation is governed

by the energy available to the solvent, the volatility of the solvent species, the vapor concentration of the local atmosphere, and the saturation concentration of the local atmosphere, which depends upon the gases in the atmosphere, the solvent species, and the temperature. Since evaporation requires an input of energy, raising the temperature of the solvent will speed the surface evaporation process by providing an excess of energy. Raising the air temperature will not only provide the energy for evaporation (heat of vaporization), but will also increase the saturation concentration of the atmosphere. Air heating greatly increases the surface evaporation rate, and that is why many tape casting machines are equipped with an air heating option to speed up the surface evaporation of the tape. In this study, only the raise of energy (by the temperature field) is considered for the drying process and the influences of saturation are neglected.

Diffusion of the solvent to the top surface of the tape is normally the rate limiting factor in drying. The rate of evaporation of surface solvent is normally so much faster than the solvent motion to the surface that a drying crust forms across the surface of the tape. Efforts to limit surface evaporation stem from the desire to avoid this skin on the surface. Ideally, the solvent concentration should stay nearly uniform throughout the tape during drying so that all parts of the tape dry at the same rate. This would be accomplished by making the rate of diffusion equal to the rate of evaporation. The ideal case, however, is unattainable. In practice, the drying conditions, tape structure, tape components, and solvent mixtures are balanced to get as close to ideal conditions as the downstream manufacturing needs allow.

The hypothetical progression of solvent concentration during the drying process is illustrated in Figure 2 graphically. On the figure, $y = 0$ represents the carrier surface whereas $y = 1$ represents tape thickness (the drying surface). It is assumed that at time equal to zero the concentration of the solvent is equal to one, and the final concentration of the solvent at $t = 1s$ is equal to $C = 0.1$. As mentioned, the ideal case shows a uniform solvent concentration through the thickness of the tape throughout the drying process (Figure 2(a)). In reality, the evaporation rate from the surface will always be faster than the motion of solvent to the surface. Thus the best-case scenario displays a dry film on the top of the tape, yet a diminishing amount of solvent at the slip/carrier interface (Figure 2(b)). This best-case scenario exists when the rates of diffusion and evaporation are as close to equal as possible. The worst-case scenario is realized when the rate of evaporation is much greater than the diffusion rate through the tape matrix. The top surface of the tape, giving off solvent much more quickly than the diffusion mechanism can replace it at the surface, forms an ever-thickening dry layer, while the solvent concentration at the slip/carrier interface does not significantly decrease (Figure 2(c)).

The speed at which the solvent can move to the surface is always the slowest mechanism of drying. The rate of motion through the body of the tape is limited mainly by the body itself. The pathway for the solvent through the tape matrix is crowded with particles, binder, plasticizer, and dispersant. As the drying process progresses, the tape shrinks, creating the dense, packed bed of particles which is the goal of tape casting. This dense, packed bed, however, limits the escape paths for the solvent at the slip/carrier interface. As a rule, liquids diffuse much more quickly through a liquid medium than through any other medium [10]. At some point in the drying process, the binder at the top surface of the cast will lose enough solvent to form a solid sheet or skin across the top of the tape. This is unavoidable since the dry tape is simply a solid piece of this skin. The diffusion rate of the underlying solvent is much slower through this skin than through the liquid matrix of the slip. This, once again, is why effort is made to slow the surface evaporation rate to delay the formation of this low-diffusion-rate skin. The dried polymer

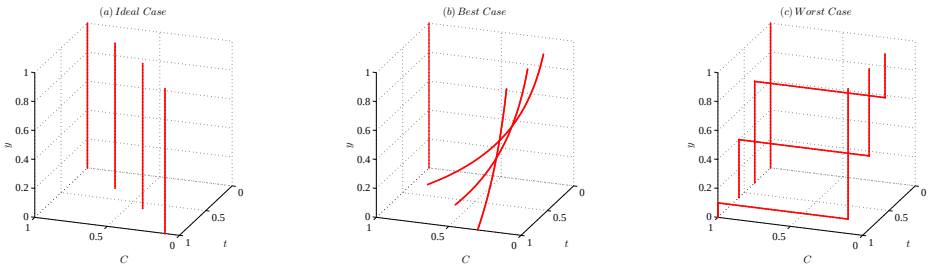


Figure 2: Schematic illustration for distribution of solvent content for (a) ideal, (b) best obtainable, and (c) worst cases [9].

effectively plugs up the inter-particulate spaces, creating a low-permeability layer across the top of the tape and limiting the bulk drying rate. This is where a balance must somehow be established between drying rate and tape porosity. Allowing some porosity in the tape will increase solvent diffusion to the top surface by keeping an open pathway to the top surface. The addition of a slow-drying solvent can also aid solvent migration speed by delaying skin formation and providing a liquid pathway from bottom to top. This type of additive would properly be called a skin retarder and may actually be used as one of the primary solvents in the slip.

Heating the tape body is the last general phenomenon which affects both drying mechanisms. This not only increases solvent evaporation rate by heating the solvent, but also increases the diffusion speed of solvent through the matrix, as the diffusion is a thermally controlled phenomenon. Heating the tape matrix promotes liquid-like behavior and increases the diffusion rate of the solvent. Many practitioners in the field find that the fastest way to dry a tape is to heat the bottom of the tape without heating the air. Heating the bottom of the tape increases solvent mobility in the tape body, driving the solvent up to the surface, while air heating tends to have a greater impact on the tape surface evaporation. In most cases, the surface evaporation does not need help.

In general, modelling of the drying process deals with complex physics, e.g. heat transfer, mass transfer (Darcy's law and diffusion), and capillary forces (pressure), which are coupled together. The theory of the drying is well discussed by Schere [8] for the sol-gel processing, where there is a polymer chain. On the other hand, only experimental and analytical investigations [7, 11] have been conducted in literature so far for the drying process of ceramic slurries. The current study is the first example of numerical investigation for coupled heat and mass transfer for drying in tape casting of ceramics. The capillary forces are neglected in this study and it is assumed that the mass transfer is governed only by diffusion of the solvent. It should, moreover, be mentioned that as the solvent used in every slurry formulation varies for every desired application, and the thermo-physical properties of each solvent are not available in literature, the solvent in this study is assumed to be water, and hence the system simulated is the mixture of ceramic and water. The first stage of drying where the solvent is evaporating from the tape matrix is simulated numerically. The 1D heat conduction equation is solved numerically to obtain the temperature field in a ceramic sheet. The change in the concentration of the water content is then used as driving force for the diffusive mass transport of water (described by Fick's second law also in 1D).

## 2 Mathematical model

### 2.1 Simulation domain

The 1D simulation domain used in this study is illustrated schematically in Figure 3. As seen, a heater with the length of $L_{heat}$ and the temperature of $T_{heat}$ is located above the tape layer, and the tape (which is a ceramic-water mixture) is passing beneath the heater with the velocity of $v_{cast}$. This means that the tape experiences the major part of the temperature load for a period of time equal to $L_{heat}/v_{cast}$. The domain is discretized into a number of control volumes (here $N$), in a way such that the air region is assumed to be one single control volume. This leads to the space increments as follows

$$\begin{cases} dx(1) = d_{gap} & air\ region \\ dx(2:N) = \frac{\delta}{N-1} & tape\ region \end{cases} \tag{1}$$

where $\delta$ is the tape thickness, and $d_{gap}$ is the distance between the heater and the top surface of the tape.

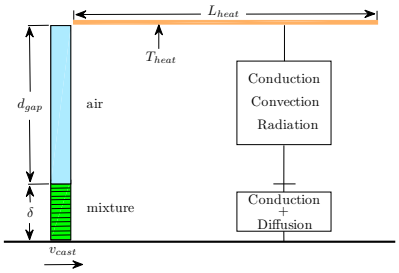


Figure 3: Schematic illustration of the simulation domain.

The physics to be considered in this numerical study, is also shown in Figure 3 for each region, and will be discussed in the following.

### 2.2 Thermal calculations

It is well-known that in the presence of a temperature gradient, energy conducts from the high temperature region to the low one. Based on Fourier's law the heat flow per unit area is proportional to the normal temperature gradient, i.e.:

$$q = -kA\frac{\partial T}{\partial x} \tag{2}$$

where $q$ is the diffusive heat flux $(W)$, $A$ is the area $(m^2)$, $k$ is the thermal conductivity $(W/mK)$, $T$ is temperature $(K$ or $^\circ$C), and $x$ is length $(m)$. Assuming a constant thermal conductivity, the integration of Fourier's law becomes

$$q = -\frac{kA}{x_2 - x_1}(T_2 - T_1) = -\frac{\triangle T}{R_{th}^{cond}} \qquad where \qquad R_{th}^{cond} = \frac{\triangle x}{kA} \tag{3}$$

in which $R_{th}^{cond}$ is the conductive thermal resistance.

Based on Newton's law of cooling the overall effect of convection can be expressed by:

$$q = -hA\left(T_\infty - T_s\right) \tag{4}$$

where $h$ is the convective heat transfer coefficient ($W/m^2K$), $T_s$ and $T_\infty$ are the body surface temperature and the cooling temperature, respectively. Comparing equations (3) and (4), the thermal convective resistance becomes

$$R_{th}^{conv} = \frac{1}{h^{conv}A} \tag{5}$$

The third mode of heat transmission taking place is radiation, which is expressed with a special version of Stefan-Boltzmann's law

$$q = -A\varepsilon\sigma\left(T_2^4 - T_1^4\right) = -A\varepsilon\sigma\left(T_1^3 + T_1^2T_2 + T_1T_2^2 + T_2^3\right)\left(T_2 - T_1\right) \tag{6}$$

where $\sigma$ is the Stefan-Boltzmann constant, and equals to $5.67 \times 10^{-8}$ ($W/m^2K^4$). This equation assumes a radiative heat exchange between two surfaces (with the same area, $A$), and accounts for the gray nature of the surface (accounting for the emissivity, $\varepsilon$). Comparing equations (3) and (6), the thermal radiative resistance can be found as

$$R_{th}^{rad} = \frac{1}{h^{rad}A} \qquad where \qquad h^{rad} = \varepsilon\sigma\left(T_1^3 + T_1^2T_2 + T_1T_2^2 + T_2^3\right) \tag{7}$$

The general heat conduction equation can be derived based on Fourier's law together with the first law of thermodynamics:

$$\rho c_p\frac{\partial T}{\partial t} = \nabla\left(k \cdot \nabla T\right) + \dot{Q} \tag{8}$$

where $\rho$ is the density ($kg/m^3$), $c_p$ is the specific heat ($J/kgK$), and $\dot{Q}$ is the generated heat per unit time per unit volume ($W/m^3$). Assuming constant thermal conductivity, the 1D heat conduction equation finally takes the form

$$\frac{\partial T}{\partial t} = \alpha\frac{\partial^2 T}{\partial x^2} + \dot{Q} \tag{9}$$

where $\alpha$ is the thermal diffusivity equal to $k/\rho c_p$. In the present study the above equation is discretized in the simulation domain via the finite volume method (FVM) in order to solve it numerically [12]. Mass-averaged thermal properties are assumed for the ceramic-water mixture in the initial stage. However, as the water evaporates the thermal properties of the solid ceramic become more dominant since the fraction of water approaches zero. The mass-averaged thermal properties assumed for the ceramic-water mixture then are as follows

$$\alpha_{mix} = f_{water}\alpha_{water} + \left(1 - f_{water}\right)\alpha_{ceramic} \tag{10}$$

where $f_{water}$ is the fraction of water in each control volume.

An implicit scheme is used to find the new temperatures in each time step [12]

$$- H_i^{Con} T_{i-1}^{t+\triangle t} + \left( H_i^{Cap} + H_i^{Con} + H_{i+1}^{Con} \right) T_i^{t+\triangle t} - H_{i+1}^{Con} T_{i+1}^{t+\triangle t} = H_i^{Cap} T_i^t + \frac{\dot{Q}_{gen,i}^{t+\triangle t}}{A} \tag{11}$$

where $T_i^{t+\triangle t}$ is the new temperature, $T_{i,}^t$ is the old temperature, and

$$\begin{aligned} H_i^{Cap} &\equiv \tfrac{\triangle x_i (\rho c_p)_i}{\triangle t} \qquad capacity\ function \\ H_i^{Con} &\equiv \tfrac{1}{\frac{\triangle x_{i-1}}{2k_{i-1}} + \frac{\triangle x_i}{2k_i}} \qquad conductivity\ function \end{aligned} \tag{12}$$

It should be noted that for node 2 ($i = 2$), the conductivity function is as follows

$$H_2^{Con} \equiv \frac{1}{\frac{1}{h^{tot}} + \frac{\triangle x_2}{2k_2}} \tag{13}$$

where $h^{tot}$ is the equivalent heat transfer coefficient for the total transfer in the air gap

$$h^{tot} = \frac{1}{R_{th}^{cond}} + h^{conv} + h^{rad} \tag{14}$$

where $h^{conv}$ is assumed to be 10 $(W/mK)$, and $h^{rad}$ is given by equation (7). The coefficients in front of the unknown temperatures on the left hand side of equation (11) are now termed $a$, $b$, and $c$, and the right hand side is called $d$. thus for $i = 2, ..., N-1$, we have

$$a_i \cdot T_{i-1}^{t+\triangle t} + b_i \cdot T_i^{t+\triangle t} + c_i \cdot T_{i+1}^{t+\triangle t} = d_i \tag{15}$$

where

$$\begin{aligned} a_i &= -H_i^{Con} \\ b_i &= H_i^{Cap} + H_i^{Con} + H_{i+1}^{Con} \\ c_i &= -H_{i+1}^{Con} \\ d_i &= H_i^{Cap} T_i^t + \dot{Q}_{gen,i}^{t+\triangle t} / A \end{aligned} \tag{16}$$

The system of equations for the inner nodes, $i = 2, ..., N-1$, as well as for node 1 and $N$ as boundary condition become a classical tri-diagonal systems of equations, i.e.:

$$\begin{array}{c} node \\ 1 \\ 2 \\ ... \\ N-1 \\ N \end{array} \begin{Bmatrix} b_1 & c_1 & & & \\ a_2 & b_2 & c_2 & & \\ & ... & ... & ... & \\ & & a_{N-1} & b_{N-1} & c_{N-1} \\ & & & a_N & b_N \end{Bmatrix} \cdot \begin{Bmatrix} T_1 \\ T_2 \\ ... \\ T_{N-1} \\ T_N \end{Bmatrix} = \begin{Bmatrix} d_1 \\ d_2 \\ ... \\ d_{N-1} \\ d_N \end{Bmatrix} \tag{17}$$

The boundary conditions express that at node $i = 1$ the temperature of the heater is $T_{heat}$, and at $i = N$ the heat flux is zero

$$\begin{aligned} i = 1 \quad &\Rightarrow \quad b_1 = 1 \qquad c_1 = 0 \quad d_1 = T_{heat} \\ i = N \quad &\Rightarrow \quad a_N = -1 \quad b_N = 1 \quad d_N = 0 \end{aligned} \tag{18}$$

The equation system is solved easily by Gaussian elimination.

### 2.3 Diffusion

Fick's second law, also known as the Diffusion Equation, states that the change of concentration in time equals to the net influx by diffusion. This leads to an equation which is totally similar to the heat conduction equation

$$\frac{\partial \phi}{\partial t} = \frac{\partial}{\partial x}\left(D\frac{\partial \phi}{\partial x}\right) \tag{19}$$

where $\phi$ is the concentration of water ($mol/m^3$), and $D$ is the diffusion coefficient ($m^2/s$), which in general is dependent on temperature in the present work. In order to solve equation (19), the same implicit scheme is used as described in section 2.2.

The diffusivity is found to vary in most systems as an exponential function of temperature, hence it is modeled by the Arrhenius relationship:

$$D_w = D_0 exp\left(-\frac{Q_a}{RT}\right) \tag{20}$$

where $Q_a$ is the activation energy for diffusion, $R$ is the gas constant, $T$ is the absolute temperature, and $D_0$ is the pre-exponential "frequency factor" which is empirically determined. The activation energy may be thought of as that energy required to produce the diffusive motion of one mole of atoms. A large activation energy results in a relatively small diffusion coefficient. Taking the natural logarithm of equation (20) yields

$$\ln D_w = \ln D_0 - \frac{Q_a}{R}\left(\frac{1}{T}\right) \tag{21}$$

or in terms of logarithms to the base 10

$$\log D_w = \log D_0 - \frac{Q_a}{2.3R}\left(\frac{1}{T}\right) \tag{22}$$

For this study such data are used through the fitted line from the experimental results published by Holz et al. [13] (shown in Figure 4), as follows:

$$\log D_w = 3 \times 10^{-7} - 8 \times 10^{-8}\left(\frac{1}{T}\right) \tag{23}$$

The mass-averaged diffusion coefficient is used for the ceramic-water mixture as follows

$$D_{mix} = f_{water} D_w + (1 - f_{water}) D_d \tag{24}$$

where $D_d$ is the diffusion coefficient in the dried control volumes which is assumed to be $\log D_d = -11$, and $D_w$ is given by equation (23).

## 3 Results and discussion

All thermo-physical properties used in this study are summarized in Table 1. It should be noted that both the thermal [12] and diffusion [10] models have been validated against proper analytical solutions. The simulation domain considered for the present study is illustrated in Figure 3. The temperature of

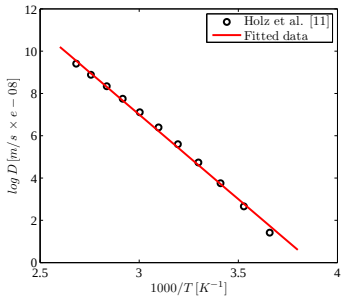


Figure 4: Fitted data used for the temperature-dependent diffusion coefficient of water.

the heater on the top region of the tape matrix is assumed to be 140°C. The initial temperature of the tape matrix and the air above it is assumed to be in the room temperature (20°C). It should also be mentioned that since the saturation of air is neglected in this study, choosing a different temperature for air from the one for tape matrix does not make any sense.

Table 1: Thermo-physical material properties used in this study.

| | Water | Ceramic | Ceramic-water mixture |
|---|---|---|---|
| $k\ (W/mK)$ | 0.6 | 2.4 | mass-averaged |
| $\rho\ (kg/m^3)$ | 997.1 | 1900 | mass-averaged |
| $c_p(J/kgK)$ | 4187 | 2000 | mass-averaged |
| $L_H^{evap}(kJ/kg)$ | 2260 | - | - |
| $\log D$ | equation (23) | $-11$ | mass-averaged |

Results of simulations for three different tape thicknesses, $\delta = 400, 300, 200\ \mu m$ with an initial water content of 12%, are shown in Figure 5(a). The results show that for each tape there is a specific time period in which the water content is not changing hence being equal to the initial value of water content (12%). This region corresponds to the period in which the tapes are heating up, and it has the highest value for the thickest tapes which of course is expected, see Figure 5(a).

As seen from the sub-plot of Figure 5(a) (which is also representative for thicknesses of 200 and 300 $\mu m$), there are two specific regions, (1) and (2), where the evaporation shows two principally different behaviors. A similar example of such plots showing these two regions can be found in the work by Kiennemann et al. [11], in which mass loss, shrinkage, Young's modulus evolution and stress development of aqueous (alumina+latex) tape cast suspensions were observed experimentally during drying. They also reported that the mass loss shows a constant drying rate period, followed by a falling rate period. In region (1) the total evaporation (mass loss) is increasing almost linearly by time. This region is called the constant rate period (CRP), in which the rate of evaporation per unit area of the drying surface is independent of time [8]. During the CRP, the liquid-vapor meniscus remains at the surface of the tape layer, and evaporation occurs at a rate close to that of a free liquid surface (e.g., an open dish of liquid).

When evaporation starts, in the early stages, the temperature at the surface of the top layer drops because of a loss of heat due to the latent heat of vaporization of the water. On the other hand, heat flows

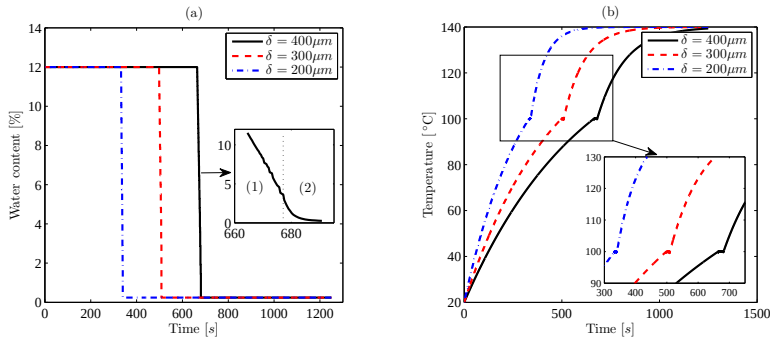


Figure 5: (a) Variation of water content due to evaporation, and (b) the temperature profiles for the top control volume in the tape.

to the surface from the atmosphere thus quickly establishing thermal equilibrium where transfer of heat to the surface balances the heat loss due to the latent heat of vaporization. However, when the amount of mass loss increases, the heat loss due to the latent heat of vaporization of the water will also increase. This reduces the evaporation rate, as a consequence of low migration of the water from the bottom layers to the top ones due to diffusion (which is highly dependent on the temperature). This is the late stage in the CRP, where the drying rate starts to decrease.

The top layers of the tape, which are already dried, will now act as a barrier for diffusion of the water from bottom to top. This is reflected by region (2), which is known as the falling rate period (FRP). Transport of liquid during drying can occur by flow if a pressure gradient exists in the liquid, and diffusion if a concentration gradient exists. The first type is categorized as flow in porous media where the liquid flow obeys Darcy's law. This type of liquid transport, however, is neglected in this study due to the low level of pressure gradient in the tapes. The latter type is the one considered in this study, which is highly sensitive to temperature. As mentioned, the temperature drop reduces the diffusion coefficient of the water, and consequently the drying rate is decreased drastically. It can, moreover, be seen from Figure 5(a) and (b) that by deceasing the tape thickness ($\delta$) the mass loss occurs in a shorter period of time. This means that the drying rate is high in the tapes with smaller tape thickness, which can be seen in Figure 6. As shown, the maximum mass loss happens in the tape with smaller thickness. This is expected, as the smaller tape thickness gives the liquid ability to diffuse to the top surface more. Such information can be used in thermo-mechanical simulation in order to predict the stress evolution during drying.

Another interesting phenomenon in the drying process is to investigate the different drying modes, i.e. fast, intermediate, and slow. Results of such investigations are shown in Figure 7 based on the variation of the non-dimensional water concentration ($C^* = C^{new}/C_0$) for the thickness of $\delta = 400\mu m$. As seen, when the drying is fast, the water in the upper region evaporates fast and makes a solid-like region in almost the entire upper half of the tape. This creates a barrier for the diffusion of the bottom water and makes the rest of the drying slow. In other words, when the drying mode is fast, the diffusion of the water from bottom to the top surface is slow. This is similar to the worst case shown in Figure 2(c), which may happen if extensive heating is used in the drying process. Moreover, it is seen that for the slow drying

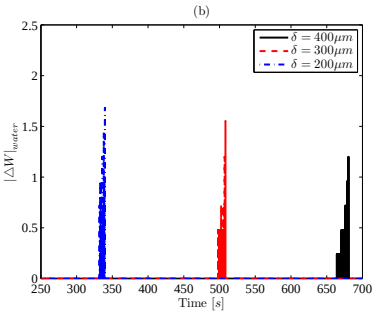


Figure 6: Amount of mass loss for three different tape thickness.

mode the evaporation of water from the top region is somewhat slow, though the drying (diffusion) from the bottom region is faster. This case is also similar to the ideal case shown in Figure 2(a). The mode of drying can hence be argued based on the competition between the evaporation rate from the top surface and the diffusion of the water from bottom to the top. As mentioned before, in reality, the evaporation rate from the top surface will always be much faster than the motion of solvent (water in this study) to the surface.

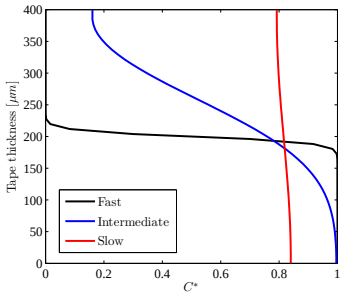


Figure 7: The results of numerical modelling for the different drying modes for the tape thickness of $\delta = 400\mu m$.

## 4 Conclusions

The evaporation of water from a ceramic-water mixture is investigated with the purpose of understanding the drying rate in the drying process of thin sheets produced by the tape casting process. The 1D coupled heat conduction and mass transport equations are solved numerically to obtain both the temperature field and the diffusive mass transport of the water.

The results showed that initially, the mass loss due to the evaporation is increasing close to linearly with the drying time corresponding to an almost constant drying rate. However, the rate starts to decrease after some time in the simulation. This is in good agreement with experimental findings of the real life

process where the drying is categorized into two stages: (1) a constant rate period (CRP), in which the rate of evaporation per unit area of the drying surface is independent of time, and (2) a falling rate period (FRP), in which the evaporation rate is reduced, as a consequence of low migration of the water from the bottom layers to the top ones due to diffusion (which is highly dependent to the temperature).

The results, moreover, showed that based on the hegemony of the evaporation rate from the top surface and the diffusion of the solvent from bottom to the top, the drying mode can vary from being fast to slow. It is concluded that too extensive surface drying results in a slow diffusion rate from the bottom, which in turn reduces the drying rate in general and hence is not favorable from a process viewpoint.

## Acknowledgment

The authors would like to acknowledge the support of the Research Council for Technology and Production Sciences (FTP) (Contract No. 09-072888, OPTIMAC), which is part of the Danish Council for Independent Research (DFF).

## References

[1] M. Jabbari and J. Hattel, "Numerical Modeling of Fluid Flow in the Tape Casting Process," vol. 1389 of *AIP Conference Proceedings Series*, pp. 143–146, Numerical Analysis and Applied Mathematics : ICNAAM, 2011.

[2] M. Jabbari, R. Bulatova, J. H. Hattel, and C. R. H. Bahl, "Quasi-Steady State Power Law Model for the Flow of $(La_{0.85}Sr_{0.15})_{0.9}\,MnO_3$ Ceramic Slurry in Tape Casting," *Materials Science and Technology*, vol. 29, pp. 1080–1087, 2013.

[3] M. Jabbari and J. Hattel, "Numerical Modeling of the Flow of a Power Law Ceramic Slurry in the Tape Casting Process," Tenth International Conference on Advances and Trends in Engineering Materials and their Applications, pp. 151–157, AES-ATEMA INTERNATIONAL CONFERENCE, 2012.

[4] M. Jabbari and J. Hattel, "Numerical Modeling of the Side Flow in Tape Casting of a Non-Newtonian Fluid," *Journal of the American Ceramic Society*, vol. 96, pp. 1414–1420, 2013.

[5] M. Jabbari and J. Hattel, "Bingham-Plastic Fluid Flow Model in Tape Casting of Ceramics Using Two Doctor Blades - An Analytical Approach," *Materials Science and Technology*, vol. 30, pp. 283–288, 2014.

[6] E. A. Olevsky, "Theory of sintering: from discrete to continuum," *Materials Science and Engineering R*, vol. 23, pp. 41–100, 1998.

[7] C. J. Martinez and J. A. Lewis, "Rheological, Structural, and Stress Evolution of Aqueous Al2O3: Latex Tape-Cast Layers," *Journal of the American Ceramic Society*, vol. 85, pp. 2409–2416, 2002.

[8] G. W. Scherer, "Theory of Drying," *Journal of the American Ceramic Society*, vol. 73, pp. 3–14, 1990.

[9] R. E. Mistler and E. R. Twiname, *Tape Casting, Theory and Practice*. The American Ceramic Society, 2000.

[10] W. D. Callister, *Fundamentals of Materials Science and Engineering*. John Wiley & Sons, Inc., 2000.

[11] J. Kiennemann, T. Chartier, C. Pagnoux, J. F. Baumard, M. Huger, and J. M. Lamérant, "Drying mechanisms and stress development in aqueous alumina tape casting," *Journal of the European Ceramic Society*, vol. 25, pp. 1551–1564, 2005.

[12] J. Hattel, ed., *Fundamentals of Numerical Modelling of Casting Processes*. 2005.

[13] M. Holz, S. R. Heil, and A. Sacco, "Temperature-dependent self-diffusion coefficients of water and six selected molecular liquids for calibration in accurate $^{1}$H NMR PFG measurements Manfred," *Physical Chemistry Chemical Physics*, vol. 2, pp. 4740–4742, 2000.